Stellingen behorende bij het proefschrift

Acoustoelastic Stress Evaluation in Metal Plate
using Absolute Shear and Longitudinal Time-of-Flight Data

1. Looptijdmetingen volgens de *Cross correlation* methode zijn gebaseerd op de veronderstelling dat storende factoren een gelijkmatige invloed hebben over de hele duur van de betrokken ultrasone golfvormen. Bij gebruik van een visceuze koppellaag is deze veronderstelling in strijd met de werkelijkheid.
   [Dit proefschrift, sectie 5.5.6.]

2. Ondanks het feit dat een directe mechanische koppeling vereist is, zijn piëzo-elektrische transducers bij uitstek geschikt voor nauwkeurige ultrasone metingen.
   [Dit proefschrift.]

3. De naam *Méér-dan-consumentengids* suggereert een gedrag bij college lopende studenten wat slechts zelden wordt waargenomen.

4. Een computerprogramma is een produkt waarin de fouten gratis worden meegeleverd, terwijl betaald moet worden om deze te laten verwijderen.

5. Hoewel volgens het promotiereglement van de TU-Delft (artikel 10, 1^{e} lid) een promovendus geacht wordt *zelfstandig onderzoek te verrichten of daaraan een essentiële bijdrage te leveren*, blijkt dit in toenemende mate niet het geval te zijn.

6. Vanwege hun reputatie zou het politici verboden moeten worden zich met politiek bezig te houden.

7. De meest effectieve manier om een goede hardlooprestatie te leveren is te zorgen voor gewichtsvermindering.

8. De opiumwet veroorzaakt een onveilig gevoel bij de burger en een enorme verspilling van belastinggeld.

9. Stellingen bij een proefschrift bieden de promovendus de mogelijkheid zijn frustraties te uiten.

10. Een meer sociaal gedrag van de automobilist wordt bevorderd door de gevolgen van zijn handelen sterker terug te koppelen. Dit kan worden bereikt door de bestuurder zelf een vast deel te laten leveren van de benodigde voortbewegingsenergie.

11. Bij het ontwerpen van verkeersdrempels in de bebouwde kom wordt ten onrechte niet uitgegaan van de dynamische eigenschappen van een BMW bij 80 Km/uur.

November 1994 Michael Janssen

Acoustoelastic Stress Evaluation in Metal Plate

using Absolute Shear and Longitudinal Time-of-Flight Data

Cover: Typical image obtained on the oscilloscope cathode-ray tube during time-of-flight measurements, representing a first and second shear wave back-face echo, the first zero crossings of which overlap.

Acoustoelastic Stress Evaluation in Metal Plate

using Absolute Shear and Longitudinal Time-of-Flight Data

Akoesto-elastische Spanningsmeting in Metaalplaat

met behulp van Absolute Transversale en Longitudinale Looptijden

PROEFSCHRIFT

ter verkrijging van de graad van doctor
aan de Technische Universiteit Delft,
op gezag van de Rector Magnificus Prof. ir. K.F. Wakker,
in het openbaar te verdedigen ten overstaan van een commissie,
door het College van Dekanen aangewezen,
op maandag 5 december 1994 te 13.30 uur

door

Michael Janssen

metaalkundig ingenieur
geboren te Soest.

Dit proefschrift is goedgekeurd door de promotor:
Prof. dr. ir. A. Bakker

Part of the research described in this thesis was sponsored by N.V. Nederlandse Gasunie and, under the coordination of the Netherlands Institute of Welding, by the Netherlands Ministry of Economic Affairs. All work was performed in the Fracture Mechanics Group of the Faculty of Chemical Technology and Materials Science at the Delft University of Technology.

Published and distributed by:

Delft University Press
Stevinweg 1
2628 CN Delft
The Netherlands
Telephone +31 15 783254
Fax +31 15 781661

CIP-DATA KONINKLIJKE BIBLIOTHEEK, DEN HAAG

Janssen, Michael

Acoustoelastic stress evaluation in metal plate using absolute shear and longitudinal time-of-flight data / Michael Janssen. - Delft : Delft University Press. - III.
Thesis Delft University of Technology. - With ref. - With summary in Dutch.
ISBN 90-407-1055-4
NUGI 841
Subject heading: acoustoelasticity / stress evaluation / ultrasonics.

Printed in The Netherlands

To the memory of my father, Dick Janssen

Preface

The research which finally led to this thesis was started in 1984 within the framework of my Master's degree in Metals Science at Delft University of Technology. It was Jan Zuidema who stimulated me to start work in the field of acoustoelasticity within the Fracture Mechanics Group. One of the reasons for this was the availability of ultrasonic equipment and know-how acquired during a previous research project concerning texture in rolled steel plate.

Initially the aim was to find an alternative means of evaluating the J-integral fracture parameter, namely by measuring the stress field surrounding the crack tip. Following a number of successful experiments and after I had obtained my Master's degree, the main goal shifted to the ultrasonic stress measurements themselves and in particular to the technique required in order to perform these experiments.

Improvements were made to the electronic part of the set-up, for which Mr H.J.A. Saeys of the *Central Electronic Service* gave expert assistance. He also introduced me to the *Development Workshop* of the Faculty of Electrical Engineering, where Mr L. Overvoorde was able to design and construct a transducer holder in accordance with the rigorous demands of the experiments.

The experimental possibilities were greatly enhanced by the co-operation of transducer manufacturers *Panametrics*. After several other suggestions, they proposed the idea of the combined shear-longitudinal transducer, as eventually used in the experiments. They also willingly provided information relating to their transducers for use in the model calculations.

A link with reality was established through experimental work on pipeline steel for *N.V. Nederlandse Gasunie*. This project was initiated thanks to Mr Jan Spiekhout. My meetings with him were both stimulating and informative.

Anton Wachters proved many times to be a valuable discussion partner. During the final stages in the preparation of this thesis he significantly minimized the number of errors and cryptic passages, thanks to his desire to reduce problems to a basic and comprehensible level. Mrs Hazel Wachters substantially improved on my use of the English language, which is of undoubted benefit to the reader.

I am grateful to all those, including persons inadvertently not mentioned above, who in any way contributed to the completion of this work. In particular I should like to thank Ad Bakker for providing the opportunity for me to complete the research in the way it was carried out and for the confidence which this expresses in the result. Finally, my special gratitude goes to my wife Ellie. I was often preoccupied with my work, but her support remained unfailing.

October 1994 Michael Janssen

The Author

Michael Janssen was born on 27 August 1952 in Soest, The Netherlands. He obtained his *MULO-B diploma* in 1969. After a preparatory year he went on to study metals science at the *Hogere Technische School* in Utrecht. As part of this course he was briefly employed by *AKZO-PLASTICS* in Zeist, the Physics Laboratory at *Philips* in Eindhoven, by *Hoogovens* in IJmuiden and the *DEMKA Staalfabrieken* in Utrecht. His final project concerned concentration-dependent diffusion of water and methanol in polyamide and the effect which this has on stress corrosion in zinc chloride solutions.

In 1974 the author commenced his studies at Delft University of Technology in the Interdisciplinary Department of Metals Science and Technology, which was later merged to become the Faculty of Chemical Technology and Materials Science. In 1975, after completing the first year, he had to interrupt his studies for military service. From 1981 to 1985 he was a student assistant supervising practical work for students in the form of physical experiments on metals. This work clearly increased his insight into experimental problems. In 1984 he joined the Fracture Mechanics Group of the Faculty, where he began research on the application of the acoustoelastic effect for the evaluation of the J fracture parameter as a contour integral. Based on this work he obtained a Master's degree (cum laude) in November 1985.

Following this, as a research assistant, he continued work on acoustoelastic stress evaluation with the aim of writing a Ph.D. thesis on the subject. In June 1990 he was appointed Assistant Professor. He is presently engaged in teaching in the field of Fracture Mechanics.

Contents

Notation

Throughout this thesis vector and tensor quantities are represented either by underlined symbols or in index notation. In the latter notation summation is implied over indices repeated in one term. Indices may take the values 1, 2 and 3, unless stated otherwise, and are denoted by the letters i, j, k, l, m, n and p, q, r, s.

The following symbols are used:

a_I	Axis intersection of linear regression line
A	Transducer area
	Scalar amplitude in Fresnel-Kirchhoff diffraction formula
A_o	Scalar amplitude at aperture in Fresnel-Kirchhoff diffraction formula
A_{ij}	Element ij of matrix relating mechanical and electrical quantities in the model transducer
b_I	Slope of linear regression line
$_b$	Subscript indicating backing layer
B_{ij}	Element ij of matrix relating mechanical quantities in the coupling layer
c	Phase velocity
$_c$	Subscript indicating coupling layer
c_{ijkl}, c_{ijklmn}	2^{nd}-, 3^{rd}-order elastic stiffness constants
C_1, C_2	Spring moduli of viscoelastic constitutive model
C_{ij}	Element ij of matrix relating the transducer electrode voltage and current density to the transmitted and received wave amplitudes
$\underline{C}$	Stiffness tensor
$\underline{C}^E$	Stiffness tensor for constant electric field
$\underline{\tilde{C}}$	Complex stiffness tensor for an attenuating medium
d	Disc diameter
d_x	Thickness of layer x
C_{ij}	Element ij of matrix relating the conditions at the transducer electrode and the transmitted wave amplitude to the driving voltage and the received wave amplitudes
$\underline{D}$	Electric displacement
e	Piezoelectric stress constant
$\underline{e}$	Piezoelectric stress tensor
E	Young's modulus
$\underline{E}$	Electric field
f_I	Coefficient relating applied stress to plane stress component T_I
$\underline{G}$	Alternative Christoffel tensor (Eq. 2.8)

h	Thickness of viscous fluid layer between transducer and specimen
$\tilde{h}$	See Equation 5.43 or 5.51 for arc or strip diffraction respectively
$\bar{h}_k$	Discrete average values for $\tilde{h}$ (Eq. 5.55)
H	Frequency-dependent transfer function
H_x	Transfer function of layer x
$\dot{H}$	Transfer function relating amplitudes at the transmitter and a point on the receiver
$\tilde{H}$	The Fourier transform of $\tilde{h}$ to frequency domain (Eq. 5.52)
$\bar{H}_n$	The discrete Fourier transform of $\bar{h}_k$ to frequency domain
I	Impulse applied to transducer
	See Equation 5.45
I_e	Transducer electrode current
I_J	Integrand of J
J	Fracture parameter
J_e	Transducer electrode current density
k	Wave number
k_x	Wave number in layer x
$\underline{k}$	Acoustoelastic tensor relating applied stress to acoustic data obtained with shear waves
K_I, K_{Ic}	Stress intensity factor, fracture toughness
$\underline{K}$	Tensor relating $\underline{G}$ and $\underline{T}$
$_l$	Subscript indicating protective layer
L	Distance of flight
$_m$	Subscript indicating propagation medium
$\underline{m}$	Acoustoelastic tensor relating absolute stress levels to acoustic data
M	Number of subtransducers
$\underline{M}$	Tensor relating $\underline{R}$ and $\underline{T}$
n	Back-face echo number
$\underline{n}$	Unit vector along wave propagation
	Unit vector normal to surface
N	Number of sample points in time domain used for model calculations
p	Pressure in fluid
	See Figure 5.8
$_p$	Subscript indicating piezoelectric plate
P	Compressive force per unit thickness
$\underline{Q}$	Tensor containing acoustic data relating to shear waves
r	Radius in polar coordinates
	Length of wave ray in diffraction calculation
R	Transducer radius

R_{xy}	Reflection coefficient of stress wave travelling in medium x against interface with medium y
$\underline{R}$	Tensor containing acoustic data relating to both shear and longitudinal waves
$\underline{R}^o$	Reference values for absolute stress evaluations
s	Arc length
s_1, s_2	Arbitrary signals
s_{ijkl}	Elastic compliance constants
S	Surface enclosing an observation point P in Fresnel-Kirchhoff diffraction formula
$\underline{S}$	Strain tensor
t	Time
	Time of flight
$\bar{t}$	Measure of average shear wave time of flight
t_o	Nominal time of flight
t_1, t_2	Shear times of flight
t_3	Longitudinal time of flight
t^e, t^n	Experimental/normalized time of flight
T	Temperature
T_y, T_u	Yield strength, tensile strength
T_{xy}	Transmission coefficient of stress wave travelling from medium x into medium y
$T_{applied}$	Stress applied to uniaxial tensile specimen
$T_{uniaxial}$	Uniaxial stress
T^e, T^n	Experimental/normalizing temperature
$\underline{T}$	Traction vector
	Stress tensor
	Cauchy stress tensor
$\tilde{\underline{T}}$	2nd Piola-Kirchhoff stress tensor
$\underline{u}$	Displacement
	Static displacement
	Velocity
$\underline{v}$	Velocity
V_e	Transducer electrode voltage
$V_{e,1}$, $V_{e,2}$	Transducer electrode voltage for 1st and 2nd back-face echo respectively
V_s	Source voltage driving the transducer
$\dot{V}_{start}$, $\dot{V}_{stop}$	Time derivatives of the amplified start and stop echo signals at their first zero crossings
$\underline{w}$	Infinitesimal dynamic displacement
W	Strain-energy density
	Stress amplitude of wave

W_{cpld}, W_{free}	Stress amplitudes of echoes against a coupled/free back face
W_r, W_t	Stress amplitude of wave received from/transmitted into propagation medium
W_{xy}	Traction force exerted by layer x onto layer y
W_I, W_R, W_T	Stress amplitude of incident/reflected/transmitted wave
$\bar{W}_r$, $\bar{W}_t$	Stress amplitude of wave received from/transmitted into propagation medium, averaged over the transducer area
W_x^+, W_x^-	Stress amplitude of wave travelling through layer x in positive/negative thickness direction
$\underline{W}$	Displacement amplitude vector of wave
x_r, x_t	X coordinate of the receiving/transmitting subtransducer
$\underline{x}$	Rectangular set of coordinates
	Coordinates of a material point in the initial state
X	Coordinate in the transmitter plane in the diffraction calculation
$\underline{X}$	Coordinates of a material point in the natural state
y_r, y_t	Y coordinate of a point on the receiving/transmitting subtransducer
$\hat{y}_r$, $\hat{y}_t$	Y coordinate of positive end of the receiving/transmitting subtransducer
Y	Coordinate in the transmitter plane in the diffraction calculation
z	Distance between transmitter and receiver in the diffraction calculation
Z	Specific wave impedance
	Coordinate normal to transmitter plane in the diffraction calculation
Z_s	Electrical impedance of voltage source driving the transducer
Z_x	Specific wave impedance in layer x
α	Polarization of shear wave associated with time of flight t_1 relative to positive x_1-axis
	Attenuation coefficient
	Coefficient of linear expansion
β	Time-of-flight temperature coefficient
β_s	Shear time-of-flight temperature coefficient
β_l	Longitudinal time-of-flight temperature coefficient
γ	Loading direction relative to positive x_1-axis
Γ	Integration contour for J
$\underline{\Gamma}$	Christoffel tensor
δ	Elongation measured during tensile test
δx	Width of subtransducer
$\underline{\delta}$	Kronecker delta
Δt	Error in time of flight
	Sample time interval used for model calculations
ΔT	Temperature change
ΔS	Aperture area in Fresnel-Kirchhoff diffraction formula
ΔV_{trig}	Error in trigger level

Δx, Δy	Absolute coordinate differences between points on transmitting and receiving subtransducers
ε^S	Permittivity constant for constant strain
$\underline{\varepsilon}^S$	Permittivity tensor for constant strain
η	Viscosity coefficient
η_1, η_2	Viscosity coefficients of viscoelastic constitutive model
θ	Transducer polarization angle
	Angle between wave ray and aperture or transmitter normal
$\underline{\kappa}$	Tensor giving a general relation between $\underline{G}$ and $\underline{T}$
λ	Lamé constant
	Wavelength
μ	Lamé constant
ν	Poisson's ratio
ν_1, ν_2, ν_3	3rd-order stiffness constants for isotropic material
ξ	Integration variable for strip diffraction calculation
ρ	Mass density
$\underline{\tau}$	Tensor containing acoustic data relating to shear waves
	Increase from nominal time of flight
τ_k	Series of discrete time intervals used for convolution in the diffraction calculation
φ	Angle in polar coordinates
	See Figure 5.8
ϕ	Electric potential
χ_{ij}	Parameters describing the magnitude of the acoustoelastic effect relative to the material orthotropy
ψ	See Equation 5.48
ω	Angular frequency
ω_n	Series of equidistant frequencies for which model calculations are performed
ω_c	Nyquist critical frequency
$\underline{\omega}$	Rotation tensor
^{o}	Superscript indicating material in the undeformed or natural state
$'$	Superscript indicating material in the final state
	Superscript indicating material adjacent to piezoelectric material
	Superscript indicating a rotated coordinate system
$''$	Superscript indicating a rotated coordinate system
$^{(m)}$	Superscript indicating m^{th} subtransducer

Chapter 1

Introduction

Stress evaluation in solids plays an important role in engineering. Many experimental techniques have therefore been developed, ranging from the destructive holedrilling method to a large number of non-destructive methods based on X-ray or neutron diffraction, photoelasticity, the determination of magnetic properties and ultrasonic measurements. Each of these techniques has its own possibilities and limitations, related to factors such as the type of material and the type and distribution of the stress to be evaluated. For this reason the various techniques do not necessarily have to compete with one other but often prove to be complementary.

The subject of this thesis is stress evaluation in metal using ultrasonic waves. The measurements are based on a phenomenon known as *acoustoelasticity*, i.e. the dependence of wave propagation on the state of deformation or stress in the material.

Chapter 1 begins with a brief description of the principle of ultrasonic stress measurements, including references relating to the historical development. This is followed by an outline of the approach underlying the experimental technique to be presented. The final section sets out the scope of the thesis.

1.1 The evolution of ultrasonic stress evaluation

Acoustoelasticity

The acoustoelastic effect depends on the elastic properties of the material. The constitutive relation between stress and strain, which is expressed by Hooke's law, is usually assumed to be linear for metals. When regarded more closely, however, this relation is found to deviate slightly from linearity. Consequently the propagation of waves, being a function of the elastic properties of the medium, will depend on the presence of stress. In addition, small mass density changes, which occur under the influence of stress, will also have an effect on wave propagation.

For metals the acoustoelastic effect is small. For example, aluminium and steel exhibit velocity changes of approximately 1 % and 0.2 % respectively at uniaxial stresses equal to the yield strength.

Wave types

Acoustoelastic stress evaluations can be based on bulk longitudinal and shear waves or on surface waves. Each wave type provides some kind of information concerning the stress state along the wave path. This work is focused exclusively on the use of *bulk waves*.

References 18 and 32 describe the use of *longitudinal waves* in order to evaluate the first stress invariant (i.e. the sum of normal or principal stresses) in two-dimensional specimens. This method is based on the determination of the longitudinal wave speed change caused by the introduction of stress in the specimen. Consequently, only the magnitude of applied stress invariants can be measured.

In spite of the experimental difficulties which have to be overcome, *shear waves* are widely used, owing to the fact that they give considerably more information concerning stress. This can be clearly illustrated in the case of an isotropic material. A stress present in such a material will generally induce a small anisotropy [52]. Consider a shear wave propagating along one of the principal stress directions. The wave is subject to the effect of *birefringence*: the arbitrarily polarized wave is split into two orthogonally polarized shear waves travelling at (slightly) different speeds. They are polarized along the remaining two principal directions and their speed changes are related to the magnitude of these principal stresses.

Material anisotropy

A complicating factor, however, is the presence of even a slight elastic *anisotropy* in the material. This will almost inevitably be present due to of texture formed during the fabrication process. In many cases (e.g. rolled material) the elastic properties are adequately de-

scribed if orthotropy is assumed, i.e. a set of three orthogonal axes of twofold symmetry. When propagating along such an orthotropic symmetry axis, a shear wave will show birefringence even in a situation without stress. Furthermore, polarization directions will generally not coincide with principal stress directions [21].

A quantity frequently used when dealing with shear wave stress measurements is the difference between the velocities of the two birefringent components expressed as a fraction of the average velocity. The use of this quantity, which will be referred to as the *birefringence*, is clearly advantageous. Measurements can be performed by using the interference between the two birefringent shear wave components, which travel at slightly different speeds [4, 20]. This technique, which bears some resemblance to photoelastic experiments [9], requires much less of the measuring system. Furthermore, the birefringence is independent of the specimen thickness and is less sensitive to influences of temperature and transducer-specimen coupling.

Hsu [14] investigated the velocity changes in specimens loaded in compression approximately along one of the orthotropic axes. Although his velocity measurements did not have a very high absolute accuracy, the birefringence was found to be proportional to the difference between the applied principal stresses. He suggested that for this loading situation the initial birefringence and the stress-induced birefringence were additive.

Arbitrary principal stress directions

A more general case arises when the principal stress directions normal to the direction of wave propagation do not coincide with orthotropic axes. A rotation of the polarization directions can be observed. Furthermore, the birefringence will not change proportionally to the magnitude of the principal stress difference. Iwashimizu and Kubomura [21] developed a theory which enabled the initial birefringence to be taken into account for materials with only a slight elastic orthotropy. Applied principal stress differences and directions could be evaluated from birefringence and polarization data through *one* acoustoelastic constant. Reference 20 contains some experimental results.

Okada [40] presented a theory in which orthotropy is assumed not only for the elastic properties of the material but also for its acoustoelastic properties. Consequently, in order to couple birefringence and polarization direction to principal stress difference and direction, *three* constants are needed. Based on this theory, reference 7 shows an experimentally determined distribution of shear stress around a crack tip in an aluminium 2024-T351 plate as caused by loading the specimen.

1.2 Stress evaluation using absolute time-of-flight data

For the evaluation of the three components of a two-dimensional stress tensor, i.e. two normal stresses and a shear stress in specimens in, for example, a plane stress state, additional information is needed besides that provided by the birefringence. This information can, for example, be obtained by using the equations for stress equilibrium [41]. However, the applicability of this method is limited to certain cases only.

Clearly the information which is potentially available when using shear waves is reduced significantly by exclusively determining the birefringence. The use of the *absolute time-of-flight* data of the two birefringent components would obviously be an improvement. By this means shear waves provide three quantities, namely two times of flight and a polarization direction. In principle this information should suffice for the evaluation of all components of a two-dimensional stress tensor. In order to relate these stress components to shear wave data, *five* constants are needed for an orthotropic material.

Stress evaluation of this kind is of a relative nature, since the change in shear wave data is measured as caused by loading a specimen mechanically. In other words, only *applied stresses* can be determined this way. This is because absolute time-of-flight values have no significance without corresponding reference values, measured, for example, in an unstressed specimen. It should also be noted the reference times of flight have to be measured at exactly the same location on the specimen, as it is impossible to determine the distance of flight with an accuracy matching the smallness of the acoustoelastic effect.[I]

An alternative approach, which is adopted in the present work, is to determine additionally the time of flight of a longitudinal wave. The extra information thus provided enables the measurement to become independent of the specimen thickness. Reference values can now be expressed exclusively in terms of the elastic constants of the material and should therefore in principle be valid at all specimen locations. This leads potentially to a technique for evaluating absolute stress levels.

The use of absolute time-of-flight data does, however, pose some serious experimental problems, such as the poor reproducibility of the transducer-specimen coupling [14, 37] and the influences of temperature on time of flight [37]. The experimental set-up must be able to solve these problems adequately before meaningful stress evaluations can be performed.

[I] This is one of the advantages of measuring only the birefringence, as the specimen thickness does not affect this quantity.

1.3 Scope of the thesis

Chapter 2 sets out the theory pertaining to acoustoelastic stress evaluation using bulk waves. Relations are established between stress and measurable acoustic data. These relations are worked out both for relative stress evaluations using shear waves and for absolute stress evaluations using both shear and longitudinal waves.

Chapter 3 describes an experimental technique designed for simultaneous measurements with shear and longitudinal waves. Special attention is given to distorting influences such as the transducer-specimen coupling, transducer misalignment, signal noise and specimen temperature. The electrical conditions necessary for accurate time-of-flight measurements are also discussed.

A number of acoustoelastic experiments performed on different metals are described in Chapter 4. Besides the calibration of the acoustoelastic tensors, they include the determination of the plane stress field around the crack tip in a compact tension specimen. Using these results, the J fracture parameter is numerically integrated.

A model for the pulse-echo method is proposed in Chapter 5. In this model the transducer and the transducer-specimen coupling play an important role. Wave diffraction in the specimen is also incorporated, as it affects the ultrasonic waveforms. Using the model, a variety of factors which affect ultrasonic measurements are assessed by means of numerical calculations.

Finally Chapter 6 establishes the relationships between the results of the preceding chapters. It also includes a number of points concerning the application of the acoustoelastic stress evaluation technique.

Chapter 2

Acoustoelastic Stress Evaluation using Ultrasonic Bulk Waves

2.1 Introduction

The first major chapter in this thesis will deal with the theory of acoustoelasticity and the description derived from this theory for ultrasonic stress evaluation using bulk waves.

Using the Christoffel equation for waves propagating in a stressed medium, an alternative eigenvalue equation may be formulated in terms of the distance of flight and mass density in the unstressed material and the time of flight. The alternative Christoffel tensor in this equation can be related to measurable acoustic quantities for the specific case of wave propagation along a direction of both principal stress and orthotropic symmetry. On the other hand, this same tensor can also be expressed as a linear function of stress. These two relations make it possible to obtain information concerning the stress state by means of acoustic measurements.

Applied stresses may consequently be evaluated by measuring shear wave data at the same location before and after the application of stress. The evaluation of absolute stress levels requires some kind of reference in unstressed material. For this purpose the additional information provided by longitudinal waves can be used.

In this chapter expressions are derived for these two types of stress evaluation. The material behaviour is described in the form of two-dimensional acoustoelastic tensors. A method to obtain numerical values for these tensors by means of calibration, is also discussed.

2.2 The acoustoelastic effect for bulk waves

2.2.1 Bulk waves in deformed elastic material

In order to describe the acoustoelastic effect, an elastic material is considered which is subject to a small but finite static deformation. The propagation of acoustic bulk waves in this material is determined by the *equation of motion* for an infinitesimal dynamic displacement superimposed on the static displacement. Following Tokuoka and Iwashimizu [52], a *wave equation* is derived for this case in Appendix 2A:

$$(C_{ijkl} + T_{jl}\delta_{ik})\frac{\partial^2 w_k}{\partial x_j \partial x_l} = \rho\frac{\partial^2 w_i}{\partial t^2} \tag{2.1}$$

where $\underline{C}$ = stiffness tensor dependent on the strain-energy function of the material and the static deformation
$\underline{T}$ = stress tensor in the deformed state
$\underline{\delta}$ = Kronecker delta
$\underline{w}$ = infinitesimal dynamic displacement
$\underline{x}$ = rectangular material coordinates
ρ = mass density in the deformed state
t = time

A solution is now sought for the dynamic displacement $\underline{w}$ in the form of a *plane wave* with angular frequency ω travelling along the *propagation direction* indicated by the unit vector $\underline{n}$:

$$w_i = W_i e^{i(\omega t - k n_j x_j)} \tag{2.2}$$

where $\underline{W}$ = displacement amplitude vector
k = wave number = $2\pi/\text{wavelength}$

Substituting this solution in the wave equation (Eq. 2.1) and defining a so-called *Christoffel tensor* $\underline{\Gamma}$ according to[1]:

$$\Gamma_{ik} = (C_{ijkl} + T_{jl}\delta_{ik})n_j n_l \tag{2.3}$$

leads to the Christoffel equation [1]:

---

[1] In the absence of static deformation/stress this definition reduces to the usual $c_{ijkl}n_j n_l$ [1], where c_{ijkl} are the 2nd-order elastic constants.

$$\Gamma_{ik}W_k = \rho c^2 W_i \tag{2.4}$$

where c = phase velocity = ω/k

The solution to this eigenvalue problem consists of three eigenvalues ρc^2 with corresponding eigenvectors $\underline{W}$. The eigenvectors represent the possible *polarization directions*, i.e. directions of particle displacement, for plane waves propagating along $\underline{n}$. These directions can be shown to form an orthogonal set.[1]

In general, no closed-form solutions can be obtained for this eigenvalue problem. However, numerical solutions can be calculated in a straightforward manner.

In Appendix 2B the stiffness tensor $\underline{C}$ is written in terms of the 2nd- and 3rd-order elastic stiffness constants of the material and the displacement gradients in the deformed state, assuming the latter to be small compared with unity. The $\underline{\Gamma}$ tensor can now be expressed as a function of these quantities, together with the stress tensor $\underline{T}$ in the deformed state and the wave propagation direction $\underline{n}$ (Eq. 2.3).

2.2.2 Wave propagation along an orthotropic symmetry direction

A more specific case arises when the elastic properties exhibit some form of symmetry. Due to previous processing, polycrystalline materials generally show a non-homogeneously distributed crystal orientation. Commonly, when caused by rolling or drawing, this texture has an orthorhombic symmetry, i.e. an orthogonal set of 2-fold symmetry axes exists. Such a symmetry will be assumed for the elastic constants, i.e. the material is said to be *orthotropic*.

Without loss of generality, the x_i coordinate axes are chosen to coincide with the orthotropic symmetry axes. Owing to the 2-fold symmetry of the elastic properties of the material, any coordinate transformation corresponding to a rotation through 180° about one of the x_i-axes must leave the 2nd- and 3rd-order elastic constants unchanged. It can be shown that as a result of this all constants with an odd number of indices 1, 2 or 3 will vanish.

By making the additional assumption that the plane waves propagate along one of the *symmetry directions*, say the x_3-axis ($n_1 = n_2 = 0$; $n_3 = 1$), Equation 2.3 is reduced to:

$$\Gamma_{ik} = C_{i3k3} + T_{33}\delta_{ik} \tag{2.5}$$

The components of $\underline{\Gamma}$ can now be concisely expressed in terms of elastic stiffness constants, strain, rotation and stress. These expressions are given in Appendix 2C.

---

[1] This stems from the fact that the Christoffel tensor $\underline{\Gamma}$ (Eq. 2.3) is a real and symmetric tensor. Consequently, its eigenvalues and eigenvectors must also be real. It can be shown [13] that $\underline{\Gamma}$ is *positive definite*, i.e. $\Gamma_{ij}p_ip_j \geq 0$ for any vector $\underline{p}$. The eigenvalues are therefore positive, leading to real values for the phase velocity c.

2.3 Acoustoelastic measurements based on time of flight and polarization direction

Experiments using ultrasonic waves propagating through elastic material yield time-of-flight values rather than phase velocities. In general, the *distance of flight* of a wave is not available with an accuracy that would permit the calculation of absolute velocities on which an acoustoelastic stress evaluation could be based. This calls for an approach which focuses on the time of flight.

2.3.1 Accounting for distance of flight and mass density

First of all, the phase velocity c in the Christoffel equation (Eq. 2.4) is replaced by the time of flight t and the distance of flight L. These quantities are related to each other through:[I]

$$c = \frac{t}{L} \tag{2.6}$$

In this context the distance of flight L is measured along the wave propagation direction indicated by the unit vector $\underline{n}$, i.e. normal to the planes of equal phase.[II]

Both the distance of flight L and the mass density ρ are deformation-dependent. It therefore seems convenient to rewrite the Christoffel equation in terms of distance of flight and mass density in the *undeformed state*. For the propagation direction under consideration here (x_3-axis), the relation:

$$\rho c^2 = \rho \frac{L^2}{t^2} = \frac{(L^2\rho)^\circ}{t^2}(1 - S_{mm} + 2S_{33}) \tag{2.7}$$

where $^\circ$ = superscript indicating the undeformed state
$\underline{S}$ = infinitesimal strain tensor (Eq. 2B.2)
$S_{mm} = S_{11} + S_{22} + S_{33}$

results in the alternative eigenvalue equation:

$$G_{ik}W_k = \frac{(L^2\rho)^\circ}{t^2}W_i \tag{2.8}$$

where $G_{ik} = \Gamma_{ik}(1 + S_{mm} - 2S_{33})$

[I] Time of flight can be measured using wave pulses or, in the case of a dispersive medium, using a continuous sinusoidal wave.

[II] This definition also holds in an anisotropic medium, in which the direction of power flow of the wave does not necessarily coincide with its propagation direction $\underline{n}$ [1].

Substituting the expressions for the Christoffel tensor $\underline{\Gamma}$ (Appendix 2C) in the definition of $\underline{G}$ and neglecting the second-order terms in strain, stress and rotation leads to the following set of expressions:

$$
\begin{aligned}
G_{11} &= c_{1313} + (2c_{1313}+c_{131311})S_{11} + c_{131322}S_{22} + c_{131333}S_{33} + T_{33} \\
G_{22} &= c_{3232} + c_{323211}S_{11} + (2c_{3232}+c_{323222})S_{22} + c_{323233}S_{33} + T_{33} \\
G_{33} &= c_{3333} + c_{333311}S_{11} + c_{333322}S_{22} + (2c_{3333}+c_{333333})S_{33} + T_{33} \\
G_{32} = G_{23} &= (2c_{333232}+c_{3333}+c_{3322}+2c_{3232})S_{32} + (c_{2233}+2c_{3232}-c_{3333})\omega_{32} \\
G_{13} = G_{31} &= (2c_{331313}+c_{3333}+c_{3311}+2c_{1313})S_{13} + (c_{3333}-c_{3311}-2c_{1313})\omega_{13} \\
G_{21} = G_{12} &= (2c_{133221}+c_{3232}+c_{1313})S_{21} + (c_{1313}-c_{2323})\omega_{21}
\end{aligned}
\tag{2.9}
$$

where c_{ijkl} = 2^{nd}-order elastic stiffness constants
c_{ijklmn} = 3^{rd}-order elastic stiffness constants
$\underline{\omega}$ = infinitesimal rotation tensor (Eq. 2C.2)

It should be noted that the terms containing the rotation $\underline{\omega}$ will vanish for isotropic material, as in this case the following isotropy conditions must hold:

$$
\begin{aligned}
c_{2233} + 2c_{3232} &= c_{3333} \\
c_{3311} + 2c_{1313} &= c_{3333} \\
c_{1313} &= c_{2323}
\end{aligned}
\tag{2.10}
$$

2.3.2 Relating the $\underline{G}$-tensor to stress

As the ultimate aim is to measure the stress $\underline{T}$, the strain tensor $\underline{S}$ in the above $\underline{G}$-tensor expression has to be eliminated by means of a strain-stress relation. For this purpose the additional assumption is made that the elastic constitutive relation of the material is almost linear, i.e. the contribution of the 3^{rd}-order elastic constants is small compared with that of the 2^{nd}-order constants. The $\underline{G}$-tensor can then be written as a linear function of the stress $\underline{T}$:

$$G_{ij} = c_{i3j3} + \kappa_{ijkl}T_{kl} + \omega_{ij}\text{-term} \tag{2.11}$$

where $\underline{\kappa}$ = 4^{th}-order tensor dependent on the 2^{nd}- and 3^{rd}-order elastic constants of the material

Owing to the symmetry of $\underline{G}$ and $\underline{T}$, it is clear that $\kappa_{ijkl} = \kappa_{jikl} = \kappa_{ijlk} = \kappa_{jilk}$. Therefore, instead of the full index notation used up till now, the *Voigt notation* may be applied [1], where pairs of indices ij (lower case) are contracted to indices I (upper case) according to Table 2.1.

Table 2.1 Full and Voigt index notation.

Full index ij	11	22	33	32, 23	13, 31	21, 12
Voigt index I	1	2	3	4	5	6

Using this notation, the $\underline{\kappa}$-tensor can be expressed in the more illustrative matrix notation. The form of this matrix is typical for an orthotropic material (see also Appendix 2C) and reads:

$$[k_{IJ}] = \begin{bmatrix} \kappa_{11} & \kappa_{12} & \kappa_{13} & 0 & 0 & 0 \\ \kappa_{21} & \kappa_{22} & \kappa_{23} & 0 & 0 & 0 \\ \kappa_{31} & \kappa_{32} & \kappa_{33} & 0 & 0 & 0 \\ 0 & 0 & 0 & \kappa_{44} & 0 & 0 \\ 0 & 0 & 0 & 0 & \kappa_{55} & 0 \\ 0 & 0 & 0 & 0 & 0 & \kappa_{66} \end{bmatrix} \tag{2.12}$$

where $\kappa_{IJ} = \kappa_{ijkl} \times 1$ for J = 1,2,3

$\kappa_{ijkl} \times 2$ for J = 4,5,6

A tedious derivation for the purpose of expressing the $\underline{\kappa}$-components in terms of the 2nd- and 3rd-order elastic constants of the orthotropic material will not be made here. The main reason for this is that using these constants would have very limited practical application. In particular the 3rd-order elastic constants which would be available for a given material show a wide spread. It is therefore more efficient to quantify the acoustoelastic effect represented by $\underline{\kappa}$ through calibration. In this respect, the approach is analogous to that followed by Okada [40].

Fixing one principal strain direction

The situation becomes more simple by assuming that the x_3-axis, which is already an orthotropic symmetry axis and the wave propagation direction, is also one of the *principal strain* directions. In Equation 2.9 the components with indices 23, 32, 31 and 13 will become zero for the $\underline{S}$-tensor and, in the absence of rigid body rotations, for the $\underline{\omega}$-tensor too. As a result the corresponding $\underline{G}$-components will vanish.

G_{21} is now the only remaining component that depends on the rotation, i.e. ω_{21}. In Appendix 2D it is argued that, regardless of the magnitude of the orthotropy of the material, the influence of this rotation component on the quantities actually measured, t_i and α, is negligible. Therefore, for the purpose of relating these acoustic quantities to stress, the rotation is discarded all together.

The relevant components of the $\underline{G}$-tensor can now be expressed as:

$$\begin{bmatrix} G_1 \\ G_2 \\ G_3 \\ G_6 \end{bmatrix} = \begin{bmatrix} c_{55} \\ c_{44} \\ c_{33} \\ 0 \end{bmatrix} + \begin{bmatrix} \kappa_{11} & \kappa_{12} & \kappa_{13} & 0 \\ \kappa_{21} & \kappa_{22} & \kappa_{23} & 0 \\ \kappa_{31} & \kappa_{32} & \kappa_{33} & 0 \\ 0 & 0 & 0 & \kappa_{66} \end{bmatrix} \cdot \begin{bmatrix} T_1 \\ T_2 \\ T_3 \\ T_6 \end{bmatrix} \tag{2.13}$$

Although the $\underline{\kappa}$-tensor is determined by calibration, the components mentioned in this equation are expressed in Appendix 2E in terms of elastic constants for *isotropic* material. These expressions can be useful in calculating the approximate acoustoelastic behaviour for a given material from 2nd- and 3rd-order stiffness constants provided in literature.

2.3.3 Relating the $\underline{G}$-tensor to acoustic data

Analogous to solving Christoffel Equation 2.4, the eigenvalue problem formulated by Equation 2.8 leads to eigenvalues $(L^2\rho)^\circ/t_i^2$ with corresponding eigenvectors $\underline{W}^{(i)}$. These vectors represent an orthogonal set of possible polarization directions of plane waves travelling along the x_3-direction.

It should be borne in mind that components G_{23}, G_{32}, G_{31} and G_{13} vanish owing to the assumption of a principal strain direction along x_3. One eigenvalue, say $(L^2\rho)^\circ/t_3^2$, is now evidently equal to component G_{33}, while the corresponding eigenvector $\underline{W}^{(3)}$ is fixed parallel to the x_3-axis. This solution represents a *pure mode* longitudinal wave, the particle displacement being exactly along the propagation direction. As they form an orthogonal set, the remaining eigenvectors $\underline{W}^{(1)}$ and $\underline{W}^{(2)}$ must lie in the x_1-x_2 plane, indicating mutually perpendicular polarization directions of two pure mode shear wave solutions. The related eigenvalues are:

$$\frac{(L^2\rho)^\circ}{t_{1,2}^2} = \frac{G_{11} + G_{22} \pm \sqrt{(G_{11} - G_{22})^2 + 4G_{12}^2}}{2} \tag{2.14}$$

Shear wave birefringence

The above results will, in their general form, i.e. unequal shear wave times of flight (Eq. 2.14), give rise to a phenomenon called *shear wave birefringence*. Consider a material interface parallel to the x_1-x_2 plane, as shown in Figure 2.1. If an arbitrarily polarized shear wave is emitted into the material at normal incidence, it will be split up into two shear wave components polarized along $\underline{W}^{(1)}$ and $\underline{W}^{(2)}$. The amplitudes of these birefringent components depend on their respective polarization directions relative to that of the incident wave. In order to quantify the two perpendicular polarization directions, a single angle α can be used, defined as the angle between the x_1-axis and the polarization direction $\underline{W}^{(1)}$ of the wave asso-

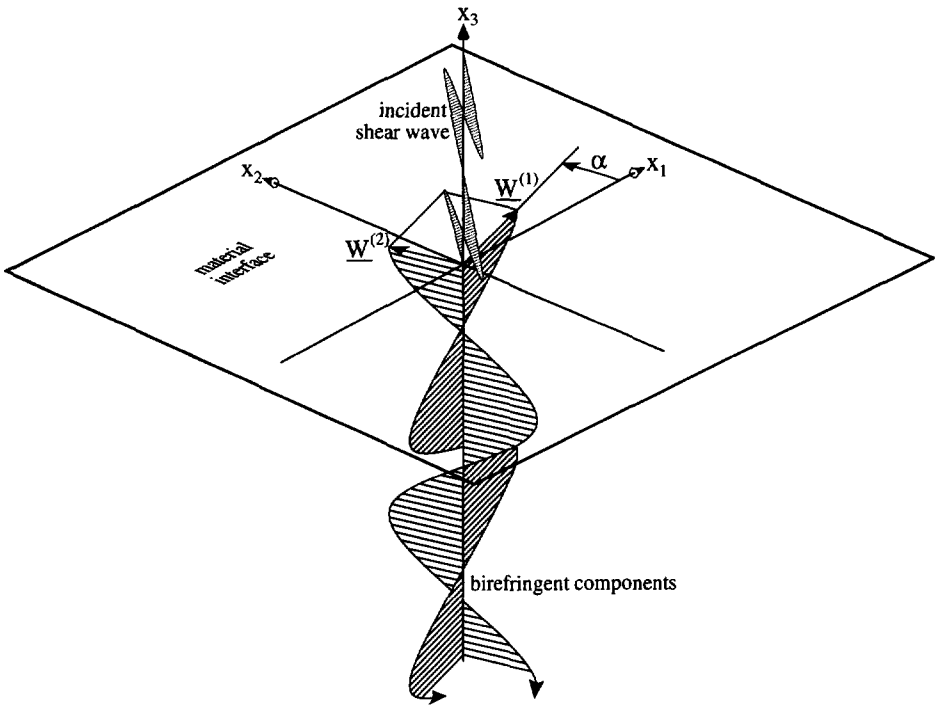

Fig. 2.1 Shear wave birefringence in stressed material.

ciated with time of flight t_1. If a rotation from the x_1-axis to $\underline{W}^{(1)}$ is anticlockwise, as seen from the positive x_3-axis, the polarization angle α is assumed to be positive (as shown in Fig. 2.1).

The components of $\underline{G}$ defined relative to axes parallel to its eigenvectors $\underline{W}^{(i)}$ are expressed by a diagonal matrix with eigenvalues $(L^2\rho)^\circ/t_i^2$ as diagonal elements G_{ii}. The $\underline{G}$-components relative to the x_i-axes follow from a coordinate transformation of this diagonal matrix corresponding to a rotation about the x_3-axis through an angle of $-\alpha$. Thus the $\underline{G}$-tensor in matrix representation reads:

$$[G_{ij}] = (L^2\rho)^\circ \begin{bmatrix} \left(\frac{\cos^2\alpha}{t_1^2} + \frac{\sin^2\alpha}{t_2^2}\right) & \left(\frac{1}{t_1^2} - \frac{1}{t_2^2}\right)\sin\alpha\cos\alpha & 0 \\ \left(\frac{1}{t_1^2} - \frac{1}{t_2^2}\right)\sin\alpha\cos\alpha & \left(\frac{\sin^2\alpha}{t_1^2} + \frac{\cos^2\alpha}{t_2^2}\right) & 0 \\ 0 & 0 & \frac{1}{t_3^2} \end{bmatrix} \tag{2.15}$$

2.4 Two-dimensional stress evaluation

First of all the assumption is made that the magnitude of the acoustoelastic effect is small, such that:

$$\kappa_{ijkl} T_{kl} << c_{i3j3} \qquad \text{for } i = j \tag{2.16}$$

Stresses will therefore induce only small relative changes in time of flight, a condition which is generally met.

Since the wave propagation is along the x_3-axis, a stress field can only be evaluated if it is not a function of x_3. Furthermore, from the assumptions made about the x_3-axis coinciding both with a principal strain and an orthotropic symmetry direction, it follows that x_3 must also be a direction of principal stress (T_{33}). In the *two-dimensional stress* field that results from these restrictions, component T_{33} is either constant or can be written as a linear combination of T_{11} and T_{22}. Thus the stress field is completely determined by components T_{11}, T_{22} and T_{21}. Typical examples are *plane stress* ($T_{33} = 0$) and *plane strain* ($S_{33} = 0$) conditions.

From this point on, therefore, T_{33} can and will be eliminated. In view of this, the symbolic indices i will take only the values 1 and 2 and consequently the Voigt indices I will take only the values 1, 2 and 6.

With regard to Equation 2.15, the problem remains that the deformation-independent term $(L^2\rho)^\circ$ generally cannot be determined accurately enough. The error should be negligible compared with the magnitude of the acoustoelastic effect, which is itself assumed small. The problem is dealt with in two ways:

- Relative stress evaluation
  For acoustic measurements which use waves travelling through the same material, the term $(L^2\rho)^\circ$ will also be the same. This knowledge can be used to evaluate stress changes by measuring at one place before and after the occurrence of these changes.

- Absolute stress evaluation
  The term $(L^2\rho)^\circ$ is eliminated altogether by using the time-of-flight ratio of shear and longitudinal waves.

2.4.1 Relative stress evaluation using shear waves

Relative evaluation of a two-dimensional stress tensor can in principle be achieved by using shear waves only. This is because shear wave measurements yield three quantities (t_1, t_2 and α) equalling the number of stress components to be determined. The $\underline{G}$-components in

Equation 2.13 which relate to shear wave propagation, i.e. G_1, G_2 and G_6, are therefore considered now and the acoustoelastic effect of T_{33} is incorporated in the T_{11} and T_{22} terms:

$$G_{ij} = c_{i3j3} + \left(\kappa_{ijkl} + \kappa_{ij33}\frac{\partial T_{33}}{\partial T_{kl}}\right)T_{kl} = c_{i3j3} + K_{ijkl}T_{kl} \tag{2.17}$$

where $\underline{K}$ = two-dimensional 4th-order tensor dependent on the elastic properties of the material and the type of two-dimensional stress field

In Equation 2.15 the $\underline{G}$-tensor is related to acoustic quantities. At this point it is convenient to split up the two-dimensional part of this expression into the term $(L^2\rho)^\circ$ and a symmetric two-dimensional 2nd-order tensor $\underline{\tau}$. This tensor contains only the acoustic data relating to shear waves and, using Equation 2.15, is implicitly defined as:

$$G_{ij} = (L^2\rho)^\circ\tau_{ij} \tag{2.18}$$

The changes ΔG_{ij} are now considered between two measurements using waves travelling through exactly the same material. Consequently the term $(L^2\rho)^\circ$ will be common to both measurements and from Equations 2.17 and 2.18 it follows that:

$$(L^2\rho)^\circ\Delta\tau_{ij} = K_{ijkl}\Delta T_{kl} \tag{2.19}$$

As a result any relative error in the term $(L^2\rho)^\circ$ will introduce an equal relative error in the stress tensor change to be evaluated. The accuracy required is therefore significantly lower.

In practice it is more appropriate to express $(L^2\rho)^\circ$ in terms of time of flight and elastic stiffness constants. For this purpose the time of flight $\bar{t}$ is introduced according to:

$$\frac{1}{\bar{t}^2} = {}^1/_2\left(\frac{1}{t_1^2} + \frac{1}{t_2^2}\right) \tag{2.20}$$

This is a measure of the average shear wave time of flight at the material location under consideration[I]. By considering the sum of G_{11} and G_{22} in Equations 2.9 and 2.15 for material in the undeformed/unstressed state, it follows that:[II]

$$(L^2\rho)^\circ = {}^1/_2(c_{1313} + c_{3232})(\bar{t}^2)^\circ = {}^1/_2(c_{1313} + c_{3232})\bar{t}^2 \tag{2.21}$$

The last step involves the use of a value for $\bar{t}$ at an arbitrary stress level[III] as an approximation in order to evaluate $(L^2\rho)^\circ$. This is permissible in view of (i) the above arguments con-

[I] If t_1 and t_2 do not differ too much, $\bar{t}$ can in fact be considered as the average shear wave time of flight.

[II] In fact if T_{33} is unequal to zero, depending on the type of stress field, its value should be added to the stiffness constants in Equation 2.21. However, in practice this value can and will be neglected.

[III] Obviously calculations must be performed with a fixed $\bar{t}$-value for a particular material location.

cerning the accuracy required for $(L^2\rho)^o$ and (ii) the assumed smallness of the acoustoelastic effect (Eq. 2.16). In cases where no measurements are available in unstressed material, this is obviously more practicable.

Substitution of $(L^2\rho)^o$ from Equation 2.21 in Equation 2.19, results in:

$$^1/_2(c_{1313} + c_{3232})\bar{t}^2\Delta\tau_{ij} = K_{ijkl}\,\Delta T_{kl} \tag{2.22}$$

Inverting this equation leads to an explicit expression for the stress tensor change:

$$\Delta T_{ij} = k_{ijkl}\,\Delta Q_{kl} \tag{2.23}$$

where $\underline{k}$ = two-dimensional 4th-order tensor dependent on the elastic properties of the material and the type of two-dimensional stress field

$\underline{Q} = \bar{t}^2\underline{\tau}$ = 2nd-order tensor containing acoustic data relating to shear waves

The matrix representation in Voigt notation of $\underline{k}$, denoted as $[k_{IJ}]$, is related to the inverse of the matrix $[K_{IJ}]$ and reads:

$$[k_{IJ}] = {}^1/_2(c_{1313} + c_{3232})[K_{IJ}]^{-1} = \begin{bmatrix} k_{11} & k_{12} & 0 \\ k_{21} & k_{22} & 0 \\ 0 & 0 & k_{66} \end{bmatrix} \tag{2.24}$$

where for $\underline{K}$, $\underline{k}$:

component IJ = component ijkl × 1 for J = 1,2

component ijkl × 2 for J = 6

From this it is clear that $\underline{k}$ can only exist if the matrix $[K_{IJ}]$ has a non-zero determinant. The $\underline{k}$-tensor has five independent components for the orthotropic case considered here. It should be noted that for material which exhibits so-called *transverse isotropy* in the x_1-x_2 plane this number is reduced to only two. For such material the elastic constants are unaffected when defined relative to coordinate axes rotated about the x_3-axis through an arbitrary angle. It can be proved that the following extra relations must then hold:

$$\begin{aligned} k_{11} &= k_{22} \\ k_{21} &= k_{12} \\ k_{66} &= k_{11} - k_{21} \end{aligned} \tag{2.25}$$

Furthermore, using the definition of the 2nd-order acoustic data tensor $\underline{Q}$ as contained in Equation 2.23 and that of the $\underline{\tau}$-tensor (Eq. 2.18), the change in $\underline{Q}$ can be expressed as:

$$\Delta\begin{bmatrix} Q_1 \\ Q_2 \\ Q_6 \end{bmatrix} = \bar{t}^2\,\Delta\begin{bmatrix} \frac{\cos^2\alpha}{t_1^2} + \frac{\sin^2\alpha}{t_2^2} \\ \frac{\sin^2\alpha}{t_1^2} + \frac{\cos^2\alpha}{t_2^2} \\ \left(\frac{1}{t_1^2} - \frac{1}{t_2^2}\right)\sin\alpha\cos\alpha \end{bmatrix} \tag{2.26}$$

2.4.2 Absolute stress evaluation using shear and longitudinal waves

In order to describe absolute stress evaluation, a symmetric two-dimensional 2nd-order tensor $\underline{R}$ is defined containing both shear and longitudinal acoustic data:

$$R_{ij} = t_3^2 \tau_{ij} \tag{2.27}$$

According to Equation 2.15 the components of this acoustic data tensor will equal the ratios G_{ij}/G_{33}, independently of the term $(L^2\rho)^\circ$. The dependence of $\underline{R}$ on the two-dimensional stress tensor is derived using Equations 2.13 and 2.17 in order to expand G_{33} and G_{ij} respectively:

$$R_{ij} = \frac{G_{ij}}{G_{33}} = \frac{c_{i3j3} + K_{ijkl}T_{kl}}{c_{3333} + \left(\kappa_{33mn} + \kappa_{3333}\dfrac{\partial T_{33}}{\partial T_{mn}}\right)T_{mn}} \approx$$

$$\approx \frac{c_{i3j3}}{c_{3333}} + \frac{1}{c_{3333}}\left\{K_{ijkl} - \frac{c_{i3j3}}{c_{3333}}\left(\kappa_{33kl} + \kappa_{3333}\frac{\partial T_{33}}{\partial T_{kl}}\right)\right\}T_{kl} =$$

$$= \frac{c_{i3j3}}{c_{3333}} + M_{ijkl}T_{kl} \tag{2.28}$$

where $\underline{M}$ = two-dimensional 4th-order tensor dependent on the elastic properties of the material and the type of two-dimensional stress field

The approximation made can be motivated by the assumed smallness of the acoustoelastic effect.

Inverting this equation, while assuming that the matrix $[M_{IJ}]$ has a non-zero determinant, gives $\underline{T}$ explicitly:

$$T_{ij} = m_{ijkl}\left(R_{kl} - \frac{c_{k3l3}}{c_{3333}}\right) \tag{2.29}$$

where $\underline{m}$ = two-dimensional 4th-order tensor dependent on the elastic properties of the material and the type of two-dimensional stress field

The matrix representation in Voigt notation $[m_{IJ}]$ will be:

$$[m_{IJ}] = [M_{IJ}]^{-1} = \begin{bmatrix} m_{11} & m_{12} & 0 \\ m_{21} & m_{22} & 0 \\ 0 & 0 & m_{66} \end{bmatrix} \tag{2.30}$$

where for $\underline{M}$, $\underline{m}$:

component IJ = component ijkl × 1 for J = 1,2
component ijkl × 2 for J = 6

The number of independent $\underline{m}$ components is reduced to two for material which is transversely isotropic in the x_1-x_2 plane owing to extra relations analogous to those for $\underline{k}$ (Eq. 2.25).

Finally, for the sake of completeness, the 2nd-order tensor $\underline{R}$ is expressed in terms of the shear and longitudinal acoustic data (Eqs. 2.18 and 2.27):

$$\begin{bmatrix} R_1 \\ R_2 \\ R_6 \end{bmatrix} = t_3^2 \begin{bmatrix} \frac{\cos^2\alpha}{t_1^2} + \frac{\sin^2\alpha}{t_2^2} \\ \frac{\sin^2\alpha}{t_1^2} + \frac{\cos^2\alpha}{t_2^2} \\ \left(\frac{1}{t_1^2} - \frac{1}{t_2^2}\right) \sin\alpha\cos\alpha \end{bmatrix} \tag{2.31}$$

2.4.3 Calibration

As already stated, quantifying the acoustoelastic effect for a given material is most conveniently effected by calibrating the $\underline{k}$ and/or $\underline{m}$-tensor. An obvious way of doing this is to measure acoustic data before and after introducing a two-dimensional stress $\underline{T}$ in the material.[I]

Given the form of $\underline{k}$ and $\underline{m}$ (Eqs. 2.24 and 2.30), a calibration of the components with Voigt indices 11, 12, 21 and 22 requires that changes in R_1 and R_2 are induced for at least two different combinations of ΔQ_1 and ΔQ_2 respectively. Furthermore, with regard to the components k_{66} and m_{66}, a non-zero ΔQ_6 or change in R_6 must be effected. To summarize, a complete calibration can be performed by introducing at least two different combinations of two-

[I] For example by inducing a plane stress or a plane strain state.

dimensional stress components in the material, including at least one non-zero shear stress.

With regard to the stress evaluation using both shear and longitudinal waves, the terms c_{i3j3}/c_{3333} (in full notation) also need to be known. Measuring the $\underline{R}$-tensor through unstressed material will yield these ratios (Eq. 2.28):

$$\frac{c_{i3j3}}{c_{3333}} = R_{ij}^{o} \tag{2.32}$$

It can be seen from Equation 2.29 that these are in fact *reference values*, as the measured data are considered relative to them. High accuracy is therefore required and in order to be able to evaluate stresses in an absolute sense the ratios of elastic stiffness constants in Equation 2.32 must be reproduced exactly from one material location to another.

Up till now all tensor quantities have been defined relative to axes which coincide with the orthotropic symmetry axes of the material. In practice, however, it may be difficult to indicate these symmetry axes beforehand. This situation arises if, for example, the rolling direction of the material is not accurately known. If the x_1- and x_2-axes are not parallel to symmetry axes, those components of the $\underline{k}$ or $\underline{m}$-tensors which should be zero according to Equations 2.24 and 2.30 will be calibrated as non-zero.[I] Moreover, a rotation of the set of coordinate axes through 180° about either the x_1- or x_2-axis would in this case affect the calibrated values of all tensor components. In such cases it is therefore convenient to define the calibrated acoustoelastic tensor(s) relative to the orthotropic symmetry axes afterwards.

[I] Note that such a calibration would involve at least *three* different combinations of stress components to be induced.

2.5 Conclusion

In this chapter discussion of the theory underlying acoustoelastic stress evaluation was followed by a description of two types of stress evaluation.

The evaluation relates to two-dimensional stress fields, e.g. emanating from plane stress or plane strain states. *Applied stresses* can be evaluated by measuring the change in shear wave data at one location before and after the application of stress. On the other hand, *absolute stress levels* can in principle be determined by measuring both shear and longitudinal data only through stressed material.

It was found that regardless of the magnitude of the orthotropy of the material, the effect of *rotation* on the acoustic data, and therefore on the stress to be evaluated, can be neglected.

The relation between acoustic data and stress levels can be concisely expressed in the form of *acoustoelastic tensors*. For absolute stress evaluation reference values for unstressed material must also be available. These tensors and reference values can be determined by means of two uniaxial tensile tests on specimens with conveniently chosen orientations.

Appendix 2A Wave equation in deformed elastic material

Three different states are considered:

- the *natural* state, in which the material is not deformed and no stresses are present. The position of a material point is denoted by the vector $\underline{X}$;
- the *initial* state, in which the material is subject to a static displacement field $\underline{u}$. The position of a point is denoted by $\underline{x} = \underline{X} + \underline{u}$;
- the *final* state, arising after an infinitesimal dynamic displacement field $\underline{w}$ has been superimposed on the static displacement field of the material in the initial state. The position of a point is denoted by $\underline{x}' = \underline{x} + \underline{w}$.

The material under consideration is assumed to be *Green-elastic* or *hyperelastic*. This type of elastic behaviour is characterized by the existence of a so-called *strain-energy function* for the material [35, 39]. Before considering the stress in the final state and deriving the wave equation for $\underline{w}$, hyperelastic material is discussed briefly.

Hyperelastic material

Consider the energy quantities used in the following to be defined per unit undeformed volume. When a volume element in the material is reversibly deformed, this is accompanied by a change of the internal energy W equal to:

$$dW = TdS + \tilde{T}_{ij}dS_{ij} \tag{2A.1}$$

where T = absolute temperature
S = entropy
$\underline{\tilde{T}}$ = Kirchhoff (or 2nd Piola-Kirchhoff) stress tensor
$\underline{S}$ = Lagrangian strain tensor

The symmetric 2nd-order Lagrangian strain tensor $\underline{S}$ is defined as:

$$S_{ij} = {}^1/_2\left(\frac{\partial x_r}{\partial X_i}\frac{\partial x_r}{\partial X_j} - \delta_{ij}\right) \tag{2A.2}$$

where δ_{ij} = Kronecker delta, which equals 1 for i = j and 0 otherwise

Discussion of the Kirchhoff stress tensor $\underline{\tilde{T}}$ is beyond the scope of this work. Reference is made to [35]. The essence is that this symmetric tensor and the Lagrangian strain tensor $\underline{S}$ are *conjugate*, which means that the expression $\tilde{T}_{ij}dS_{ij}$ yields the work done by stress during deformation.

In Equation 2A.1 the internal energy is written as a function of strain and entropy. The Kirchhoff stress can be expressed as the partial derivative at constant entropy of the internal energy W with respect to strain:

$$\tilde{T}_{ij} = \left(\frac{\partial W}{\partial S_{ij}}\right)_S \tag{2A.3}$$

Thus, by postulating a strain-energy function that expresses W as a function of strain only, while assuming adiabatic deformation[I], a constitutive relation between stress and strain is established for the material. This function, W(S), is the strain-energy per unit undeformed volume under adiabatic conditions and will from this point on be referred to as the *strain-energy density* W.

(Cauchy) stress tensor

The stress associated with the small dynamic displacement $\underline{w}$ is more conveniently expressed by means of the symmetric 2nd-order *Cauchy stress tensor* $\underline{T}$. This is because the tensor represents the traction forces per unit deformed area, i.e. using the initial coordinates $\underline{x}$. It is related to the Kirchhoff stress tensor through [13, 35]:

$$T_{ij} = \frac{\rho}{\rho^o}\frac{\partial x_i}{\partial X_k}\frac{\partial x_j}{\partial X_l}\tilde{T}_{kl} \tag{2A.4}$$

where ρ^o, ρ = mass density in natural and initial state respectively

Thus the (Cauchy) stress in terms of the strain-energy density W reads:

$$T_{ij} = \frac{\rho}{\rho^o}\frac{\partial x_i}{\partial X_k}\frac{\partial x_j}{\partial X_l}\frac{\partial W}{\partial S_{kl}} \tag{2A.5}$$

Stress in the final state

The change in the strain tensor when going from the initial to the final state is conveniently written as:[II]

$$\delta S_{ij} = S'_{ij} - S_{ij} = {}^1/_2\left(\frac{\partial x'_r}{\partial X_i}\frac{\partial x'_r}{\partial X_j} - \frac{\partial x_r}{\partial X_i}\frac{\partial x_r}{\partial X_j}\right) = \frac{\partial x_r}{\partial X_i}\frac{\partial w_r}{\partial X_j} = \frac{\partial x_r}{\partial X_i}\frac{\partial x_s}{\partial X_j}\frac{\partial w_r}{\partial x_s} \tag{2A.6}$$

using the symmetry $S_{ij} = S_{ji}$. In this and the following expressions the second- and higher-order terms of the infinitesimal displacement $\underline{w}$ are neglected. The stress in the final state

[I] The ultimate aim is to derive a wave equation for evaluating *wave propagation* in deformed elastic material. Deformation associated with all but very low frequency waves may be assumed to be adiabatic.

[II] Primed quantities refer to material in the final state.

follows from Eq. 2A.5 and 2A.6:

$$T'_{ij} = \frac{\rho'}{\rho^o}\frac{\partial x'_i}{\partial X_k}\frac{\partial x'_j}{\partial X_l}\frac{\partial W'}{\partial S_{kl}} =$$

$$= \frac{\rho}{\rho^o}\left(1 - \frac{\partial w_p}{\partial x_p}\right)\left(\frac{\partial x_i}{\partial X_k} + \frac{\partial w_i}{\partial X_k}\right)\left(\frac{\partial x_j}{\partial X_l} + \frac{\partial w_j}{\partial X_l}\right)\left(\frac{\partial W}{\partial S_{kl}} + \frac{\partial^2 W}{\partial S_{kl}\partial S_{mn}}\delta S_{mn}\right) =$$

$$= T_{ij}\left(1 - \frac{\partial w_m}{\partial x_m}\right) + T_{im}\frac{\partial w_j}{\partial x_m} + T_{jm}\frac{\partial w_i}{\partial x_m} + C_{ijkl}\frac{\partial w_k}{\partial x_l} \qquad (2A.7)$$

where $C_{ijkl} = \frac{\rho}{\rho^o}\frac{\partial x_i}{\partial X_p}\frac{\partial x_j}{\partial X_q}\frac{\partial x_k}{\partial X_r}\frac{\partial x_l}{\partial X_s}\frac{\partial^2 W}{\partial S_{pq}\partial S_{rs}}$

Wave equation

In the absence of body forces the equilibrium in the static initial state is described by:

$$\frac{\partial T_{ij}}{\partial x_j} = 0 \qquad (2A.8)$$

and the motion in the dynamic final state by:

$$\frac{\partial T'_{ij}}{\partial x'_j} = \rho'\frac{\partial^2 w_i}{\partial t^2}. \qquad (2A.9)$$

Using:

$$\frac{\partial T'_{ij}}{\partial x'_j} = \left(\delta_{jn} - \frac{\partial w_n}{\partial x_j}\right)\frac{\partial T'_{ij}}{\partial x_n} \qquad (2A.10)$$

and, from Eq. 2A.7:

$$\frac{\partial T'_{ij}}{\partial x_n} = \frac{\partial T_{ij}}{\partial x_n}\left(1 - \frac{\partial w_n}{\partial x_m}\right) - T_{ij}\frac{\partial^2 w_m}{\partial x_n \partial x_m} + \frac{\partial T_{im}}{\partial x_n}\frac{\partial w_j}{\partial x_m} + T_{im}\frac{\partial^2 w_j}{\partial x_n \partial x_m} +$$

$$+ \frac{\partial T_{jm}}{\partial x_n}\frac{\partial w_i}{\partial x_m} + T_{jm}\frac{\partial^2 w_i}{\partial x_n \partial x_m} +$$

$$+ \frac{\partial}{\partial x_n}\left(C_{ijkl}\frac{\partial w_k}{\partial x_l}\right) \qquad (2A.11)$$

it follows that:

$$\frac{\partial T'_{ij}}{\partial x'_j} = -T_{ij}\frac{\partial^2 w_m}{\partial x_j \partial x_m} + \frac{\partial T_{im}}{\partial x_j}\frac{\partial w_j}{\partial x_m} + T_{im}\frac{\partial^2 w_j}{\partial x_j \partial x_m} + T_{jm}\frac{\partial^2 w_i}{\partial x_j \partial x_m} + \\ + \frac{\partial}{\partial x_j}\left(C_{ijkl}\frac{\partial w_k}{\partial x_l}\right) - \frac{\partial T_{ij}}{\partial x_n}\frac{\partial w_n}{\partial x_j} \qquad (2A.12)$$

Since the 1st and 3rd terms and also the 2nd and 6th terms will vanish, the equation of motion in the final state (Eq. 2A.9) leads to the *wave equation*:

$$T_{jl}\frac{\partial^2 w_i}{\partial x_j \partial x_l} + \frac{\partial}{\partial x_j}\left(C_{ijkl}\frac{\partial w_k}{\partial x_l}\right) = \rho\frac{\partial^2 w_i}{\partial t^2} \qquad (2A.13)$$

If a homogeneous static deformation is assumed, this can be rewritten as:

$$(C_{ijkl} + T_{jl}\delta_{ik})\frac{\partial^2 w_k}{\partial x_j \partial x_l} = \rho\frac{\partial^2 w_i}{\partial t^2} \qquad (2A.14)$$

Appendix 2B C-tensor components for slightly deformed material

In Appendix 2A the $\underline{C}$-tensor is defined as:

$$C_{ijkl} = \frac{\rho}{\rho^o}\frac{\partial x_i}{\partial X_p}\frac{\partial x_j}{\partial X_q}\frac{\partial x_k}{\partial X_r}\frac{\partial x_l}{\partial X_s}\frac{\partial^2 W}{\partial S_{pq}\partial S_{rs}} \tag{2B.1}$$

If the displacement gradient $\partial\underline{u}/\partial\underline{X}$ is assumed to be small compared with unity, second- and higher-order terms in $\partial\underline{u}/\partial\underline{X}$ can be neglected. The strain $\underline{S}$ may then be alternatively defined as an infinitesimal strain tensor:

$$S_{ij} = {}^1/_2\left(\frac{\partial u_i}{\partial X_j} + \frac{\partial u_j}{\partial X_i}\right) \tag{2B.2}$$

and the strain-energy density W may be written as a cubic polynomial function of this strain tensor:

$$W(\underline{S}) = \frac{c_{ijkl}}{2!}S_{ij}S_{kl} + \frac{c_{ijklmn}}{3!}S_{ij}S_{kl}S_{mn} \tag{2B.3}$$

where c_{ijkl}, c_{ijklmn} = 2^{nd}-, 3^{rd}-order elastic stiffness constants

The second derivative of the strain-energy density in Equation 2B.1 can thus be expressed as:

$$\frac{\partial^2 W}{\partial S_{ij}\partial S_{kl}} = c_{ijkl} + c_{ijklmn}S_{mn} \tag{2B.4}$$

Using this and the relations:

$$\frac{\partial x_i}{\partial X_j} = \delta_{ij} + \frac{\partial u_i}{\partial X_j} \tag{2B.5}$$

$$\frac{\rho}{\rho^o} = 1 - S_{mm} \tag{2B.6}$$

where $S_{mm} = S_{11} + S_{22} + S_{33}$

the $\underline{C}$-tensor (Eq. 2B.1) may be approximated by:

$$C_{ijkl} = c_{ijkl}(1 - S_{mm}) + c_{ijklmn}S_{mn} + c_{mjkl}\frac{\partial u_i}{\partial X_m} + c_{imkl}\frac{\partial u_j}{\partial X_m} + c_{ijml}\frac{\partial u_k}{\partial X_m} + c_{ijkm}\frac{\partial u_l}{\partial X_m} \tag{2B.7}$$

Appendix 2C Christoffel tensor for wave propagation along an orthotropic symmetry direction

Let the orthotropic symmetry axes of the material coincide with the x_i-axes. For this case all elastic constants c_{ijkl} and c_{ijklmn} with an odd number of indices 1, 2 or 3 are zero.[I] The Christoffel tensor $\underline{\Gamma}$ for wave propagation along the x_3-direction (Eq. 2.3) is now expanded using the $\underline{C}$-tensor expression derived in Appendix 2B:

$$\Gamma_{11} = c_{1313}(1 - S_{mm}) + c_{131311}S_{11} + c_{131322}S_{22} + c_{131333}S_{33} + \\ + c_{1313}S_{11} + c_{1313}S_{33} + c_{1313}S_{11} + c_{1313}S_{33} + \quad T_{33} =$$

$$= c_{1313}(1-S_{mm}+2S_{11}+2S_{33}) + \quad c_{131311}S_{11} + c_{131322}S_{22} + c_{131333}S_{33} + \quad T_{33}$$

Likewise:

$$\Gamma_{22} = c_{3232}(1-S_{mm}+2S_{22}+2S_{33}) + \quad c_{323211}S_{11} + c_{323222}S_{22} + c_{323233}S_{33} + \quad T_{33}$$

$$\Gamma_{33} = \qquad c_{3333}(1-S_{mm}+4S_{33}) + \quad c_{333311}S_{11} + c_{333322}S_{22} + c_{333333}S_{33} + \quad T_{33}$$

$$\Gamma_{32} = \Gamma_{23} = \quad (2c_{333232}+c_{3333}+c_{3322}+2c_{3232})S_{32} + \quad (c_{2233}+2c_{3232}-c_{3333})\omega_{32}$$

$$\Gamma_{13} = \Gamma_{31} = \quad (2c_{331313}+c_{3333}+c_{3311}+2c_{1313})S_{13} + \quad (c_{3333}-c_{3311}-2c_{1313})\omega_{13}$$

$$\Gamma_{21} = \Gamma_{12} = \qquad (2c_{133221}+c_{3232}+c_{1313})S_{21} + \qquad (c_{1313}-c_{2323})\omega_{21} \qquad \text{(2C.1)}$$

where ω_{ij} = component of the infinitesimal rotation tensor = $^1/_2\left(\frac{\partial u_i}{\partial X_j} - \frac{\partial u_j}{\partial X_i}\right)$ (2C.2)

[I] Defining these constants relative to a set of axes rotated 180° about either symmetry axis will prove this.

Appendix 2D Influence of rotation on measured data

In orthotropic material the rotation component ω_{21} will contribute to the value of G_{21} (Eq. 2.9).[1] The extent to which this affects the outcome of acoustoelastic measurements is determined by the influence on the measured quantities which depend on G_{21}, namely polarization angle α and times of flight t_1 and t_2.

From Equations 2.14 and 2.15 respectively it can be seen that:

$$2\frac{(L^2\rho)^o}{t_{1,2}^2} = G_{11} + G_{22} \pm \sqrt{(G_{11} - G_{22})^2 + 4G_{21}^2} \tag{2D.1}$$

$$\tan 2\alpha = \frac{2G_{21}}{G_{11} - G_{22}} \tag{2D.2}$$

Parameters χ_{ij} are now defined. These are a measure of the magnitude of the acoustoelastic effect relative to that of the orthotropy of the material:

$$\chi_{ij} = \frac{\Delta G_{ij}(\underline{S},\underline{T})}{c_{1313} - c_{3232}} \tag{2D.3}$$

where $\Delta G_{ij}(\underline{S},\underline{T})$ is the *change* in G_{ij} caused by the presence of stress and strain, thus excluding rotation. Using Equation 2.9, the expressions 2D.1 and 2D.2 may be rewritten as:

$$2\frac{(L^2\rho)^o}{t_{1,2}^2} = (c_{1313} + c_{3232}) + (c_{1313} - c_{3232}) \times \\ \times \left\{\chi_{11} + \chi_{22} \pm \sqrt{1 + 2(\chi_{11} - \chi_{22}) + (\chi_{11} - \chi_{22})^2 + 4(\chi_{21} + \omega_{21})^2}\right\} \tag{2D.4}$$

$$\tan 2\alpha = \frac{2(\chi_{21} + \omega_{21})}{(1 + \chi_{11} - \chi_{22})} \tag{2D.5}$$

Now consider two cases:

- Slightly orthotropic material
  The orthotropy is of the order of the acoustoelastic effect, i.e. the χ-parameter is typically near unity in stressed material. Therefore, as the rotation $\omega_{21} << 1$, it is negligible when compared with χ_{21}. As a result t_1, t_2 and α can be considered to be rotation-independent.

[1] In isotropic material ω_{21} plays no part at all.

- Largely orthotropic material

  This case is characterized by $\chi_{ij} << 1$. In the expression for $t_{1,2}$ (Eq. 2D.4), the terms which are second-order in χ_{ij} and/or ω_{21} may be neglected, leading to:

$$2\frac{(L^2\rho)^o}{t_{1,2}^2} = (c_{1313} + c_{3232}) + (c_{1313} - c_{3232})\{\chi_{21} + \chi_{22} \pm (1+\chi_{11}-\chi_{22})\} \qquad (2D.6)$$

  Thus, time of flight is virtually independent of ω_{21}.

  The polarization angle α may be approximated by:

$$\tan 2\alpha = 2(\chi_{21} + \omega_{21}) \qquad (2D.7)$$

  and has a near-zero value. Although the relative error in α can be large, the absolute error is only equal to the rotation angle ω_{21}, which is assumed to be small. In practice, experimental errors will be dominant.

Appendix 2E Acoustoelastic behaviour for isotropic material

Firstly, to comply with the expression for the $\underline{G}$-tensor (Eq. 2.9), the elastic behaviour of an isotropic material must be defined in terms of 2nd- and 3rd-order stiffness constants. The 2nd-order constants c_{ijkl} can be expressed in terms of the Lamé constants λ and μ:

$$c_{ijkl} = \lambda\delta_{ij}\delta_{kl} + \mu(\delta_{ik}\delta_{jl}+\delta_{il}\delta_{jk}) \tag{2E.1}$$

where $\underline{\delta}$ = Kronecker delta

In this isotropic case the 3rd-order constants c_{ijklmn} can be represented by 3 constants. One way of doing this is by using the constants ν_1, ν_2 and ν_3, defined according to [53]:

$$\begin{aligned} c_{ijklmn} = {} & \nu_1\delta_{ij}\delta_{kl}\delta_{mn} + \\ & \nu_2\{\delta_{ij}(\delta_{km}\delta_{ln}+\delta_{kn}\delta_{lm}) + \delta_{kl}(\delta_{im}\delta_{jn}+\delta_{in}\delta_{jm}) + \delta_{mn}(\delta_{ik}\delta_{jl}+\delta_{il}\delta_{jk})\} + \\ & \nu_3\{\delta_{ik}(\delta_{jm}\delta_{ln}+\delta_{jn}\delta_{lm}) + \delta_{jl}(\delta_{im}\delta_{kn}+\delta_{in}\delta_{km}) + \\ & \qquad + \delta_{il}(\delta_{jm}\delta_{kn}+\delta_{jn}\delta_{km}) + \delta_{jk}(\delta_{im}\delta_{ln}+\delta_{in}\delta_{lm})\} \end{aligned} \tag{2E.2}$$

Using Equation 2.9, while discarding the rotation and substituting the strain components with the isotropic form of Hooke's law, the following expressions are obtained for all $\underline{\kappa}$-components mentioned in Equation 2.13:

$$\kappa_{11} = \kappa_{22} = \kappa_{13} = \kappa_{23} = \frac{1}{(3\lambda+2\mu)\mu}\{\lambda(2\mu+\nu_3) + \mu(2\mu+\nu_2+2\nu_3)\}$$

$$\kappa_{12} = \kappa_{21} = \frac{1}{(3\lambda+2\mu)\mu}\{-\lambda(\mu+2\nu_3) + \mu\nu_2\}$$

$$\kappa_{31} = \kappa_{32} = \frac{1}{(3\lambda+2\mu)\mu}\{-\lambda(\lambda+2\mu+2\nu_2+4\nu_3) + \mu(\nu_1+2\nu_2)\}$$

$$\kappa_{33} = \frac{1}{(3\lambda+2\mu)\mu}\{\lambda(2\lambda+9\mu+4\nu_2+8\nu_3) + \mu(6\mu+\nu_1+2\nu_2+8\nu_3)\}$$

$$\kappa_{66} = \frac{\mu+\nu_3}{\mu} \tag{2E.3}$$

Chapter 3

An Experimental Technique

3.1 Introduction

In Chapter 2 a theoretical basis is formulated for ultrasonic stress evaluation. It requires the measurement of time of flight and polarization direction of birefringent shear wave components and optionally also that of the longitudinal time of flight. In this chapter an experimental technique is described implementing this method with the aim of measuring *absolute stress* levels by the use of both wave types. The technique permits reproducible and semi-automated measurements on two-dimensional (plate-shaped) specimens.

The experimental technique is intended for use on steel, which compared with a metal such as aluminium is known to have a small acoustoelastic effect [42] in combination with a high acoustic impedance. This means that while on the one hand the ultrasonic signal-to-noise ratio is reduced, on the other hand accurate measurements are required in order to perform a meaningful stress evaluation. The experimental accuracy must therefore be high.

The first section of the chapter explains the principle underlying the technique. Subsequently the factors which influence experimental accuracy are considered. They are illustrated by means of various measurements, most of which involve steel specimens. Finally, the actual set-up is described.

It should be noted that the theory contained in Chapter 2 applies to two-dimensional stress fields. As the experimental technique will be used on plates, a plane stress state is assumed, as would result from in-plane loading of the plate, i.e. zero stress in the plate thickness direction. The wave propagation direction is necessarily in the thickness direction.

3.2 Experimental principle

Any experimental method for acoustoelastic stress evaluation must provide sufficient accuracy to accommodate the typically small magnitude of acoustoelastic material response. It is clear that for a measurement based on both shear and longitudinal waves this accuracy is greatly reduced if the outcome is not determined by wave propagation through exactly the same stressed material. In addition, influences which affect both wave types, for example those related to material temperature and the acoustic coupling between transducer and specimen, will have more effect if they are not common to both. On these grounds, and also in order to facilitate and speed up measurements, a set-up was developed using a single transducer capable of transmitting and receiving both shear and longitudinal waves.

3.2.1 The pulse-echo method

A well-established method for measuring the time of flight of ultrasonic waves travelling in the thickness direction of a plate is the pulse-echo technique (Fig. 3.1). A short electrical pulse is supplied to an ultrasonic transducer, causing this to emit a wave pulse through an acoustic coupling medium into the specimen at normal incidence.

As the plate surface opposite to the transducer is assumed to be stress-free, a transmitted wave pulse will reflect totally, i.e. with a 180° phase shift in stress amplitude. The *echo* of the transmitted pulse can thus be received by the same transducer. The conditions on the transducer side of the plate are generally such that an echo is partially reflected here too. Consequently, the wave pulse will travel several times through the thickness of the specimen, showing a gradual decrease in amplitude. The transducer is thus able to receive a series of successive back-face echoes (Fig. 3.2).

This received signal is amplified, after which it can be electronically processed in order to

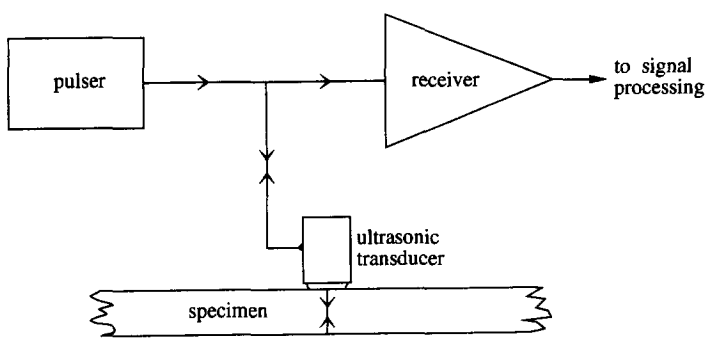

Fig. 3.1 Experimental principle of pulse-echo method

evaluate quantities such as time of flight and polarization direction. The time interval between two consecutive back-face echoes is taken to be the wave time of flight corresponding to a distance of flight of twice the plate thickness. The advantage of this approach is that the unavoidable time delays occurring in the transducer, coupling medium and electronic circuitry are common to all echoes and are therefore automatically compensated for.

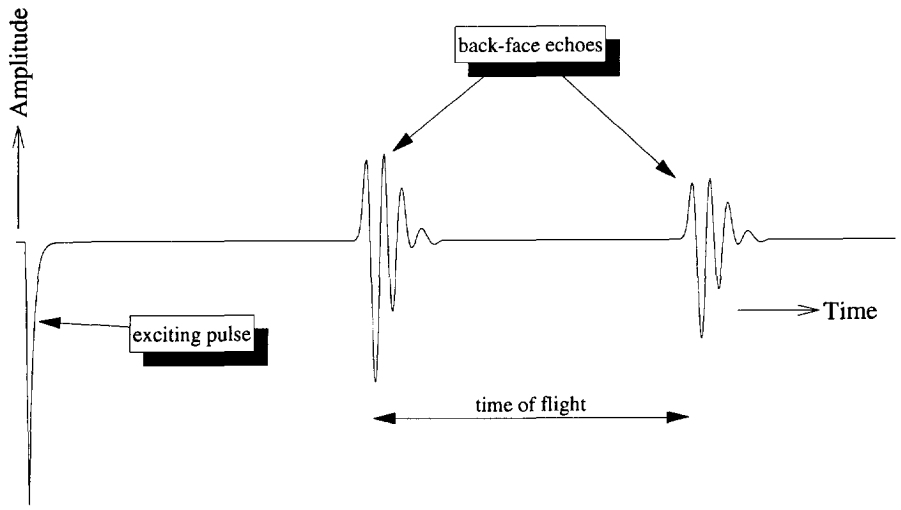

Fig. 3.2 Time of flight measured by the pulse-echo method

3.2.2 The ultrasonic transducer

Piezoelectric transducers

Ultrasonic waves can be generated in a variety of ways. Although there are certain inherent disadvantages, transducers based on the piezoelectric effect are most frequently used for this purpose. Typically the transducer consists of a thin disc of piezoelectric material coated on both surfaces with electrically conductive layers, which act as electrodes. One of the disc surfaces is coupled acoustically to the medium in which waves are to be transmitted or from which they are to be received. The other surface may be attached to a backing material in order to obtain specific transducer characteristics. The electrodes are used to induce an electric field in the disc, which will consequently show a mechanical reaction in the form of a changing stress field. Alternatively, any changes in the mechanical strain of the disc will induce an electric charge on the electrodes. Appendix 5B contains an extensive description of wave excitation and detection in a piezoelectric transducer.

Piezoelectric material properties determine the nature of the electromechanical coupling and thus also that of the acoustic waves which can be transmitted and received by a

transducer. These properties can be described by means of *piezoelectric constitutive equations*, which may take the form of [1]:

$$D_i = \varepsilon_{ij}^S E_j + e_{iJ} S_J \tag{3.1}$$

$$T_I = C_{IJ}^E S_J - e_{Ij} E_j \tag{3.2}$$

where $\underline{D}$ = electric displacement vector
$\underline{E}$ = electric field vector
$\underline{T}$ = stress tensor
$\underline{S}$ = strain tensor
$\underline{e}$ = 3rd-order piezoelectric stress tensor
$\underline{C}^E$ = stiffness tensor for constant electric field
$\underline{\varepsilon}^S$ = 2nd-order permittivity tensor for constant strain

Here the Voigt notation is used for those indices which are upper case (see Table 2.1)[I].

An ultrasonic transducer can be built with a single crystal of a suitable piezoelectric material, quartz for example. In order to obtain a strong electromechanical coupling specific sintered ceramics can be used, of which Lead Zirconate Titanate (PZT) is a typical example [22, 33]. After pressing and sintering, the piezoelectric properties are introduced separately by *poling*. The material is polarized at a high temperature in a strong electric field, after which it is cooled below a characteristic temperature (Curie temperature). By this means piezoelectric properties are obtained which are isotropic in the plane normal to the poling axis. It follows that the components of the $\underline{e}$-tensor are insensitive to any coordinate transformation consisting of a rotation about this axis. Thus, defined on a rectangular set of axes x_i with x_3 as the poling axis, the matrix representation of the $\underline{e}$-tensor can be derived as:

$$[e_{iJ}] = \begin{bmatrix} 0 & 0 & 0 & 0 & e_{15} & 0 \\ 0 & 0 & 0 & e_{15} & 0 & 0 \\ e_{31} & e_{31} & e_{33} & 0 & 0 & 0 \end{bmatrix} \tag{3.3}$$

Obviously the orientation of the poling axis (x_3) relative to the disc geometry also determines the nature of the electromechanical coupling. It is customary to specify this orientation as the direction normal to the cut used. Commonly implemented cuts are:

- The Z-cut
  The x_3 poling axis is orientated normal to the disc surface. In a thin disc, i.e. with a thickness which is small compared with the diameter, it may be assumed that the elec-

[I] For the 3rd-order piezoelectric stress tensor $\underline{e}$, it can be shown that $e_{ij} = e_{ji}$ [1].

tric field $\underline{E}$ caused by applying a voltage across the electrodes is directed in the thickness direction, i.e. $E_1 = E_2 = 0$ and $E_3 \neq 0$. From the form of the $\underline{e}$-tensor (Eq. 3.3) it follows that only normal stress components will be excited ($T_1 = T_2$, T_3). Alternatively, only normal strain components (S_1, S_2 and S_3) will induce an electric displacement component D_3 and hence an electric charge on the electrodes. This type of transducer is therefore used in a *thickness extensional* mode for transmitting and receiving longitudinal waves.

- The X-cut
  In this case the x_1-axis is the normal direction and the poling axis (x_3) lies in the plane of the disc. It is convenient to define an $\underline{e}'$-tensor relative to a coordinate system x_i'. This system is obtained by rotating the x_i-axes through 90° about the x_2-axis in order to orientate the x_3'-axis normal to the disc. This leads to:

$$[e_{ij}'] = \begin{bmatrix} e_{11}' & e_{12}' & e_{12}' & 0 & 0 & 0 \\ 0 & 0 & 0 & 0 & 0 & e_{35}' \\ 0 & 0 & 0 & 0 & e_{35}' & 0 \end{bmatrix} \tag{3.4}$$

  The electromechanical coupling is limited to mechanical components T_5' and S_5' through component e_{35}'. This cut is used in a *thickness shear* mode as a transmitter/receiver of shear waves. The shear waves excited are linearly polarized in the x_1' poling direction (x_3). Furthermore, this type of transducer has a maximum sensitivity for receiving such waves but is insensitive to shear waves polarized in the x_2'-direction (x_2).

Transducer characteristics

Consider a transducer consisting of a piezoelectric disc with a backing medium attached on one side and a wave propagation medium on the other. When this transducer is electrically driven, plane waves are excited at both disc interfaces [33] which propagate into the disc and the surrounding media. Their stress amplitudes are proportional to[1]:

$$\frac{Z}{Z+Z'} \quad \text{for waves propagating into the disc} \tag{3.5}$$

$$\frac{Z'}{Z+Z'} \quad \text{for waves propagating from the disc} \tag{3.6}$$

where Z, Z' = specific wave impedance in disc and adjacent medium respectively.

The specific impedance of a plane wave is dealt with in Appendix 3A.

[1] Assuming no wave conversions occur at the disc interfaces.

In the case of a pulsed operation, as used for the pulse-echo method, the piezoelectric disc is driven for a very short period of time by a high electric voltage. Owing to reflection at the two interfaces, the wave pulses excited in the disc will traverse the disc thickness back and forth a number of times. This process can be considered as a mechanical oscillation of the disc with a basic period equal to twice the time needed for the waves to traverse the disc thickness. The amplitude of the oscillation will then decrease as a result of:

- mechanical damping in the disc material itself;
- electrical damping via the electromechanical coupling in the piezoelectric disc material, depending on the conditions on the electrical side of the transducer;
- wave energy which is radiated on either side of the disc into adjacent material, depending on the local transmission coefficients.

Reflection and transmission coefficients at the interfaces, which play an important role, are a function of the specific wave impedances of the respective materials. This is described in Appendix 3B.

It is clear that the shape of the emitted wave pulse depends on the constitution of the transducer, e.g. the properties of the materials from which it is made and its geometry, and also on external factors such as the specific wave impedance of the propagation medium and the conditions on the electrical side. These same factors are also relevant with regard to wave reception.

Transducer characteristics range from highly damped, resulting in short pulses covering a large frequency range around a nominal value, to only slightly damped and hence narrow-banded. For time-of-flight measurements with the pulse-echo method short wave pulses have distinct advantages. Echo overlap, which can occur if the pulse duration is not much smaller than the time of flight, is avoided as much as possible. Furthermore, it is easier to identify corresponding points within two successive back-face echoes. This will prove to be a useful feature for the experimental technique applied here. The echoes shown in Figure 3.3 are typical for highly damped transducers.

Shear-longitudinal transducer

As stated at the beginning of this chapter, the transducer must be capable of transmitting and receiving both shear and longitudinal waves. One way to achieve this is by stacking discs of piezoelectric material with different cuts on top of each other [54]. Longitudinal and shear waves can thus be transmitted and received independently. It is even possible to simultaneously use shear waves polarized normal to each other [8]. A disadvantage of these stacked transducers, however, is that the characteristics of the individual discs will necessarily differ. An alternative is the use of a transducer composed of a piezoelectric disc surrounded by a

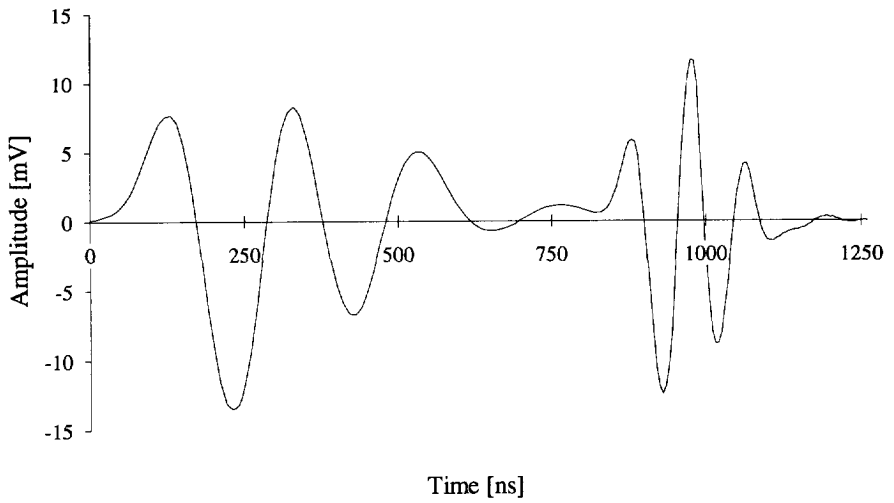

Fig. 3.3 First shear and second longitudinal back-face echo in 15 mm structural steel using a 45° rotated Z-cut PZT transducer

piezoelectric ring for transmitting and receiving shear and longitudinal waves respectively. In this case, however, it is to be expected that the two wave types will not propagate through exactly the same material, owing to differences in the shape of the emitted wave bundles.

The solution for this experimental set-up is sought in a transducer with only a *single* piezoelectric disc. It was specially designed by *Panametrics* and has reference number *X1013*. To accommodate both wave types yet another cut is used rather than the Z- or X-cuts described previously. When the disc thickness direction is at an angle of 45° with respect to the x_3 poling axis, a *rotated Z-cut*, the electromechanical coupling will include both normal and shear stresses and strains [31]. This can be deduced from the $\underline{e}''$-tensor, defined on axes x_i'' resulting from a 45° rotation of the original coordinate system about the x_1-axis:

$$[e_{ij}''] = \begin{bmatrix} 0 & 0 & 0 & 0 & e_{15}'' & e_{15}'' \\ e_{31}'' & e_{33}'' & e_{23}'' & e_{34}'' & 0 & 0 \\ e_{31}'' & e_{32}'' & e_{33}'' & e_{34}'' & 0 & 0 \end{bmatrix} \tag{3.7}$$

This transducer type is used in a mixed thickness elongation and thickness shear mode. Emitted shear waves are polarized in the x_2''-direction and these waves can also be received, but the transducer is not capable of receiving shear waves polarized in the x_1''-direction (x_1).

For the rotated Z-cut two plane waves will be induced in the disc simultaneously, namely a quasi-shear and a quasi-longitudinal type[1]. As these waves have different propaga-

[1] They are not pure mode waves owing to elastic material anisotropy and piezoelectric coupling [1].

tion velocities, the excited oscillation will comprise thickness elongation and thickness shear with unequal periods. The longitudinal wave pulse will therefore have a higher frequency than the shear wave pulse, a phenomenon which is clearly illustrated by Figure 3.3. Partially overlapping shear and longitudinal wave echoes are shown with nominal frequencies of 5 and 10 MHz respectively, transmitted and received with the rotated Z-cut PZT transducer.

In one respect this frequency difference can be regarded as favourable for the proposed stress evaluation technique. The reason for this is that the propagation velocity ratio of shear and longitudinal waves in the propagation medium, i.e. stressed steel, will roughly equal that in the piezoelectric ceramic and therefore their wavelengths will not differ very much. Consequently, the shape of the transmitted wave bundle for the two wave types will be roughly similar, as this feature depends on wavelength rather than frequency [33].

It should be noted that the fact that shear and longitudinal waves are necessarily excited simultaneously by this type of transducer is a disadvantage. Overlap of echoes for the two wave types (Fig. 3.3) can hinder measurements, as will be discussed below.

3.2.3 Measuring acoustic data

The quantities relevant to the method of acoustoelastic stress evaluation considered here are *times of flight* for shear and longitudinal waves and the shear wave *polarization direction*. They are measured by the pulse-echo method using the combined shear-longitudinal transducer described above.

Time of flight

Several procedures have been proposed for measuring time of flight by the pulse-echo method with a single transmitting and receiving transducer:

- The sing-around method [9, 33]
  Initially the transducer is excited by a pulse, after which one back-face echo, selected from the received series, is used to trigger successive pulses. The period of the pulse repetition rate is taken as a measure of the time of flight in the specimen.

  This method can easily be automated but a systematic error is inherent, as time delays occurring in electronic circuitry, transducer and coupling are also included in the result. Considering the accuracy and reproducibility required for time-of-flight measurements, the sing-around method is obviously not suitable for this purpose.

- The pulse-echo-overlap method [14, 43]
  A separate oscillator is used to trigger both the time base of an oscilloscope and, after frequency division, a pulse generator. The pulses excite the transducer and the received

echoes are displayed on the oscilloscope. A particular pair of echoes is selected by intensifying them on the display by means of a strobe technique. The oscillator frequency is then adjusted until the echoes overlap exactly, after which the time of flight between them can be read off as the reciprocal of this frequency.

The fact that the echoes can be selected arbitrarily makes this method more flexible than the sing-around method. However, as overlap must be established before each measurement, this method relies on having echoes with similar waveforms. Moreover, for this same reason, measurements cannot easily be automated - an experimental aspect which will prove to be indispensable.

- The phase-slope & cross-correlation methods [17]
  The relevant echoes are digitized, each in its own time window, and subsequently transformed to the frequency domain by means of a discrete Fourier transform algorithm. With the phase-slope method a range is chosen around the nominal frequency, where the derivative $^{d\theta}/_{d\omega}$ of the phase angle θ with respect to the angular frequency ω is approximately constant for the signals. These slopes represent the time delays of the echoes within their respective time windows. The time of flight between the echoes then follows by taking into account the time delay between the two windows.

  The cross-correlation method is based on calculating the cross correlation of the two echoes [5]. This function of time can be obtained by multiplying the complex conjugate of the Fourier transform of the first echo by the Fourier transform of the second echo and subsequently transforming this back to the time domain. The position of the maximum for this function directly gives the difference in the time delays for the echoes within their respective time windows. Again, the time of flight follows by considering the delay between the two time windows.

  A disadvantage of the phase-slope technique is that it requires the selection of a suitable frequency range on more or less arbitrary grounds. The cross-correlation technique is reported to give good results on highly attenuating and/or dispersive materials[I], where the echoes have a low signal-to-noise ratio and are distorted [34]. However, as will be argued in Section 5.5.6, this method is not suitable for the purpose of acquiring accurate data for the acoustoelastic experiments under consideration.

- The direct-pulse-interval method [55]
  A characteristic point is chosen in the echoes between which the time of flight is to be evaluated, e.g. a zero crossing or an extreme value. The time of flight is then measured directly using an electronic counter-timer triggered at these points to start and stop a time interval measurement. Basically, the resolution in time is determined by the inter-

[I] Dispersive materials exhibit frequency-dependent propagation properties.

nal clock period of the counter-timer, but it can be enhanced significantly by performing a large number of measurements and averaging the result.

Once the appropriate trigger conditions are set, the direct-pulse-interval method needs no further manual adjustments and will follow time-of-flight changes immediately. As was the case for the pulse-echo-overlap method, erroneous results can occur if the shapes of the "start" and "stop" echoes are not similar.

For this experimental set-up the direct-pulse-interval technique is used to measure the time of flight. The first zero crossings in the respective echoes are chosen as the trigger points to start and stop the time interval measurement. Zero crossings provide easily recognizable points within each echo and their level is not influenced by wave attenuation.

Differences in shape between the start and stop echoes are caused by distortion of the wave pulse. At the applied nominal frequencies of 5 and 10 MHz it is not to be expected that dispersion of the wave, while propagating in steel, will make a significant contribution. Another more likely source for distortion, however, is the occurrence of additional reflections in the transducer and/or coupling medium. Typically this has the effect of wave energy shifting to later parts of the pulse, since these reflections travel over longer distances. Therefore, of the zero crossings available, the first will be the least influenced by such wave distortion. This subject is discussed further when dealing with the influence of the transducer-specimen coupling.

It should be noted that whatever method is used for time-of-flight evaluation, the results will inherently be influenced by diffraction effects [43]. The reason for this is that a wave source with finite dimensions, such as a transducer, cannot produce a homogeneous field of plane waves in a specimen. These effects, which in general cannot be ignored on the scale of stress-induced time-of-flight changes, will be studied in Chapter 5.

Time of flight is preferably determined between the first and the second back-face echo, as these signals have the largest amplitude. However, as a combined shear-longitudinal transducer is used, echoes of the two wave types can overlap, depending on the propagation properties of the stressed material. If such overlap includes the first zero crossing of an echo, it will not then be available for time-of-flight measurements.

Figure 3.4 schematically illustrates this phenomenon for two materials, namely structural steel and aluminium alloy 2024-T351. The series of back-face echoes are shown as they would be received by the combined transducer after travelling through 10 mm thick specimens of these materials. The delays occurring in transducer and coupling layer during transmission and reception, which are estimated to be about 340 ns and 170 ns for shear and

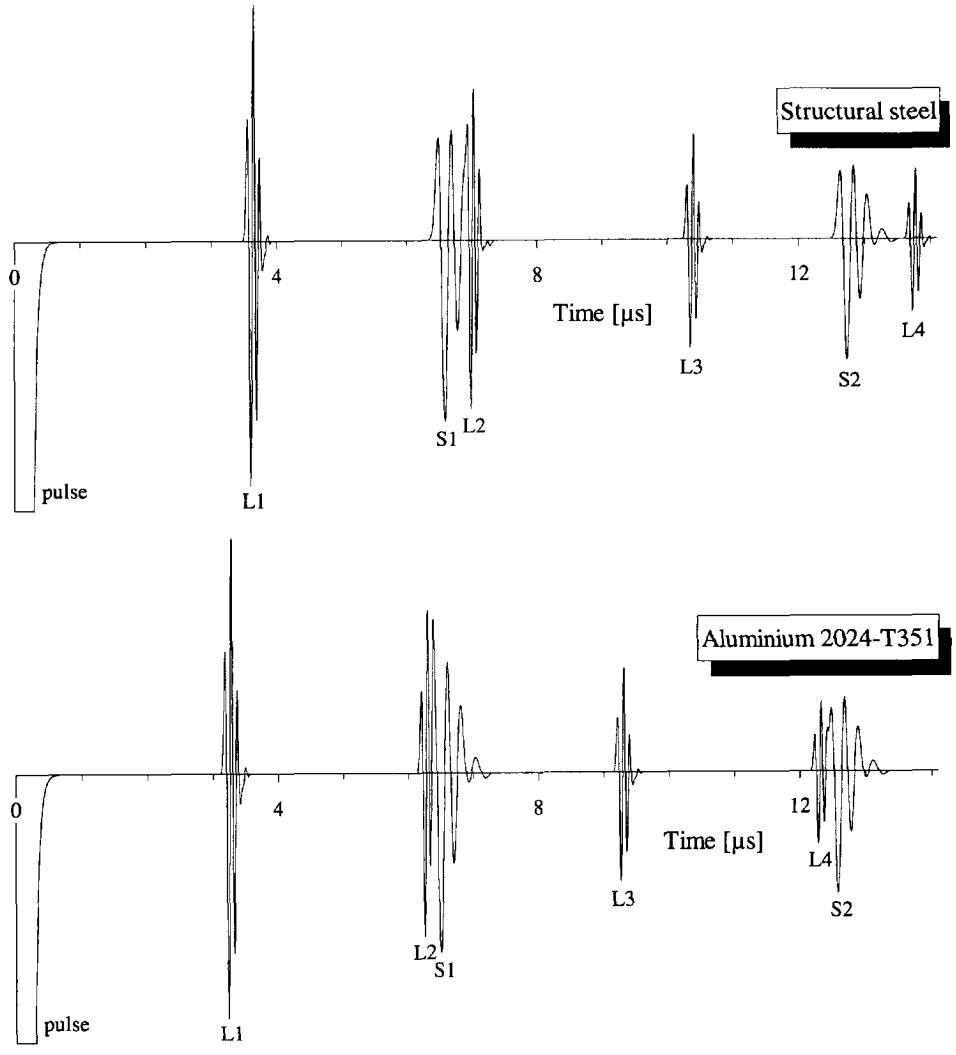

Fig. 3.4 Schematic representation of series of back-face echoes in 10 mm thick structural steel and aluminium 2024-T351 specimens using the combined shear-longitudinal transducer.

longitudinal waves respectively[1], have been taken into account. The echoes are denoted as L and S for longitudinal and shear waves respectively, followed by the *echo number*, i.e. the number of round trips through the specimen.

It is clear that the shear wave time of flight in steel can be determined between the 1st and 2nd echo. For the measurement of the longitudinal time of flight the 2nd echo is unavailable, ow-

[1] This estimate is based on the position of shear and longitudinal echoes with respect to each other, together with the presumption that delays are related to wave propagation and thus have a shear-to-longitudinal ratio of roughly 2.

ing to overlap by the 1st shear echo. Consequently, the 3rd echo must be used instead to function as stop echo. The aluminium alloy, however, has a longitudinal-to-shear velocity ratio which is slightly greater than 2. Only longitudinal echoes can therefore be used for time-of-flight evaluation, as the first zero crossings of all shear wave echoes are overlapped.

Echo overlap will decrease with increasing distance of flight. For aluminium, however, this will provide a solution only in extreme cases, such as very thick specimens or high echo numbers. In this context it is obvious that short pulses are advantageous.

Shear wave birefringence

The shear wave emitted by the transducer is linearly polarized in what will be referred to as the *transducer polarization direction.* When the wave enters stressed material the effect of shear wave birefringence will generally occur, i.e. two orthogonally polarized shear waves will be induced, propagating at different speeds (Fig. 2.1). The amplitude of a birefringent wave component depends on the angle between its polarization direction and that of the transducer. From equating the boundary conditions at the material interface, it follows that the amplitude is proportional to the cosine of this angle, i.e. a maximum value for coinciding polarization directions and zero for the normal case.

The transducer, acting as a receiver for shear waves, will show a sensitivity which is also proportional to the cosine of the angle between the shear wave and transducer polarization directions. Consequently, in a pulse-echo configuration, a birefringent shear wave component will make a contribution to the signal ultimately received proportional to the square of the cosine of the angle between wave and transducer polarization directions. Using this knowledge, the received shear wave signal s(t) for an arbitrary transducer polarization direction can be written as a linear combination of $s_1(t)$ and $s_2(t)$, the signals for the respective transducer polarization directions which coincide with those of the two birefringent shear wave components:

$$s(t) = s_1(t)\cos^2(\alpha - \theta) + s_2(t)\sin^2(\alpha - \theta) \tag{3.8}$$

where α = polarization direction of wave component associated with s_1 relative to x_1-axis

θ = transducer polarization direction relative to x_1-axis

Similar equations form the basis of acoustoelastic techniques which are aimed at determining the fractional velocity difference of birefringent wave components (birefringence) [4, 20].

Acoustoelastic stress evaluation requires measurements using both birefringent components. As shear waves may be polarized in any direction, it follows from Equation 3.8 that the transducer polarization direction must be variable. This is achieved by rotating the trans-

ducer about its axis. The time of flight of a birefringent shear wave component is then evaluated by aligning the transducer polarization direction with that of the particular wave, leading to extinction of the other component.

Shear wave polarization

It is clear from Equation 3.8 that a shear polarization direction can be determined as the transducer polarization direction for a maximum echo amplitude. The measurement involves *scanning* the echo amplitude with a rotating transducer in a range which includes the presumable maximum. However, for transducer orientations on either side of the maximum, the other shear wave component will have a non-zero amplitude. As the two shear echoes will generally show some overlap, interference may occur. This can be avoided by using only the first birefringent component to arrive in order to evaluate the polarization direction.

In spite of this, a problem may still arise if the echoes of the two birefringent shear wave components show only a small difference in the time of arrival. For differences considerably less than a quarter of the shear wave period, e.g. 50 ns in the case of a 5 MHz shear wave, the amplitude variations will be too small to be useful. In this case, however, the composite echo formed by the two almost completely overlapping shear wave components will resemble that of a single shear wave with a time of flight dependent on the transducer polarization direction.

In order to assess this effect, a calculation is performed based on Equation 3.8. The 5

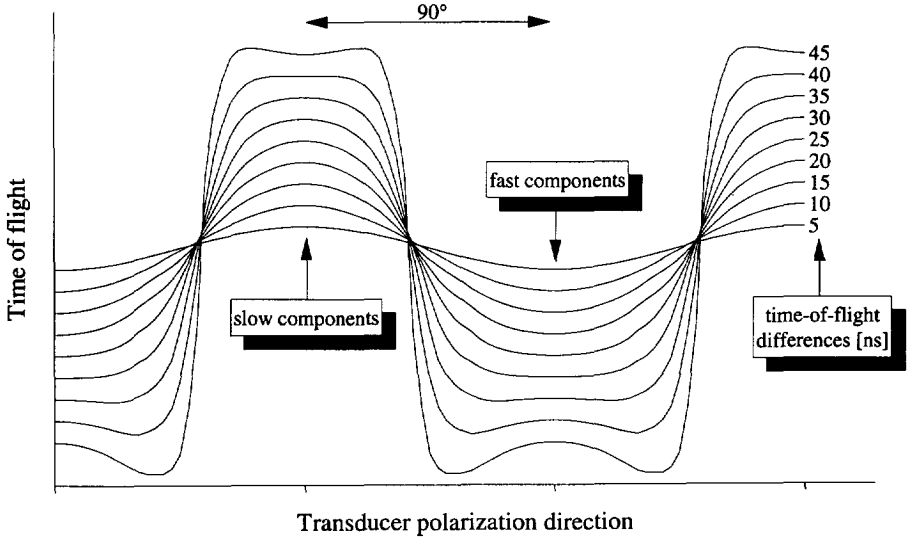

Fig. 3.5 Calculated time of flight as a function of transducer polarization direction for an echo composed of birefringent components of a 5 MHz shear wave pulse with increasing time-of-flight differences.

MHz shear wave echo, shown in the first part of Figure 3.3, is used for both $s_1(t)$ and $s_2(t)$, the signals for the transducer polarization directions which coincide with those of the two shear wave components. The shape of the first and second composite back-face echoes are calculated as a function of the transducer polarization direction for time-of-flight differences varying from 5 to 45 ns. The positions of the first zero crossings within these echoes determine the time of flight which would be found using the measuring technique described above. Figure 3.5 shows the calculated values as a function of the transducer polarization direction.

Up to time-of-flight differences of 25 ns the shear polarization of the components can be found in a straightforward manner as the directions for which time of flight takes an extreme value. For larger differences the extremes become less pronounced. They are eventually accompanied by other extremes, a situation which makes an accurate evaluation difficult. Owing to the asymmetry of the waveform relative to the first zero crossing, this effect is found to be more manifest for the faster shear wave component.

To summarize, the criterion most suitable for determining the shear wave polarization direction depends on the time-of-flight difference between the birefringent components relative to the period of the wave pulse. For small and large differences respectively optimal accuracy is obtained by measuring the transducer polarization direction for either a maximum time-of-flight value of the composite shear wave echo or the maximum amplitude of the fastest birefringent component. In both cases the polarization of the other component must be assumed to be normal to the direction found.

3.2.4 Transducer-specimen coupling

The transmission and reception of ultrasonic waves by a piezoelectric transducer requires the transfer of mechanical energy to and from the stressed material. In this particular case both shear and longitudinal waves must be accommodated simultaneously. A number of options are available in order to create an acoustic coupling of this kind:

- Fixed bond
  Creating a fixed bond between transducer and specimen [43] is a possible method but it is not a very practical, as the transducer polarization must be variable.
- Pressure coupling
  Acoustic coupling is achieved by attaching the transducer to a metal coupling piece which is pressed onto the specimen [9]. However, the interface pressure required for an effective coupling (≈140 MPa) is so high that the stress state in the specimen is likely to be influenced. Furthermore, the coupling cannot be maintained while varying the transducer polarization.

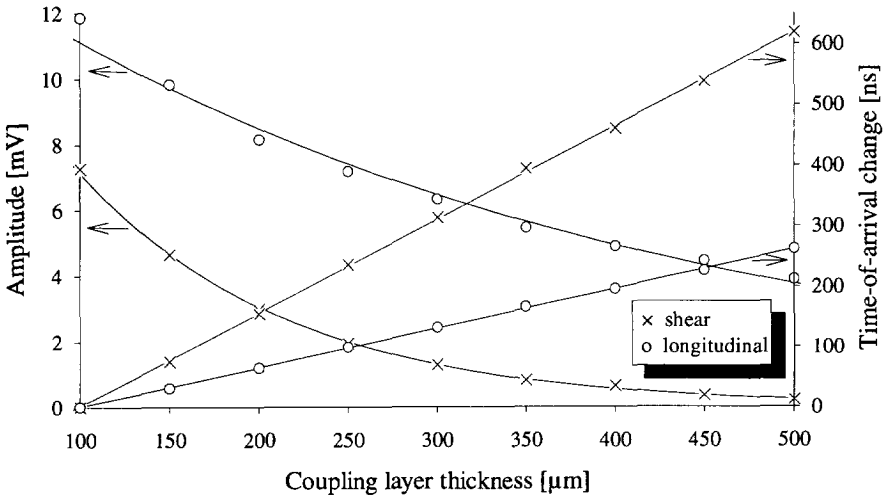

Fig. 3.6 Results from measurements in a 15.4 mm thick structural steel specimen as a function of coupling layer thickness, showing the amplitude and change in time of arrival of the first longitudinal and shear wave echoes.

- Fluid coupling medium

  For longitudinal waves, water and light oil are most frequently used as coupling media. However, in order to couple shear waves, the fluid must also allow shear stresses to build up. This is possible at ultrasonic frequencies if the viscosity is sufficiently high. Such fluids are therefore widely used for shear wave measurements. One advantage is that the coupling function is maintained during slow transducer rotation [14].

Obviously, from an experimental viewpoint, a viscous fluid is the most suitable coupling medium and this is therefore what was used for the experimental set-up. The fluid is manufactured by *Panametrics* and designated as *Shear Wave Couplant*. The composition is unknown.

The propagation of longitudinal waves through the couplant does not present any problems, as only hydrostatic stresses are involved and these can build up in any fluid. Shear wave propagation, however, depends on viscous behaviour and is therefore inherently also a function of frequency. In order to gain a rough impression[1] of the ultrasonic properties of the couplant, measurements were performed using the combined shear-longitudinal transducer, i.e. with 5 MHz shear and 10 MHz longitudinal wave pulses.

The experiments were performed on a steel specimen, varying the coupling layer thickness from 100 to 500 µm. The time of arrival of the first longitudinal and shear wave back-face

[1] Rough in the sense that dispersion in the couplant is neglected.

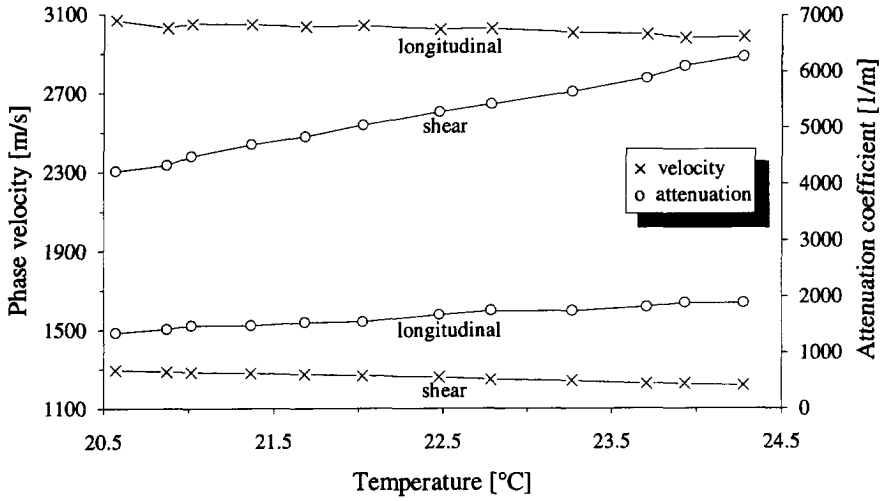

Fig. 3.7 Estimated longitudinal and shear wave phase velocities and attenuation coefficients in shear wave couplant as a function of temperature.

echoes was determined relative to the pulse exciting the transducer. This quantity includes the time needed for the waves to traverse the coupling layer twice. The amplitude of the first maximum of the first back-face echoes was also measured, as it is a measure of wave attenuation in the couplant. The results, shown in Figure 3.6, have no accuracy in an absolute sense, but their dependence on the coupling layer thickness gives an indication of the phase velocity and attenuation coefficient[I] in the shear wave couplant.

It was found, however, that temperature has a significant influence on the properties of the couplant. In order to assess this effect the time of arrival and amplitude were recorded for a fixed layer thickness of 110 μm while increasing the temperature from 20.5 to 24.5 °C. By correcting the time-of-arrival data for time-of-flight changes in the steel specimen (see below) and attributing all other changes to the couplant, estimates for the velocity and attenuation coefficient are calculated as a function of temperature. The results, shown in Figure 3.7, indicate an increase in the wave attenuation with temperature, especially for shear waves. At the same time the phase velocities exhibit a slight decrease.

To summarize, it may be concluded that the shear wave couplant can effectively couple transducer and specimen for both shear and longitudinal waves, provided that only a thin layer is used. The coupling characteristics will, however, be temperature-dependent.

[I] The attenuation coefficient α describes an exponential amplitude decrease proportional to $e^{-\alpha x}$, where x is the distance of flight.

3.3 Distorting influences

Before describing the actual set-up, certain factors which influence the results of the acoustoelastic experiments under consideration will be considered. These factors played an important role in the development of the technique. Experimental data will be presented to illustrate the distorting influences.

3.3.1 Transducer-specimen coupling

There are many examples in literature indicating that the transducer-specimen coupling is the weak link in time-of-flight measurements using a piezoelectric transducer [3, 7, 14]. This was probably the main reason for considering alternative transducer types which do not need to be in direct mechanical contact with the specimen in order to function correctly, e.g. transducers based on electro-magnetic principles (EMAT). It is the lack of reproducibility which creates the problems, especially if the time-of-flight data obtained are required to have a high and virtually absolute accuracy, as is the case here.

Wave distortion

A reproducible coupling can be obtained by allowing waves to travel longer distances in the coupling medium before entering the specimen, for example when an *immersion technique* in a water bath is used [16, 32]. Time of flight can then be determined as the time interval between echoes from the front and back face of the specimen. During their travel through the coupling medium both these signals will be distorted due to dispersion and diffraction effects. The reflections occurring at the front and back faces are also (unequal) functions of the acoustic properties of the fluid. Nevertheless, there is no reason for these effects not to be reproducible, provided that the transducer-specimen distance and the acoustic behaviour of the couplant (generally related to temperature) are kept constant. One problem, however, is that

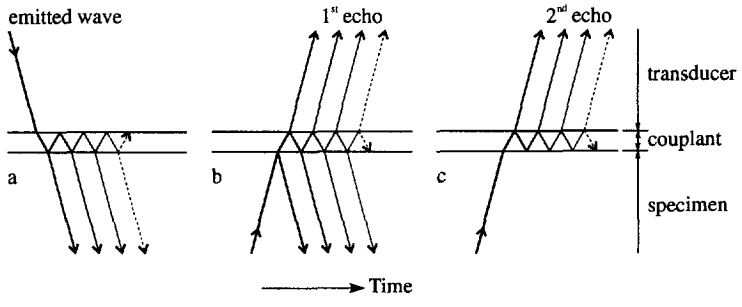

Fig. 3.8 Reflections within a thin coupling layer while entering the specimen (a), reflecting against the couplant from the specimen (b) and leaving the specimen (c).

the immersion technique is limited to longitudinal waves, as shear waves will be attenuated too much in the couplant due to the large distance of flight. Moreover, this technique is not always a very practicable solution.

A completely different situation arises when *thin coupling layers*[I] are used and the time of flight is measured between successive back-face echoes. Waves which are transmitted through or reflected against the couplant will be reflected within the layer a number of times, as is shown schematically in Figure 3.8. For both shear and longitudinal waves the specific wave impedance in the fluid couplant is considerably lower than in either transducer or specimen. Consequently, the extra reflections within the layer will be numerous and without phase reversal, as they involve a reflection coefficient near unity (Appendix 3B). They have the effect of shifting wave energy to later parts of the waveform. Together with dispersion in the viscous coupling fluid, the extra reflections give rise to waveform distortion in a manner which is obviously a function of the coupling layer thickness.

There are a number of reasons why the wave emitted by the transducer is distorted before it is ultimately received in the form of back-face echoes:

- transmission through the coupling layer on entering and leaving the specimen. The influence is common to all echoes;
- diffraction in the specimen, which being a function of the distance of flight, distorts each back-face echo differently;
- reflection against the coupling layer.[II] Each echo is affected differently, since the number of times this reflection occurs depends on the echo number.

Clearly the last two phenomena lead to dissimilar back-face echoes. The presence of the coupling-related influences will therefore cause these *different* shapes to be *different* functions of layer thickness. Consequently time-of-flight evaluations will be reproducible only if this thickness is controlled.

Layer thickness

In order to obtain a reproducible coupling layer, it is common practice to press the transducer onto the specimen surface using a constant pressure [6, 7, 8, 15]. Furthermore, after positioning the transducer, some time is allowed for the viscous couplant to squeeze out between transducer and specimen before the actual measurements are performed.

In Appendix 3C the case is considered of a circular transducer which is pressed onto a speci-

---

I In this context *thin* refers to the situation in which time of flight through the coupling layer is small compared with the pulse length.

II It should be noted that as it is receiving an echo at the same moment, the transducer will act as a transmitter and so contribute to distortion of later echoes as well.

men with a viscous fluid in between. The layer thickness h is derived as:

$$h = \sqrt{\frac{3\pi\eta R^4}{4I}} \tag{3.9}$$

where η = viscosity coefficient of couplant

R = transducer radius

I = impulse exerted on transducer, equal to the time integral of the applied force ($\int F(t)dt$)

assuming the initial layer thickness, i.e. before applying any pressure, to be much larger than the ultimate values. Rotation of the transducer about its axis does not influence the thickness obtained.

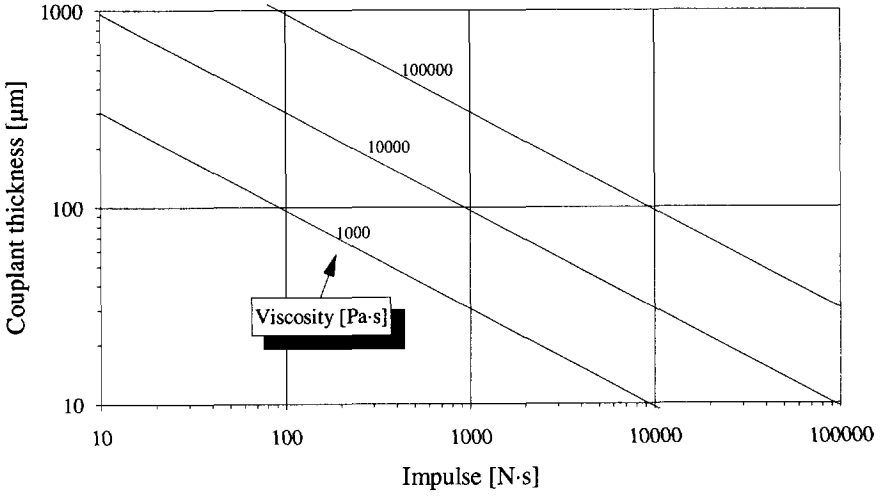

Fig. 3.9 Calculated coupling layer thickness as a function of applied impulse for a 9 mm diameter transducer and couplant viscosity coefficients ranging from 1000 to 100 000 Pa·s.

This equation expresses that as a result of applying a constant pressure, the layer thickness will be reduced continuously at a decreasing velocity, depending on the transducer radius, fluid viscosity and applied force. Figure 3.9 illustrates this for a transducer in a 9 mm diameter casing. This value and a couplant viscosity coefficient of 10 000 Pa·s are typical for the set-up under consideration. It is found that for this case an impulse of about 23 000 N·s is needed to obtain a layer thickness of 20 µm. At an applied pressure of 0.69 MPa, for example, this would take almost 9 minutes [15]. Although the thickness will only decrease slowly at this point, time-of-flight evaluation will continue to be influenced until the pressure is removed. An alternative approach would be to release the pressure after a certain thickness is obtained, using some mechanical means. However, considering the thinness of a typical layer

and therefore the accuracy required, this solution will be difficult to realize.

Effect of thickness on time of flight

The way in which the coupling layer thickness influences time-of-flight evaluation was determined experimentally. Using the combined shear-longitudinal transducer in a pulse-echo configuration, the time of flight was measured through a 15 mm thick structural steel specimen. The layer thickness varied between 20 and 200 μm. Thinner layers could not be achieved with the set-up used, while thicker layers would lead to an unacceptably high attenuation. The results, which are presented in Figure 3.10, show that from 20 μm onwards the time of flight increases with thickness for both wave types. Above a certain *limit thickness*, approximately 80 μm for shear waves and 90 μm for longitudinal waves, the time of flight is found to be no longer influenced.

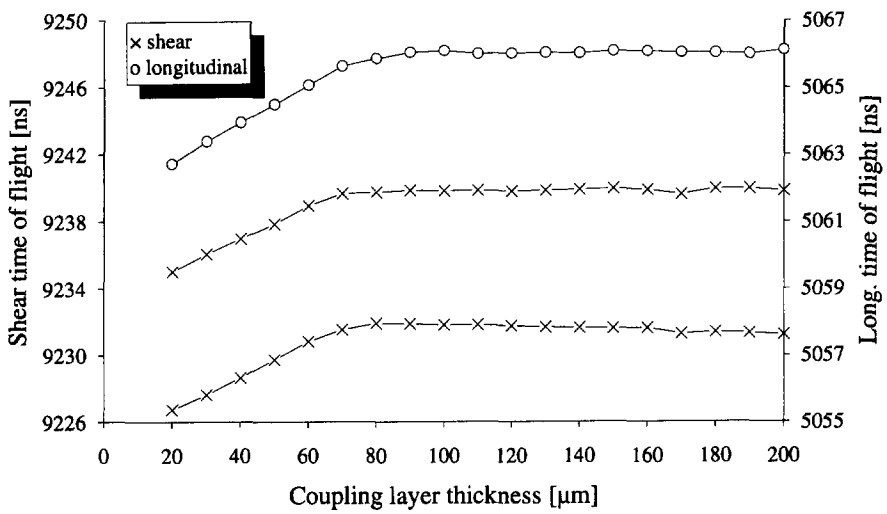

Fig. 3.10 Measured shear and longitudinal wave times of flight in a 15 mm thick structural steel specimen as a function of coupling layer thickness.

A highly probable explanation for this limit thickness is based on the fact that reflections within the couplant, which are a cause of time-of-flight dependence, are delayed proportionally to the layer thickness. If this delay is large enough, waves are distorted only *after* the first zero crossing and the time-of-flight evaluation is then no longer affected.

The observed time-of-flight dependence below the limit thickness can be qualitatively explained by considering an important difference between successive echoes, namely the distortion introduced during reflection from the specimen against the coupling layer. For this purpose an approximate calculation was performed. It is based on the 5 MHz shear wave echo shown in the first part of Figure 3.3. In this calculation the waveform is assumed to rep-

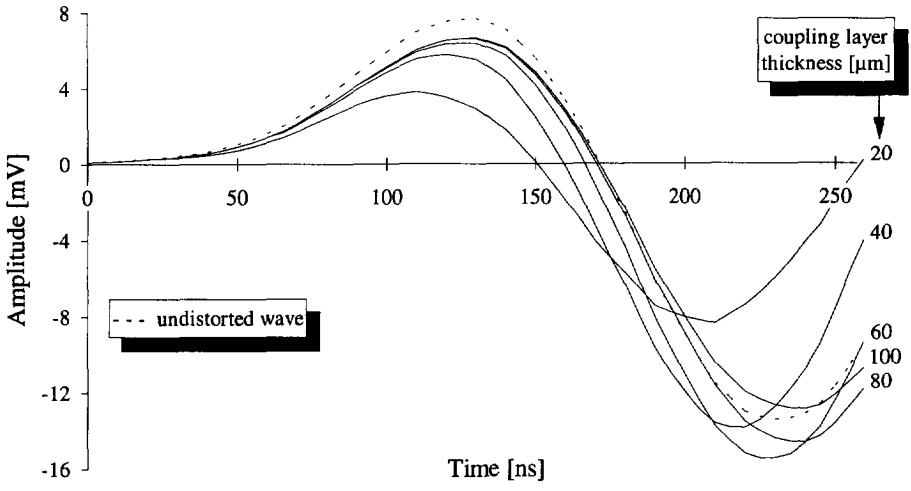

Fig. 3.11 Calculated distortion of the second back-face echo of a 5 MHz shear wave pulse in steel caused by reflection against the coupling layer, for increasing layer thicknesses.

resent the second echo in a steel specimen in a situation in which there is no coupling layer to reflect against, i.e. a free surface corresponding to a reflection coefficient of −1. The necessary reflection and transmission coefficients are derived from the specific shear wave impedances in steel, couplant[I] and transducer, which are taken to be 25.3, 1.8 and 18 MPa·$^{s}/_{m}$ respectively. For the phase velocity and attenuation coefficient in the couplant the respective values of 1250 $^{m}/_{s}$ and 5000 m^{-1} are used, which are estimates based on experiments (see Figs. 3.6 and 3.7). Finally, the transducer is considered as a passive element, i.e. no re-transmission of received echoes is assumed to occur.

Figure 3.11 shows the calculated distortion of the first and most relevant part of the waveform for layer thicknesses varying from 20 to 100 µm. As time of flight is measured using the first available zero crossing in the echoes, it is obvious that the thickness dependence does at least qualitatively correspond to that found experimentally. It therefore seems likely that the effect of the coupling layer thickness on time-of-flight evaluation (Fig. 3.10) is mainly due to distortion introduced during reflection of the wave from the specimen against the coupling layer.

Increased layer thickness

It may be concluded from the above that as far as time-of-flight evaluation is concerned a layer thickness above the limit value is the most favourable for obtaining a reproducible

[I] In fact, the attenuation of the coupling fluid calls for a description using a complex impedance. For the sake of simplicity a real impedance is assumed here and a full treatment is postponed until Chapter 5.

coupling. A layer thickness of 100 μm was therefore chosen, which is just above the limiting value for both shear and longitudinal waves.

A clear disadvantage of an increased thickness is the higher attenuation of the signal. For example, based on an attenuation coefficient of 5000 m^{-1}, the amplitude of a shear wave after traversing the coupling layer twice is reduced 2.2 times as much for a thickness of 100 μm compared with a thickness of 20 μm. This amplitude ratio will even be somewhat higher if the reflections within the coupling layer are taken into account; these tend to increase the amplitude, due to the fact that reflection coefficients are near unity. For thinner layers this effect is more pronounced, since then these extra reflections are less attenuated and less delayed. The signal-to-noise ratio will not decrease by the same amount, however, since to a large extent this is determined by spurious echoes in the signal received by the transducer and these will also be attenuated.

It should be noted that an increased layer thickness does not guarantee a reproducible coupling. As discussed earlier, the back-face echoes inherently have unequal shapes and therefore unequal frequency spectra. Dispersion, i.e. frequency-dependent propagation, in the couplant will therefore affect successive echoes differently. This effect is amplified as layers become thicker and thickness variations may still influence time-of-flight evaluation. This subject will be considered further in Chapter 5, where a calculation model for the current pulse-echo technique is worked out.

Transducer rotation

It is essential that ultrasonic measurements can be performed as a function of the transducer polarization direction. Quantities such as time of flight and echo amplitude are *scanned*, i.e. measured while rotating the transducer. Obviously the characteristic of the transducer-specimen coupling must remain as constant as possible during such a scan. As an example the results are presented of both amplitude and time-of-flight scans measured on a low-textured structural steel. The scans were recorded in both rotation directions using a transducer rotation velocity of 2 °/s. The coupling layer thickness was 100 μm.

The results of the echo amplitude scans, shown in Figure 3.12, indicate differences of up to 2.5 % between the two rotation directions. Since these amplitude variations do not always occur in the same manner, it is thought that they are related to a non-homogeneous coupling fluid and/or fluctuations in the electronic circuitry driving the transducer.

Experiments show that the received echo amplitude can become somewhat time-dependent when transducer rotation has just begun or finished, especially in the case of thin coupling layers. It is believed that this effect is caused by temperature changes in the couplant, combined with the fact that attenuation in the shear wave couplant increases with temperature.

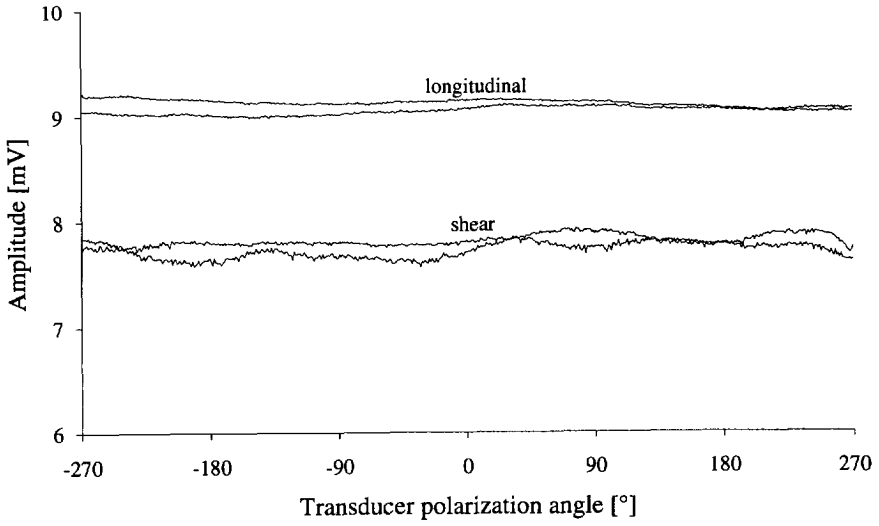

Fig. 3.12 Scans of longitudinal and shear wave echo amplitude in a 29 mm thick structural steel specimen made in both rotation directions. The first positive peak value in each first back-face echo is measured.

Temperature changes can be induced by the mechanical work involved in rotating the transducer, which is dissipated in the viscous fluid. These changes become more pronounced for thinner layers, since (i) more mechanical work is done and (ii) the fluid volume dissipating this work is smaller. In order to avoid this influence, scans are performed in such a way that a virtually stationary situation is achieved during the relevant part of the scans.

Figure 3.13 gives the results for the longitudinal and shear wave time-of-flight scans. They show that the time-of-flight values do not deviate by more than 0.1 ns and 0.2 ns from each other for longitudinal and shear waves respectively. Apparently the relative amplitude variations which occur during a scan are not accompanied by comparable time-of-flight variations. The unequal extreme values for the shear time of flight and the varying longitudinal time of flight are attributed to transducer misalignment, an aspect which is discussed below.

It should be noted that no significant differences were found between values measured while rotating at 2 °/s and those determined statically. However, the use of significantly higher scan speeds can cause deviating results, especially for thin coupling layers. The explanation for this is thought to be related to non-parallelism of the transducer and specimen surfaces. While rotating, the viscous couplant will be compressed on one side of the transducer and expanded on the other. During compression the fluid is partly squeezed out between the surfaces, due to the high pressure occurring. The supply of fluid needed for expansion, however, cannot take place at the same speed, since only atmospheric pressure is available in order to achieve this. As a result *cavities* can be formed in the fluid, resulting in loss of the

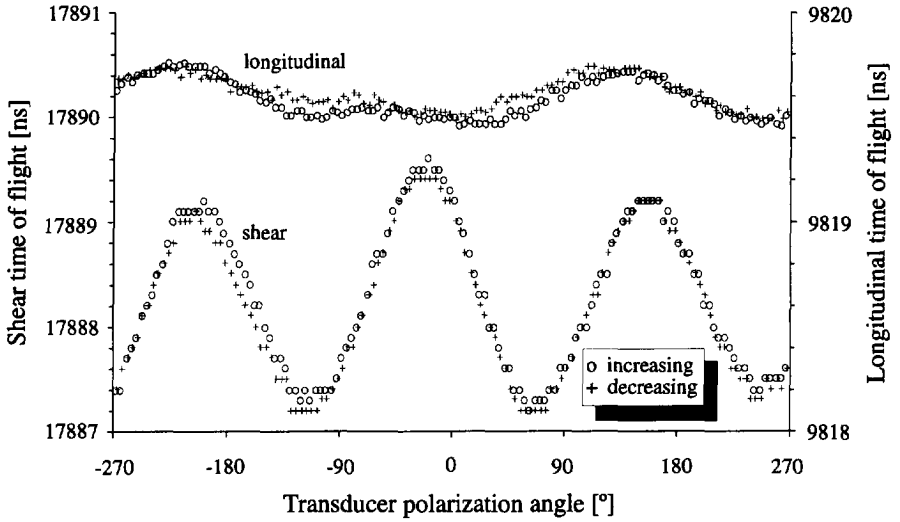

Fig. 3.13 Longitudinal and shear time-of-flight scans made in both rotation directions and measured through a 29 mm thick structural steel specimen.

coupling function. Observations using a transparent specimen, where on one side of the transducer a colour change in a thin couplant layer (20 μm) could be detected during rotation, confirm this explanation.

As is argued below, a slight tilt of the transducer is difficult to avoid in practice. As a result the present set-up, in which the layer thickness is mechanically fixed, is not very suitable for thin layers in combination with the high viscosity couplant. For larger thicknesses, however, this phenomenon does not play an important role.

3.3.2 Transducer misalignment

In a conventional configuration, where a direct-contact transducer is placed on a specimen using a low viscosity fluid as a couplant, parallelism of the transducer and specimen surfaces is ensured. Correct alignment of the transducer axis with the specimen normal is no longer guaranteed when a high viscosity shear wave couplant is used. For example, if a constant pressure is applied to position the transducer, the pressure in the coupling fluid has a maximum value at the centre and decreases to zero towards the edge (Appendix 3C). Therefore, depending on both the construction and the stiffness of the mechanical set-up used for positioning the transducer, misalignment can occur. With an increased layer thickness, as is the case here, pressure is zero in the couplant and misalignment is entirely determined by the accuracy of the positioning construction.

Misalignment of the transducer will cause distortion of the ultrasonic waves for two

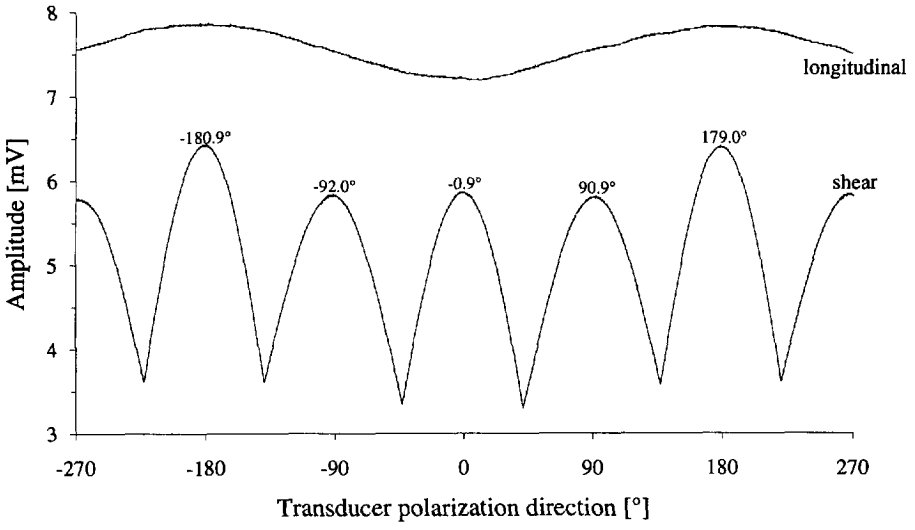

Fig. 3.14 Shear and longitudinal echo peak amplitude as a function of transducer polarization direction for a highly textured pipeline steel (10.26 mm thickness), showing the influence of transducer misalignment.

reasons:

- The coupling layer thickness varies over the transducer surface.
- After traversing the specimen a number of times a shift of the wave bundle occurs relative to the receiving transducer.

Refraction at the couplant-specimen interface also plays an important role in the latter effect. According to Snell's law [1], the angle of refraction at the interface between two media depends on the respective phase velocities. Generally the phase velocity in the coupling fluid is lower than in the specimen, leading to a wave bundle in the specimen, which is more tilted than the transducer. For example, based on the experimentally obtained velocities given previously for the couplant (Fig. 3.7), the ratio of these angles is 2.5 and 2 respectively for shear and longitudinal wave bundles emitted in steel.

Wave distortion, as caused by transducer misalignment, is likely to affect both time-of-flight and amplitude measurements. Misalignment can also be a function of transducer orientation. To understand this, the misalignment of a rotatable transducer can be divided into two parts:

- the angle between the transducer and the rotation axes;
- the angle between the rotation axis and the specimen normal.

When both of these kinds of misalignment occur simultaneously, the resultant distorting effect is dependent on the transducer orientation. This will particularly affect shear wave po-

larization measurements when they are based on the determination of amplitude maxima. The wave amplitude will vary not only because of shear wave birefringence but also due to a changing misalignment.

Figure 3.14 shows an example of an amplitude scan for a highly textured steel, measured with the combined shear-longitudinal transducer. The maximum of the amplitudes for the first echoes of the two birefringent shear wave components is plotted as a function of transducer polarization direction. The angles for a maximum value, which are a measure of the polarization directions of the two shear wave components, are also indicated in the graph. In addition, the amplitude of the first longitudinal echo is shown. It is estimated that during the measurement the transducer axis was tilted 0.5° relative to the rotation axis and that this axis in turn was tilted 0.2° relative to the specimen surface normal.

The fact that the longitudinal amplitude varies with a period of 360° is attributed to transducer misalignment. This same variation also seems to be part of the shear amplitude. The graph clearly shows the effect which this has on the position of the shear wave amplitude maxima. These should be 90° apart, but are now shifted 1 to 2° at angles where there is an amplitude gradient. Two amplitude maxima originating from the same shear wave component but 180° apart will be shifted in opposite directions. The error introduced by misalignment can therefore be minimized by normalizing these maxima so that they are exactly 180° apart.

An example of the effect of misalignment on time-of-flight measurements has already been given in Figure 3.13. The influence of a tilted transducer on both amplitude and time-of-flight measurements is considered further in Chapter 5.

3.3.3 Signal noise

Obviously noise in the received transducer signal can affect measurements. As far as random noise is concerned, the influence will be very small. This is because the ultrasonic signal is repetitive, which enables averaging to take place, thereby cancelling all random noise. It is found, however, that the transducer itself also produces a small *background signal*, which decreases in amplitude from the exciting pulse onwards. This is probably caused by echoes occurring within the transducer, e.g. the backing medium. Acoustic coupling reduces the amplitude of the background signal.

Measured from the start of the exciting pulse, the influence of the pulse becomes negligible at about 3 μs, after which the peak amplitude of the background signal is no more than 0.13 mV. An exception is formed by the time range between 5.5 and 8 μs, where peaks of up to 0.38 mV occur. These values were observed while coupling the transducer via a 100 μm couplant layer to a thick steel specimen, i.e. the first (longitudinal) back-face echo only oc-

curred after about 10 µs.

The background signal will not greatly affect the evaluation of stress-induced time-of-flight *changes*, since these changes are small relative to the period of the signal. However, the *absolute* value of measured time-of-flight data can deviate somewhat. It is estimated that the maximum effect is approximately 1 ns for shear waves and 0.2 ns for longitudinal waves. It would be possible to compensate for this error by measuring the background signal separately and correcting time-of-flight data, dependent on the position of start and stop echoes relative to the background.

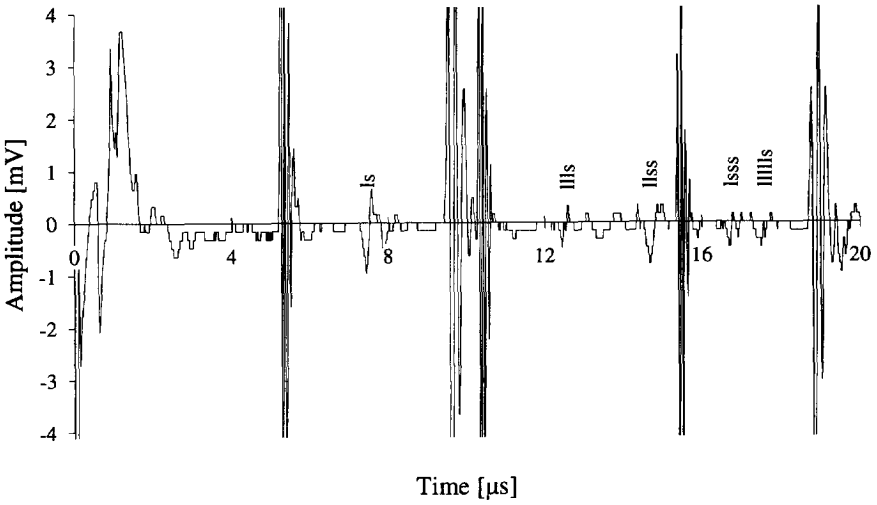

Fig. 3.15 Magnified view of the ultrasonic signal measured with the combined shear-longitudinal transducer through a 15 mm thick structural steel specimen. Small additional echoes are shown, attributed to mode conversion of the wave during reflections, due to the finite dimensions of the wave beam.

It is noteworthy in this context that the background signal would seem to be larger at first sight. Figure 3.15 shows a magnified view of the first 20 µs of the ultrasonic signal as measured through a 15 mm thick structural steel specimen. Between the longitudinal and shear echoes small perturbations can be observed with peak amplitudes up to 0.9 mV. However, their positions correspond exactly to wave components which have been converted from longitudinal to shear or vice versa during reflections. For example, if a small part of the longitudinal wave emitted by the transducer is reflected as a shear wave at the back face of the specimen, it would arrive exactly in-between the 1st longitudinal and the 1st shear echo. This echo is denoted as "ls" in Figure 3.15. Likewise, the positions of other echoes resulting from mode conversion are indicated, together with multiple reflections.

For plane waves at normal incidence, mode conversion cannot be expected. However, the

term *plane wave* is a simplification of reality, as the transducer and therefore the wave beam transmitted by it, have finite dimensions. This same phenomenon could also occur when using a shear or a longitudinal transducer. However, as the transducer is only sensitive then to one or the other wave mode, it would not be noticeable. For structural steel the longitudinal to shear velocity ratio is such (1.82) that the extra echoes do not interfere with the regular ones. This would only be the case for ratios of $^5/_3$, $^7/_3$ or 3.

3.3.4 Temperature

Experiments reveal that in metals such as steel and aluminium the time of flight of ultrasonic waves depends on temperature. As an example, Figure 3.16 shows this dependence for structural steel over a small temperature range. It can be seen that variations of only 1 °C cause significant time-of-flight changes when compared with those induced by stress.

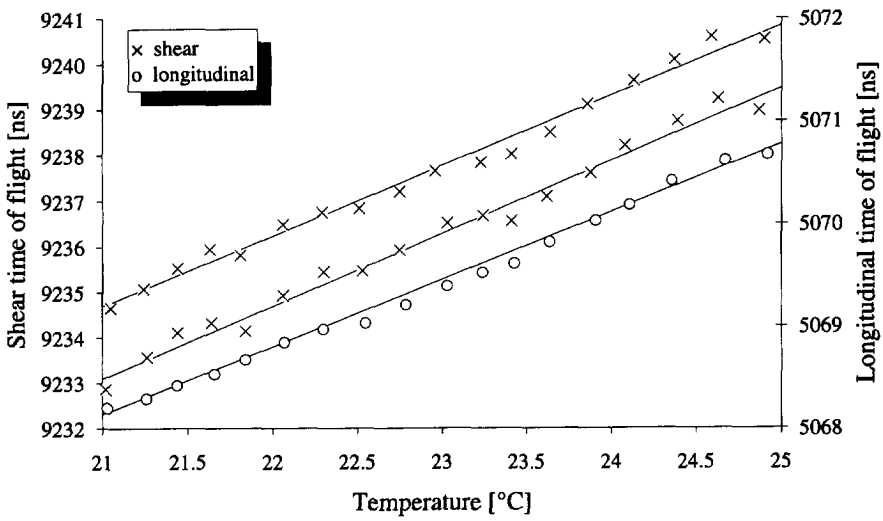

Fig. 3.16 Temperature dependence of shear and longitudinal time of flight measured in a 15 mm thick structural steel specimen.

Some influence of temperature is to be expected through thermal expansion, as this affects both mass density and distance of flight. Let the time of flight t be determined by the distance of flight L, mass density ρ and some elastic stiffness C, according to:

$$t = \sqrt{\frac{L^2 \rho}{C}} \tag{3.10}$$

The effect of linear expansion on the relative time-of-flight change $^{\Delta t}/_t$ can now be written as:

$$\frac{\Delta t}{t} = -\frac{\alpha \Delta T}{2} \tag{3.11}$$

where α = coefficient of linear expansion
ΔT = temperature change

However, for structural steel, which has an expansion coefficient of 12.10^{-6} K^{-1}, this would lead to dependence opposite to that found experimentally and with a much smaller magnitude. It must be concluded, therefore, that the elastic properties of the material are a function of temperature.

As the temperature influence on time of flight is linear in nature, at least in the small range shown in Figure 3.16, it seems appropriate to use a linear coefficient to describe it. All times of flight determined experimentally can then be normalized to one temperature using:

$$t^n = t^e \left\{ 1 + \beta (T^n - T^e) \right\} \tag{3.12}$$

where t^e, t^n = experimental and normalized times of flight respectively
T^e, T^n = experimental and normalizing temperatures respectively
β = temperature coefficient for time of flight

For example, the data presented in Figure 3.16 for a structural steel lead to coefficients β of $170 \cdot 10^{-6}$ K^{-1} and $130 \cdot 10^{-6}$ K^{-1} for shear and longitudinal waves respectively.

The question arises as to whether this temperature dependence is affected by stress. Reference [6] describes measurements of temperature-induced velocity changes as a function of applied uniaxial stress in a structural steel. The propagation direction of the shear and longitudinal waves was perpendicular to the stress. Expressed in terms of the temperature coefficient β, the dependence of a uniaxial stress $T_{uniaxial}$ was found to be:

$\beta = +135 + 0.070 \cdot T_{uniaxial}$ ..... for shear waves polarized parallel to stress

$\beta = +135 - 0.065 \cdot T_{uniaxial}$ ..... for shear waves polarized normal to stress

$\beta = +110 + 0.065 \cdot T_{uniaxial}$ ..... for longitudinal waves

where β and $T_{uniaxial}$ are expressed in K^{-1} and MPa respectively. Even for stresses of several hundreds of MPa it would only involve a correction of a correction. Therefore no stress dependence is assumed and Equation 3.12 is used.

3.4 Experimental set-up

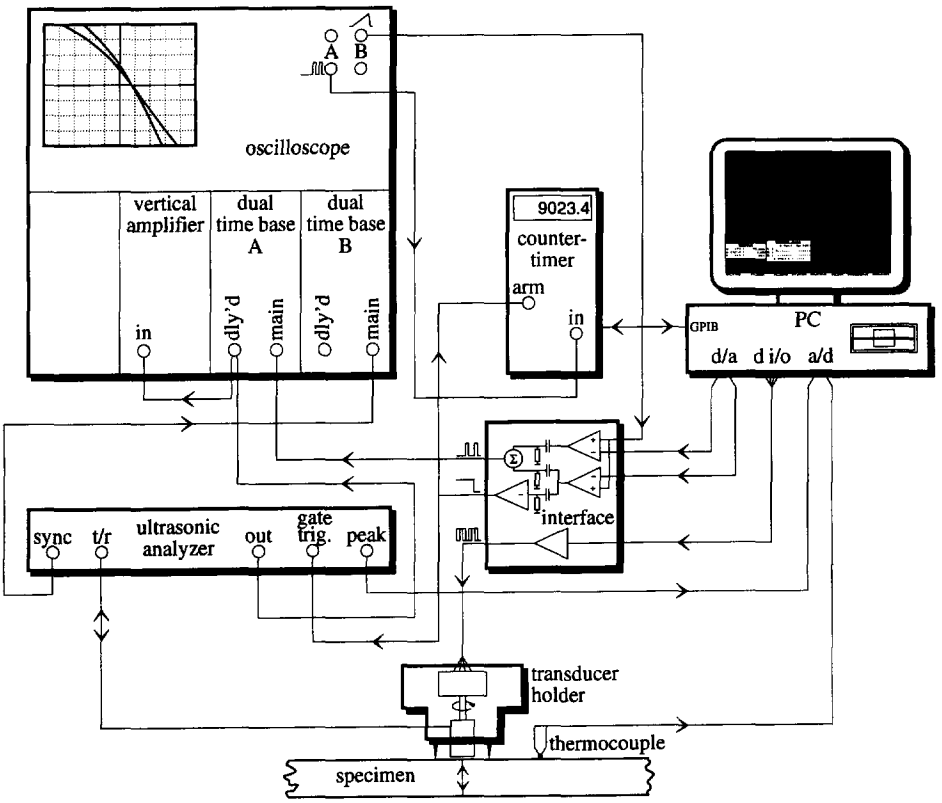

Fig. 3.17 Overview of the experimental set-up for acoustoelastic stress measurements.

In Figure 3.17 an overview is shown of the experimental set-up used for acoustoelastic stress evaluations. It consists of the following items:

- a specially designed *transducer holder* for positioning and rotating the transducer;
- a *Panametrics 5052UA ultrasonic analyzer*, used for driving the transducer, amplifying the received signal and measuring peak amplitudes;
- a *Tektronix 7904 oscilloscope* (500 MHz), equipped with two *7B92A dual time bases* and a *7A26 vertical amplifier*, to observe the ultrasonic signal and set the trigger levels;
- a *Tektronix DC5009 counter-timer* for accurately determining time intervals;
- a *personal computer*, fitted with a *Scientific Solutions IEEE488 interface board* and a *Data Translation DT2805 analog and digital I/O board*, for performing control tasks

and acquiring data;

- a *computer interface* to provide trigger and arm signals and drive the stepper motor in the transducer holder.

The set-up is described in detail in the following. Certain aspects of accuracy not discussed above will also be discussed, as they are closely linked to the actual set-up.

3.4.1 Transducer holder

Based on the foregoing discussion of the experimental principle and the distorting influences, the construction used for positioning the transducer on the specimen surface should have the following features:

- A certain gap must be maintained between transducer and specimen surfaces, i.e. approximately 100 µm for the current transducer type and shear wave couplant.
- It must be possible to rotate the transducer about its axis at a controllable speed and to measure its polarization direction accurately.
- The transducer and rotation axes and also the rotation axis and the specimen normal must be correctly aligned.

In addition to these requirements, it is convenient if during a measurement the transducer can have a fixed position on either a horizontal or a vertical specimen surface.

In order to achieve all this a *transducer holder* was specially designed. A drawing of the holder is shown in Figure 3.18. The holder rests on the specimen (9) on three steel *legs* (8) forming an equilateral triangle with the transducer (1) in the centre. These legs are mounted on a ring (3), which can be rotated relative to the holder by using a very fine thread. By this means it is possible to adjust the transducer-specimen distance with a resolution of 10 µm.

Rotation of the transducer is performed using a stepper motor (7) in conjunction with a gear box (6), ultimately providing a step size of $^1/_8°$. The construction of the gear box is such that all clearance is eliminated. The transducer orientation is therefore determined exactly by the position of the motor and is thus known to within $^1/_8°$ by simply counting all steps made from a particular calibrated position onwards.

The transducer itself is held by a separate fixture, which in turn is mounted in the holder by three pairs of small screws (2) 120° apart. The screws are used to ensure the correct alignment of the transducer axis with respect to the rotation axis. The extent to which these axes are aligned can be accurately checked by observing an optical reflection on the transducer surface during rotation. It should be noted that the alignment of the rotation axis relative to

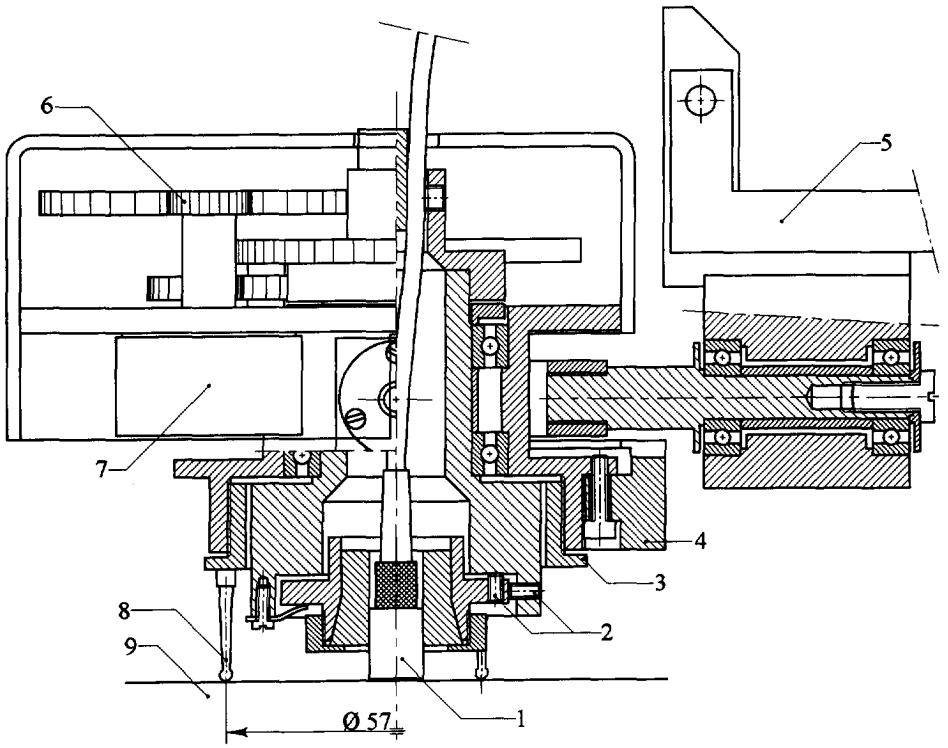

Fig. 3.18 Sketch of transducer holder, showing transducer (1), screws for adjusting transducer alignment (2), ring for adjusting transducer-specimen distance (3), counterweight (4), mounting bar (5), gear box (6), stepper motor (7), positioning legs (8) and specimen (9).

the specimen normal is inherently determined by the accuracy with which the holder as a whole has been made.

The design of the holder is such that the three legs are uniformly pressed by its weight onto either a horizontal or a vertical surface. This is achieved by (i) the location of the centre of gravity of the holder, which is largely determined by a counterweight (4) and (ii) the various centres of rotation in the connection between the holder and the mounting bar (5). The mounting bar itself is perpendicularly joined to another bar in such a way that the holder can be moved manually over the specimen surface. Its position can be read to within 0.1 mm.

As mentioned earlier, the relation between transducer polarization direction and stepper motor position must be calibrated. For this purpose a plate-shaped specimen is used consisting of a material which exhibits a measurable but not necessarily known shear wave birefringence. First the stepper motor position is determined for which the transducer polarization coincides with that of one of the two shear wave components. Next the specimen is turned about some arbitrary axis in the plane of the plate. The transducer is then placed on

the opposite side at exactly the same location and the stepper motor position is again determined for coincidence with the polarization direction of the same shear wave component. Averaging these two stepper motor positions yields the position for which the transducer polarization is either parallel to or normal to the axis used for turning the specimen. The ambiguity can often be eliminated, since the polarization direction of the transducer is approximately indicated on the casing. If there is no such indication, known time-of-flight values for certain shear wave components can also resolve the ambiguity.

3.4.2 Electronic circuitry

Pulser-receiver

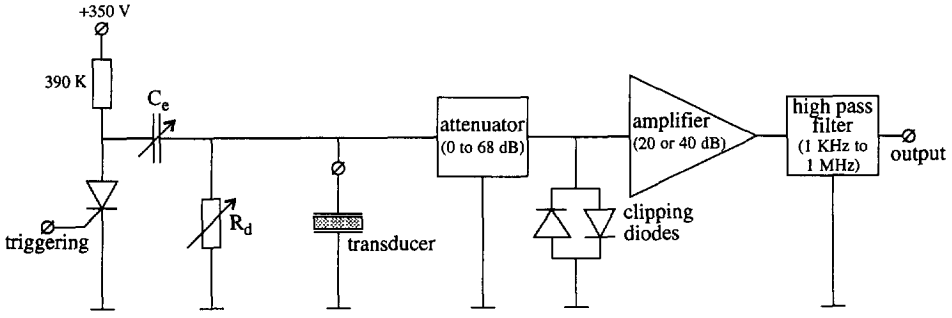

Fig. 3.19 Outline of the electronic circuitry of the pulser-receiver.

Figure 3.19 contains a schematic layout of the electronic circuitry of the *pulser-receiver*, forming part of the ultrasonic analyzer. It is used for exciting the transducer and receiving the resulting series of back-face echoes. A pulse is generated by triggering a thyristor, which in a very short time becomes conductive and so induces a high negative voltage across the transducer terminals. This voltage goes back to zero, as the *energy capacitor* (C_e) discharges through the transducer and the *damping resistor* (R_d) in parallel, producing a pulse with short rise and fall times. Pulses can be generated with a repetition rate which is adjustable from 100 to 5000 Hz.

The capacitance C_e and the resistance R_d can be varied from 300 to 1800 pF and 10 to 500 Ω respectively. Increasing either of them causes the pulse to have a larger amplitude and width. Obviously the pulse shape is also determined by the transducer itself and its mechanical load. According to the specifications of the transducer, the peak voltage should not exceed 2 V per μm thickness of the piezoelectric disc[1], and therefore a value of 300 pF is consistently used

[1] In addition, the polarity should always be such that the voltage of the electrode between the piezoelectric disc and the backing medium becomes negative with respect to the grounded electrode on the side of the propagation medium.

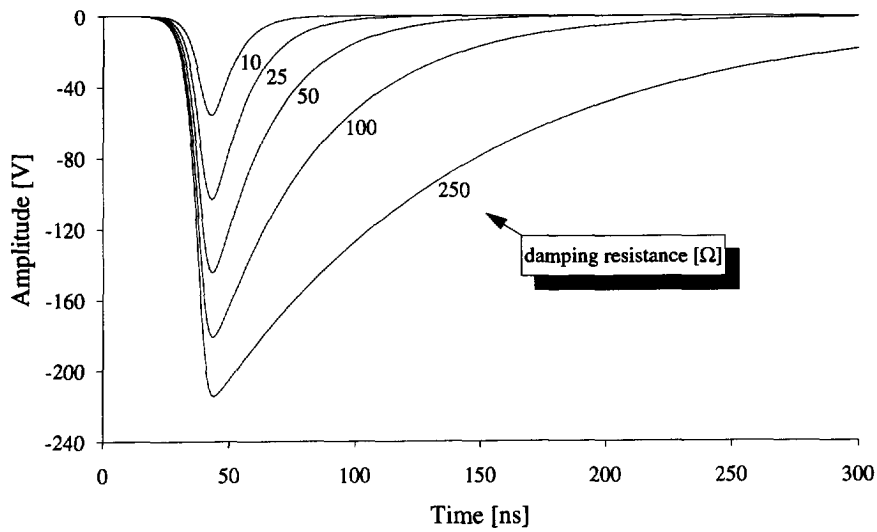

Fig. 3.20 Pulser output for various R_d-values, C_e = 300 pF and no transducer attached.

for C_e. In Figure 3.20 the pulse shape is shown as it is produced by the pulser for C_e = 300 pF, various R_d-values and no transducer attached.

During wave reception the damping resistor also plays an important role. It forms the electrical load for the transducer and therefore partly determines the transducer characteristics. After an adjustable attenuation the received signal is clipped in order to prevent the high voltage from the pulser from reaching the amplifier. The amplifier has a bandwidth of 40 or

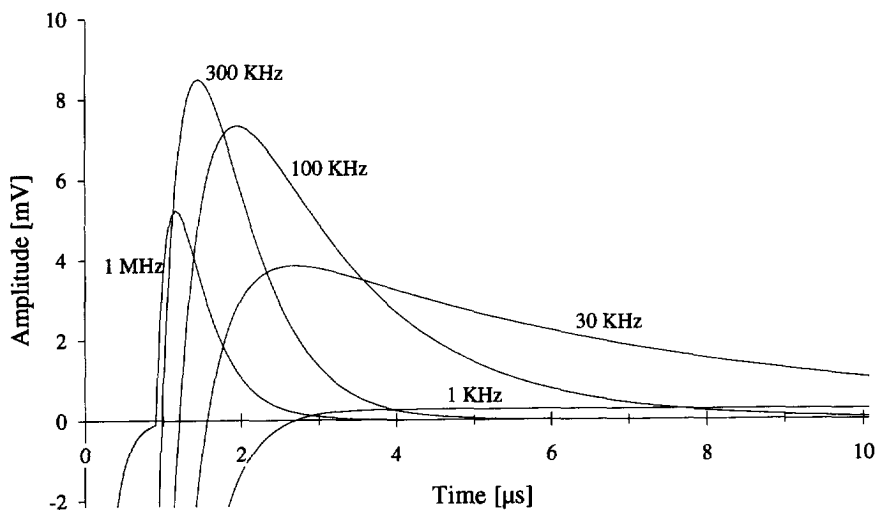

Fig. 3.21 Calculated receiver output just after the occurrence of the exciting pulse for different lower cut-off frequencies. The voltage scale refers to the receiver input.

35 MHz for low or high amplification respectively. Finally, a high-pass filter provides an adjustable lower cut-off frequency.

This filter frequency must be chosen with care, as it can influence time-of-flight measurements significantly. Despite the fact that the signal is clipped, the amplifier will be driven into saturation by the pulse exciting the transducer. In this case the output voltage of the amplifier is typically –0.7 V during 1 μs, after which it gradually recovers[I]. The resulting output of the high-pass filter strongly depends on its setting.

Figure 3.21 shows the receiver output signal as calculated for various cut-off frequencies, assuming a pulse repetition rate of 5 KHz. The output signal is converted to an equivalent input voltage in order to facilitate comparisons. The series of back-face echoes received by the transducer are superimposed on the signal shown. It is obvious that successive echoes are offset differently, especially for cut-off frequencies of 30 and 100 KHz. As time of flight is measured using zero crossings, erroneous data will result. A setting of 1 KHz reduces this effect but has the disadvantage of decreasing the signal-to-noise ratio. When a cut-off frequency of 300 KHz is used, the offset is minimized for echoes which occur at least 4 μs after the exciting pulse. A higher setting would noticeably affect the shape of the 5 MHz shear wave echo.

Time-of-flight evaluation

Signals relevant to the time-of-flight measurement technique are shown in Figure 3.22. The signal designations refer to Figure 3.17. The pulser in the ultrasonic analyzer excites the transducer at a repetition rate of 5 KHz and simultaneously generates a synchronization pulse. This pulse triggers main time base B of the oscilloscope, which is set to run until after the last relevant back-face echo is received. The sweep signal of this time base (⟋ in Fig. 3.17) is led to two voltage comparators in the computer interface. Each of these compares the signal with an analog DC signal, which is controlled by a digital-to-analog converter in the personal computer. The output of the two comparators is then added and used to trigger main time base A (⎍). Using appropriate settings for the two analog signals, the main time base A starts running just before the occurrence of both the start and stop echoes in the ultrasonic signal.[II]

Delayed time base A is triggered by the first zero crossing with a negative slope in these two echoes, and the oscilloscope will therefore display the signals on top of each other. Moreover, part of the echo before the trigger points is also visible, as the signal is delayed by propagation through the cable and the vertical amplifier. The gate signal of time base A (⎍) consists of two short pulses and is led to the counter-timer. Using a period measuring mode

[I] This behaviour was observed using 10 dB attenuation and 40 dB amplification.

[II] This requires that the total duration of the sweep is less than the time of flight to be measured.

the wave time of flight is found as the time interval between the leading flanks. The computer interface also provides a signal (⌐) to disarm the counter-timer during the stop echo, in order to prevent it from measuring the complement of the desired time-of-flight value.

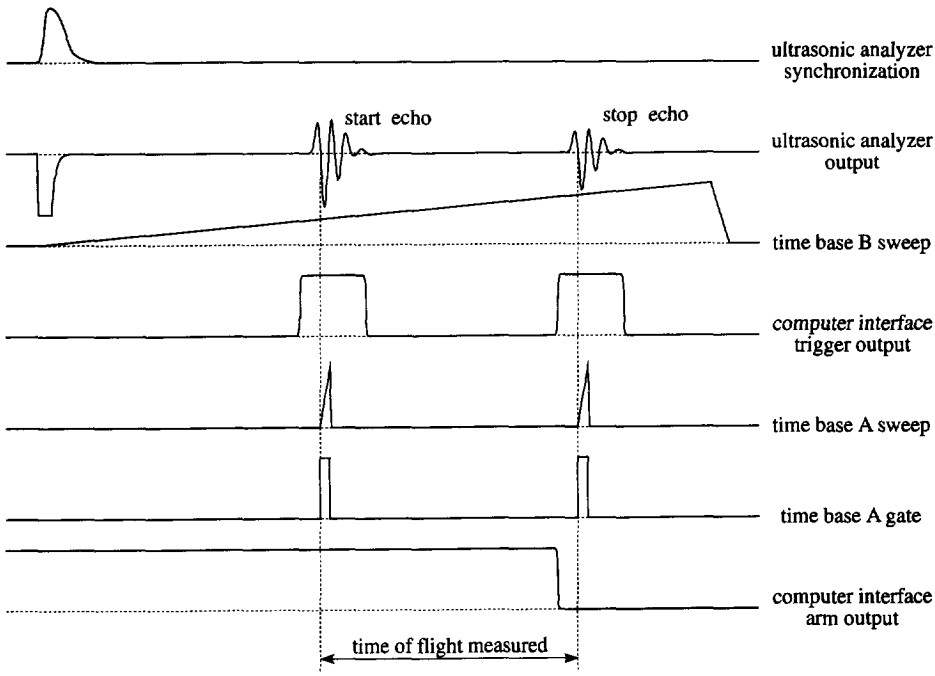

Fig. 3.22 Various signals during time-of-flight determination.

The whole path from the transducer to the counter-timer is the same for both the start and stop signals. This means that factors which could affect a time-of-flight reading, such as differences in trigger level, cable length and propagation delay in the electronic circuitry, are eliminated. The accuracy is now mainly determined by:

- The trigger level of delayed time base A
  As this level applies to both start and stop echo, the exact trigger point is visible on the oscilloscope display as the intersection of two negative slopes. Using a fast sweep rate for the delayed time base, i.e. 2 or 5 ns per division, the trigger level can easily be set to zero within ±5 mV. The time-of-flight error Δt caused by a trigger level error ΔV_{trig} depends on the time derivatives $\dot{V}_{start}$ and $\dot{V}_{stop}$ of the amplified start and stop echo signals at their first zero crossings, according to:

$$\Delta t = \left(\frac{1}{\dot{V}_{stop}} - \frac{1}{\dot{V}_{start}}\right)\Delta V_{trig} \tag{3.13}$$

The attenuation and amplification of the receiver is adjusted in such a way during measurements that the available output range of the amplifier (±0.6 V) is used to the maximum extent possible. Clipping of the signal at any point in the echoes is avoided, as this can cause distortion of the waveform. Thus typical $\dot{V}_{start}$- and $\dot{V}_{stop}$-values for the amplified signal from the combined shear-longitudinal transducer are −13 and −7 $mV/_{ns}$ respectively for the shear echoes (1st and 2nd) and −50 and −15 $mV/_{ns}$ respectively for the longitudinal echoes (1st and 3rd). The error in the time-of-flight determination due to the imprecision in the trigger level is therefore approximately 0.3 ns for shear waves and 0.2 ns for longitudinal waves.

- The counter-timer
  The counter-timer has an internal clock frequency of 100 MHz, which means that the accuracy with which a time interval can be determined, the so-called *single shot resolution*, is 10 ns. Fortunately, the ultrasonic signal is repetitive, so that a large number of measurements can easily be performed. The counter-timer has a special feature which prevents the internal clock from running synchronously with the measured signal. Consequently, the error in the results will be random and it is possible to increase accuracy significantly by averaging. Averaging over n results will yield a resolution of $10/\sqrt{n}$ ns. With a 5 KHz repetition rate for the ultrasonic signal an accuracy of 0.1 ns can be achieved by measuring over 2 seconds.

Amplitude evaluation

The ultrasonic analyzer also offers the possibility of determining the amplitude of a back-face echo. For this purpose the receiver output is lead through a *gate module*, which lets through only that part of the signal which falls within a certain time window. The gated signal is then used as input for a *peak detector*, which produces a signal proportional to the positive or negative peak amplitude in the selected window. The peak detector requires a number of pulse periods before reaching its final output value. After 10 pulses the output is reset to zero.

The position of the time window is roughly controlled by a trigger pulse coming from the computer interface. A specific echo can thus be selected for amplitude measurement. Furthermore, the width and also the position can be finely adjusted by hand. In this way it is possible to determine the peak amplitude either of the echo as a whole or of individual peaks.

3.4.3 Controlling computer

It is clear that performing an acoustoelastic experiment requires virtually simultaneous control over several features and the acquisition of different data. For this purpose a MSDOS-

based personal computer is used, fitted with the appropriate boards and running a dedicated program.

Hardware

A GPIB interface board provides:

- Communication to and from the counter-timer
  A *General Purpose Interface Bus* (GPIB, according to standard IEEE-488), connects the computer to the counter-timer. Through this digital bus all settings, such as measuring mode and trigger levels, are controlled and the acquired time-interval data are read.

A board for analog and digital I/O permits:

- Stepper motor control
  Using 4 bits of a digital output port, each step made by the two-phase stepper motor originates from the computer. In this way motor position and speed are fully controlled.
- Echo selection for time-of-flight and amplitude measurement
  Two digital-to-analog converters (0 to +5 V; 12 bits) provide analog signals which are used in the computer interface to produce trigger pulses for main time base A and the gate module in the ultrasonic analyzer.
- Peak amplitude measurement
  An analog-to-digital converter (±1 V; 12 bits) is used to read the peak voltage determined by the ultrasonic analyzer.
- Temperature measurement
  Using a calibrated copper-constantan thermocouple mounted on the specimen, the temperature is measured to within 0.2 °C. This is achieved by means of an analog-to-digital converter (±20 mV; 12 bits), which successively measures the thermocouple voltage, the output of a cold junction compensation circuit and a short-circuited input. The latter signal is used to compensate drift in the DC-amplifier of the converter. Finally, averaging is performed in order to achieve the accuracy mentioned above.

Software

A program called ACOELA was written in *Pascal*[1] to form the heart of ACOustoELAstic experiments. The main features are:

- The use of a parameter set
  The program uses a modifiable set of parameters including relevant echo numbers, nominal time-of-flight values, a transducer angle calibration value, the quantity to be

[1] A few small and time-critical sections were directly written in machine code.

scanned (time of flight or amplitude) and the scan speed.

- Trigger calibration
  In order to achieve sufficient accuracy, the trigger control requires calibration, i.e. the relation must be established between the analog output voltage of the computer and the location of the trigger pulse relative to the synchronization pulse from the ultrasonic analyzer. The program does this by using the counter-timer in order to determine this position for a low and a high analog output voltage and then calculating a linear fit.

- Scanning
  A scan is recorded by driving the stepper motor at a constant speed using the internal clock of the computer. The relevant quantity, i.e. time of flight or echo amplitude, is measured simultaneously and the results are immediately displayed in a graph.

  For time-of-flight scans the number of averages performed by the counter-timer is adjusted in such a way as to obtain one value per 2° transducer rotation. In the case of amplitude scans one measurement is performed after every step made by the motor. Optionally, both shear and longitudinal echo amplitudes can be measured by selecting each echo alternately. It should be noted that owing to the way in which the peak detector functions, determining an amplitude value typically involves taking 10 measurements at intervals equal to the pulse period and thus using the maximum result.

- Actual data measurement
  The following procedure is used:
  1) For determination of the shear polarization angle the program allows a range to be manually selected (±15° to ±45°) around a maximum in the amplitude or time-of-flight scan. The polarization angle is then calculated as the maximum of a parabolic fit. This method reduces the influence of experimental noise.
  2) The transducer polarization is aligned with one of the birefringent shear wave components.
  3) The time of flight is determined.
  4) The current specimen temperature is determined.
  5) Points 2 to 4 are repeated for the other shear wave component.
  6) Points 3 and 4 are repeated for the longitudinal wave.
  7) Additional data is recorded, such as applied load and/or transducer position.

3.5 Conclusion

This chapter dealt with an experimental technique designed for the evaluation of absolute stress levels in steel specimens. After an outline of the principle, possible disturbing influences and the actual set-up were described.

The use of a single transducer for emitting and receiving *shear and longitudinal waves simultaneously* was found to be practicable for steel specimens. The times of flight of the two wave types and the shear wave polarization can be determined through the same material at virtually the same moment. This means that measurement accuracy is increased considerably.

Experiments showed that below a certain limit value the thickness of the viscous *coupling layer* between transducer and specimen strongly affects the time of flight measured by the pulse-echo method. It is concluded, therefore, that conventional practice, in which the transducer is pressed onto the specimen surface, inevitably leads to deviating time-of-flight data. Reproducible measurements can be performed only by sufficiently increasing the thickness of the coupling layer. Additional advantages of a thicker layer are (i) the possibility of proceeding with the acoustic measurements almost immediately after positioning the transducer and (ii) the fact that transducer rotation has only a very limited effect on the transducer-specimen coupling.

Transducer misalignment was found to affect both time-of-flight and echo amplitude measurements. This means that the determination of shear wave polarization, when based on amplitude maxima, may also be affected. Correct transducer alignment must be considered essential.

The effect of *temperature* on time of flight can be reduced by monitoring the specimen temperature during acoustic measurements. Times of flight are corrected afterwards using linear temperature coefficients. These coefficients may be assumed to be independent of stress.

The *transducer holder*, specially designed for this stress measurement technique, permits the required accurate transducer positioning. Using the holder in combination with the ultrasonic equipment, the controlling computer and the software, semi-automated measurements can be performed in a relatively short time ($\approx$ 3 min.).

Appendix 3A Specific impedance of a plane wave

The stress field $T_{ij}(\underline{x})$ for a harmonic plane wave with angular frequency ω, wave number k and travelling in the direction of unit vector $\underline{n}$, is proportional to:

$$T_{ij} \div e^{i(\omega t - kn_k x_k)} \tag{3A.1}$$

and therefore:

$$\frac{\partial T_{ij}}{\partial x_j} = -\frac{kn_j}{\omega}\frac{\partial T_{ij}}{\partial t} \tag{3A.2}$$

The equation of motion in the absence of body forces reads:

$$\frac{\partial T_{ij}}{\partial x_j} = \rho\frac{\partial^2 u_i}{\partial t^2} \tag{3A.3}$$

where $\underline{u}$ = particle displacement
ρ = mass density

By substitution of Equation 3A.2 in 3A.3 and subsequent integration with respect to time, a relation is found between the negative traction force acting on a plane normal to the wave propagation direction $-T_{ij}n_j$ and the corresponding particle velocity $\partial u_i/\partial t$:

$$-T_{ij}n_j = Z\frac{\partial u_i}{\partial t} \tag{3A.4}$$

where Z = specific wave impedance = $\frac{\rho\omega}{k}$

The specific wave impedance is a scalar quantity and can also be written as the product of mass density and phase velocity, since this latter quantity is equal to ω/k.

Appendix 3B Reflection and transmission at an interface for a normally incident plane wave

The reflection and transmission of acoustic waves at an interface between two rigidly bonded materials is determined by the mechanical boundary conditions, i.e. continuity across the interface of (i) the traction force acting on the interface plane and (ii) the particle velocity.

Consider a plane harmonic wave propagating in medium 1 at normal incidence towards an interface with medium 2. Assume also that one of the wave solutions for propagation normal to the interface in medium 2 has the same polarization, i.e. direction of particle velocity. The boundary conditions can now be satisfied by assuming that the incident wave induces a reflected and a transmitted wave travelling normal to the interface into media 1 and 2 respectively with the same polarization as the incident wave.

The *stress amplitude* of an acoustic plane wave may be defined as the magnitude of the traction force acting on a plane normal to the propagation direction. Denoting the stress amplitudes at the interface of the incident, reflected and transmitted waves as W_I, W_R and W_T respectively, the first of the above boundary conditions implies:

$$W_I + W_R = W_T \tag{3B.1}$$

Using the specific wave impedance to relate the particle velocity to the traction force acting on the plane normal to the wave propagation direction (Appendix 3A), the second boundary condition leads to:

$$\frac{W_I}{Z_1} - \frac{W_R}{Z_1} = \frac{W_T}{Z_2} \tag{3B.2}$$

where Z_1, Z_2 = specific wave impedance in media 1 and 2 respectively

From these equations the *stress reflection* and *transmission coefficients*, R_{12} and T_{12}, can be computed as:

$$R_{12} = \frac{W_R}{W_I} = \frac{Z_2 - Z_1}{Z_2 + Z_1} \tag{3B.3}$$

$$T_{12} = \frac{W_T}{W_I} = \frac{2Z_2}{Z_2 + Z_1} \tag{3B.4}$$

Appendix 3C Thickness of viscous coupling layer as a function of impulse applied to the transducer

Consider an incompressible Newtonian fluid[1] with a constant viscosity coefficient η between two smooth but not necessarily flat surfaces moving at velocities $\underline{u}$ and $\underline{v}$ respectively. A rectangular coordinate system is chosen with the x_1-x_2 plane virtually parallel to the surfaces. The pressure field in the fluid, $p(x_1,x_2)$, can be described using the *Reynolds equation* [38]:

$$\frac{\partial}{\partial x_1}\left(h^3\frac{\partial p}{\partial x_1}\right)+\frac{\partial}{\partial x_2}\left(h^3\frac{\partial p}{\partial x_2}\right)= 6\eta\left\{\frac{\partial h}{\partial x_1}(u_1-v_1)+\frac{\partial h}{\partial x_2}(u_2-v_2)+h\frac{\partial(u_1+v_1)}{\partial x_1}+h\frac{\partial(u_2+v_2)}{\partial x_2}-2(u_3-v_3)\right\} \qquad (3C.1)$$

where h = distance between surfaces

This equation is derived excluding inertia forces and assuming that (i) pressure is not a function of x_3, (ii) fluid flow in the x_3-direction is negligible and (iii) no slip flow occurs, i.e. the fluid adjacent to the surfaces has the same velocity as the surfaces.

The Reynolds equation is now applied to the situation of a couplant between the flat and parallel surfaces of a specimen and a circular transducer, i.e. $\partial h/\partial x_1 = \partial h/\partial x_2 = 0$ and h is only a function of time t. The specimen velocity $\underline{u}$ is taken to be zero and a transition is made to cylindrical coordinates by substituting $x_1 = r\cos\varphi$ and $x_2 = r\sin\varphi$:

$$h^3\left\{\frac{\partial^2 p}{\partial r^2}+\frac{1}{r}\frac{\partial p}{\partial r}+\frac{1}{r^2}\frac{\partial^2 p}{\partial \varphi^2}\right\}=6\eta\left\{h\frac{\partial v_r}{\partial r}+\frac{h}{r}\left(v_r+\frac{\partial v_\varphi}{\partial \varphi}\right)+2\frac{dh}{dt}\right\} \qquad (3C.2)$$

where v_r, v_φ = radial and tangential transducer surface velocities respectively

It is assumed that the transducer is not translated in the x_1-x_2 plane and therefore v_r is zero and p and v_φ are independent of φ. Thus:

$$\frac{\partial}{\partial r}\left(r\frac{\partial p}{\partial r}\right)=\frac{12\eta r}{h^3}\frac{dh}{dt} \qquad (3C.3)$$

It should be noted that rotation of the transducer about its axis is still permitted.

Integrating twice with respect to r and using the boundary conditions:

---

[1] In a fluid of this kind shear stress is equal to the product of a viscosity coefficient and the shear deformation rate.

$$\frac{\partial p}{\partial r} = 0 \quad \text{..... for } r = 0 \text{ [I]} \qquad (3C.4^a)$$

$$p = 0 \quad \text{..... for } r = R \qquad (3C.4^b)$$

where R = transducer radius

yields an expression for the pressure as a function of r:

$$p(r) = \frac{3\eta(r^2 - R^2)}{h^3}\frac{dh}{dt} \qquad (3C.5)$$

The force F, used to press the transducer onto the specimen, must be in equilibrium with the couplant pressure averaged over the transducer area:

$$F(t) = \int_0^R 2\pi r p(r) dr = \frac{-3\pi\eta R^4}{2h^3}\frac{dh}{dt} \qquad (3C.6)$$

If the coupling layer thickness is h_0 at time t_0, an *impulse* defined as:

$$I = \int_{t_0}^{t} F(t) dt \qquad (3C.7)$$

exerted on the transducer will cause the layer thickness to become:

$$h = \sqrt{\frac{1}{\frac{1}{h_0^2} + \frac{4I}{3\pi\eta R^4}}} \qquad (3C.8)$$

[I] It follows from the rotation symmetry that the fluid will not flow at the centre of the transducer and hence no pressure gradient can be present there.

Chapter 4

Acoustoelastic Experiments

4.1 Introduction

Chapter 2 contains a theoretical treatise of a method for acoustoelastic stress evaluation using shear and optionally longitudinal bulk waves. Chapter 3 describes an experimental technique which implements this method. Acoustoelastic experiments played an important role during the development of both the theory and the experimental set-up. The present chapter deals with these experiments and their results. The greater part of the work presented in this chapter is also published in references [23] to [29].

The experiments were performed using *plate-shaped* specimens taken from rolled plate. The specimens are loaded only in the plane of the plate, allowing a plane stress state to be assumed in all cases. In principle all tensor quantities are defined relative to a set of co-ordinate axes x_i, which will be referred to as the *material axes*.[I] The x_1- and x_3-axes are chosen parallel to the rolling direction and normal to the plate respectively. The material axes may therefore be expected to coincide with the orthotropic symmetry axes of the material.

Four different metals are investigated, namely:

- aluminium alloy 2024-T351
- two hot-rolled structural steel qualities
- hot-rolled/cold-deformed pipeline steel

For all materials the experiments include the *calibration* of their acoustoelastic behaviour, i.e. the effect of stress on the acoustic quantities measured.

The experiments on the aluminium alloy were the first to be carried out. A considerably less advanced set-up is used compared with the set-up described in Chapter 3. Nevertheless, the results are believed to be a good illustration of the theory. Additional experiments performed on aluminium specimens include a disc loaded diametrically in several directions under compression and a compact-tension specimen in which the two-dimensional plane stress field is determined around the crack tip. Based on the latter results, a numerical integration of the J-integral fracture parameter is performed along several contours.

All experiments on steel specimens were performed using the set-up described in Chapter 3.

[I] The stress data evaluated in the aluminium compact tension specimen are defined otherwise.

The two structural steel qualities have comparable specifications, but originate from different manufacturers. The results of the calibration experiments can therefore provide information concerning the *reproducibility* of elastic and acoustoelastic material behaviour. These aspects are essential for the determination of stress in an absolute sense. The cold-deformed pipeline steel has a large texture and residual stresses are present in the material. Both these phenomena can be expected to affect acoustoelastic stress measurements, and are therefore investigated.

It should be noted that, unless stated otherwise, the Voigt notation will be used throughout this chapter. Therefore, in the two-dimensional case considered here the indices may take the values 1, 2 and 6.

4.2 Acoustoelastic calibration

In the description contained in Chapter 2 acoustoelastic material behaviour is represented by the $\underline{k}$- or $\underline{m}$-tensor (Eqs. 2.23 and 2.29 respectively). It was concluded in Section 2.4.3 that a complete calibration of either of these tensors requires at least two different combinations of the two-dimensional stress components T_1, T_2 and T_6 to be introduced in the material, including at least one non-zero shear stress.

Uniaxial tensile specimens are used for this purpose, as they allow the generation of a well-defined stress state. By varying the orientation with which these specimens are cut from the plate, different stress component combinations are obtained. Although two orientations would suffice, calibrations are performed using *three specimens* with tensile directions making an angle of 0°, 45° or 90° relative to the x_1 material axis. The reason for this is that $\underline{k}$- or $\underline{m}$-tensor components with indices 11, 12, 21 and 22 are most accurately determined using the 0° and 90° orientations. For the components k_{66} or m_{66} the 45° orientation permits the most accurate determination. Furthermore, the use of three orientations provides a means of checking the consistency of both the acoustoelastic theory and the experimental results.

In the actual calibration, acoustic data is evaluated at the centre of each specimen. First the unloaded values are determined. Then the tensile load is increased slightly and the next measurement is performed. This is repeated until the tensile stress has reached a substantial amount ($\approx 60\%$) of the yield strength of the material.

For the purpose of the calculations, all acoustic data are expressed in terms of the $\underline{Q}$- or $\underline{R}$-data tensor (Eqs. 2.26 and 2.31). The three components of these tensors are then correlated to the applied uniaxial stress by means of linear regression. The results are in the form of:

$$\Delta Q_I = b_I T_{applied} \qquad \text{or} \qquad R_I = a_I + b_I T_{applied} \tag{4.1^{ab}}$$

where a_I, b_I = axis intersection and slope respectively of the linear regression line

Furthermore, the plane stress components in the tensile specimens can be related to the applied stress through:

$$T_I = f_I T_{applied} \tag{4.2}$$

where f_I = factor depending on the orientation of the tensile specimen

Substitution of the above equations in Equation 2.23 and the differential form of Equation 2.29 respectively leads to:

$$f_I = k_{IJ} b_J \qquad \text{or} \qquad f_I = m_{IJ} b_J \tag{4.3^{ab}}$$

Using the results of all tensile tests, three sets of three equations can be formulated. Numbering the tests from 1 to 3, such a set is in the form of:

$$\begin{aligned} f_I^{(1)} &= k_{IJ} b_J^{(1)} \\ f_I^{(2)} &= k_{IJ} b_J^{(2)} \\ f_I^{(3)} &= k_{IJ} b_J^{(3)} \end{aligned} \qquad \text{or} \qquad \begin{aligned} f_I^{(1)} &= m_{IJ} b_J^{(1)} \\ f_I^{(2)} &= m_{IJ} b_J^{(2)} \\ f_I^{(3)} &= m_{IJ} b_J^{(3)} \end{aligned} \qquad (4.4^{ab})$$

The solutions to these sets of equations are the desired $\underline{k}$- and $\underline{m}$-tensor components.

For absolute stress evaluation using both shear and longitudinal waves the reference values R_I^o (defined in Eq. 2.32 in full index notation) also need to be determined. By assuming the material to be free from residual stresses, these values are found as the intersection of the regression lines with the line of zero applied load, i.e. the coefficients a_I in Equation 4.1^b.

4.3 Aluminium

4.3.1 Introduction

Material

As stated in the introduction to this chapter, the initial measurements were performed on aluminium. The reason for this is that aluminium is known to have a high acoustoelastic effect relative to other metals which are important in engineering [9, 18, 48]. At the same time the specific wave impedance is fairly low. These circumstances clearly facilitate acoustoelastic stress measurements.

Table 4.1 Chemical composition of the aluminium alloy 2024-T351 [Wt%].

Cu	Mg	Mn	Fe	Si	Zn	Cr	Al
4.4	1.36	0.67	0.26	0.08	0.07	0.01	balance

All experiments were performed on specimens taken from a 6 mm thick rolled plate of the aluminium alloy 2024-T351. The surface of the rolled plate was not machined in any way as the roughness was found not to have any effect on ultrasonic measurements. Tables 4.1 and 4.2 summarize the chemical composition of the material and its mechanical properties respectively.

Table 4.2 Mechanical properties of the aluminium alloy 2024-T351.

Yield strength T_y	395 MPa
Tensile strength T_u	500 MPa
Elongation δ	17 %
Young's modulus E	73.7 GPa
Poisson's ratio ν	0.34
Fracture toughness K_{Ic}	40 MPa$\sqrt{m}$

The temperature coefficients β (Eq. 3.12) for shear and longitudinal waves travelling in the thickness direction of the aluminium 2024-T351 plate were measured separately. The results are summarized in Table 4.3.

Table 4.3 Time-of-flight temperature coefficients for aluminium 2024-T351.

Shear wave β_s	$+360 \cdot 10^{-6}$ K^{-1}
Longitudinal wave β_l	$+160 \cdot 10^{-6}$ K^{-1}

Experimental conditions

The set-up used for the experiments involves a relatively simple transducer holder for which

the transducer polarization angle is set by hand with an estimated accuracy of 1°. The holder does, however, allow a fixed transducer-specimen distance to be maintained, in view of the increased coupling layer thickness required. The electronics relevant to the pulse-echo method, i.e. the pulser-receiver and the part of the set-up used for time interval determination, is the same as or comparable with that used in the set-up described in Chapter 3.

A combined shear-longitudinal transducer was not available at the time of these measurements. It would not have offered any advantage in any case, owing to the echo overlap occurring in aluminium. Separate transducers were therefore used for shear and longitudinal waves, namely a:

- 20 MHz, 6.3 mm diameter, 4 μs delay line, shear wave transducer (*Panametrics*, reference number V222).
- 25 MHz, 6.3 mm diameter, longitudinal wave transducer (*Panametrics*, reference number V324).

In principle the shear wave polarization is determined as the maximum of the shear echo amplitude as a function of the transducer orientation. Time of flight is used as the criterion only when the times of flight of the birefringent shear wave components are approximately the same (analogous to the procedure discussed in Section 3.2.3 for 5 MHz shear waves).

All experiments were carried out in a conditioned environment of 21 °C. For those measurements involving data acquisition at successively increased load levels the specimen temperature was not determined explicitly. During the more lengthy experiment with the compact-tension specimen, however, the temperature was recorded and the time of flight corrected afterwards.

Reference [24] contains more specific information relating to the experimental conditions.

4.3.2 Acoustoelastic behaviour

Figure 4.1 shows the geometry of the tensile specimens used for the calibration of the acoustoelastic behaviour. The three specimens, cut from the plate with orientations of 0°, 45° and 90° relative to the material x_1-axis, were tested on a 20 KN hand-driven mechanical testing machine at intervals of 2 KN (27.8 MPa) up to a load of 16 KN (222 MPa).

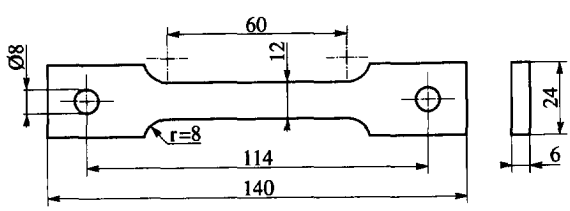

Fig. 4.1 Geometry of the aluminium 2024-T351 tensile specimens used for calibration.

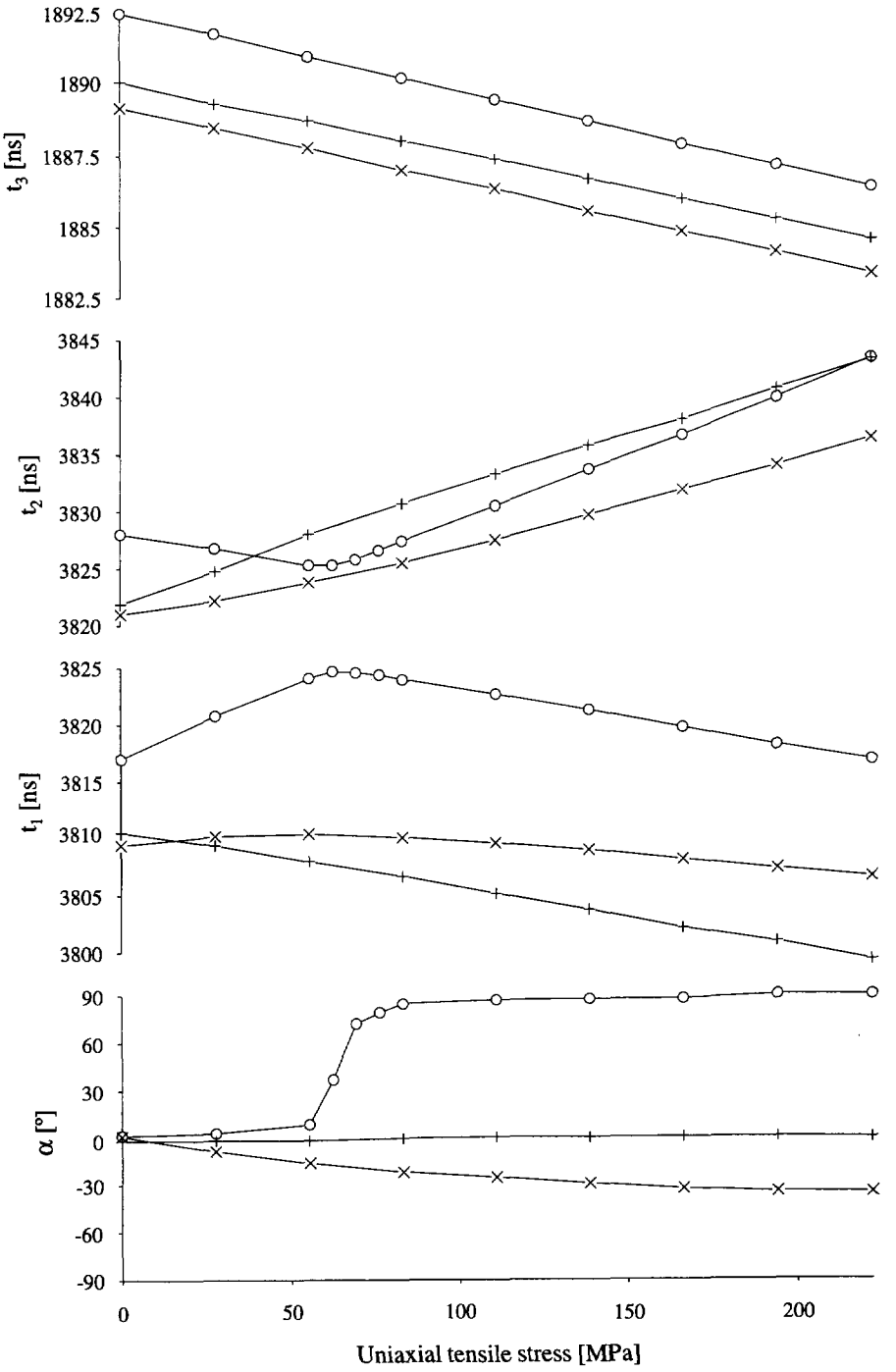

Fig. 4.2 Shear (t_1 and t_2) and longitudinal (t_3) time of flight and the polarization angle α as a function of the uniaxial tensile stress applied in aluminium 2024-T351 specimens. The loading directions relative to the material x_1-axis are: o = 0°, × = 45°, + = 90°.

Figure 4.2 gives an overview of the experimental results. First of all it is found the initial times of flight vary somewhat from one specimen to another. However, the differences between the shear times of flight t_1 and t_2 are roughly equal (11 to 11.6 ns), a result which is also described in references [7, 20, 40]. Furthermore, the ratio between the shear and longitudinal values is almost the same. This aspect will be discussed further during the treatment of the results obtained from the experiment on the aluminium compact-tension specimen.

For all specimens there is a linear decrease in the longitudinal time of flight (t_3) as a function of the applied stress. For the 90° specimen the shear wave times of flight t_1 and t_2 also show a linear change, while the polarization angle remains constant. For the 0° specimen the time-of-flight changes are initially linear and opposite to those for the 90° specimen. At a stress level of 60 MPa they become almost equal and the polarization is suddenly rotated through 90°. At higher loads the times of flight show a linear dependence in the same direction as for the 90° specimen. Finally, for the 45° specimen, there is a gradual rotation of the polarization such that the birefringent wave with the largest time of flight (t_2) turns towards the tensile loading direction. The times of flight themselves clearly do not have a linear dependence on the stress applied.

Acoustoelastic tensors

Figure 4.3 shows the calculated changes of the tensor components Q_1, Q_2 and Q_6 as a function of the applied stress. The calculated values for the $\underline{R}$-tensor components are shown analogously in Figure 4.4. In all cases a linear dependence is found, which was already suggested by Equations 2.23 and 2.29. The results of the linear regression calculations are indicated by the lines drawn in the two graphs. The resulting plane stress $\underline{k}$- and $\underline{m}$-tensors for this aluminium alloy, expressed in GPa, are (using the form of Eqs. 2.24 and 2.30 resp.):

$$[k_{IJ}] = \begin{bmatrix} -21.5\ (0.9) & -11.6\ (1.0) & 0.0\ (1.4) \\ -11.4\ (1.0) & -26.3\ (1.2) & 0.5\ (1.7) \\ 0.0\ (0.7) & 0.6\ (1.0) & -14.8\ (0.9) \end{bmatrix} \tag{4.5}$$

$$[m_{IJ}] = \begin{bmatrix} -45.6\ (0.7) & -0.3\ (0.8) & -0.4\ (3.0) \\ 1.7\ (0.8) & -54.2\ (1.0) & 1.6\ (3.7) \\ 0.8\ (1.0) & -1.7\ (2.0) & -60.7\ (3.4) \end{bmatrix} \tag{4.6}$$

The numbers between brackets are estimates for the standard deviation. They are based on estimated experimental errors of 0.5 ns in the shear time of flight, 0.1 ns in the longitudinal time of flight and 2° in the polarization angle. Moreover, a variation in the specimen temperature of ±0.2 °C is assumed during the tensile experiments, which has an effect on the

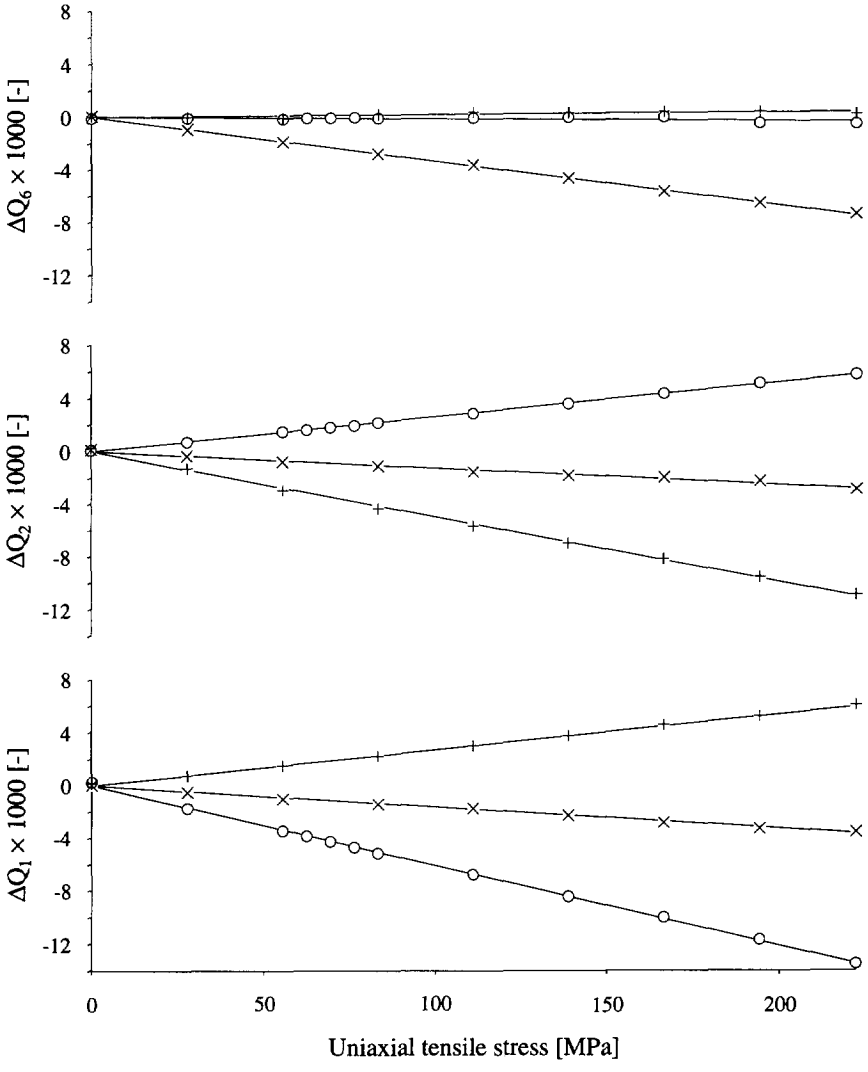

Fig. 4.3 Calculated changes in the Q-tensor components as a function of the stress applied in aluminium 2024-T351 specimens. The loading directions relative to the material x_1-axis are: o = 0°, x = 45°, + = 90°. The lines indicate the results of linear regression calculations.

measured time of flight. The standard deviation estimates are determined by calculating the k- and m-tensors a large number of times (e.g. 10 000) using experimental data to which noise with a normal distribution is added. The standard deviation of the normal distribution is equal to the errors assumed above.

The reference values R_I^o calculated for the three tensile specimens are summarized in Table 4.4.

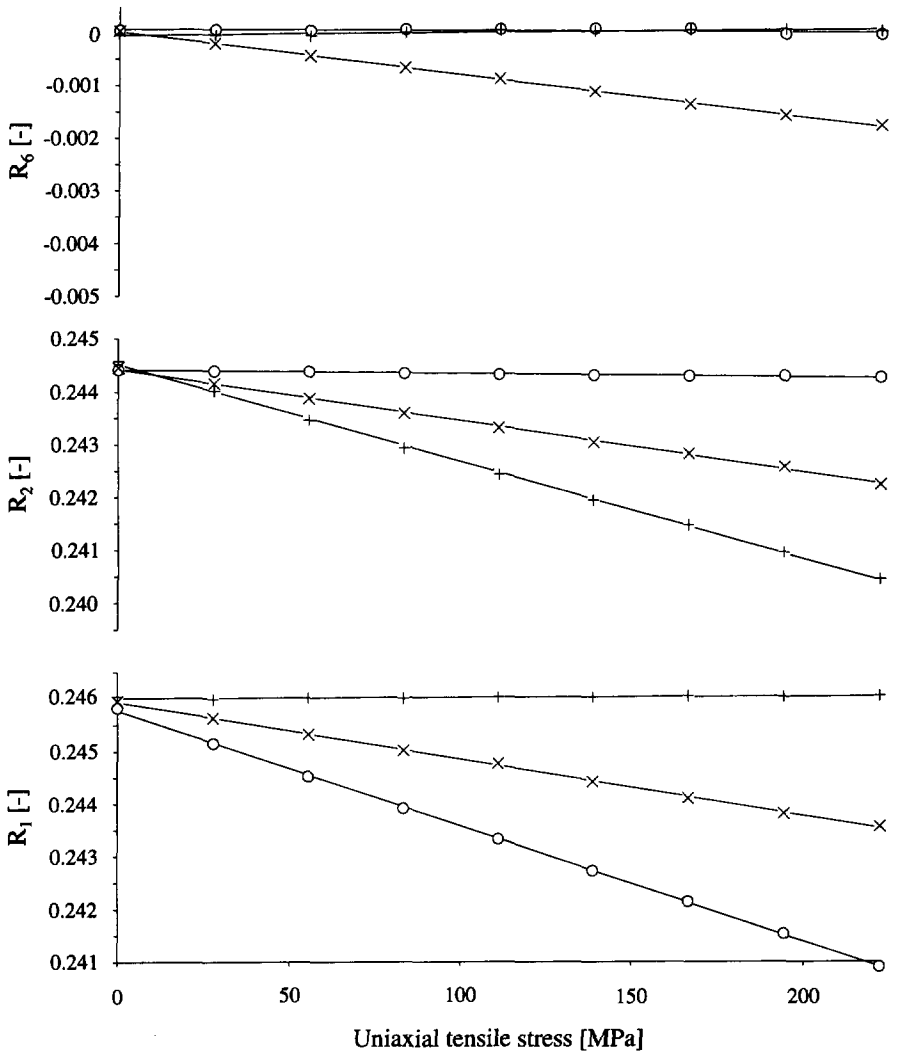

Fig. 4.4 Calculated R-tensor components as a function of the stress applied in aluminium 2024-T351 specimens. The loading directions relative to the material x_1-axis are: o = 0°, × = 45°, + = 90°. The lines indicate the results of linear regression calculations.

Discussion

It is seen that the form of the k- and m-tensors agrees with that suggested theoretically for an orthotropic material, i.e. vanishing tensor components 16, 26, 61 and 62 (Eqs. 2.24 and 2.30). Furthermore, the difference between components 11 and 22 indicates that the material is not isotropic as far as its acoustoelastic behaviour is concerned. It is noteworthy that components m_{21} and m_{12} are close to zero. As can be deduced from Equation 2.29, this implies that the data tensor components R_1 and R_2 are almost uniquely determined by the stresses T_1 and T_2 respectively.

Table 4.4 Reference values R_i^o for the aluminium 2024-T351 tensile specimens [-].

Specimen	0°	45°	90°
R_1^o	0.24577 (0.00004)	0.24593 (0.00005)	0.24601 (0.00004)
R_2^o	0.24441 (0.00004)	0.24443 (0.00005)	0.24451 (0.00004)
R_6^o	0.00005 (0.00003)	0.00000 (0.00003)	–0.00007 (0.00006)

Analysis shows that tensor components 11, 12, 21 and 22 are mostly affected by errors in time of flight, components 61 and 62 by errors in the polarization angle and components I6 by both quantities. The results show that experimental errors propagate particularly strongly into the values for components 16 and 26. The reason for this is that when a shear stress is induced in a tensile specimen, normal stresses are also inevitably introduced. Hence changes in ΔQ_6 or R_6 will always be accompanied by changes in ΔQ_1 and ΔQ_2 or R_1 and R_2. This lowers the accuracy with which the relations between ΔQ_6 or R_6 and the normal stresses T_1 and T_2 can be established. An alternative would be setting components 16 and 26 at zero by presuming material orthotropy.

A first estimate for the accuracy of absolute stress evaluations can be deduced from the spread in the reference values between the specimens (Table 4.4). Using the largest occurring variation in R_i^o together with the calibrated $\underline{m}$-tensor, *equivalent stresses* are calculated which would give rise to equal changes in the acoustic data tensor $\underline{R}$. The results in MPa are:

$$\begin{bmatrix} T_1 \\ T_2 \\ T_6 \end{bmatrix} = \begin{bmatrix} 11 \\ 5 \\ 7 \end{bmatrix} \tag{4.7}$$

These values are small relative to the yield strength for aluminium 2024-T351 (395 MPa).

4.3.3 Disc under diametrical compression

In reference [51] an elastic solution is given for the (plane) stress tensor in the centre of a disc compressed diametrically. For a disc with diameter d loaded by a force P per unit disc thickness at an angle γ relative to the x_1-axis, this solution reads:

$$\begin{bmatrix} T_1 \\ T_2 \\ T_6 \end{bmatrix} = \begin{bmatrix} (2\sin^2\gamma - 6\cos^2\gamma)\dfrac{P}{\pi d} \\ (2\cos^2\gamma - 6\sin^2\gamma)\dfrac{P}{\pi d} \\ -8\sin\gamma\cos\gamma\dfrac{P}{\pi d} \end{bmatrix} \tag{4.8}$$

Thus compressing a disc in different directions induces several combinations of the stress components. A test of this kind therefore provides a means of analysing the applicability of the acoustoelastic stress measurement technique. An additional advantage is that all measurements can be performed on the same material location, reducing errors caused by repositioning the transducer. Only shear waves are used in this experiment, limiting the measurement to applied stresses.

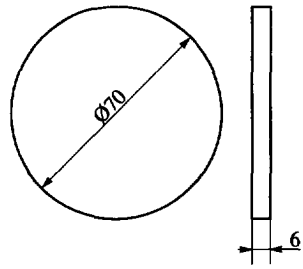

Fig. 4.5 Geometry of the aluminium 2024-T351 disc.

Figure 4.5 gives the geometry of the specimen used for this experiment. The Q-tensor was measured in the unloaded state and during compressive loading by 15 KN in 8 arbitrary directions. No larger force is used, in order to avoid excessive plastic deformation at the contact areas. This would result in loading conditions which deviate too much from those assumed when deriving the elastic solution.

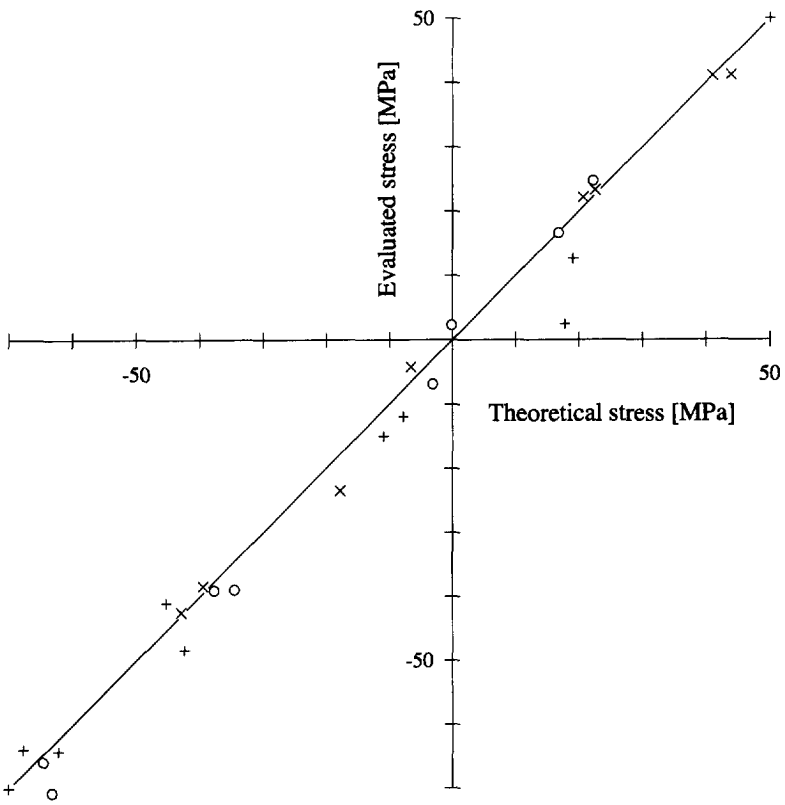

Fig. 4.6 Evaluated vs. theoretical stress components for an aluminium 2024-T351 disc compressed by 15 KN in various directions (o = T_1, + = T_2, × = T_3).

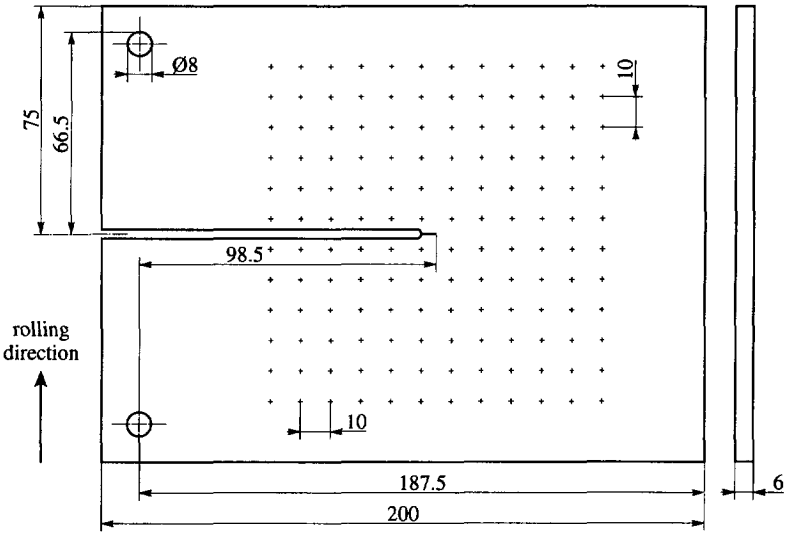

Fig. 4.7 Geometry of aluminium 2024-T351 compact-tension specimen. The grid of measuring locations is indicated by + signs.

The stresses at the centre are calculated using the $\underline{k}$-tensor given in Equation 4.5. Figure 4.6 indicates the correlation between evaluated and theoretical stress components. The results show deviations for the evaluated stress components of at most 8, 16 and 5 MPa for T_1, T_2 and T_6 respectively. These values may be considered small relative to the yield strength of this material.

4.3.4 Stress field in a compact-tension specimen

Figure 4.7 shows the geometry of the compact-tension (CT) specimen in which the plane stress field is evaluated. The measurements are performed on a grid of 12 × 12 points (10 mm apart) arranged symmetrically around the crack tip. First all shear and longitudinal data are gathered in the unloaded specimen. Figure 4.8 gives an impression of the variation of time of flight, corrected for temperature, over the scanned area of the unloaded specimen. The contour lines are calculated using linear interpolation of the data at the measuring points.

Next the specimen is subjected to a constant load of 8200 N and all measurements are repeated. At this load the stress intensity factor K_I is equal to 39.9 MPa$\sqrt{m}$ [50], which is close to the fracture toughness for this alloy. According to Irwin's analysis [11], the plastic zone at the crack tip will have a diameter of 3.1 mm.[I] Therefore, considering the 6.3 mm diameter transducers used, the material behaviour can be assumed to be elastic at all measuring locations.

[I] The stress intensity factor mentioned is in fact corrected for this crack tip plasticity, i.e. it is calculated with a crack length extended by half the plastic zone diameter.

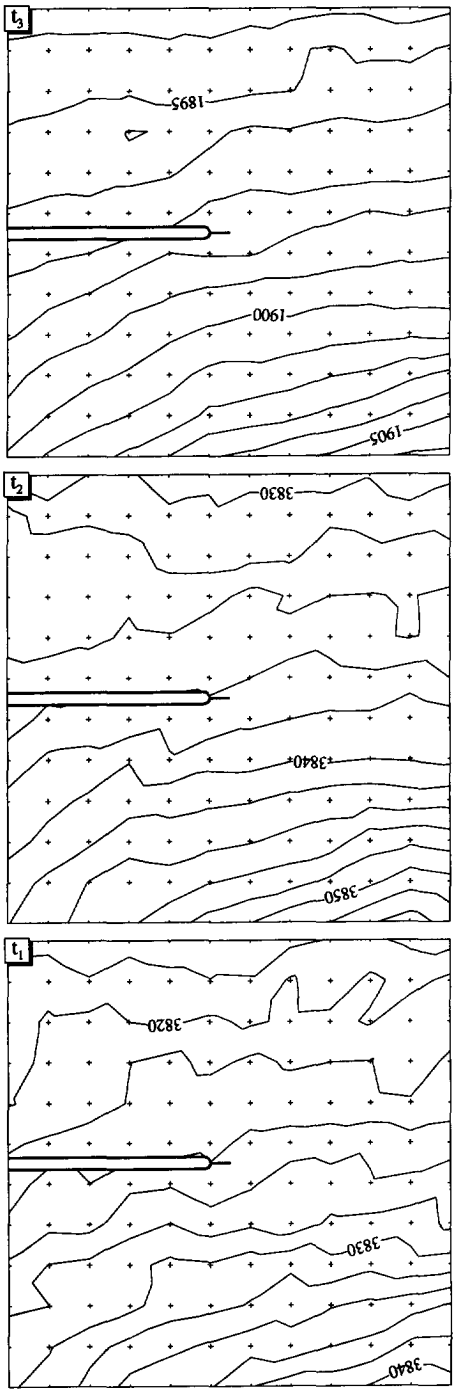

Fig. 4.8 Variation of shear (t_1 and t_2) and longitudinal (t_3) time of flight [ns] over the scanned area of the aluminium CT specimen.

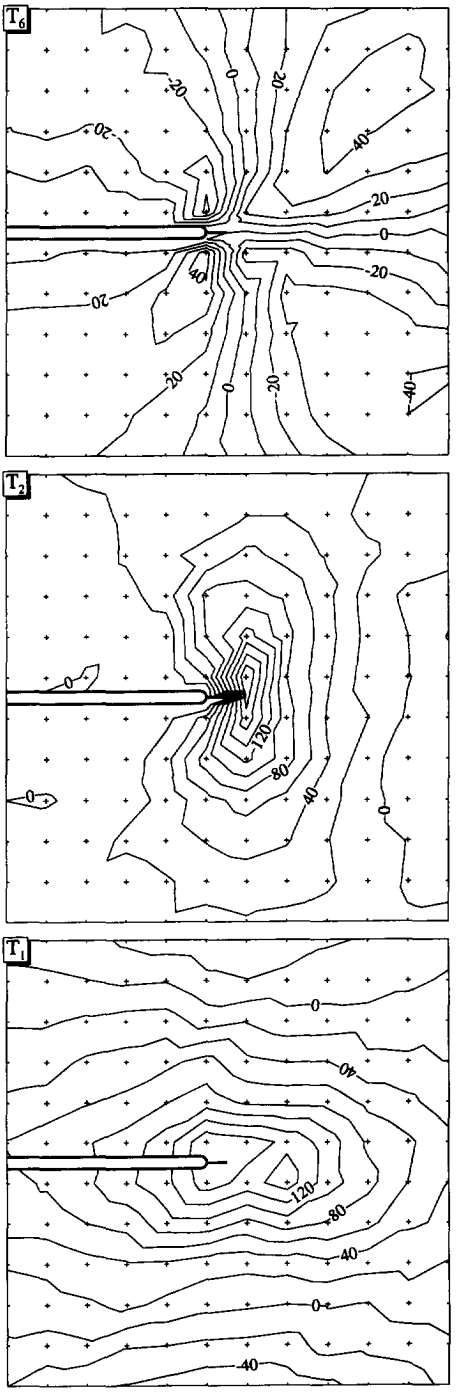

Fig. 4.9 Distribution of applied plane stress components [MPa] in an aluminium CT specimen, evaluated with shear waves only.

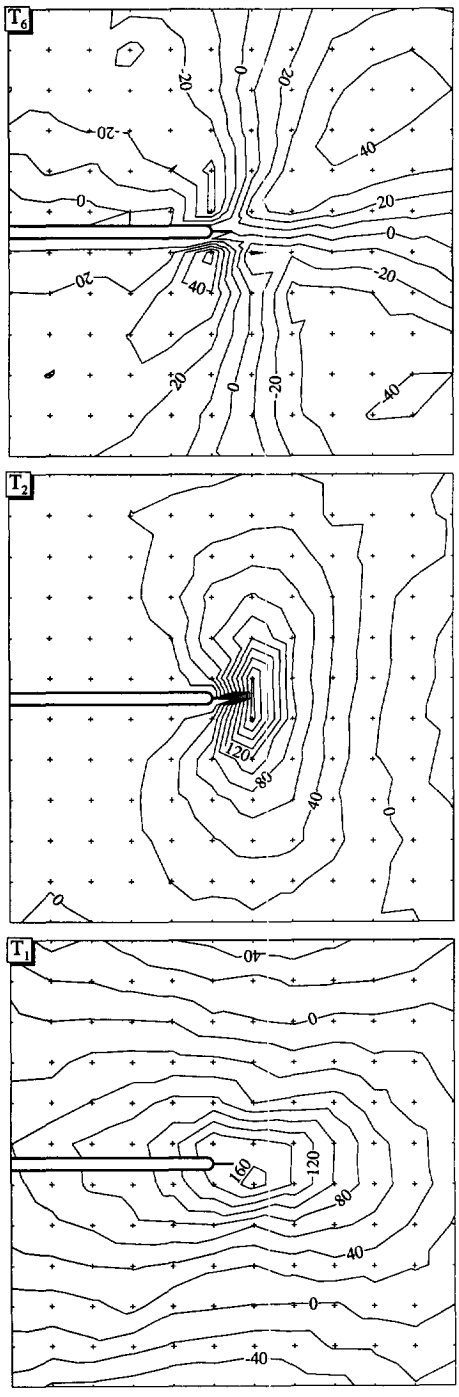

Fig. 4.10 Distribution of absolute plane stress components [MPa] in an aluminium CT specimen, evaluated with shear and longitudinal waves.

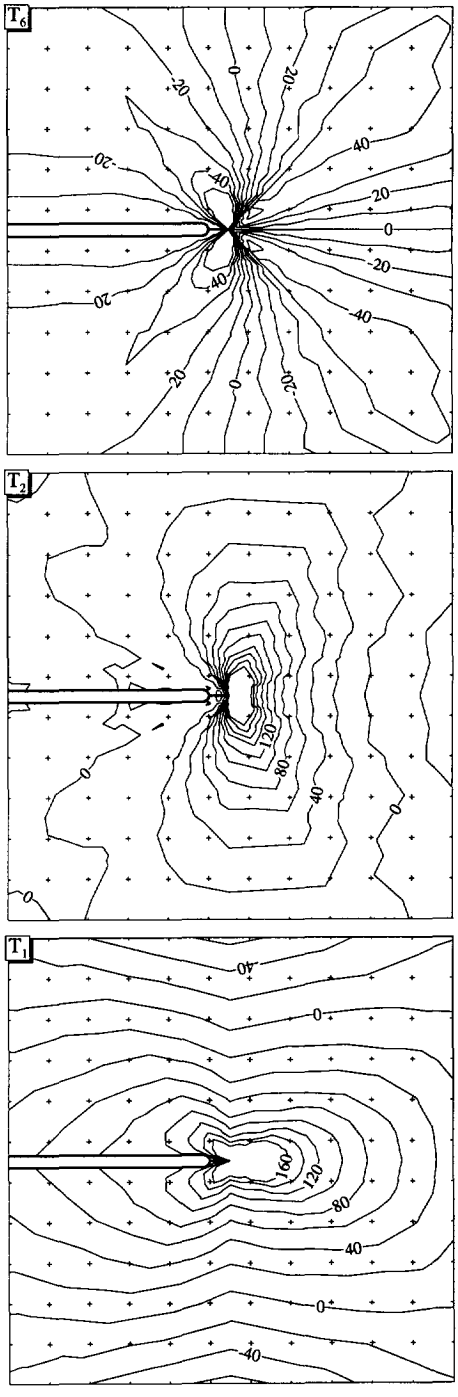

Fig. 4.11 Distribution of plane stress components [MPa] in an aluminium CT specimen, calculated by the finite element method.

Again the *applied* stresses are calculated, using the $\underline{k}$-tensor given in Equation 4.5. The results are plotted in Figure 4.9. As is customary in fracture mechanics, the stresses are defined relative to a set of coordinate axes with the x_1- and x_2-axes respectively parallel to and normal to the crack. In order to draw the contour lines the additional knowledge is used that T_2 and T_6 become zero along the crack edges.

The $\underline{m}$-tensor of Equation 4.6 is used to calculate *absolute* stress levels. However, instead of using the reference values R_i^o determined for the tensile specimens (Table 4.4), the data available at the 12 × 12 points in the unloaded CT specimen are used. Averaging over these data can be expected to yield a more reliable value and also to provide information concerning the reproducibility. Obviously the assumption is made that the unloaded specimen is stress-free. Table 4.5 summarizes the results, including the standard deviation found. The stress components calculated using these reference values are shown in Figure 4.10.

Table 4.5 Averaged reference values R_i^o for the aluminium 2024-T351 CT specimen [-].

R_1^o	0.24612 (0.00010)
R_2^o	0.24458 (0.00011)
R_6^o	-0.00001 (0.00004)

In order to make an assessment of the errors involved in the acoustoelastic stress field evaluation, an incremental elastic-plastic finite element analysis is performed. A plane stress situation is presumed in this calculation. The elastic properties of the aluminium alloy are characterized by its Young's modulus and Poisson's ratio (Table 4.2), while a model for plastic behaviour is used based on a uniaxial stress-strain curve. The results are contained in Figure 4.11.

Discussion

Roughly speaking, the shapes of the three types of stress contours, i.e. the experimentally-determined applied and absolute stresses and the calculated stresses, compare well. For the normal stress components differences of 20 MPa can be found in a few areas, but at most places the agreement is better. The asymmetry of the experimental normal stress data is of the same magnitude.

For the shear stress plots the differences are considerably smaller. This is not surprising, as shear stress data are evaluated from the difference between the shear wave times of flight, i.e. the birefringence.[1] Consequently factors such as acoustic coupling, temperature and specimen thickness hardly influence the measurement. Experimental and calculated values agree to within about 10 MPa. The most significant deviations occur in the areas along diagonal lines

[1] This can be deduced from the definition of components Q_6 and R_6 (Eqs. 2.26 and 2.31) and the form of the $\underline{k}$- and $\underline{m}$-tensors for orthotropic material.

through the crack tip at angles of 45 and 135°. This is probably due to averaging of the measured data over the transducer diameter. A systematic error is introduced proportional to the second derivative of stress, a quantity which is relatively large in these areas.

The (anti-)symmetry of the experimentally-determined shear stresses appears to be slightly disturbed by a systematic positive error. It is suspected that it is caused by a slight rotation of the transducer with respect to its holder, resulting in a shift in the polarization angle measurement during the experiment.

The results for the absolute stress levels, evaluated with both shear and longitudinal waves, seem to be more symmetric and in better agreement with the finite element results. This is in spite of the fact that the shear and longitudinal data are obtained separately, reducing the potential advantages of simultaneous measurements (see Chapter 3). A possible explanation is the fact that the shear wave data leading to the applied stresses are also obtained separately, namely before and after loading the specimen. The absolute stresses, however, follow exclusively from loaded specimen data in combination with the averaged reference values R_I^o. In this way fewer experimental errors propagate into the final results.

It is noteworthy that the spread in the R_I^o-values over the scanned area (Table 4.5) is roughly the same or smaller than that measured between the tensile specimens. The reference values will not therefore give rise to errors in the absolute stress levels larger than those mentioned in Equation 4.7.

The times of flight in the unloaded specimen (Fig. 4.8) confirm the tendency found for the tensile specimens: the difference between the times of flight for the birefringent shear wave components is approximately constant. The same is true for the ratio between shear and longitudinal times of flight. These findings indicate that the time-of-flight variations are mainly due to differences in specimen thickness. Over the scanned area in the CT specimen the differences would amount to 40 μm on a nominal thickness of 6 mm. Despite the limited accuracy of the micrometer, such differences were actually found in the specimen.

A consequence of the thickness variations is the occurrence of relatively high time-of-flight gradients of up to 0.4 and 0.2 $^{ns}/_{mm}$ for shear and longitudinal waves respectively. It is clear that an accurate positioning of the transducer is required in order to minimize errors.

4.3.5 Evaluation of the J-integral fracture parameter

The J-integral fracture parameter is usually evaluated by energetic principles, i.e. the determination of load versus load displacement. In view of the availability of the complete plane stress field around the crack tip, another method presents itself: the numerical integration of J along a contour around the crack tip. The numerical integration provides not only an

alternative method for determining J, but also a means of further checking the consistency of the stress data evaluated.

Numerical J-integration

The J-integral is defined in Appendix 4A. Integrating along a contour Γ surrounding the crack tip, starting at the lower and ending at the upper crack surface, will yield a J-value independent of the exact path. This feature generally permits Γ to be chosen outside a possible plastic zone at the crack tip. Material behaviour is then linear-elastic along the whole of Γ, in which case the strain-energy density, the traction vector and the displacement gradient can be expressed in terms of stress components and the rotation component ω_6. Assuming a plane stress state, Equation 4A.10 gives the resulting expression for the integrand of J.

For the numerical integration the contour Γ is chosen through points at which stress data is evaluated. The J-integrand is determined at all evaluation points along Γ and the trapezoidal rule is used to calculate J. In order to extend the integration to the actual crack surfaces, the integrand at these surfaces is also required.[1] This quantity follows from Equation 4A.10 by substituting zero for T_2 and T_6 and using the value at the nearest evaluation point as an estimate for T_1. The results will show the possible effect of this estimate.

The contour will necessarily have an angular shape. Since the direction of the contour is different before and after a corner point, the J-integrand is double-valued there. For the integration the average is used.

The rotation or rather the rotation change from one location to another can be expressed in terms of stress gradients. Equation 4A.13 does this for a plane stress state. Theoretically, knowing only the rotation change and not the absolute value would suffice for integrating J. However, due to experimental errors in the stress data, an estimate for the absolute rotation level will increase accuracy. Based on the symmetry of the specimen, the rotation may be assumed to be zero ahead of the crack along the centre line of the specimen. Using *forward integration* [19] starting at the centre line (Eq. 4A.14), the rotation ω_6 can be determined at other locations.

The rotation values at the contour points could be calculated by integrating along several different paths. However, it is convenient if J-evaluation can be based on a smaller number of stress measurements than the 12 × 12 available. The forward integration is therefore performed along the contour itself, after which the values are shifted in such a way that the rotation is zero at the intersection with the centre line of the specimen. Consequently the only stress data needed are those on and directly beside the contour. A slight complication arises

[1] The crack surfaces do not extend parallel to the x_1-axis up to the crack tip. The integrand at the width transition is roughly equal to $-T_2^2/2E$ (Eq. 4A.10), leading to an error smaller than 0.01 N/mm.

at the points beside the crack surfaces, as the derivative $\partial T_1/\partial x_2$ cannot be estimated there. This is circumvented by making the contour approach the crack surfaces perpendicularly, eliminating the need for this derivative. The derivatives $\partial T_2/\partial x_2$ and $\partial T_6/\partial x_2$ are estimated using the knowledge that T_2 and T_6 become zero at the crack surfaces.

Results and discussion

Integration is performed along five contours, as shown in Figure 4.12. The integration direction is also indicated. Four of the contours (A to D) surround the crack tip at increasing distances, providing a means of checking the path independence of J. Contour E is closed and should theoretically yield a zero J-value.

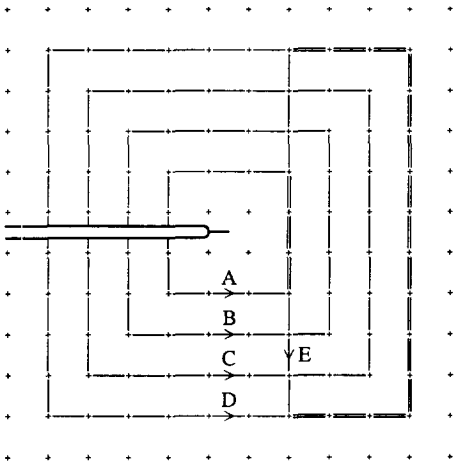

Fig. 4.12 The four contours around the crack tip (A to D) and the closed contour (E) considered for numerical J-integration.

In Figure 4.13 the rotation values ω_6, calculated from the applied stresses, are plotted as a function of the arc length s for all contours. The results derived from the absolute stresses are approximately analogous and are therefore omitted. As is to be expected, the rotations are positive in the lower half and negative in the upper half of the specimen. The asymmetry is less than approximately 10 %.

Near the crack surfaces the rotations are roughly equal (≈5.5 ‰). This indicates that the crack surfaces remain straight in the loaded specimen. During the experiment the crack mouth opening displacement was determined to be about 1.5 mm. Using the rotation difference between the two crack surfaces (11 ‰), a hinge point can be calculated at 25 mm before the crack tip. The stress field does indeed show that the strain in the x_2-direction is near zero at this point.

Figure 4.14 shows the integrand values I_J, again calculated from the applied stresses, as

a function of the arc length s. The discontinuities at the corner points are clearly visible. The asymmetry is somewhat larger than for the rotations, especially for the contours near the crack tip. This is probably due to the larger stress gradients there. It is to be expected, therefore, that contour A is the most error-prone.

The integrand values at the crack surfaces may deviate, owing to the estimate for T_1 made there. From the plots it is clear that the effect on the total integrated area leading to J cannot possibly be significant.

The integrated J-values are summarized in Table 4.6. The values for the contours surrounding the crack tip agree to within 13 and 11 % for the applied and absolute stress fields respectively. The closed contour J-values are respectively 1.6 and 0.6 % of the nominal J-value. The results based on the absolute stress field seem to be somewhat more accurate.

Two estimates for J are also given in the table. The first is based on the finite-element calcu-

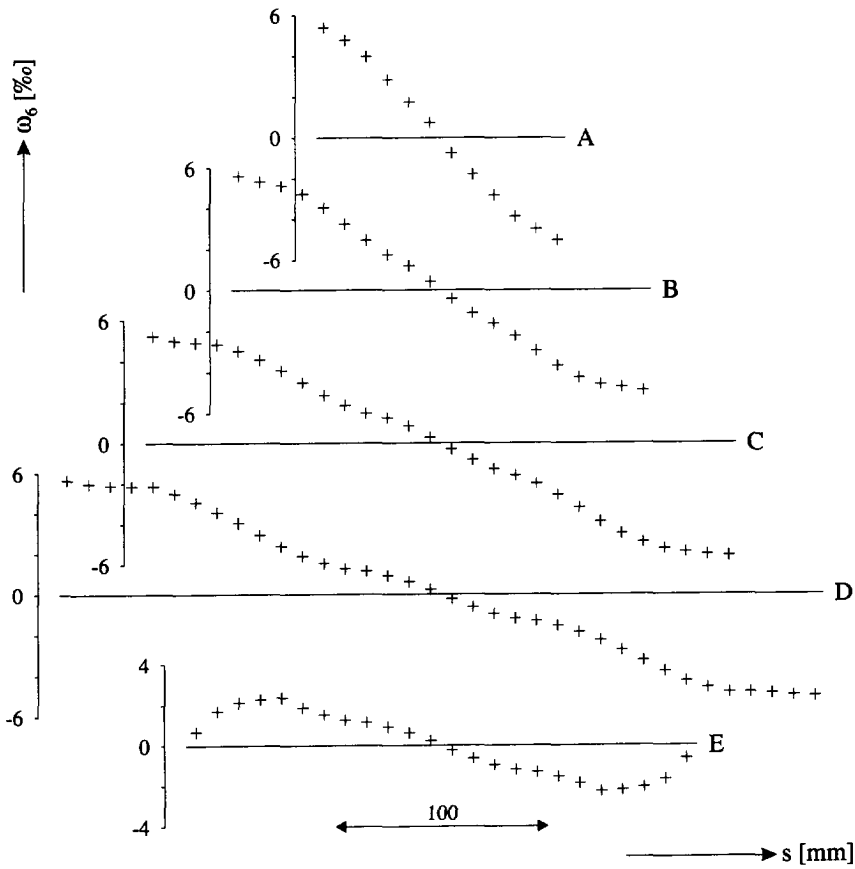

Fig. 4.13 The rotation ω_6, calculated from the applied stresses, as a function of the arc length s for the five contours considered.

lations used to calculate the plane stress field, while for the second estimate linear-elastic fracture mechanics is used. This value is based on the stress intensity factor K_I, which, as was mentioned previously, is equal to 39.9 MPa$\sqrt{m}$ for the present geometry and load. The J-estimate is then calculated using:

$$J = \frac{K_I^2}{E} \tag{4.9}$$

The average J-values over contours A to D based on applied and absolute stresses are 22.3 and 21.8 $^{N}/_{mm}$ respectively. These values are both very close to the fracture mechanics estimate. The reason why the finite-element estimate turns out to be somewhat lower is not known.

The sensitivity of the integrated J-value for the absolute rotation level along the contour,

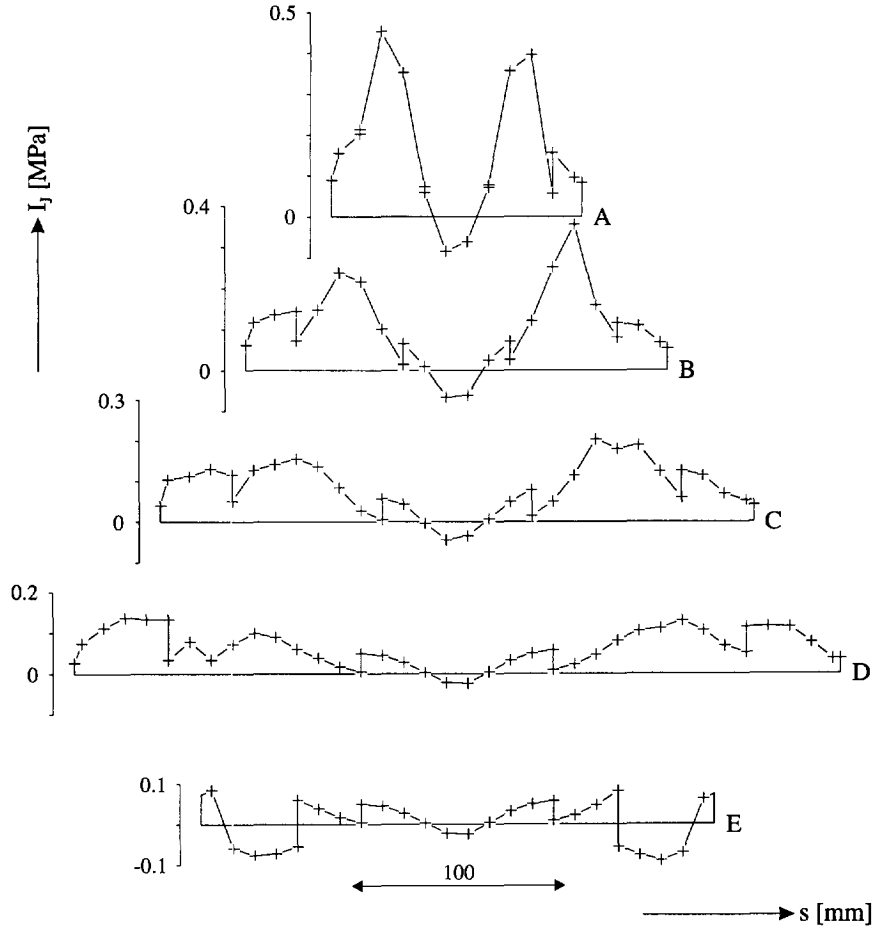

Fig. 4.14 The J-integrand I_J, calculated from the applied stresses, as a function of the arc length s for the five contours considered.

$dJ/d\omega$, is also indicated in Table 4.6. This quantity is a measure of the experimental errors in T_2 and T_6 along the contour (Appendix 4A). For the worst case, i.e. the calculation using applied stresses along contour B, the sensitivity amounts to 0.95 N/mm per ‰ rotation. The overall tendency is a lower sensitivity for the results based on absolute stresses. Again this suggests a lower error level in these data.

Table 4.6 Results of J-integration along several contours together with estimates using the finite-element method and linear-elastic fracture mechanics.

	Source stress field	Contours A	B	C	D	E	Estimates FEM	LEFM
$J\ [N/mm]$	applied	20.8	21.8	23.6	22.8	0.36	20.6	21.6
	absolute	20.6	21.7	21.9	22.9	0.14		
$dJ/d\omega\ [N/mm]$	applied	+290	−950	−520	−730	−230	–	–
	absolute	−20	−470	−180	−330	−280		

4.4 Structural steels

4.4.1 Introduction

Material

The experiments are performed on specimens taken out of hot-rolled steel plate. This material typically shows only a slight texture. Two steel qualities are used, originating from different manufacturers but having more or less similar specifications:

A) T St E355 according to standard *DIN 17102*.

B) Fe E355-KT according to *Euronorm 113-72*.

Henceforth these qualities will be denoted as steels A and B. They are in the form of plate hot-rolled to a thickness of 22 and 30 mm respectively and then normalized. The chemical composition is summarized in Table 4.7, while the mechanical properties, measured by tensile tests in the plane of the plate normal to the rolling direction, are given in Table 4.8.

Table 4.7 Chemical composition of the structural steel qualities [Wt%].

Steel	C	Si	Mn	P	S	Al	Cr	Cu
A	0.17	0.35	1.34	0.014	0.003	0.035	0.04	0.02
B	0.19	0.40	1.30	0.014	0.007	0.048	0.036	0.018

Mo	N	Nb	Ce	Ni	Ti	V	Fe
0.02	0.007	0.030	–	0.12	0.01	0.01	bal.
0.002	0.005	0.029	0.014	0.025	–	–	bal.

Table 4.8 Mechanical properties of the structural steel qualities.

Steel	A	B
Yield strength T_y	377 - 417	367 - 395 MPa
Tensile strength T_u	541 - 571	534 - 572 MPa
Elongation (l-5D) δ	27 - 36	22 - 32 %

The separately measured time-of-flight temperature coefficients β can be found in Table 4.9.[1]

Table 4.9 Time-of-flight temperature coefficients for the structural steel qualities.

Steel	A	B
Shear wave β_s	$+180 \cdot 10^{-6}$	$+170 \cdot 10^{-6}$ K^{-1}
Longitudinal wave β_l	$+125 \cdot 10^{-6}$	$+130 \cdot 10^{-6}$ K^{-1}

[1] The experimental results for steel B are shown in Figure 3.16.

Experimental conditions

All experiments on the structural steel qualities are carried out with the set-up described in Chapter 3, which uses the combined shear-longitudinal transducer.

Preliminary measurements through 15.0 mm thick specimens of both steel qualities reveal nominal time-of-flight values of 5070 and 9250 ns for the longitudinal and shear waves respectively. The birefringent shear wave components differ by only 2 to 4 ns.

As discussed in Section 3.2.3, the 2nd longitudinal echo is not available, owing to overlap with the 1st shear echo (Fig. 3.4), and the 1st and the 3rd longitudinal echoes are used for the measurements. Given the small time-of-flight difference between the birefringent shear components relative to the wave period of 200 ns, the polarization measurements are based exclusively on the determination of shear time-of-flight maxima as a function of the transducer orientation.

4.4.2 Acoustoelastic behaviour

In order to calibrate the acoustoelastic effect, three tensile specimens are cut from each steel plate. Their tensile directions are at angles of 0, 90 and –45° (steel A) and +45° (steel B) relative to the material x_1-axis. The 15 mm specimen thickness originates from the centre part of the plate thickness. Figure 4.15 shows an outline of the specimen geometry.

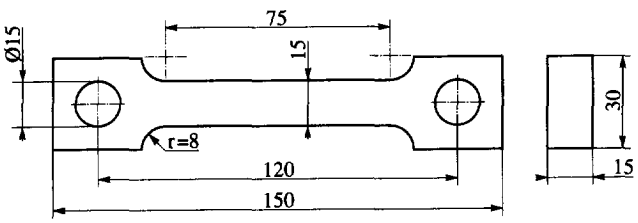

Fig. 4.15 Geometry of the structural steel tensile specimens used for calibrations.

The tensile tests were performed on a 100 KN electromechanical testing machine. Acoustic data were obtained at load intervals of 5 KN (22.2 MPa) up to a load of 55 KN (244 MPa).

Figure 4.17 gives as an illustration the results of the tests on steel B in terms of shear and longitudinal time of flight and polarization angle as a function of the applied uniaxial tensile stress. It should be noted that the data measured at zero applied stress were obtained separately from the tensile tests, using a different orientation of the transducer holder relative to the specimens. This fact, combined with a certain transducer misalignment, causes these values to deviate somewhat, and they were therefore discarded for the purpose of calibration.

The results as far as the shear waves are concerned are clearly illustrated by Figure 4.16. The development of the shear wave time-of-flight scans with the applied load is shown

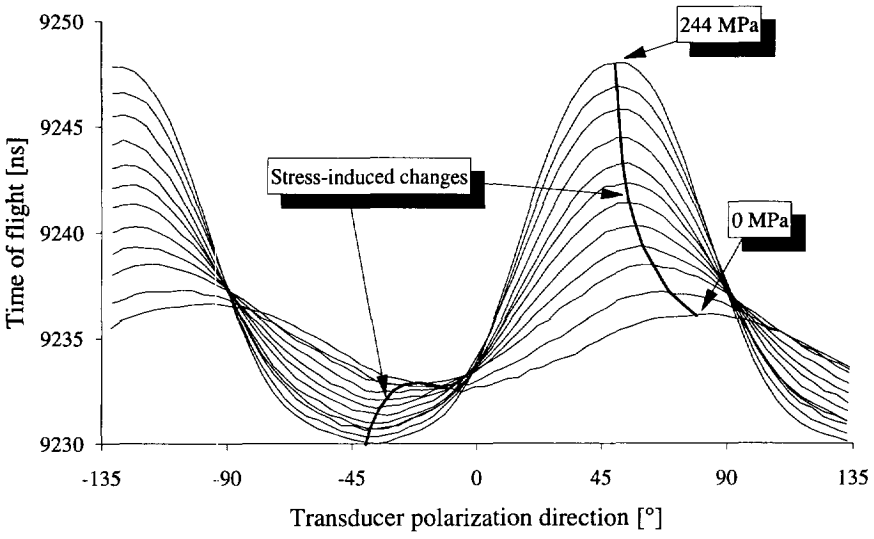

Fig. 4.16 Time-of-flight scans at increasing levels of applied uniaxial tensile stress, ranging from 0 to 244 MPa, for the specimen of structural steel quality B orientated 45° relative to the material x_1-axis. The shear wave time-of-flight and polarization changes are indicated separately.

for the tensile specimen of steel B with an orientation of 45°. The time-of-flight and polarization changes are indicated separately in the plot as lines which connect the extreme values of the scanned time of flight. It is interesting to note that, given the magnitude of the shear wave birefringence, i.e. the time-of-flight difference between the two shear wave components, the shape of the scans is similar to the calculated results shown in Figure 3.5.

In the unloaded state the birefringent wave components show a time-of-flight difference of 3.5 ns, and are polarized at angles of −10 and +80° respectively. The application of load causes the polarization of the slower shear wave component to rotate towards the tensile direction. Furthermore, the time of flight of this wave increases, while that of the other component decreases somewhat. At maximum load the times of flight differ by about 18 ns, and the waves are almost polarized in the tensile direction (+45°) and normal to this.

As for the longitudinal time of flight shown in Figure 4.17, all specimens show an almost equal linear decrease as a function of the applied tensile load.

Acoustoelastic $\underline{m}$-tensor [1]

The $\underline{R}$-tensor is calculated from the experimental data. Linear regression is used to correlate the components of the tensor to the applied stress, the results being shown in Figure 4.18 for steel quality B. These slopes lead to the calibrated values for the acoustoelastic $\underline{m}$-tensor for the two structural steel qualities. In GPa, the results are:

[1] The acoustoelastic $\underline{k}$-tensor is not considered for the structural steel qualities.

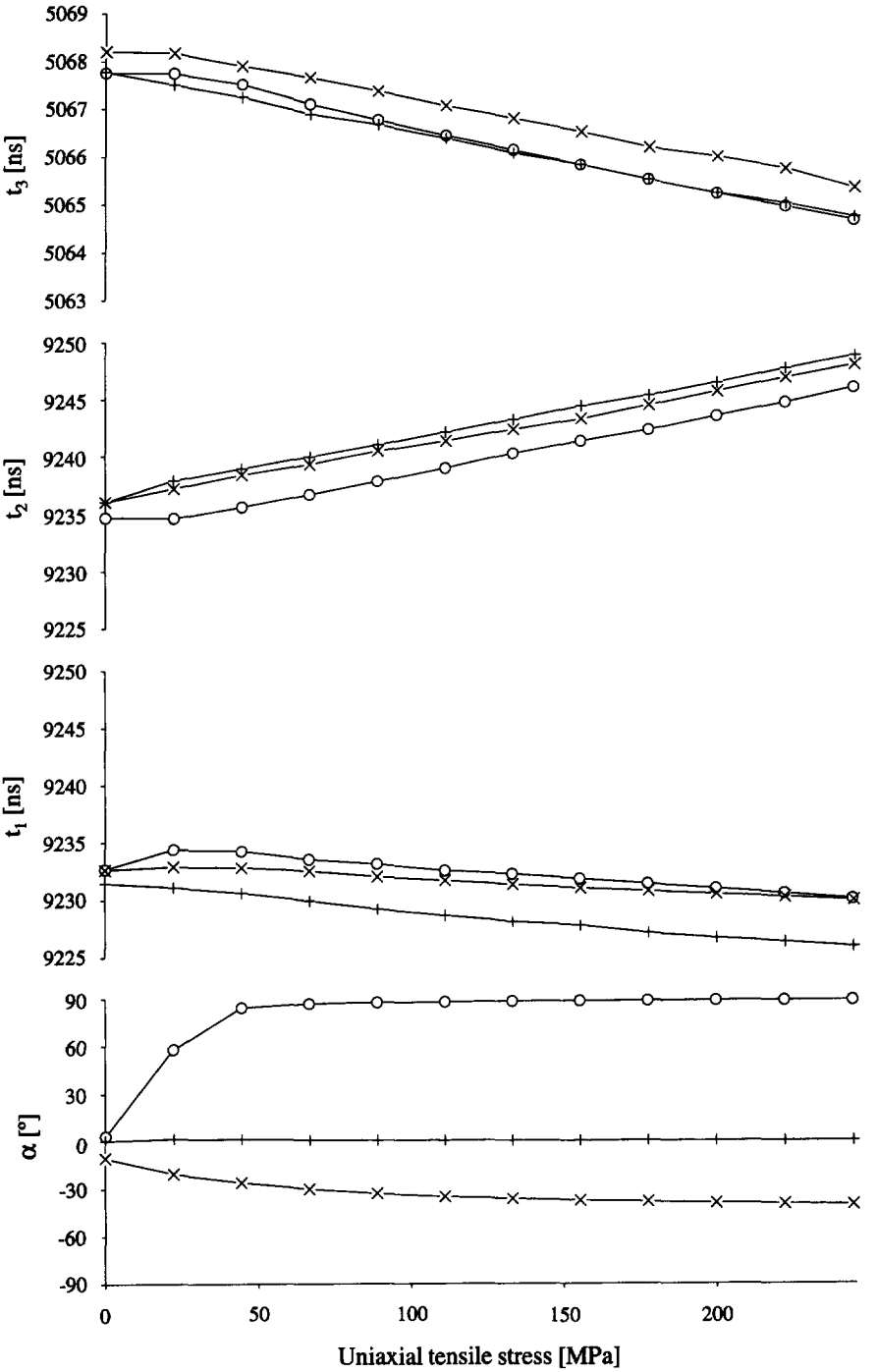

Fig. 4.17 Shear (t_1 and t_2) and longitudinal (t_3) times of flight and the polarization angle α as a function of the uniaxial tensile stress applied in specimens of structural steel quality B. The loading directions relative to the material x_1-axis are: o = 0°, × = 45°, + = 90°.

Table 4.10 Reference values R_i^o for the tensile specimens of the two structural steel qualities [-].

Specimen		0°	±45°	90°
Steel A	R_1^o	0.30106 (0.00003)	0.30116 (0.00003)	0.30117 (0.00003)
	R_2^o	0.30102 (0.00003)	0.30099 (0.00003)	0.30102 (0.00003)
	R_6^o	0.00004 (0.00002)	0.00005 (0.00001)	0.00001 (0.00002)
Steel B	R_1^o	0.30128 (0.00003)	0.30135 (0.00003)	0.30137 (0.00003)
	R_2^o	0.30117 (0.00003)	0.30112 (0.00003)	0.30102 (0.00003)
	R_6^o	0.00001 (0.00002)	–0.00005 (0.00001)	0.00001 (0.00003)

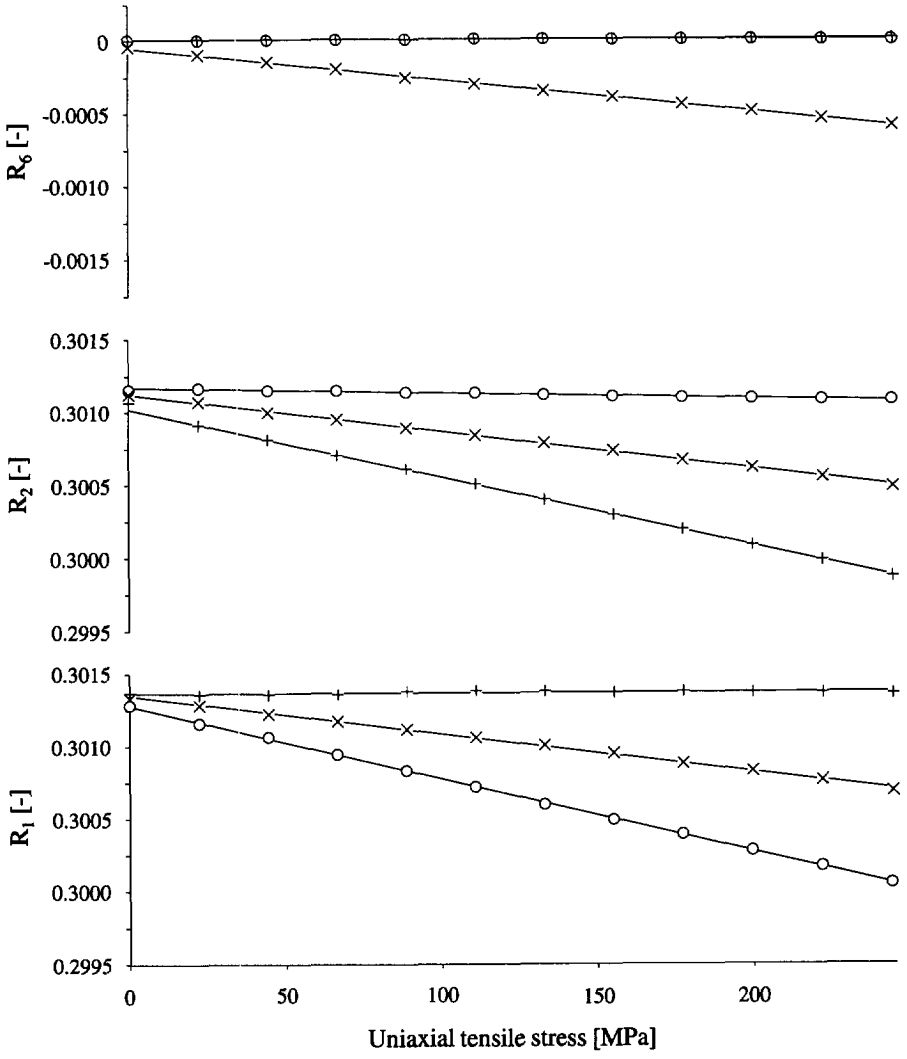

Fig. 4.18 Calculated R-tensor components as a function of the stress applied in specimens of structural steel type B. The loading directions relative to the material x_1-axis are: o = 0°, × = 45°, + = 90°. The lines indicate the results of linear regression calculations.

$$\text{Steel quality A:}\quad [m_{IJ}] = \begin{bmatrix} -207\,(8) & +4\,(8) & -27\,(28) \\ 0\,(8) & -208\,(8) & -15\,(28) \\ 4\,(9) & -4\,(10) & -239\,(20) \end{bmatrix} \qquad (4.10^a)$$

$$\text{Steel quality B:}\quad [m_{IJ}] = \begin{bmatrix} -199\,(7) & -2\,(8) & 13\,(26) \\ 16\,(7) & -214\,(8) & 2\,(27) \\ 0\,(7) & -1\,(12) & -228\,(19) \end{bmatrix} \qquad (4.10^b)$$

The experimental error estimates used in order to calculate the standard deviation shown between brackets are 1 in 20 000 for the times of flight, 0.2 °C for the specimen temperature and 3° for the shear wave polarization.

It should be noted that the experimental uncertainty in the polarization angle actually depends on the magnitude of the shear wave birefringence. For differences of 2 ns and 20 ns, for example, the error in the polarization angle will be about 20 and 1° respectively. However, the propagation of this error into the calculated $\underline{R}$-tensor and consequently into the calibrated $\underline{m}$-tensor values is such that this variation will be compensated for: the polarization angle becomes less important as the birefringence decreases.

The reference values R_I^o, calculated for all six specimens by extrapolating the regression lines to zero load, are summarized in Table 4.10.

Discussion

Acoustoelastic material behaviour

With regard to the calibrated values for the $\underline{m}$-tensor (Eq. 4.10), the following can be noted:

- The $\underline{m}$-tensor values for the two steel qualities do not differ significantly.
- The components m_{16}, m_{26}, m_{61} and m_{62} do not deviate significantly from zero, which is in agreement with Equations 2.24 and 2.30 for an orthotropic material.
- The differences between the components m_{11} and m_{22}, those between m_{21} and m_{12} and the values for m_{66} are such that the two steel qualities may be considered transversely isotropic in the x_1-x_2 plane as far as their acoustoelastic behaviour is concerned (analogous to Eq. 2.25).
- Components m_{21} and m_{12} are close to zero, implying that R_1 and R_2 are almost uniquely determined by the normal stresses T_1 and T_2 respectively (see Eq. 2.29).

All experimental results indicate that the two steel qualities have approximately similar

elastic and acoustoelastic properties. The only significant distinction is the magnitude of the elastic anisotropy, which is expressed by the difference between R_1^o and R_2^o in Table 4.10 and is slightly larger for steel B. The fact that this similarity occurs in spite of the difference in origin leads to the expectation that the material behaviour will be sufficiently reproducible to enable stress evaluation in an absolute sense.

Error analysis

The points mentioned in the discussion of the calibration results for the aluminium alloy 2024-T351, concerning the propagation of experimental errors into the various components of the acoustoelastic tensor, also apply to these results.

When evaluating stress *changes*, the resolution which can be achieved is determined by the errors in the experimental data in combination with the magnitude of the acoustoelastic effect, i.e. in this case the value for the $\underline{m}$-tensor. Based on the experimental uncertainties assumed previously, the accuracy is estimated to be:

- ±15 MPa for normal stresses.
- ± 7 MPa for shear stress.

The accuracy with which *absolute* stress levels can be evaluated also depends on the reproducibility of the reference values R_1^o for the material. An impression of this can be obtained by analysing the reference values determined for the steel specimens (Table 4.10). The largest variation is translated into stress levels which introduce an equal effect on the acoustic data tensor $\underline{R}$. Expressed in MPa, these equivalent stresses are:

$$\text{Steel quality A: } \begin{bmatrix} T_1 \\ T_2 \\ T_6 \end{bmatrix} = \begin{bmatrix} 22 \\ 6 \\ 12 \end{bmatrix} \qquad \text{Steel quality B: } \begin{bmatrix} T_1 \\ T_2 \\ T_6 \end{bmatrix} = \begin{bmatrix} 18 \\ 30 \\ 14 \end{bmatrix} \qquad (4.11^{ab})$$

These values can be understood as a first estimate for the absolute accuracy of the stress measurements. However, the spread in the reference values R_1^o could also be attributed to the presence of residual stresses, induced, for example, during the rolling process or the machining of the specimen. More specific research would be required to clarify this aspect.

It should be noted that residual stresses can erroneously affect the measurements. In the theory underlying these measurements a plane stress situation is assumed, meaning that only the in-plane stress components are non-zero and not a function of the thickness coordinate. It is not known to what extent this may be of influence.

4.5 Pipeline steel

4.5.1 Introduction

Material

The pipeline steel investigated is a quality denoted as Ste 415.7 TM according to standard *DIN 17172.*

This steel is produced by a basic oxygen process and is continuously cast in the form of a 195 mm thick slab. It is then transformed to plate by a thermomechanical rolling process. In this process the material is heated to 1100-1200 °C, after which prerolling is performed in line with and normal to the casting direction. The final plate thickness (16.3 mm) is obtained by temperature-controlled rolling at 700-870 °C. Forming at this low temperature range prevents re-crystallisation of the austenite, resulting in grain elongation. Material strength and toughness properties are thus improved.

Subsequently a so-called U-O-E process is used to transform the plate to pipeline. Roughly described, the process consists of successively forming the plate in a "U" and "O" shape, welding the longitudinal seam and mechanically Expanding the pipeline (= 1%) to obtain the desired geometry. All deformation in this process is applied at ambient temperature and will thus induce texture and residual stresses. The final product is a longitudinally welded pipeline with an outer diameter of 1067 mm and a wall thickness of 16.1 mm.

The chemical composition of the pipeline steel, the mechanical properties measured by tensile tests in the tangential pipeline direction and the experimentally determined time-of-flight temperature coefficients β are summarized in Tables 4.11, 4.12 and 4.13 respectively.

Table 4.11 Chemical composition of the pipeline steel [Wt%].

C	Si	Mn	P	S	Al	Cr	Cu
0.09	0.26	1.44	0.018	0.003	0.045	0.07	0.03

Mo	N	Nb	Ni	Ti	V	Fe
0.02	0.006	0.027	0.06	0.003	0.00	bal.

Table 4.12 Mechanical properties of the pipeline steel.

Yield strength T_y	453 - 480 MPa
Tensile strength T_u	560 - 585 MPa
Elongation (l-5D) δ	23 - 25 %

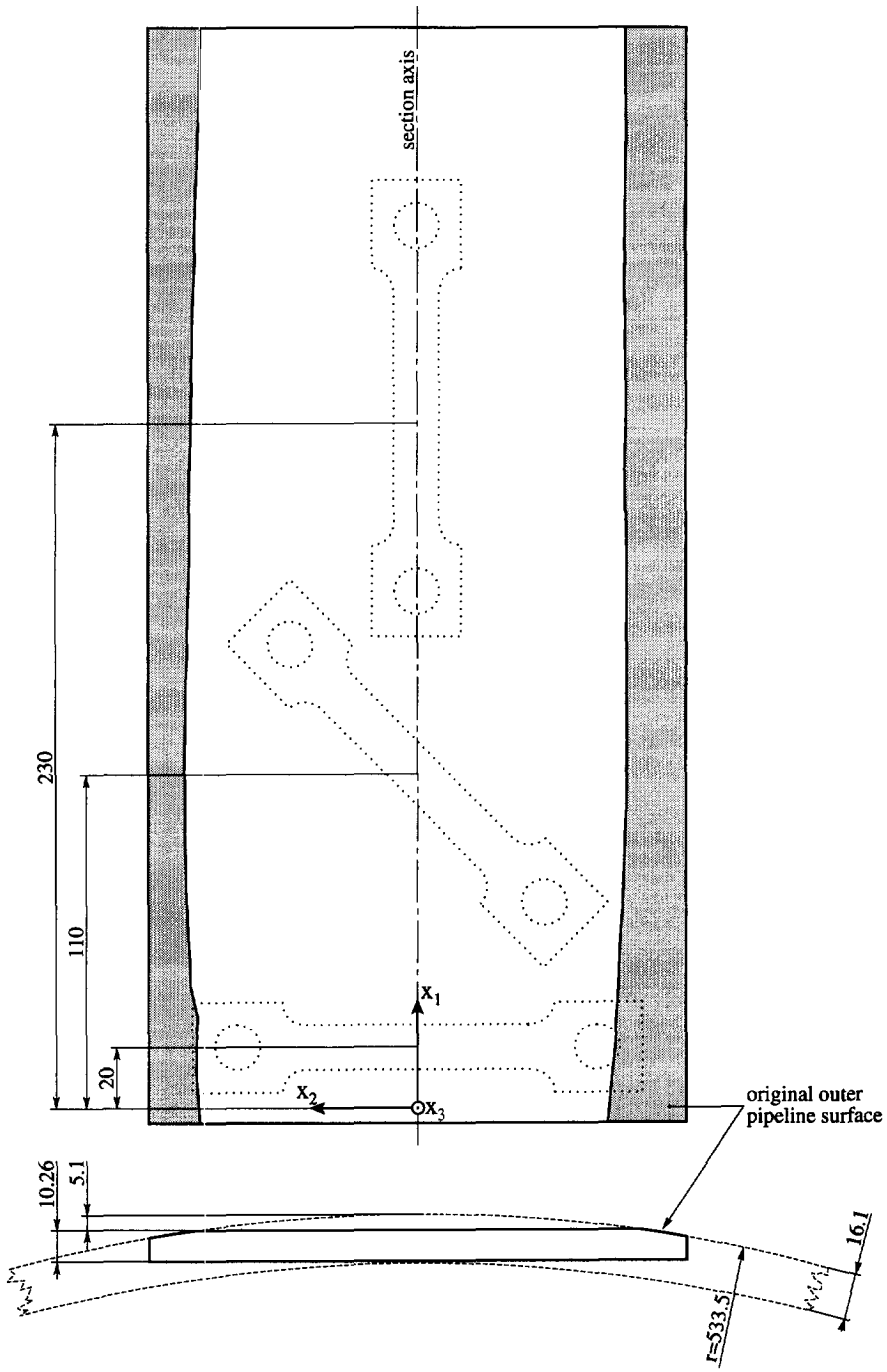

Fig. 4.19 Geometry of the section taken from the pipeline, showing the axis along which all acoustic measurements are performed. The positions are also indicated from which the tensile specimens are cut out during the course of the experiments.

Table 4.13 Time-of-flight temperature coefficients for the pipeline steel.

Shear wave β_s	$+160 \cdot 10^{-6}$ K^{-1}
Longitudinal wave β_l	$+125 \cdot 10^{-6}$ K^{-1}

Experimental conditions

A section is taken out of the pipeline exactly opposite the welding seam. The dimensions are shown in Figure 4.19.

Positioning of the transducer, using the holder designed for these experiments (Fig. 3.18), requires a flat specimen area. In order to provide this the outer surface of the *pipeline section* is machined to a depth of 5.1 mm, thus creating a 147 mm wide flat area. This width, larger than would be strictly necessary for positioning purposes ($\approx$ 60 mm), is chosen in order to be able to cut out a tensile specimen orientated perpendicular to the pipeline axis. The inner surface of the section is also flattened in order to obtain parallelism. Consequently only 10.26 mm thickness remains, which originates roughly from the inner part of the original 16.1 mm wall thickness. Although the measurements will probably be influenced by removing the material, it is expected that a qualitative impression of the ultrasonic properties and acoustoelastic behaviour of the material can still be gained.

In Figure 4.19 it can also be seen that the contours of the flat outer surface of the pipeline section are curved. This is attributed to the presence of residual stresses in the original pipeline. Cutting out the section and removing material from the inner and outer surfaces evidently caused the section to bend.

For the ultrasonic measurements wave propagation along a texture symmetry axis is presumed, which in this case is the direction of the pipeline radius. Measurements are therefore only meaningful if performed at locations on the machined surface of the pipeline section where the radius coincides with the surface normal. These locations form a line parallel to the pipeline axis and will be denoted as the *section axis*. In this case the material axes x_i are defined such that x_1 is along the section axis, as the processing history makes it likely that this is a symmetry axis for the material texture.

All experiments use the set-up described in Chapter 3. Preliminary measurements through the machined pipeline section reveal nominal time-of-flight values of 3500, 6060 and 6430 ns for the longitudinal and the birefringent shear wave components respectively. Due to overlap the 2nd longitudinal echo is not available for time-of-flight measurements and the 3rd echo is used instead. Given the large shear wave birefringence, the polarization measurements are based on the amplitude maxima of the fastest component as a function of the transducer polarization.

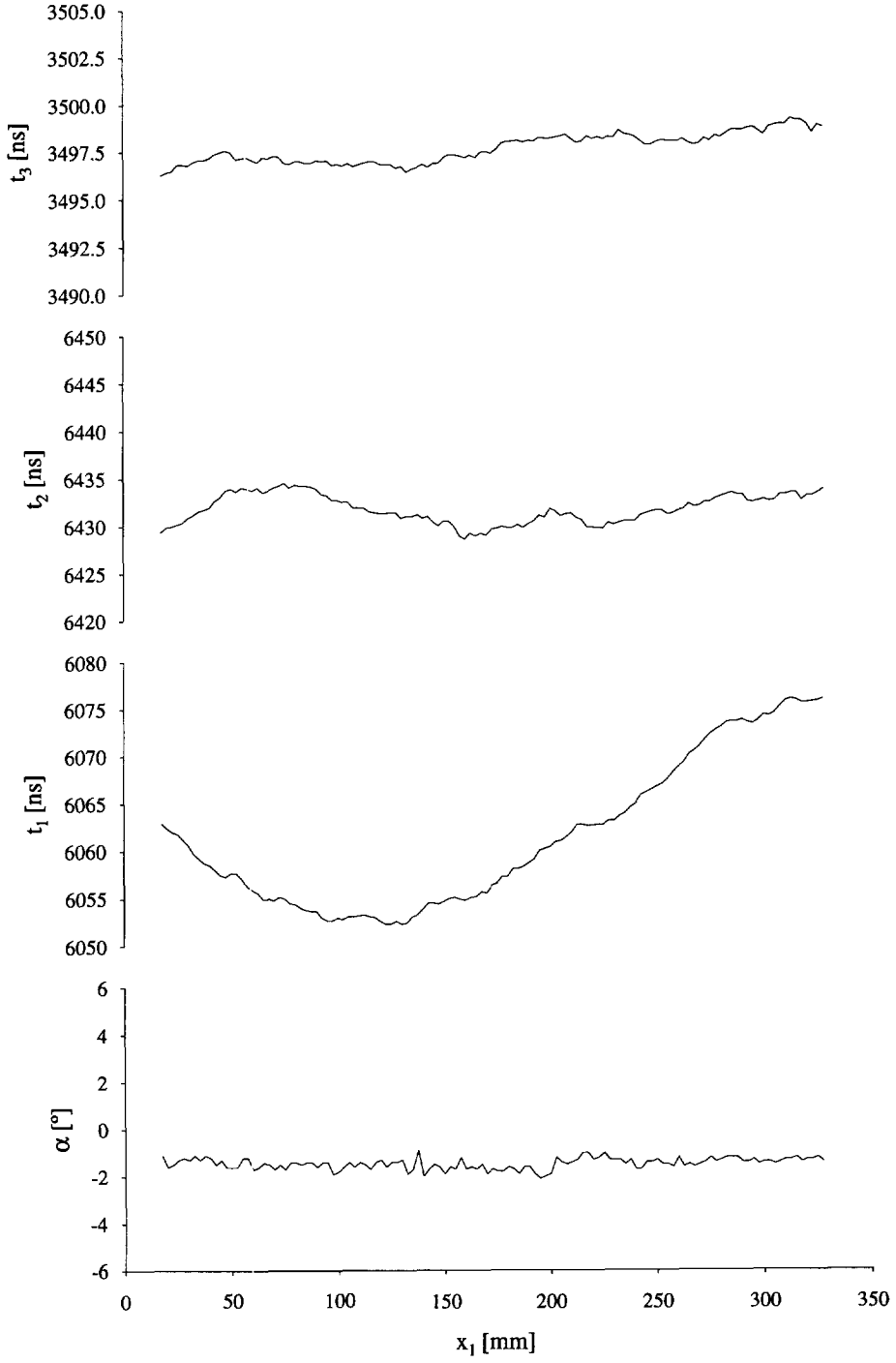

Fig. 4.20 Distribution of shear (t_1 and t_2) and longitudinal (t_3) time of flight and the polarization angle α along the axis of the pipeline section.

4.5.2 Scan over pipeline section

Before cutting tensile specimens from the pipeline section, measurements are performed along the entire section axis in order to gain an impression of the distribution of the acoustic data t_1, t_2, t_3 and α. Figure 4.20 gives the results.

They show the following significant features:

- Along the whole scan the polarization angle α is very consistently almost zero. This means that the shear waves are polarized parallel to and normal to the pipeline axis.
- The shear wave polarized in the direction of the pipeline axis shows a relatively large time-of-flight variation (t_1), while the value for the other shear component (t_2) is much more constant.
- The longitudinal time of flight (t_3) varies only slightly.

The observed constant shear polarization confirms the assumption that the pipeline axis is a symmetry direction for texture. As for the variation in time of flight, two phenomena could be responsible:

- Residual stresses
  It is to be expected that cold deformation, by converting a flat plate to a cylindrical shape followed by expanding, generates residual stresses which vary through the wall thickness of the pipeline. Cutting a section from the pipeline and machining the surfaces may result in a stress redistribution, which could be the origin of the varying times of flight. Taking out tensile specimens could cause further stress changes, as one of the in-plane dimensions is reduced to a small value. It is therefore interesting to compare acoustic data measured at the specimen centres before and after cutting. Since the measuring conditions before and after the cutting process are not exactly the same, only a rough comparison can be made, with an accuracy of about 2 ns. Table 4.14 summarizes the results.

Table 4.14 Acoustic data before and after cutting out tensile specimens.

Specimen		t_1 [ns]	t_2 [ns]	t_3 [ns]	α [°]
0°	before	6063	6430	3498	−1.3
	after	6063	6430	3499	−1.1
45°	before	6053	6432	3497	−1.4
	after	6053	6433	3497	−0.4
90°	before	6062	6430	3496	−1.6
	after	6064	6431	3497	−0.5

It is easily seen that no significant changes have occurred. This means that residual

stresses are a less likely cause for the observed time-of-flight distribution.

- Material heterogeneity
  As mentioned above, the pipeline section was bent as a result of stress relaxation. The material along the section axis will therefore originate from differing positions relative to the original pipeline surfaces. During pipeline manufacturing the nature of the applied deformation is such that the material texture is not evenly distributed through the wall thickness. The material along the section axis may therefore have varying acoustic properties. An indication that this has indeed contributed to the observed time-of-flight distribution is the fact that minimum values for t_1 occur approximately at the location where the width of the machined plane is at a maximum, i.e. $x_1 = 110$ mm.

4.5.3 Acoustoelastic behaviour

Three tensile specimens were cut from the pipeline section with orientations of 0, 45 and 90° relative to the pipeline (section) axis. They have the same geometry as the structural steel specimens (Fig. 4.15), except for their thickness, which now equals that of the pipeline section (10.26 mm). The specimen centres, where the acoustic measurements are performed, coincide with the section axis. The exact locations are indicated in Figure 4.19.

Uniaxial tensile tests were performed on these specimens using a 100 KN electromechanical testing machine. Acoustic data were obtained at intervals of 5 KN (32.5 MPa) up to a maximum load of 45 KN (293 MPa).

Figure 4.21 gives the resulting acoustic data t_1, t_2, t_3 and α as a function of the applied tensile stress. As was the case with the experiments on structural steel, the data measured at zero applied stress are obtained separately from the tensile tests, using a different orientation of the transducer holder relative to the specimens. These slightly deviating values will again be discarded for the purpose of the acoustoelastic calibration.

The results show the following:

- Shear wave polarization
  For the tensile directions 0° and 90° this is not affected by the applied stress. Such a response is to be expected, as the shear stress defined on the x_i-axes remains zero during load application. For the 45° specimen a rotation of about −1.5° can be detected.

- Shear time of flight
  The stress-induced changes range from a linear increase for waves polarized in the tensile direction to a slight linear decrease when polarized normal to this direction.

- Longitudinal time of flight
  A linear decrease can be observed for all three specimens.

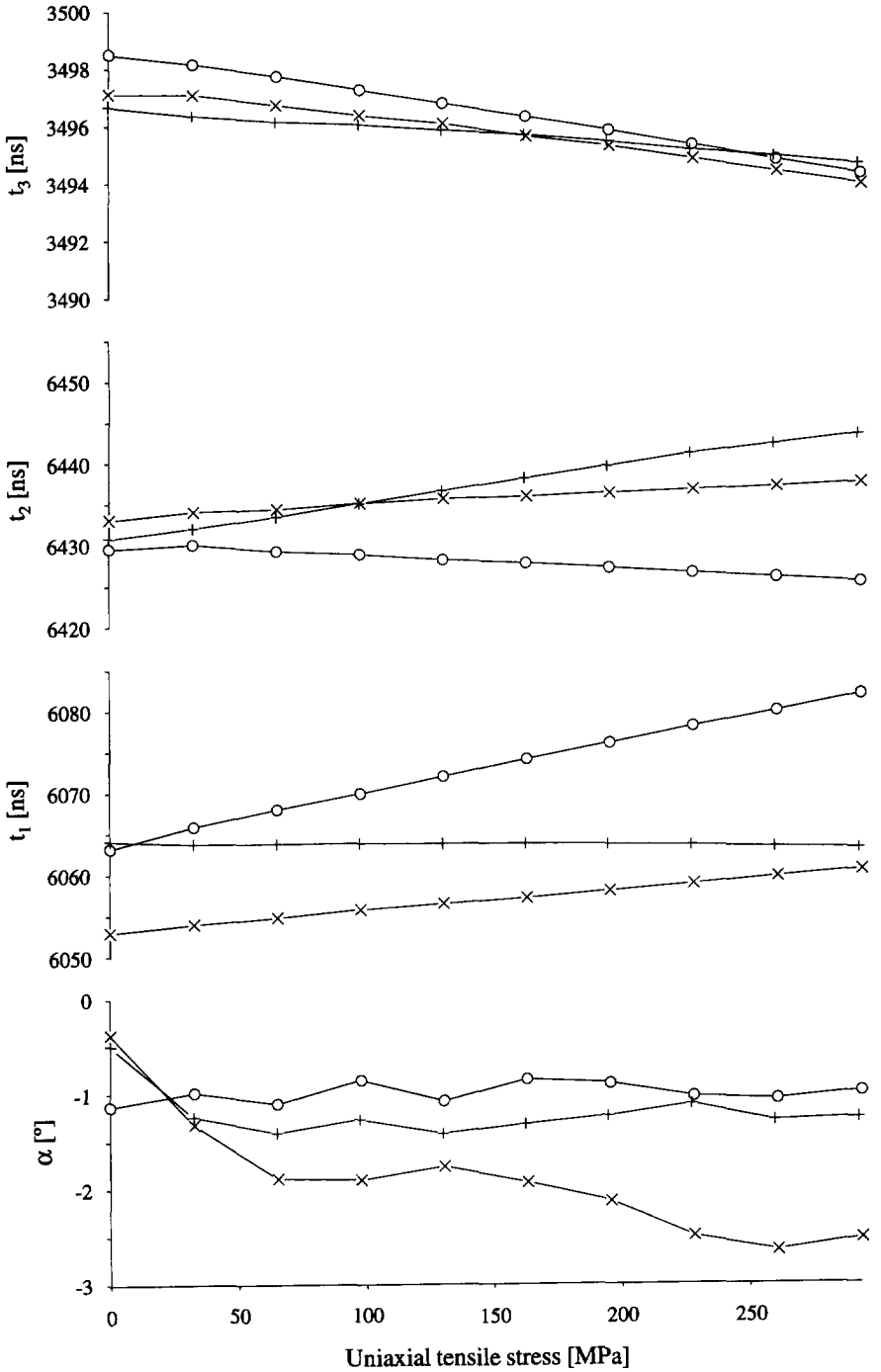

Fig. 4.21 Shear (t_1 and t_2) and longitudinal (t_3) times of flight and the polarization angle α as a function of the applied uniaxial tensile stress in pipeline steel specimens. The loading directions relative to the pipeline axis are: o = 0°, × = 45°, + = 90°.

Acoustoelastic m-tensor

The R-tensor is calculated from the experimental data. These values, together with linear regression lines, are plotted in Figure 4.22. Expressed in GPa, the acoustoelastic m-tensor calculated from the regression slopes is found to be:

$$[m_{II}] = \begin{bmatrix} -107\,(\ 2) & 20\,(\ 4) & -1\,(\ 9) \\ 18\,(\ 4) & -197\,(\ 7) & -2\,(16) \\ -2\,(13) & -5\,(28) & -165\,(80) \end{bmatrix} \qquad (4.12)$$

The standard deviation shown between brackets is calculated using estimated experimental errors of 1 in 20 000 for time of flight, 0.2 °C for the specimen temperature and 0.25° for the shear wave polarization. The latter value is derived from the standard deviation found for the polarization data obtained during the scan over the pipeline section (Fig. 4.20). It is a significantly smaller value than used for both the aluminium and the structural steel measurements. This can be attributed to (i) the different measuring method, i.e. determining amplitude instead of time-of-flight maxima, and (ii) the extremely large birefringence.

It is obvious from Figure 4.22 that the determination of the reference values R_I^o, which would complete the acoustoelastic calibration, does not lead to a location-independent value for the material of the pipeline section.

Discussion

Acoustoelastic material behaviour

The calibrated m-tensor (Eq. 4.12) gives rise to the following remarks:

- The components m_{15}, m_{26}, m_{61} and m_{62} do not deviate significantly from zero, which suggests that the material is orthotropic as far as the acoustoelastic behaviour is concerned.
- The difference between m_{11} and m_{22} indicates that the material is largely anisotropic with respect to the acoustoelastic effect. The values are such that normal stresses in the axial direction can be measured with a considerably higher sensitivity than circumferential stresses. The ratio is about 1.8 to 1.
- The reliability of the value for m_{66} is low, due to the very small rotation of the shear wave polarization induced by shear stresses. The elastic properties of the material are such that a shear wave birefringency of about 6% is induced, with polarization directions parallel to and normal to the pipeline axis (Fig. 4.21). As this relative difference is much larger than the magnitude of the acoustoelastic effect, shear stresses can only induce very small rotations of the polarization. This is confirmed by the results of the

45° orientated tensile specimen, where roughly speaking a shear stress of 150 MPa causes a rotation of 1.5°. Consequently the sensitivity for measuring shear stresses is very low.

It is clear that the acoustoelastic properties of the pipeline steel are strongly influenced by the large elastic anisotropy caused by the cold deformation during the forming process and that this becomes particularly manifest in the stress-measuring sensitivity.

This investigation is concerned with steel from longitudinally welded pipeline. The

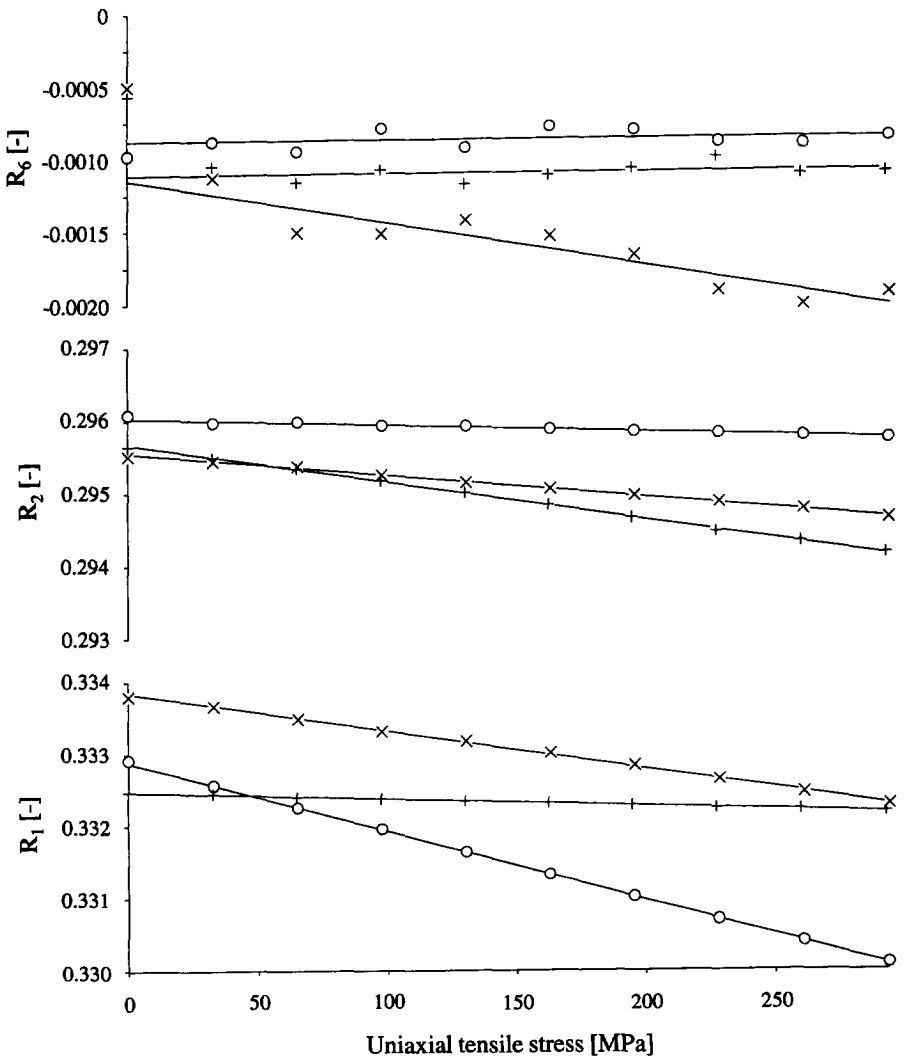

Fig. 4.22 Calculated R-tensor components as a function of the stress applied in pipeline steel specimens. The loading directions relative to the pipeline axis are: o = 0°, × = 45°, + = 90°. The lines indicate the results of linear regression calculations.

pipeline axis can be expected to be an orthotropic symmetry direction, based on both the hot-rolling process and the subsequent cold forming. The magnitude of the anisotropy is such, however, that the cold deformation can be considered to be the dominant factor. This means that the findings above could to some extent also be applicable to spirally welded pipeline, where the rolling direction does not coincide with the pipeline axis.

Error analysis

Based on the calibrated $\underline{m}$-tensor, the resolution when evaluating normal stress *changes* is estimated to be:

- ± 7 MPa for axial stresses.
- ±13 MPa for circumferential stresses.

The resolution for shear stress depends almost entirely on the accuracy of the polarization measurement. As for this material these measurements are based on the determination of amplitude maxima, the outcome can be affected by transducer misalignment. The amplitude scan in Figure 3.14 clearly illustrates that errors of up to 2° can be introduced. As is argued in Section 3.3.2, this influence will be reduced by determining two successive maxima of the same shear wave component and normalizing them so they are 180° apart.[1] If the transducer alignment is also improved, the resolution of the polarization measurement could eventually reach an estimated value of about 0.25°. A rough evaluation of shear stress would then be possible, but it is questionable whether transducer positioning with such accuracy can be achieved in practice.

Measuring *absolute* stress levels seems to be impossible, in view of the fact that the reference values R_i^0 are not reproducible along the pipeline section. However, the results also show that material heterogeneity in the thickness direction plays a major part in this. In order to evaluate properly the reproducibility of the reference values, measurements at different locations on a pipeline through a well-defined part of the wall thickness would be required.

It should be noted that although residual stresses are not thought to be the cause for the observed variations in acoustic data, they can still influence the stress measurements. On grounds of symmetry it is likely that in spite of the cold deformation applied during the pipeline forming process the x_3 thickness direction remains a principal stress direction. However, the in-plane residual stress components T_1, T_2 and T_6 will probably be some function of x_3. This does not agree with the plane stress situation assumed in the theory underlying the measurement. It is not known what the effect of this through-thickness variation is.

[1] This procedure is not followed in the experiments presented here. A systematic error may therefore be present in the polarization data.

Experimental aspects

The transducer holder used here (Fig. 3.18) is designed for a flat surface with a minimum diameter of 60 mm. Measurements on the surface of an actual pipeline obviously require some solutions. One possibility would be creating a flat surface. For example, the present pipeline with its 1067 mm outer diameter would only show a decrease in wall thickness of 0.84 mm. An alternative solution is to design a holder specially for cylindrical surfaces, capable of maintaining a constant couple layer thickness together with an exact alignment of the transducer axis and the pipeline radius. It is not known however what effect the pipeline curvature or the condition of the inner and outer surfaces would have on the measurement.

4.6 Conclusion

A number of acoustoelastic experiments have been presented in this chapter. They were performed on different metals with a wide range of both acoustic and acoustoelastic properties.

In all cases it may be concluded that the *signal-to-noise ratio* obtained for longitudinal and shear waves was adequate for accurate evaluation of time of flight and amplitude. The experiments performed with the set-up described in Chapter 3 show an estimated time-of-flight evaluation error of 1 in 20 000.

The acoustoelastic behaviour of the materials is found to be strongly affected by the magnitude of the *elastic anisotropy*. The two hot-rolled structural steel qualities are almost (transversely) isotropic with regard to both elastic and acoustoelastic behaviour. The aluminium alloy under investigation shows some elastic anisotropy (0.3 % birefringence) in combination with a significant acoustoelastic anisotropy (20 %). The pipeline steel is largely anisotropic (6 % birefringence), while the acoustoelastic effect is about 1.8 times higher for normal stresses in the axial direction compared with the circumferential direction. The magnitude of the elastic anisotropy also determines the extent to which the shear polarization direction rotates under the influence of shear stresses. In the largely anisotropic pipeline steel this rotation is barely measurable.

The magnitude of the *acoustoelastic behaviour* itself, calibrated for the different metals in the form of $\underline{k}$- and $\underline{m}$-tensors, can be compared with values provided in literature. In reference [48], 2nd- and 3rd-order elastic constants can be found which have been determined for a number of approximately isotropic aluminium and steel qualities. These constants can be substituted in the expressions given in Appendix 2E for $\underline{\kappa}$-tensor components. Substituting these components in Equations 2.17 and 2.28, while assuming plane stress, and inverting the results obtained (Eqs. 2.24 and 2.30) leads to the $\underline{k}$- and $\underline{m}$-tensors respectively for these isotropic metals. In Table 4.15 tensor values are summarized for an aluminium and a steel qual-

Table 4.15 Isotropic $\underline{k}$- and $\underline{m}$-tensors [GPa], calculated from 2nd- and 3rd-order elastic constants [48].

Aluminium 2S (99.3 % Al)	$[k_{IJ}] = \begin{bmatrix} -16.5 & -6.2 & 0.0 \\ -6.2 & -16.5 & 0.0 \\ 0.0 & 0.0 & -10.2 \end{bmatrix}$ $[m_{IJ}] = \begin{bmatrix} -39.8 & 1.9 & 0.0 \\ 1.9 & -39.8 & 0.0 \\ 0.0 & 0.0 & -41.6 \end{bmatrix}$
Steel Hecla 37 (0.4 % C;0.3 % Si;0.8 % Mn)	$[m_{IJ}] = \begin{bmatrix} -223 & 15 & 0 \\ 15 & -223 & 0 \\ 0 & 0 & -238 \end{bmatrix}$

ity. They are selected so that their 2^{nd}-order elastic constants approximately agree with those found for the aluminium and structural steel qualities investigated here.

The tensors for aluminium show the same form as those calibrated (Eqs. 4.5 and 4.6), but the absolute values for the various components are somewhat smaller (20 - 30 %). The values for steel are extremely close to those calibrated (Eq. 4.10^{ab}). It should be noted that the steel qualities investigated here may also be considered isotropic.

It is concluded that the actual *stress measurements* performed in the experiments with the aluminium disc and CT specimen were successful. All three plane stress components are determined with an error level which is small compared with the yield strength of the material. Based on these stress values, it was also found to be possible to numerically integrate the J fracture parameter along different contours, achieving good reproducibility and good agreement with estimates obtained both from the finite-element method and linear-elastic fracture mechanics.

The results for the stress field in the CT specimen determined using both shear and longitudinal waves show that *absolute stress levels* can also be determined. Obviously the reference values should be reproducible from one location to another. The results for the structural steel specimens are an indication that this is indeed is a realistic assumption. In particular this is confirmed by the correspondence between the reference values of the two steel qualities from different manufacturers.

Measurements using both shear and longitudinal waves reduce the effect which temperature has on the ultimate results. The time-of-flight temperature coefficients β are such that the influences on the two wave types partially cancel each other out in the calculation of the acoustic data tensor $\underline{R}$.

Appendix 4A The J-integral: numerical integration through elastic material

Definition of J

Consider an arbitrarily-shaped two-dimensional body containing a crack, as shown in Figure 4A.1. An orthogonal set of axes x_i is defined, with the x_1- and x_2-axes respectively parallel and normal to the crack. All relevant quantities are assumed to be independent of the x_3-coordinate. Non-linear elastic material behaviour is used as a model for possible plasticity. This is known as the *deformation theory of plasticity*. A restriction is that no unloading may occur in any part of the body, as plastic deformation is irreversible. Under these assumptions Rice [46] defined the J-integral as:[1]

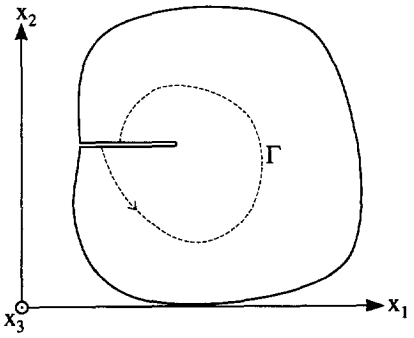

Fig. 4A.1 Cracked two-dimensional non-linear elastic body.

$$J = \int_{\Gamma} \left(W n_1 - T_i \frac{\partial u_i}{\partial x_1} \right) ds \qquad (4A.1)$$

where Γ = any contour surrounding the crack tip

W = strain-energy density, defined as $W(S_{mn}) = \int_0^{S_{mn}} T_{ij} dS_{ij}$

T_{ij} = stress tensor component

S_{ij} = strain tensor component

T_i = component of traction vector on Γ, i.e. $T_i = T_{ij} n_j$

u_i = displacement component

n_i = component of outward directed unit vector normal to Γ

s = arc length along Γ (positive when measured anticlockwise)

Integrating through linear elastic material

Using the infinitesimal forms of the strain and rotation tensors $\underline{S}$ and $\underline{\omega}$:

$$S_{ij} = \tfrac{1}{2}\left(\frac{\partial u_i}{\partial x_j} + \frac{\partial u_j}{\partial x_i} \right) \quad \text{and} \quad \omega_{ij} = \tfrac{1}{2}\left(\frac{\partial u_i}{\partial x_j} - \frac{\partial u_j}{\partial x_i} \right) \qquad (4A.2^{ab})$$

the integrand of J, denoted as I_J, can be rewritten as:

---

[1] In order to avoid confusion between components of the traction vector T_i and components of the stress tensor T_{ij}, the full index notation is used here instead of the Voigt notation.

$$I_J = n_1 \int_0^{S_{mn}} T_{ij} dS_{ij} - T_{ij} n_j (S_{i1} + \omega_{i1}) \tag{4A.3}$$

If the integration contour Γ is chosen in linear elastic material, the strain can be expressed in terms of stress components using the compliance constants s_{ijkl}:

$$S_{ij} = s_{ijkl} T_{kl} \tag{4A.4}$$

leading to:

$$I_J = \tfrac{1}{2} n_1 s_{ijkl} T_{ij} T_{kl} - T_{ij} n_j (s_{i1kl} T_{kl} + \omega_{i1}) \tag{4A.5}$$

From the two-dimensional nature of the problem, it follows that:

$$n_3 = 0 \qquad \text{and} \qquad \omega_{31} = S_{31} \tag{4A.6^{ab}}$$

and from the definition of the $\underline{\omega}$-tensor:

$$\omega_{11} = 0 \tag{4A.6^{c}}$$

Applying Equations 4A.6 to the integrand I_J yields:

$$\begin{aligned} I_J = n_1 T_{kl} (\tfrac{1}{2} s_{ijkl} T_{ij} - s_{i1kl} T_{i1} - s_{31kl} T_{31}) + \\ - n_2 T_{kl} (s_{i1kl} T_{i2} - s_{31kl} T_{32}) + \\ - \omega_{21} (T_{21} n_1 + T_{22} n_2) \end{aligned} \tag{4A.7}$$

In isotropic material the non-zero compliance constants are ($i \neq j$):

$$s_{iiii} = \frac{1}{E} \qquad s_{iijj} = \frac{-\nu}{E} \qquad s_{ijij} = s_{ijji} = \frac{1+\nu}{2E} \tag{4A.8^{abc}}$$

where E = Young's modulus
ν = Poisson's ratio

Substitution yields:

$$\begin{aligned} I_J = \frac{n_1}{E} \{ \tfrac{1}{2} (T_{22}^2 + T_{33}^2 - T_{11}^2) - \nu T_{22} T_{33} + (1+\nu)(T_{32}^2 - T_{31}^2) \} + \\ - \frac{n_2}{E} T_{21} (T_{11} + T_{22} - \nu T_{33}) + \\ - \omega_{21} (T_{21} n_1 + T_{22} n_2) \end{aligned} \tag{4A.9}$$

Assumption of a plane stress field, i.e. $T_{i3} = T_{3i} = 0$, leads to an expression for I_J in terms of stress components and the rotation component ω_{21}:

$$I_J = \frac{1}{E}\left\{ \tfrac{1}{2}(T_{22}^2 - T_{11}^2)n_1 - T_{21}(T_{11}+T_{22})n_2 \right\} - \omega_{21}(T_{21}n_1 + T_{22}n_2) \qquad (4A.10)$$

The term between brackets multiplying ω_{21} is equal to component T_2 of the traction vector. As the body is in equilibrium and T_2 is zero along the crack surfaces, this term should integrate to zero along Γ. Consequently a constant part of ω_{21} should not contribute to J and only the change of ω_{21} along Γ would need to be considered.

Determining the rotation component

Consider the rotation component ω_{21} as a function of x_1 and x_2. The change $d\omega_{21}$ between two neighbouring points can be written as [19]:

$$d\omega_{21} = \frac{\partial \omega_{21}}{\partial x_1} dx_1 + \frac{\partial \omega_{21}}{\partial x_2} dx_2 \qquad (4A.11)$$

Using:

$$\frac{\partial \omega_{21}}{\partial x_1} = \frac{\partial S_{21}}{\partial x_1} - \frac{\partial S_{11}}{\partial x_2} \quad \text{and} \quad \frac{\partial \omega_{21}}{\partial x_2} = -\frac{\partial S_{21}}{\partial x_2} + \frac{\partial S_{22}}{\partial x_1} \qquad (4A.12^{ab})$$

and again substituting stress components by means of the compliance tensor $\underline{s}$ leads to the following expression for the change $d\omega_{21}$ in the case of a plane stress state:

$$d\omega_{21} = \frac{1}{E}\left[\left\{ (1+\nu)\frac{\partial T_{21}}{\partial x_1} - \frac{\partial T_{11}}{\partial x_2} + \nu\frac{\partial T_{22}}{\partial x_2} \right\} dx_1 - \left\{ (1+\nu)\frac{\partial T_{21}}{\partial x_2} - \frac{\partial T_{22}}{\partial x_1} + \nu\frac{\partial T_{11}}{\partial x_1} \right\} dx_2 \right] \qquad (4A.13)$$

As stated above, calculating the rotation change would suffice to numerically integrate J. However, experimental errors in T_{22} and T_{21} will inevitably cause some dependence of J on the absolute rotation value. Accuracy will benefit if an estimate of the absolute rotation value is made. If the rotation ω_{21} is known at a point x_1°, x_2°, the rotation at an arbitrary point can be calculated according to:

$$\omega_{21}(x_1,x_2) = \omega_{21}(x_1^\circ,x_2^\circ) + \int_{x_1^\circ,x_2^\circ}^{x_1,x_2} d\omega_{21} \qquad (4A.14)$$

Chapter 5

A Model for the Pulse-Echo Method

5.1 Introduction

Chapter 3 contains an extensive description of an experimental technique for acoustoelastic stress measurements. Several factors which affect experimental accuracy were discussed in that chapter. The present chapter is concerned with developing a model for the pulse-echo method and using this model to calculate results for a number of relevant parameter sets. Part of the work presented in this chapter has been published in reference [30].

Objectives

Although a number of distorting effects have already been assessed experimentally, the outcome of model calculations is expected to provide additional information. The main incentive, however, is the fact that more insight is required into the pulse-echo technique based on a piezoelectric transducer. This is due to the particular emphasis placed on accuracy owing to the smallness of the acoustoelastic effect and the desire to obtain *absolute* time-of-flight data. Moreover, the technique proposed in Chapter 3 uses a relatively thick and dispersive coupling layer, a situation which clearly differs from normal practice. The consequences of this with regard to the pulse-echo measurement need to be evaluated. One of the objectives is therefore also to compare the use of thick coupling layers with that of thin layers.

Summarized, the objectives of the work presented in this chapter are to analyse the effect of:

- diffraction in the specimen
- the coupling layer
- electrical settings

on time-of-flight measurements and of:

- transducer misalignment

on both time-of-flight and polarization measurements.

Approach

The model will not refer exactly to the set-up described in Chapter 3. One of the reasons for this is that the properties of the electronic circuitry, the transducer and the coupling fluid are only partly known. It is believed, however, that the approximate model presented here is

adequate as far as the specified objectives are concerned. Consequently the results of the calculations need not be limited to this specific set-up, but may apply to a whole range of pulse-echo configurations, depending on the parameters used.

A simple one-dimensional model is adopted for the piezoelectric transducer. The model may represent either a shear or a longitudinal transducer type.[1] The model transducer is either driven by a voltage source with a given impedance or terminated by this impedance, depending on whether the transducer is transmitting or receiving. The couplant is added to the one-dimensional model as an extra layer. The ultrasonic properties of the fluid, which are essential to the calculation, are based on experimental results. Diffraction in the specimen is also taken into account; it is treated separately, as it requires a three-dimensional approach.

Calculations are performed using two different models. The first one is for a perfectly aligned circular transducer, in which rotation symmetry is used to advantage. In the second a tilted transducer is simulated by dividing the circular transducer into a number of strip-shaped subtransducers electrically connected in parallel. These subtransducers are coupled to the specimen through layers with varying thicknesses.

[1] Developing a model for a combined shear-longitudinal transducer would complicate matters significantly.

5.2 Description

As mentioned in the introduction, the calculation is divided into two parts, namely (i) a one-dimensional model covering pulser-receiver, transducer and coupling layer and (ii) a model for diffraction in the specimen. This division is not coincidental, but is dictated by the nature of the problem. The elements which make up the first part must be solved simultaneously, since the properties of each influence the behaviour of the others. This is not the case for diffraction in the specimen, which in principle can be considered as a system with an independent input and output. In spite of this the pulser, transducer and coupling layer are first discussed separately and are not combined till later to form one system with a single input and output. This approach will prove more suitable for dealing with a tilted transducer.

Developing a model for the pulser-receiver/transducer/couplant combination could mean numerically solving a set of differential equations thus interrelating the various electrical and mechanical quantities and their time derivatives. However, such an approach in the time domain would significantly complicate the treatment of the viscous couplant, in view of its frequency-dependent properties.[1] For this reason, and also because it is more convenient, all calculations will be performed in the frequency domain, using the *Fourier transform* (Appendix 5A). Time-varying quantities such as wave stresses, voltages and currents will be considered as complex functions of frequency, with modulus and argument representing their amplitude and phase respectively.

At this point it is important to define the nature of the *systems* to which the calculation will be applied. In this context a system is considered to be any element, which transforms an input signal to an output signal. Simple examples in the electrical area are resistors and capacitors, where voltage and current are the input and output signals or vice versa. Mechanical examples are (i) the constitutive behaviour of a material, with stress and strain as the input and output, and (ii) wave propagation, where the wave introduced into a medium is the input and the wave delayed and attenuated after propagation is the output.

It is now assumed that the input signals $s_1(t)$ and $s_1'(t)$ cause the responses $s_2(t)$ and $s_2'(t)$ respectively, all being functions of time t. The systems considered here are said to be:

- *Linear*, in the sense that an input signal $s_1(t) + s_1'(t)$ causes a response $s_2(t) + s_2'(t)$ for any $s_1(t)$ and $s_1'(t)$.
- *Time-invariant*, in the sense that an input signal $s_1(t + \tau)$ causes a response $s_2(t + \tau)$ for any $s_1(t)$ and τ.

[1] Similarly the diffraction calculation cannot be performed in the time domain, but this would not present any problems, as this part of the calculation can be treated separately.

It is possible to describe the response for these systems in the frequency domain [5, 10]. More specifically, given a harmonic input signal with angular frequency ω:

$$s_1(t) = e^{i\omega t} \tag{5.1}$$

the response can always be written in the form:

$$s_2(t) = H(\omega)e^{i\omega t} \tag{5.2}$$

where $H(\omega)$ = frequency response or *transfer function* of the system

Thus, the response of a linear and time-invariant system is again a harmonic signal with the same frequency. The transfer function $H(\omega)$, defined in Eq. 5.2, is a complex function of frequency. Its modulus is the ratio of the input and output signal amplitudes, and its argument is the phase difference between these signals.

In short, the calculations involve the evaluation of a number of transfer functions for the pulser-receiver/transducer/coupling combination and for the diffraction phenomenon. Using the waveform generated by the pulser, the waveforms received in a pulse-echo configuration are then determined.

5.2.1 Pulser-receiver

The model for the pulser-receiver will not be based on the electronic circuitry which was schematically shown in Figure 3.19. The reason is the presence of a *thyristor* in the pulser part, a device which has a response which is far from linear. It is possible, however, to create a model for the pulser in the time domain, although calculation based on such a model cannot be coupled to the calculations for the transducer and coupling layer, as these are performed in the frequency domain.

The pulser output shown in Figure 3.20 in fact results from calculations in the time domain.[1], The model is therefore reduced to a simple voltage source V_s with an impedance Z_s equal to that of the damping resistor (see Fig. 5.1). For the voltage delivered by this source the results of time-domain calculations are used. It is believed that this approach has little effect on the ultimate result, as the thyristor will become non-conductive very soon (10 ns) after the start of the pulse. From that point in time the output impedance of the pulser is equal to the damping resistance. The actual voltage across the electrodes of the transducer, V_e, now simply depends on the current I_e through

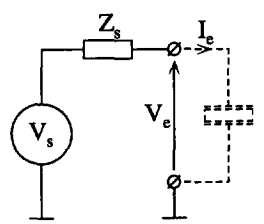

Fig. 5.1 Simplified pulser model.

[1] The results of these calculation agree with the manufacturer's specifications.

these electrodes, according to the relation:

$$V_e = V_s - Z_s I_e \tag{5.3}$$

As far as the receiver part is concerned, the same model applies, except that the source voltage V_s is assumed to be zero. Consequently the transducer is simply terminated by the damping resistor Z_s.

It is beyond the scope of this work to go into detail regarding the calculation of the time-domain model for the pulser. The result, however, is in the form of a series of N real numbers representing the pulser voltage V_s at equidistant times, with a time interval Δt between consecutive values. The *discrete Fourier transform* (Appendix 5A) is applied to this pulse, leading to a series of complex numbers.[1] They are the amplitude and phase at a series of equidistant frequencies ω_n, ranging from zero to the *Nyquist critical frequency*, i.e.:

$$\omega_n = \frac{2\pi n}{N\Delta t} \quad \ldots\ldots\ldots\ldots \text{ for } n = 0..N/2 \tag{5.4}$$

These frequency-domain pulse data form the input for further calculations carried out at the frequencies ω_n.

5.2.2 Transducer

The transducer model

Figure 5.2 shows the model used for the piezoelectric ultrasonic transducer. At the heart of the transducer is a thin plate of piezoelectric material (p). Conductive layers on both flat surfaces form the transducer electrodes. These are assumed to be so thin that it is possible to neglect any influence on the propagation of elastic waves through them. The piezoelectric plate is sandwiched between a *backing medium* (b) on one side, which partly determines the transducer characteristic, and a *protective layer* (l) on the other. An acoustic *coupling medium* (c) is adjacent to the protective layer.

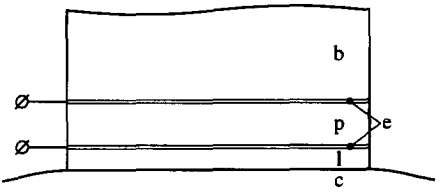

Fig. 5.2 Transducer model with piezoelectric plate (p), electrodes (e), backing medium (b), protective layer (l) and coupling (c).

The *excitation* and *detection* of plane waves in a piezoelectric plate surrounded by two

[1] A Fast Fourier Transform algorithm (FFT) is in fact used, which requires that N should be an integer power of 2. If needed, therefore, an adequate number of zeros are added to the original pulse data.

non-piezoelectric media is extensively treated in Appendix 5B. A one-dimensional approach is used, i.e. all relevant quantities are assumed to be independent of coordinates in the plane of the plate. Such an assumption is permitted only if the plate thickness is small relative to its other dimensions [1]. It means that only *plane waves* travelling in the plate thickness direction are considered.

Furthermore, the equations derived are the result of a simplified analysis. The simplification implies an electromechanical coupling involving only a single wave component. Defined on a set of coordinate axes x_i with the x_3-axis parallel to the plate thickness, this coupling is signified by components e_{3i3} of the 3rd-order *piezoelectric stress tensor* $\underline{e}$. These components form a vector parallel to the polarization direction of the coupled plane wave, the length of which will be concisely denoted by the scalar *piezoelectric stress constant* e (Eq. 5B.16).

Finally, it is assumed that plane waves with the same polarization direction as the coupled wave can propagate through the media adjacent to the piezoelectric plate. For one thing, this means that no wave conversions occur during reflection and transmission at interfaces. Stresses associated with plane waves in the transducer can now be denoted by scalar quantities, as they are equivalent to traction forces acting on planes normal to the plate thickness, forces which always point in the same direction.

It will be assumed in the transducer model that waves propagating into the backing medium will not return, either because reflections do not arrive within the time frame used for the calculations or because they are too greatly attenuated. Therefore, waves in this medium are not considered at all.

As far as the protective layer is concerned, it should be noted that the assumption made concerning the thinness of the piezoelectric plate also applies here. Diffraction effects could otherwise become important, and the one-dimensional description would no longer be appropriate.

Plane waves in the layered structure

The relevant mechanical waves which propagate through the different layers in the transducer are indicated in Figure 5.3. An arrow expresses the wave propagation direction, while a point is used to mark the location for which the stress amplitude is defined. The arrows without a point indicate traction forces between layers, e.g. W_{lc} is the traction force exerted by the protective layer onto the couplant.

The various plane waves and traction forces must be related to each other. These relations are derived by considering wave propagation through the layers and reflection and transmission at the interfaces. The propagation delay to which a plane wave is subject when a

layer is traversed will be described using a *transfer function*.[I] For layer x with thickness d_x and a propagating wave with wave number k_x the transfer function H_x is defined as:

$$H_x = e^{-ik_x d_x} \tag{5.5}$$

Through k, this quantity is a complex function of frequency. It should be noted that plane wave propagation in the piezoelectric plate is described by means of the *stiffened* Christoffel tensor (Eq. 5B.11), i.e. the influence of electromechanical coupling is taken into account.

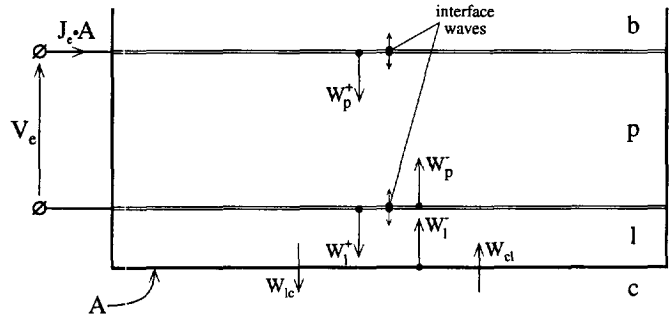

Fig. 5.3 Relevant electric and acoustic quantities in the transducer calculation.

Reflection and transmission of plane waves at the interfaces between the various layers is described using the usual coefficients (Appendix 3B). It should be noted that the reflection and transmission coefficients at the interface between the protective layer and the couplant are complex quantities. The reason for this is that the couplant will be considered as an attenuating medium in which the specific wave impedance is therefore complex (see Appendix 5C).

Excitation and detection of plane waves

Plane waves, indicated as *interface waves* in Figure 5.3, are excited at each of the two interfaces of the piezoelectric plate. They travel into the plate and the neighbouring medium with amplitudes proportional to the *electrode current density* J_e, which is the electrode current I_e per unit transducer area A. As formulated in Equations 5B.25 and 5B.26, the wave amplitudes are equal to:

$$W = -i\frac{Z}{Z+Z'}\frac{e}{\omega\varepsilon^S}J_e \tag{5.6}$$

$$W' = +i\frac{Z'}{Z+Z'}\frac{e}{\omega\varepsilon^S}J_e \tag{5.7}$$

[I] Wave attenuation is neglected in the materials forming the transducer.

where W, Z = stress amplitude and specific impedance of the plane wave travelling into the piezoelectric plate

W', Z' = stress amplitude and specific impedance of the plane wave travelling into the adjacent non-piezoelectric medium

e = piezoelectric stress constant for the plate material

ω = angular frequency

ε^S = permittivity constant for the plate material, i.e. ε_{33}^S

The detection of plane waves is described in Equation 5B.30, which reads:

$$J_e = \frac{i\omega\varepsilon^S}{d_p} V_e + \frac{e(1-H_p)}{d_p Z_p}(W_p^+ + W_p^-) \tag{5.8}$$

where V_e = voltage across electrodes

d_p = plate thickness

H_p = transfer function plate layer

W_p^+, W_p^- = stress amplitudes of plane waves travelling in the plate in positive and negative thickness directions respectively

The transducer solution

The solution sought for the transducer model relates the electrical quantities, i.e. the electrode voltage V_e and the current density J_e, to the traction forces, W_{lc} and W_{cl}, which are exerted on and by the coupling layer. In order to obtain this solution, the set of equations describing the whole model must be solved simultaneously. These equations relate all waves, using the appropriate reflection and transmission coefficients and layer transfer functions. The waves induced electrically at the plate interfaces must also be taken into account, as also the effect which the waves travelling in the plate have on the electrical conditions. The complete set of equations is:

$$J_e = \frac{i\omega\varepsilon^S}{d_p} V_e + \frac{e(1-H_p)}{d_p Z_p}(W_p^+ + W_p^-)$$

$$W_p^+ = H_p R_{pb} W_p^- \qquad - \frac{iZ_p}{Z_p+Z_b}\frac{e}{\omega\varepsilon^S} J_e$$

$$W_p^- = H_p R_{pl} W_p^+ + H_l T_{lp} W_l^- \qquad - \frac{iZ_p}{Z_p+Z_l}\frac{e}{\omega\varepsilon^S} J_e$$

$$W_l^+ = H_l R_{lp} W_l^- + H_p T_{pl} W_p^+ \qquad + \frac{iZ_l}{Z_l+Z_p}\frac{e}{\omega\varepsilon^S} J_e$$

$$W_l^- = H_l R_{lc} W_l^+ \qquad + W_{cl}$$

$$W_{lc} = H_l T_{lc} W_l^+ \tag{5.9}$$

It is convenient to write this set of equations in matrix notation:

$$\begin{bmatrix} \frac{-i\omega\varepsilon^S}{d_p} & 1 & \frac{e(H_p-1)}{d_p Z_p} & \frac{e(H_p-1)}{d_p Z_p} & 0 & 0 \\ 0 & \frac{iZ_p}{Z_p+Z_b}\frac{e}{\omega\varepsilon^S} & 1 & -H_p R_{pb} & 0 & 0 \\ 0 & \frac{iZ_p}{Z_p+Z_l}\frac{e}{\omega\varepsilon^S} & -H_p R_{pl} & 1 & 0 & -H_l T_{lp} \\ 0 & \frac{-iZ_l}{Z_l+Z_p}\frac{e}{\omega\varepsilon^S} & -H_p T_{pl} & 0 & 1 & -H_l R_{lp} \\ 0 & 0 & 0 & 0 & +H_l T_{lc} & 0 \\ 0 & 0 & 0 & 0 & -H_l R_{lc} & 1 \end{bmatrix} \begin{bmatrix} V_e \\ J_e \\ W_p^+ \\ W_p^- \\ W_l^+ \\ W_l^- \end{bmatrix} = \begin{bmatrix} 0 \\ 0 \\ 0 \\ 0 \\ W_{lc} \\ W_{cl} \end{bmatrix} \tag{5.10}$$

Denoting element ij of the *inverted* matrix as A_{ij}, the desired solution can be written as:

$$\begin{bmatrix} V_e \\ J_e \end{bmatrix} = \begin{bmatrix} A_{15} & A_{16} \\ A_{25} & A_{26} \end{bmatrix} \begin{bmatrix} W_{lc} \\ W_{cl} \end{bmatrix} \tag{5.11}$$

5.2.3 Coupling layer

It should first be noted that the thickness of the coupling layer is assumed to be small relative to its other dimensions. This assumption must be made in order to be able to use a one-dimensional approach, as was the case for the piezoelectric plate and protective layer of the transducer.

Wave propagation in viscous fluid

The constitutive behaviour of a viscous fluid such as the shear wave couplant can be expected to depend on frequency. The propagation of waves through this medium therefore requires a separate treatment. In Appendix 5C a medium is considered with a frequency-dependent complex stiffness tensor $\underline{\tilde{C}}$ relating a harmonically varying stress tensor to a harmonically varying strain tensor. Assuming an attenuated plane wave solution, an alternative Christoffel equation is derived (Eq. 5C.6). The complex eigenvalues of this Christoffel tensor are not only a measure of the phase velocity ω/k, but also of the attenuation coefficient α.

The transfer function for the coupling layer now takes the form of:

$$H_c = e^{-i(k_c - i\alpha_c)d_c} \tag{5.12}$$

where k_c, α_c = wave number and attenuation coefficient of a plane wave in the couplant

d_c = coupling layer thickness

The coupling solution

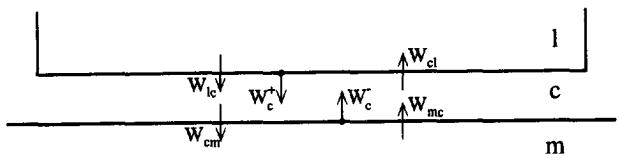

Fig. 5.4 Waves and traction forces relevant to the coupling layer (c), which is sandwiched between the protective layer of the transducer (l) and the propagation medium (m).

The waves travelling in positive and negative thickness directions through the coupling layer and the traction forces acting on the two interfaces are indicated in Figure 5.4. The aim is to establish a relation between the four traction forces, using the transfer function H_c and the various reflection and transmission coefficients. Owing to the attenuating nature of the couplant, these coefficients will be complex. The available equations are:

$$\begin{aligned} W_c^+ &= H_c R_{cl} W_c^- + W_{lc} \\ W_{cl} &= H_c T_{cl} W_c^- \\ W_{cm} &= H_c T_{cm} W_c^+ \\ W_c^- &= H_c R_{cm} W_c^+ + W_{mc} \end{aligned} \tag{5.13}$$

or in matrix notation:

$$\begin{bmatrix} 1 & 0 & -1 & +H_cR_{cl} \\ 0 & 1 & 0 & -H_cT_{cl} \\ 0 & 0 & +H_cT_{cm} & 0 \\ 0 & 0 & -H_cR_{cm} & 1 \end{bmatrix} \begin{bmatrix} W_{lc} \\ W_{cl} \\ W_c^+ \\ W_c^- \end{bmatrix} = \begin{bmatrix} 0 \\ 0 \\ W_{cm} \\ W_{mc} \end{bmatrix} \tag{5.14}$$

Denoting element ij of the *inverted* matrix as B_{ij}, it follows that:

$$\begin{bmatrix} W_{lc} \\ W_{cl} \end{bmatrix} = \begin{bmatrix} B_{13} & B_{14} \\ B_{23} & B_{24} \end{bmatrix} \begin{bmatrix} W_{cm} \\ W_{mc} \end{bmatrix} \tag{5.15}$$

5.2.4 Operation of a coupled transducer

The problem of a transducer connected to a pulser-receiver and acoustically coupled to a propagation medium will be completely solved by combining the separately derived solutions for pulser-receiver, transducer and coupling layer. At this point it is convenient to define the stress amplitudes of the waves *transmitted* into and *received* from the propagation medium as W_t the W_r, according to (see also Fig. 5.4):

$$W_t = W_{cm} + R_{mc} W_r \tag{5.16}$$

$$W_r = \frac{W_{mc}}{T_{mc}} \tag{5.17}$$

Three situations are considered, namely the cases of a:

- Transmitting transducer
  The received wave amplitude is assumed to be zero and a *transfer coefficient* is derived between the source voltage, delivered by the pulser, and the amplitude of the transmitted wave.
- Receiving transducer
  For a zero source voltage a transfer coefficient is determined between the amplitude of the received wave and the transducer electrode voltage.
- Reflecting transducer
  Again for a zero source voltage, the amplitude of the re-transmitted wave is expressed in terms of the received wave amplitude.

As mentioned in the introduction, two different cases are considered, namely that of a perfectly aligned and that of a slightly tilted transducer. The solutions derived so far apply to both, but they will be combined differently. It should be noted that the transducer is assumed to be circular in shape.

A perfectly aligned transducer

The configuration of transducer and coupling layer is now described by combining their respective solutions (Eqs. 5.11 and 5.15). Simultaneously the traction forces at the interface between couplant and propagation medium, W_{cm} and W_{mc}, are expressed in terms of the

transmitted and received wave amplitudes W_t and W_r:

$$\begin{bmatrix} V_e \\ J_e \end{bmatrix} = \begin{bmatrix} C_{11} & C_{12} \\ C_{21} & C_{22} \end{bmatrix} \begin{bmatrix} W_t \\ W_r \end{bmatrix} \tag{5.18}$$

$$\text{where} \begin{bmatrix} C_{11} & C_{12} \\ C_{21} & C_{22} \end{bmatrix} = \begin{bmatrix} A_{15} & A_{16} \\ A_{25} & A_{26} \end{bmatrix} \begin{bmatrix} B_{13} & B_{14} \\ B_{23} & B_{24} \end{bmatrix} \begin{bmatrix} 1 & -R_{mc} \\ 0 & T_{mc} \end{bmatrix}$$

Using the relation between electrode voltage V_e and current I_e, resulting from the pulser-receiver model (Eq. 5.3), and writing the current I_e as the product of the transducer area A and electrode current density J_e, it follows that:

$$\begin{bmatrix} 1 & Z_sA & 0 \\ \frac{1}{C_{12}} & 0 & \frac{-C_{11}}{C_{12}} \\ 0 & \frac{1}{C_{22}} & \frac{-C_{21}}{C_{22}} \end{bmatrix} \begin{bmatrix} V_e \\ J_e \\ W_t \end{bmatrix} = \begin{bmatrix} V_s \\ W_r \\ W_r \end{bmatrix} \tag{5.19}$$

The solution to this set of equations expresses the electrical conditions at the transducer electrodes and the transmitted mechanical wave as a function of the source voltage of the pulser and the received mechanical wave. Element ij of the *inverted* matrix will be denoted as D_{ij}.

Transmitting transducer

By setting the received wave amplitude W_r to zero, the wave amplitude W_t of a transmitting transducer can be expressed in terms of the source voltage V_s through the following transfer coefficient:

$$\left(\frac{W_t}{V_s}\right)_{W_r=0} = D_{31} = \frac{1}{C_{11}+Z_sAC_{21}} \tag{5.20}$$

The transducer/coupling solution is based on a one-dimensional model. Consequently the transmitted wave has the same amplitude over the whole of the transducer area. This may be considered a reasonable description of reality.

Receiving transducer

For a zero source voltage V_s the transfer coefficient between the received wave amplitude W_r

and the electrode voltage V_e of a receiving transducer is:

$$\left(\frac{V_e}{W_r}\right)_{V_s=0} = D_{12} + D_{13} \tag{5.21}$$

Strictly speaking this equation is valid only if the received wave amplitude W_r is constant over the transducer area. However, due to diffraction effects in the specimen, this cannot be expected. For a receiving transducer this problem is approached by imagining that the transducer is divided into a number of *subtransducers*. These are electrically connected in parallel and each receives a slightly different wave amplitude.[1] The electrode current density in a subtransducer is proportional to the local received amplitude (Eq. 5.11). In turn the electrode voltage V_e, common to all subtransducers, is a function of the total electrode current I_e (Eq. 5.3) and thus of the average current density. Therefore, in order to include the case of received waves with varying amplitude, the transfer coefficient is described in terms of the *average* received wave amplitude $\overline{W}_r$:

$$\left(\frac{V_e}{\overline{W}_r}\right)_{V_s=0} = D_{12} + D_{13} = \frac{Z_s A(C_{12}C_{21} - C_{11}C_{22})}{C_{11} + Z_s A C_{21}} \tag{5.22}$$

where $\overline{W}_r = \frac{1}{A}\int_A W_r dA$

Reflecting transducer

The wave W_t, which is re-transmitted when a wave W_r is received, follows from the setting of V_s to zero in Equation 5.19. Following the argumentation used above average wave amplitudes can be used:

$$\left(\frac{\overline{W}_t}{\overline{W}_r}\right)_{V_s=0} = D_{32} + D_{33} = -\frac{C_{12} + Z_s A C_{22}}{C_{11} + Z_s A C_{21}} \tag{5.23}$$

However, the *local* amplitude of the re-transmitted wave is not defined by this relation. Using the transducer/coupling solution (Eq. 5.18), this amplitude can be written as:

$$W_t = \frac{1}{C_{11}} V_e - \frac{C_{12}}{C_{11}} W_r \tag{5.24}$$

[1] In order for the one-dimensional approach to remain applicable, it is required that the size of the subtransducers is large compared with the thickness of the piezoelectric plate, protective layer and coupling layer. Consequently it must be assumed that significant changes in the received wave amplitude occur only over distances which are large relative to these thicknesses.

The first term in this equation is constant throughout the transducer area and can be considered to be the amplitude of a transmitted wave which is induced by electrode voltage V_e, which in turn depends on the average received wave amplitude (Eq. 5.22). This is described by the transfer coefficient:

$$\left(\frac{W_t}{V_e}\right)_{W_r=0} = \frac{1}{C_{11}} \tag{5.25}$$

The second term depends on the local received amplitude and thus has the characteristics of a wave component which is simply reflected, with a *reflection coefficient* equal to:

$$\left(\frac{W_t}{W_r}\right)_{V_e=0} = -\frac{C_{12}}{C_{11}} \tag{5.26}$$

A slightly tilted transducer

In the case of a tilted transducer the coupling layer has a varying thickness over the transducer surface. As a consequence of this it is no longer possible to use the one-dimensional approach, in which all relevant quantities are assumed independent of the coordinate in the plane of the piezoelectric disc.

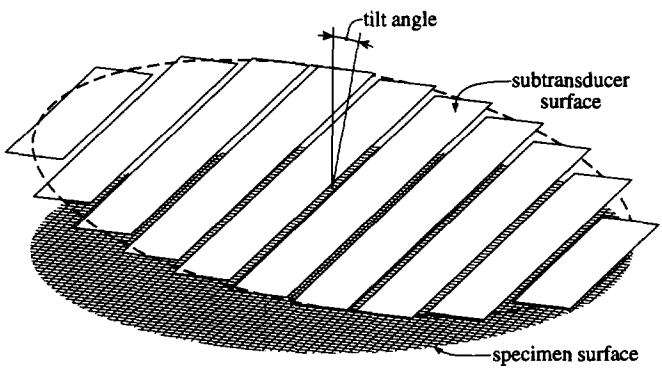

Fig. 5.5 The division of a tilted circular transducer into a number of strip-shaped subtransducers.

What was only an exercise of the imagination when describing a receiving transducer will be actually implemented in the model of a *slightly tilted* transducer, resulting in the division of the circular transducer into a number of subtransducers. As shown in Figure 5.5, they are strip-shaped and orientated perpendicular to the plane through the transducer normal and the normal on the surface of the propagation medium. The surfaces of the subtransducers are assumed to be parallel to that of the propagation medium. Using this model, the one-dimensional calculation can still be applied to each subtransducer separately. As mentioned

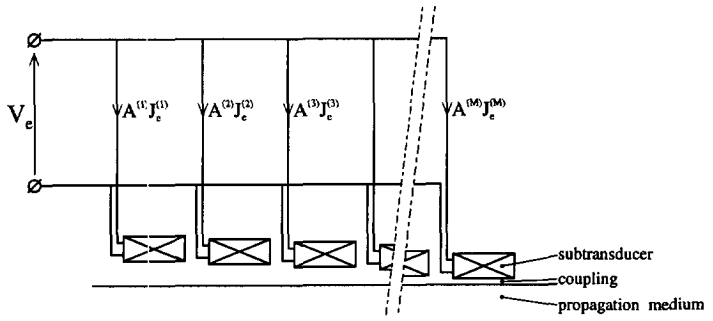

Fig. 5.6 Schematic representation of the tilted transducer model with M subtransducers electrically connected in parallel and acoustically coupled to a propagation medium through layers with varying thicknesses.

before (see Footnote I on p. 133), it must be assumed that the in-plane dimensions of each subtransducer remain large compared with the thicknesses of the various layers.

Figure 5.6 shows a schematic representation of the tilted transducer model using M subtransducers electrically connected in parallel. The relevant electrical quantities are indicated, i.e. the common electrode voltage V_e and the individual electrode currents, equal to the product of the electrode areas $A^{(m)}$ and electrode current densities $J_e^{(m)}$, with m ranging from 1 to M. For the m^{th} subtransducer with its corresponding coupling layer, the relation between the relevant electrical and mechanical quantities is written in the form of:

$$\begin{bmatrix} V_e \\ J_e^{(m)} \end{bmatrix} = \begin{bmatrix} C_{11}^{(m)} & C_{12}^{(m)} \\ C_{21}^{(m)} & C_{22}^{(m)} \end{bmatrix} \begin{bmatrix} W_t^{(m)} \\ W_r^{(m)} \end{bmatrix} \tag{5.27}$$

Matrix elements $C_{ij}^{(m)}$ are derived as in Equation 5.18. The transducer solution (Eq. 5.11) is common to all subtransducers and thus only needs to be evaluated once.

The relation between the electrode voltage V_e and the total electrode current I_e, resulting from the pulser-receiver model (Eq. 5.3), takes the form of:

$$V_e = V_s - Z_s\left(A^{(1)}J_e^{(1)} + A^{(2)}J_e^{(2)} + \cdots + A^{(M)}J_e^{(M)}\right) \tag{5.28}$$

A set of 2M+1 equations can now be formulated. It expresses all electrical quantities and the amplitudes of the waves which are transmitted by each subtransducer into the propagation medium as a function of the source voltage of the pulser and the amplitudes of the waves received by each subtransducer:

$$\begin{bmatrix} 1 & Z_s A^{(1)} & Z_s A^{(2)} & Z_s A^{(3)} & \cdots & Z_s A^{(M)} & 0 & \cdots & 0 \\ \frac{1}{C_{12}^{(1)}} & 0 & \cdots & 0 & -\frac{C_{11}^{(1)}}{C_{12}^{(1)}} & 0 & \cdots & 0 \\ 0 & \frac{1}{C_{22}^{(1)}} & 0 & \cdots & 0 & -\frac{C_{21}^{(1)}}{C_{22}^{(1)}} & 0 & \cdots & 0 \\ \frac{1}{C_{12}^{(2)}} & 0 & \cdots & 0 & 0 & -\frac{C_{11}^{(2)}}{C_{12}^{(2)}} & 0 & \cdots & 0 \\ 0 & 0 & \frac{1}{C_{22}^{(2)}} & 0 & \cdots & 0 & 0 & -\frac{C_{21}^{(2)}}{C_{22}^{(2)}} & 0 & \cdots & 0 \\ \vdots & & & & & & & & & & \vdots \\ \frac{1}{C_{12}^{(M)}} & 0 & \cdots & 0 & 0 & \cdots & 0 & -\frac{C_{11}^{(M)}}{C_{12}^{(M)}} \\ 0 & \cdots & 0 & \frac{1}{C_{22}^{(M)}} & 0 & \cdots & 0 & -\frac{C_{21}^{(M)}}{C_{22}^{(M)}} \end{bmatrix} \begin{bmatrix} V_e \\ J_e^{(1)} \\ J_e^{(2)} \\ \vdots \\ J_e^{(M)} \\ W_t^{(1)} \\ W_t^{(2)} \\ \vdots \\ W_t^{(M)} \end{bmatrix} = \begin{bmatrix} V_s \\ W_r^{(1)} \\ W_r^{(1)} \\ W_r^{(2)} \\ W_r^{(2)} \\ \vdots \\ W_r^{(M)} \\ W_r^{(M)} \end{bmatrix} \quad (5.29)$$

Element ij of the *inverted* matrix will be denoted as D_{ij}.

Transmitting transducer

The transfer coefficient between the source voltage V_s and the amplitude $W_t^{(m)}$ of the wave transmitted by the m^{th} subtransducer can be found by assuming that none of the subtransducers is receiving a wave. Thus:

$$\left(\frac{W_t^{(m)}}{V_s}\right)_{W_r^{(n)}=0} = D_{(M+m)(1)} \cdots \text{for } n = 1..M \quad (5.30)$$

Receiving transducer

The transfer coefficient between the amplitude $W_r^{(m)}$ received by the m^{th} subtransducer and the resulting electrode voltage V_e is found by setting V_s and all wave amplitudes received by the other subtransducers to zero. Based on the same arguments as used for the aligned transducer, the received wave amplitude is averaged, in this case over the area of the subtransducer. Denoting this average amplitude as $\overline{W}_r^{(m)}$, the coefficient becomes:

$$\left(\frac{V_e}{\overline{W}_r^{(m)}}\right)_{V_s=0;\overline{W}_r^{(n)}=0} = D_{(1)(2m)} + D_{(1)(2m+1)} \cdots \text{for } n = 1..M \text{ and } n \neq m \quad (5.31)$$

The electrode voltage V_e, which results when all subtransducers connected in parallel are receiving waves, follows from the inverse of Equation 5.29, i.e. it is obtained by simply adding all individual contributions.

Reflecting transducer

Analogous to the discussion for the aligned transducer, the amplitude of a wave re-transmitted by the m^{th} receiving subtransducer is expressed in terms of the electrode voltage V_e, which is induced by the waves received by the transducer as a whole. The transfer coefficient reads:

$$\left(\frac{W_t^{(m)}}{V_e}\right)_{W_r^{(m)}=0} = \frac{1}{C_{11}^{(m)}} \tag{5.32}$$

The reflection of waves received by the m^{th} subtransducer is described in terms of a reflection coefficient:

$$\left(\frac{W_t^{(m)}}{W_r^{(m)}}\right)_{V_e=0} = -\frac{C_{12}^{(m)}}{C_{11}^{(m)}} \tag{5.33}$$

5.2.5 Diffraction in the specimen

Waves emitted into a specimen by an ultrasonic transducer cannot be considered as homogeneous plane waves. The reason for this is that the transducer has finite dimensions and that consequently the phenomenon of *diffraction* will occur. This can be expected to affect the shape of the wave pulse and therefore also the result of time-of-flight measurements.

In the following a relation is derived between the wave amplitude transmitted into the specimen and the amplitude received after the plate-shaped specimen has been traversed a number of times. As the latter amplitude varies over the area of the receiving (sub-)transducer, it will be averaged. The final result, therefore, is in the form of a transfer function between transmitted and averaged received amplitudes and can be used directly as a link between the corresponding transducer calculations.

First the diffraction itself is described, after which the calculation is discussed for the cases of a perfectly aligned transducer and one which is slightly tilted.

The Kirchhoff diffraction theory

The basis for the Kirchhoff diffraction theory is the *Helmholtz-Kirchhoff integral theorem* [12]. Consider a volume in which a point P is located and which is completely enclosed by a surface S. A time-harmonic *scalar* wave is assumed to be present, generated outside the enclosed volume and with a complex amplitude field $A = A(\underline{x})$.[1] The theorem reads:

[1] The amplitude of such a wave is a scalar quantity, as is, for example, the pressure of compressional waves in gases or non-viscous fluids.

$$A(P) = -\frac{1}{4\pi}\int_S \left\{ A\,\nabla\left(\frac{1}{r}e^{-ikr}\right) - \left(\frac{1}{r}e^{-ikr}\right)\nabla A \right\} \cdot \underline{n}\, dS \tag{5.34}$$

where r = distance from point P to surface element dS

$\underline{n}$ = outwards-directed unit normal on element dS

This equation relates the wave amplitude at point P to the amplitude A and its normal derivative $\underline{n}\cdot\nabla A$ on the surface S.

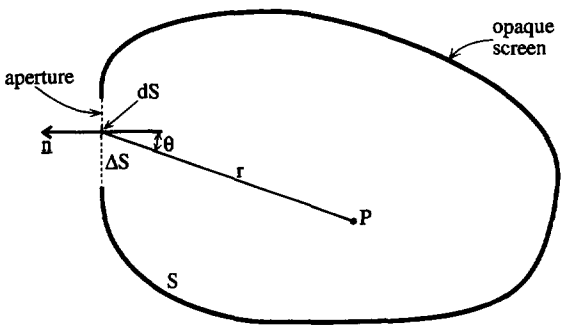

Fig. 5.7 Opaque screen with aperture, used to derive the Fresnel-Kirchhoff diffraction formula

As illustrated by Figure 5.7, the surface S enclosing point P is now chosen to coincide with an opaque screen in which an aperture is present. It is assumed that at the aperture the amplitude of the wave emanating from some source outside S is unaffected by the presence of the screen. At the screen itself, due to its opaqueness, both amplitude and normal derivative are assumed to vanish. These assumptions originate from geometrical optics[I] and are called the *Kirchhoff boundary conditions.*

In this specific case a flat aperture is considered, and for the externally generated wavefield a plane wave is chosen with wave number k, propagating in the direction opposite to the unit normal $\underline{n}$ at the aperture. Denoting its amplitude at the aperture as A_o, the boundary conditions become:

$$A = A_o \quad \text{and} \quad \underline{n}\cdot\nabla A = ikA_o \ldots\ldots\ldots\ldots \text{at the aperture} \tag{5.35}$$

$$A = \underline{n}\cdot\nabla A = 0 \ldots\ldots\ldots\ldots \text{at the screen} \tag{5.36}$$

Using the integral theorem the wave amplitude at P can now be calculated as:

[I] In the geometrical optics model the wavelength is assumed to be small compared with any other dimension. Waves are considered to propagate along *rays*, which are straight lines in a homogeneous medium.

$$A(P) = -\frac{1}{4\pi}\int_{\Delta S}\left\{ A_o\left(-\frac{1}{r}-ik\right)\frac{1}{r}e^{-ikr}\cos\theta - \frac{1}{r}e^{-ikr}ikA_o \right\} dS =$$

$$= \frac{1}{4\pi}A_o\int_{\Delta S}\left\{ \left(\frac{1}{r}+ik\right)\cos\theta + ik \right\}\frac{e^{-ikr}}{r}dS \qquad (5.37)$$

where θ = angle between the aperture normal and the ray to P

ΔS = aperture area

For points P at distances r much larger than the wavelength, i.e. $^1/_r \ll k$, the *Fresnel-Kirchhoff diffraction formula* is obtained, which for this case reads:

$$A(P) = \frac{ik}{2\pi}A_o\int_{\Delta S}{}^1/_2(\cos\theta + 1)\frac{e^{-ikr}}{r}dS \qquad (5.38)$$

The amplitude at P is found to be proportional to $^1/_r$ and to the so-called *obliquity factor* $^1/_2(\cos\theta + 1)$, which introduces a dependence on the inclination angle θ. It is also important to note that a phase advance of 90° is introduced in the diffracted wave.

In order for the diffraction formula to be a good approximation, all dimensions, such as aperture size and distance r, should be large compared with the wavelength. Furthermore, strictly speaking the formula is only valid for scalar waves. However, it can be argued [12] that if the different wave rays travelling from the aperture to point P make only a small angle relative to the aperture normal (< 10 to 15°), the formula will also provide a good description for vector waves, such as longitudinal or shear waves in a solid.

Arc diffraction

In order to treat wave diffraction for a perfectly aligned transducer, the Kirchhoff diffraction formula (Eq. 5.38) is applied to a *circular* aperture coinciding with the area of a transmitting transducer. First the transfer function is calculated between the transmitted wave amplitude, which is assumed to be constant throughout the area of the transducer, and the amplitude at some observation point. The resulting transfer function is then averaged over the area of a receiving transducer.

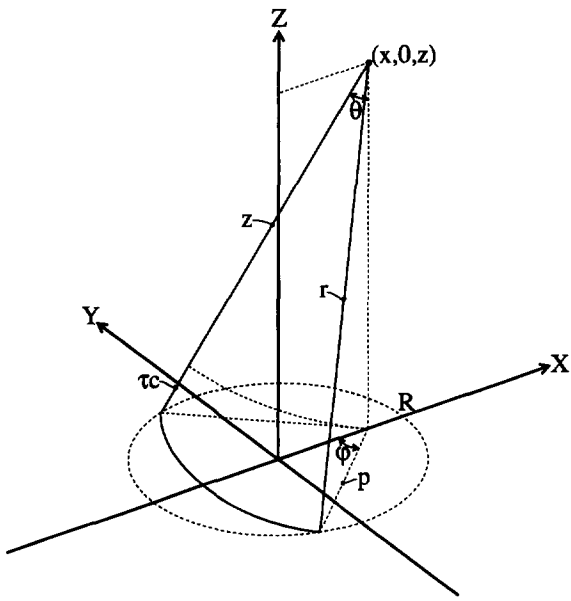

Fig. 5.8 Relevant quantities concerning the diffraction calculation for a perfectly aligned transducer.

Transfer function from transmitter to a point

Figure 5.8 shows the geometry involved. A rectangular set of axes X,Y,Z is defined with its origin in the centre of the circular transmitting area and the Z-axis normal to it. Consider an observation point located at (x,0,z). The locus of points on the transmitter having the same inclination angle θ and distance of flight r is an arc. The radius of the arc is p and its length is $2\varphi p$.

Instead of the area S as the integration variable in the diffraction formula, it will prove more convenient to use the increase τ from the *nominal time-of-flight* value. Using the phase velocity c, this increase is defined as:

$$\tau = \frac{r - z}{c} \tag{5.39}$$

Since $p = \sqrt{r^2 - z^2}$, it follows for $p > 0$:[1]

$$dS = 2\varphi p dp = 2\varphi p \frac{\partial p}{\partial \tau} d\tau = 2\varphi p \frac{\partial p}{\partial r}\frac{\partial r}{\partial \tau} d\tau = 2\varphi p \frac{r}{p} c d\tau = 2\varphi r c d\tau \tag{5.40}$$

Together with the relation:

[1] In fact, in the limit of $p \to 0$ Equation 5.40 still holds.

$$e^{-ikr} = e^{-i\omega/c(z+\tau c)} = e^{-i\omega t_o} e^{-i\omega\tau} \tag{5.41}$$

and ignoring the term $e^{-i\omega t_o}$, which expresses the nominal time of flight, the diffraction formula can be rewritten in terms of a transfer function $\dot{H}$, relating the transmitted wave amplitude to the amplitude at the observation point. Denoting the transducer radius as R and considering only positive x-values[I], $\dot{H}$ becomes:

$$\dot{H}(x) = \frac{A(x)}{A_o} = \frac{i\omega}{2\pi} \int_{-\infty}^{+\infty} \left(\frac{z}{z+\tau c} + 1\right) \varphi\{p(\tau),x\}\, e^{-i\omega\tau} d\tau \tag{5.42}$$

where $p(\tau) = \sqrt{2z\tau c + (\tau c)^2}$

$$\begin{aligned} \varphi(p,x) &= \pi \quad \text{..... for } 0 \le p \le R - x \\ &= \arccos\left(\frac{x^2+p^2-R^2}{2xp}\right) \quad \text{..... for } x > 0 \text{ and } |R-x| < p < R+x \\ &= 0 \quad \text{..... elsewhere} \end{aligned}$$

Transfer function from transmitter to receiver

The receiving transducer in a pulse-echo configuration is identical to the transmitting transducer. The transfer function obtained above is therefore now averaged over an area similar to the transmitter area but translated along the Z-axis over a distance z.[II] Using circular symmetry, the resulting transfer function H is obtained as:

$$\begin{aligned} H &= \frac{1}{\pi R^2} \int_0^{2\pi} \int_0^R x\, \dot{H}(x)\, dx d\alpha = \frac{2\pi}{\pi R^2} \int_0^R x\, \dot{H}(x)\, dx = \\ &= \frac{2}{R^2} \frac{i\omega}{2\pi} \int_{-\infty}^{+\infty} \left(\frac{z}{z+\tau c} + 1\right) \left[\int_0^R x\, \varphi\{p(\tau),x\}\, dx\right] e^{-i\omega\tau} d\tau = \\ &= \frac{i\omega}{2\pi} \int_{-\infty}^{+\infty} \tilde{h}(\tau)\, e^{-i\omega\tau} d\tau \end{aligned} \tag{5.43}$$

where $\tilde{h}(\tau) = \frac{2}{R^2}\left(\frac{z}{z+\tau c} + 1\right) \int_0^R x\, \varphi\{p(\tau),x\}\, dx$

[I] For reasons of symmetry negative x-values are not considered.

[II] The way in which the diffraction calculation is actually implemented for the pulse-echo configuration will be dealt with separately.

Strip diffraction

In the model used for a slightly tilted transducer, a division was made into strip-shaped subtransducers (Fig. 5.5). The diffraction calculation must now be focused on these subtransducers, as each has its own characteristic, due to the varying coupling layer thickness. Figure 5.9 shows the geometry involved in performing the calculation. The transmitter and receiver areas and the set of coordinate axes are similar to those used for the calculation of arc diffraction.

Two strips are considered, one on the transmitter and one on the receiver surface, both directed parallel to the Y-axis, with their centres at $X=x_t$ and $X=x_r$ respectively. Their width, δx, is small relative to the distance z, permitting the assumption that the inclination angle θ and distance of flight r are independent of x within the area of the strips. First the transfer function is derived between a transmitting strip and a point on a receiving strip. The transfer function between two strips is then determined by averaging over the area of the receiving strip.

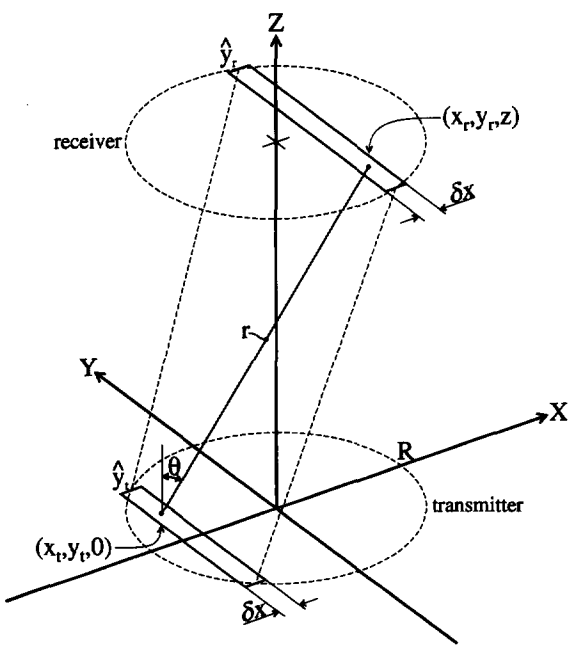

Fig. 5.9 Relevant quantities for diffraction calculation in the case of a tilted transmitter and receiver.

The division into subtransducers may conflict with an assumption made when deriving the Kirchhoff diffraction formula, namely regarding the smallness of the wavelength compared with all other dimensions. This would mean that the width of the strips cannot be taken

too small.[I] However, the requirement can also be interpreted in the sense that the amplitudes transmitted by neighbouring subtransducers may not differ too much. In other words, the transducer tilt must remain restricted in the calculation. Apart from this, it is also to be expected that a certain minimum number of subtransducers is required, in order to avoid the ultimate results being affected by the discrete nature of the calculation.

Transfer function from strip to point

Using the Kirchhoff diffraction formula (Eq. 5.38), the transfer function $\dot{H}$ from a transmitting strip to a point on the receiving strip at $Y=y_r$ is found as:

$$\dot{H}(y_r) = \frac{A(y_r)}{A_o} = \frac{ik}{2\pi}\int_{\substack{\text{transmitting}\\ \text{strip}}} {}^1\!/_2(\cos\theta + 1)\frac{e^{-ikr}}{r}\,dS = \delta x \frac{ik}{4\pi}\int_{-\hat{y}_t}^{+\hat{y}_t}\left(\frac{z}{r(y_t)}+1\right)\frac{e^{-ikr(y_t)}}{r(y_t)}\,dy_t \qquad (5.44)$$

where $r = \sqrt{(x_t-x_r)^2 + (y_t-y_r)^2 + z^2}$

$\hat{y}_t = \sqrt{R^2-x_t^2}$

R = transmitter and receiver radius

The distance of flight r depends on the *absolute* coordinate difference $\Delta y = |y_t - y_r|$ rather than on y_t. For positive y_r-values[II] it follows that:

$$\dot{H}(y_r) = I(\hat{y}_t+y_r) + I(\hat{y}_t-y_r) \quad \ldots\ldots \text{ for } 0 \le y_r \le \hat{y}_t \qquad (5.45^a)$$

$$\dot{H}(y_r) = I(y_r+\hat{y}_t) - I(y_r-\hat{y}_t) \quad \ldots\ldots \text{ for } 0 < \hat{y}_t \le y_r \qquad (5.45^b)$$

where $I(\xi) = \delta x \frac{ik}{4\pi}\int_0^{\xi}\left(\frac{z}{r(\Delta y)}+1\right)\frac{e^{-ikr(\Delta y)}}{r(\Delta y)}\,d(\Delta y)$

Analogous to the treatment of arc diffraction, it is convenient to use the increase τ from the nominal time-of-flight value (Eq. 5.39) as the integration variable in the I-function. From the relation:

$$\Delta y = \sqrt{r^2 - \Delta x^2 - z^2} \qquad (5.46)$$

where $\Delta x = |x_t - x_r|$

[I] This requirement is similar to that arising from the one-dimensional transducer model.

[II] In view of symmetry there is no need to consider negative y_r-values.

it follows that for $\Delta y \neq 0$:

$$d(\Delta y) = \frac{r}{\Delta y} dr = \frac{r}{\Delta y} \frac{\partial r}{\partial \tau} d\tau = \frac{rc}{\Delta y} d\tau \tag{5.47}$$

Together with Equation 5.41 and again ignoring the term $e^{-i\omega t_0}$, the I-function is rewritten as:

$$I(\xi) = \delta x \frac{i\omega}{4\pi} \int_{-\infty}^{+\infty} \left(\frac{z}{z+\tau c}+1\right) \frac{\psi\{\Delta y(\tau),\xi\}}{\Delta y(\tau)} e^{-i\omega\tau} d\tau \tag{5.48}$$

where $\Delta y(\tau) = \sqrt{(\tau c)^2 + 2z\tau c - \Delta x^2}$

$\psi(\Delta y,\xi) = 1$ ..... for $0 \leq \Delta y \leq \xi$

$= 0$ ..... otherwise

It should be noted that this integral is *improper*, as the integrand becomes infinite at a τ-value corresponding to $\Delta y=0$.

Transfer function from strip to strip

The transfer function H between two strips is found by averaging $\dot{H}(y_r)$ over the area of the receiving strip:

$$H = \frac{1}{2\hat{y}_r} \int_{-\hat{y}_r}^{+\hat{y}_r} \dot{H}(y_r) dy_r = \frac{1}{\hat{y}_r} \int_{0}^{\hat{y}_r} \dot{H}(y_r) dy_r \tag{5.49}$$

where $\hat{y}_r = \sqrt{R^2 - x_r^2}$

Substituting the expressions for $\dot{H}$ (Eqs. 5.45[ab]) leads to:

$$H = \frac{1}{\hat{y}_r} \left\{ \int_0^{\hat{y}_r} I(\hat{y}_t + y_r) dy_r + \int_0^{\hat{y}_r} I(\hat{y}_t - y_r) dy_r \right\} =$$

$$= \frac{1}{\hat{y}_r} \left\{ \int_{\hat{y}_t}^{\hat{y}_t+\hat{y}_r} I(\xi) d\xi - \int_{\hat{y}_t}^{\hat{y}_t-\hat{y}_r} I(\xi) d\xi \right\} = \frac{1}{\hat{y}_r} \int_{\hat{y}_t-\hat{y}_r}^{\hat{y}_t+\hat{y}_r} I(\xi) d\xi \quad \text{..... for } \hat{y}_r \leq \hat{y}_t \tag{5.50[a]}$$

and:

$$H = \frac{1}{\hat{y}_r}\left\{\int_0^{\hat{y}_t} I(\hat{y}_t+y_r)dy_r + \int_0^{\hat{y}_t} I(\hat{y}_t-y_r)dy_r + \int_{\hat{y}_t}^{\hat{y}_r} I(y_r+\hat{y}_t)dy_r - \int_{\hat{y}_t}^{\hat{y}_r} I(y_r-\hat{y}_t)dy_r\right\} =$$

$$= \frac{1}{\hat{y}_r}\left\{\int_{\hat{y}_t}^{2\hat{y}_t} I(\xi)d\xi + \int_0^{\hat{y}_t} I(\xi)d\xi + \int_{2\hat{y}_t}^{\hat{y}_r+\hat{y}_t} I(\xi)d\xi - \int_0^{\hat{y}_r-\hat{y}_t} I(\xi)d\xi\right\} = \frac{1}{\hat{y}_r}\int_{\hat{y}_r-\hat{y}_t}^{\hat{y}_r+\hat{y}_t} I(\xi)d\xi \quad \text{..... for } \hat{y}_t \le \hat{y}_r. \quad (5.50^b)$$

Thus for all $\hat{y}_t$ and $\hat{y}_r$ the transfer function H becomes:

$$H = \frac{\delta x}{\hat{y}_r}\frac{i\omega}{4\pi}\int_{|\hat{y}_t-\hat{y}_r|}^{\hat{y}_t+\hat{y}_r}\left\{\int_{-\infty}^{+\infty}\left(\frac{z}{z+\tau c}+1\right)\frac{\psi\{\Delta y(\tau),\xi\}}{\Delta y(\tau)}e^{-i\omega\tau}d\tau\right\}d\xi =$$

$$= \frac{\delta x}{\hat{y}_r}\frac{i\omega}{4\pi}\int_{-\infty}^{+\infty}\left(\frac{z}{z+\tau c}+1\right)\frac{1}{\Delta y(\tau)}\left\{\int_{|\hat{y}_t-\hat{y}_r|}^{\hat{y}_t+\hat{y}_r}\psi\{\Delta y(\tau),\xi\}d\xi\right\}e^{-i\omega\tau}d\tau =$$

$$= \frac{i\omega}{2\pi}\int_{-\infty}^{+\infty}\tilde{h}(\tau)\,e^{-i\omega\tau}d\tau \qquad (5.51)$$

where $\tilde{h}(\tau) = \frac{\delta x}{2\hat{y}_r}\left(\frac{z}{z+\tau c}+1\right)\frac{1}{\Delta y(\tau)}\int_{|\hat{y}_t-\hat{y}_r|}^{\hat{y}_t+\hat{y}_r}\psi\{\Delta y(\tau),\xi\}d\xi$

Numerical diffraction calculation

The transfer functions for both arc and strip diffraction (Eqs. 5.43 and 5.51) are in the form:

$$H(\omega) = \frac{i\omega}{2\pi}\tilde{H}(\omega) \qquad (5.52)$$

$$\text{where } \tilde{H}(\omega) = \int_{-\infty}^{+\infty} \tilde{h}(\tau)\, e^{-i\omega\tau}\, d\tau$$

i.e. $H(\omega)$ is equal to the product of $i\omega/2\pi$ and the Fourier transform of $\tilde{h}(\tau)$. The Fourier transform is described briefly in Appendix 5A.

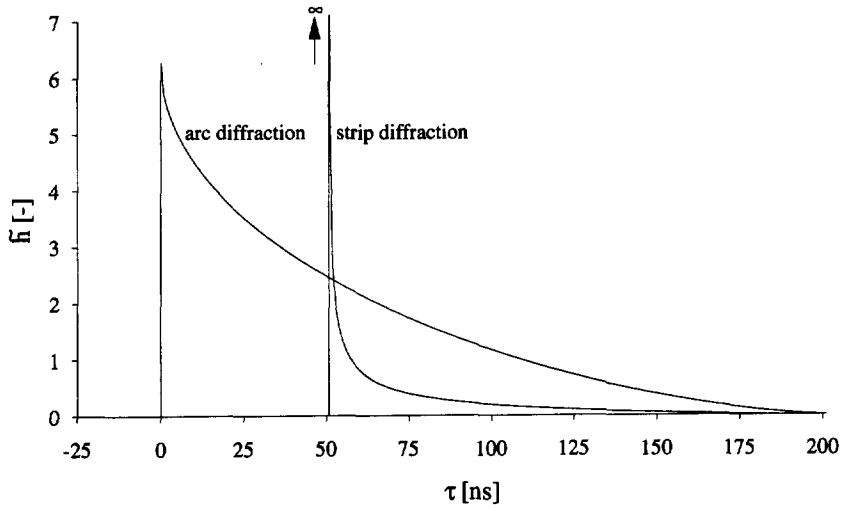

Fig. 5.10 Typical examples of $\tilde{h}(\tau)$ for arc and strip diffraction, calculated for a phase velocity of 3250 m/s and a 6.3 mm diameter transmitter and receiver 30 mm apart. The transmitting and receiving strips were taken as 6 and 4.5 mm long respectively ($2\hat{y}_t$ and $2\hat{y}_r$), displaced 3.15 mm relative to each other (Δx) and 0.63 mm wide (δx).

In Figure 5.10 typical examples are given of $\tilde{h}(\tau)$ for both types of diffraction calculation. They show a discontinuity at the lower end of the non-zero range, while for strip diffraction $\tilde{h}$ in fact goes to infinity at that point. Immediately after this maximum the two functions, especially that of the strip calculation, fall steeply, after which they decrease more gradually to zero.

Convolution

Equation 5.52 can also be regarded in terms of *convolution*. The convolution of two functions of time f(t) and g(t) is itself a function of time and is defined as:

$$\int_{-\infty}^{+\infty} f(u)g(t-u)du \tag{5.53}$$

This convolution may be interpreted as the response to an *input signal* f(t) of some physical

process having a *response function* g(t). The signal f(t) is smeared in time as prescribed by the response function g(t): the value g(x) is a measure of how much of f(t) is shifted to time t+x.

The *convolution theorem* states that the Fourier transform of the convolution of two functions is equal to the product of the transforms of the individual functions [5]. Consequently Equation 5.52 implies that the transmitted waveform is convolved with one of the above functions $\tilde{h}(\tau)$. In view of their shape parts of the wave are shifted to later times, which is obviously in accordance with physical reality.

Discrete response function

In the *numerical* diffraction calculation the transmitted waveform is available in the form of samples at equidistant times, with a time interval Δt between consecutive values. Convolving this waveform necessarily means shifting parts of it over *discrete* time intervals. For arc diffraction these discrete intervals are equal to[1]:

$$\tau_k = k \cdot \Delta t \quad \text{..... for } 0 \le k \le \frac{\sqrt{z^2+4R^2} - z}{c\Delta t} \tag{5.54}$$

as the maximum τ-value is $(\sqrt{z^2+4R^2} - z)/c$. In the case of strip diffraction a certain subrange applies.

The response function must be in the form of a series of values at times τ_k. However, instead of simply evaluating $\tilde{h}(\tau)$ at τ_k, *average* values $\bar{h}_k$ are used for this purpose, defined as:

$$\bar{h}_k = \frac{1}{\Delta t} \int_{\tau_k - \Delta t/2}^{\tau_k + \Delta t/2} \tilde{h}(\tau)\, d\tau \tag{5.55}$$

Convolving with these average values means that the part of the waveform which is shifted over an interval τ_k is equal to the average of all parts which would be shifted over intervals between $\tau_k - \Delta t/2$ and $\tau_k + \Delta t/2$ in the continuous case. It is found that when using this procedure the results for the arc diffraction calculation converge at larger Δt-values. For the strip diffraction calculation, applying the averaging procedure is in fact essential. Erroneous results will otherwise occur, depending on the accidental position of the singularity in $\tilde{h}(\tau)$ relative to the series of times τ_k.

In the actual evaluation of the $\bar{h}_k$-values all integrals are solved by numerical integration according to the trapezoidal rule. The singularity in $\tilde{h}(\tau)$ for strip diffraction does not

[1] Here k is an index used for series of time-domain values and is not to be confused with the wave number.

present any problems if Δy is used as the integration variable instead of τ. Using Equations 5.47 and 5.51, it follows that:

$$\bar{h}_k = \frac{1}{\Delta t}\int_{\tau_k-\Delta t/2}^{\tau_k+\Delta t/2}\left[\frac{\delta x}{2\hat{y}_r}\left(\frac{z}{z+\tau c}+1\right)\frac{1}{\Delta y(\tau)}\int_{|\hat{y}_t-\hat{y}_r|}^{\hat{y}_t+\hat{y}_r}\psi\{\Delta y(\tau),\xi\}\,d\xi\right]d\tau =$$

$$= \frac{\delta x}{2\hat{y}_r c\Delta t}\int_{\Delta y(\tau_k-\Delta t/2)}^{\Delta y(\tau_k+\Delta t/2)}\left\{\left(\frac{z}{\sqrt{\Delta x^2+\Delta y^2+z^2}}+1\right)\frac{1}{\sqrt{\Delta x^2+\Delta y^2+z^2}}\int_{|\hat{y}_t-\hat{y}_r|}^{\hat{y}_t+\hat{y}_r}\psi(\Delta y,\xi)d\xi\right\}d(\Delta y) \qquad (5.56)$$

Discrete transfer function

According to Equation 5.52, the response function $\tilde{h}(\tau)$ must be transformed to the frequency domain in order to obtain the transfer function $H(\omega)$. In this discrete case the transfer function must be available at the series of frequencies ω_n defined in Equation 5.4. This is achieved by padding the values $\bar{h}_k$ with sufficient zeros in order to exactly match the number of data points N in the transmitted wave. After applying the discrete Fourier transform (Eq. 5A.3[a]), values $\bar{H}_n$ are found, which lead to the desired series $H(\omega_n)$ according to:

$$H(\omega_n) = \frac{i\omega_n}{2\pi}\tilde{H}(\omega_n) \approx \frac{i\omega_n}{2\pi}\Delta t\,\bar{H}_n = \frac{i2\pi n}{2\pi N\Delta t}\Delta t\,\bar{H}_n = i\frac{n}{N}\bar{H}_n \qquad (5.57)$$

For the second step the definition of the discrete Fourier transform is used.

At this point it is important to recall that in the diffraction calculation parts of the transmitted waveform are delayed over time intervals within the range specified by Equation 5.54. Since, in the discrete Fourier transform, time-domain data are regarded as cyclic over N, the tail of the waveform will affect its head, a phenomenon called *spoiling* [44]. In order therefore to avoid this the wave data are padded with at least as many zeros as there are non-zero τ_k-values in the time interval range.

5.3 Calculation

5.3.1 Procedure

The procedure for evaluating the pulse-echo configuration as a whole can be divided into a number of steps, namely the calculation of:

- The *discrete Fourier transform* of the pulser waveform
  The pulse becomes available in the form of the sum of a series of time-harmonic signals at frequencies ω_n (Eq. 5.4), each signal having its own amplitude and phase.

- The *transducer transfer coefficients*
  These coefficients describe the behaviour of a transmitting, receiving and reflecting transducer for a certain frequency. They are respectively:

  -) $\left(\frac{W_t}{V_s}\right)_{W_r=0}$, relating the transmitted stress wave amplitude W_t to the pulser voltage V_s (Eqs. 5.20 and 5.30 for the aligned and tilted transducer models respectively).

  -) $\left(\frac{V_e}{\overline{W}_r}\right)_{V_s=0}$, relating the average received wave amplitude $\overline{W}_r$ to the transducer electrode voltage V_e (Eqs. 5.22 and 5.31 respectively).

  -) $\left(\frac{W_t}{V_e}\right)_{W_r=0}$, relating the re-transmitted wave amplitude W_t to the transducer electrode voltage V_e (Eqs. 5.25 and 5.32 respectively).

  -) $\left(\frac{W_t}{W_r}\right)_{V_e=0}$, relating the re-transmitted wave amplitude W_t to the local received wave amplitude W_r (Eqs. 5.26 and 5.33 respectively). In fact this is a reflection coefficient.

  In the tilted transducer model each subtransducer is treated separately. Therefore, in this case transducer behaviour is described by four M-dimensional *transducer transfer vectors*, where M is the number of subtransducers.

  The coefficients or vectors are determined for each frequency ω_n.

- The *diffraction transfer coefficients*
  These coefficients give the ratio of the average received wave amplitude after diffraction, $\overline{W}_r$, and the transmitted wave amplitude W_t. They are calculated for each frequency ω_n and, in view of the pulse-echo configuration, for two different cases, namely:

  -) $\left(\frac{\overline{W}_r}{W_t}\right)_{Z=2d_m}$, for diffraction over twice the specimen thickness d_m, corresponding to the distance travelled by the first back-face echo.

-) $\left(\frac{\overline{W}_r}{W_t}\right)_{z=4d_m}$, for diffraction over four times the specimen thickness d_m, corresponding to the distance travelled by the second back-face echo.

Thus reflection at the free specimen back face is assumed not to affect the diffraction phenomenon, apart of course from a change of sign for the stress wave amplitude.

In the tilted transducer model each combination of a transmitting and a receiving subtransducer is considered separately. This leads for each frequency and diffraction distance to an M×M *diffraction transfer matrix*, element ij of which represents the transfer coefficient between the j^{th} transmitting and the i^{th} receiving subtransducer.[1]

- The *first back-face echo*

  The transducer electrode voltage for this echo, $V_{e,1}$, follows straightforwardly from the pulser voltage V_s. This relation can be written for the aligned transducer model as:

$$V_{e,1} = \left(\frac{V_e}{\overline{W}_r}\right)_{V_s=0} \cdot \left(\frac{\overline{W}_r}{W_t}\right)_{z=2d_m} \cdot \left(\frac{W_t}{V_s}\right)_{W_r=0} \cdot V_s \qquad (5.58)$$

  For the tilted model the relation is roughly comparable: the transfer coefficients for the transmitting and receiving transducers are replaced by the corresponding vectors, while the diffraction transfer coefficient is replaced by the M×M transfer matrix.

- The *second back-face echo*

  This case is more complicated, as the second echo reflects twice not only against the free back face of the specimen but also against the transducer-couplant combination at the moment the first back-face echo is being received. The second echo is divided into two parts, namely:

  -) a fraction which is reflected back into the specimen by the transducer-couplant combination and which is calculated using the reflection coefficient $(W_t/W_r)_{V_e=0}$. For the diffraction a transmitter-receiver distance of four times the specimen thickness is assumed.

  -) a fraction which is re-transmitted by the transducer while receiving the first back-face echo. This is calculated using the electrode voltage $V_{e,1}$ and the transfer coefficient $(W_t/V_e)_{W_r=0}$. As the amplitude of this wave part is constant over the transducer area, the diffraction is calculated for a distance of only twice the specimen thickness.

  The electrode voltage $V_{e,2}$ for the second back-face echo in the aligned transducer model thus amounts to:

[1] Using symmetry arguments the number of calculations needed can be reduced considerably.

$$V_{e,2} = \left(\frac{V_e}{\overline{W}_r}\right)_{V_s=0} \cdot \left(\frac{W_t}{W_r}\right)_{V_e=0} \cdot \left(\frac{\overline{W}_r}{W_t}\right)_{z=4d_m} \cdot \left(\frac{W_t}{V_s}\right)_{W_r=0} \cdot V_s + \\ + \left(\frac{V_e}{\overline{W}_r}\right)_{V_s=0} \cdot \left(\frac{\overline{W}_r}{W_t}\right)_{z=2d_m} \cdot \left(\frac{W_t}{V_e}\right)_{W_r=0} \cdot V_{e,1} \qquad (5.59)$$

In order to calculate $V_{e,2}$ for the tilted transducer model, the transducer transfer coefficients in the above relation, with the exception of the reflection coefficient $(W_t/W_r)_{V_e=0}$, are replaced by the corresponding vectors. Moreover, the diffraction transfer coefficient in the second term is replaced by the appropriate diffraction transfer matrix. In the first term, however, the diffraction transfer coefficient together with the reflection coefficient are replaced by a single M×M matrix. Element ij of this matrix represents the transfer coefficient between the j^{th} transmitting and the i^{th} receiving subtransducer, taking into account the wave reflection from the specimen against couplant and transducer. On geometrical grounds, therefore, this element is equal to the product of element ij of the diffraction transfer matrix and the reflection coefficient $(W_t/W_r)_{V_e=0}$ at a location half-way between the i^{th} and the j^{th} subtransducer. If the difference i − j is even, the reflection coefficient of subtransducer $(i+j)/2$ is used, while otherwise the average is taken of the coefficients of subtransducers $(i+j-1)/2$ and $(i+j+1)/2$.

- The *discrete Fourier transform* to the echo waveforms
  If the two series of time-harmonic waves constituting the 1^{st} and 2^{nd} back-face echoes are transformed back to the time domain, the echo waveforms become available. Quantities such as echo amplitude and time of flight can now be determined.

5.3.2 Implementation

In order to perform the model calculations a computer program called TRANAL (TRANsducer ANalysis) was developed. It was written in *Pascal* and runs on a MSDOS-based personal computer. In this program all model parameters can be interactively set, different types of calculations can be performed and calculated waveforms are displayed in a graph. Parameter sets and waveforms can be loaded from or saved to file.

To ensure the correctness of the results produced by the program, the results were compared with the outcome of time-domain calculations. These were performed for a configuration which was comparable apart from the couplant, which necessarily had to be non-dispersive. A comparison was also made with the results of an analytical calculation for a simple piezoelectric transducer [10]. For a zero tilt angle the analysis of the tilted transducer was verified by comparing it with the straightforward analysis.

It is important to choose a suitable time interval for the calculations. On the one hand the interval must be small enough to yield sufficient accuracy. This will be the case if the highest frequency components expected to be present in the calculated back-face echoes fall well below the Nyquist frequency, i.e. $1/2\Delta t$ for a time interval Δt (Appendix 5A).

On the other hand the time interval cannot be unrestrictedly small. The reason for this is that due to limitations of the program language used the number of data points per waveform is limited to 4096. A small time interval would therefore imply that the waveforms are not calculated for their complete duration. The problem which then occurs is related to the fact that in discrete Fourier analysis the time-domain signal is regarded as cyclic over the total time span of the signal. Thus the pulse exciting the transducer would seem to have such a high repetition rate that the waveforms partially overlap. Therefore, in order to ensure an accurate calculation the back-face echoes are always included in their entirety and the time interval is chosen accordingly.

In the analysis of the tilted transducer it is necessary to choose the number of subtransducers required for an accurate calculation. This is done empirically, i.e. when a further increase in this number does not significantly affect the outcome, it is assumed to be sufficiently large.

5.4 Parameters

As stated in the introduction, the model is not intended as a calculated imitation of the set-up described in Chapter 3. However, the parameters used for the model will be based on actual properties, as far as they are known. They will be completed with estimated and experimentally determined values.

For the pulser-receiver a pulse waveform will be calculated for a variable value of the damping resistance. The properties of the transducer and couplant require a more detailed discussion and will be treated below. Finally, for the propagation medium a structural steel is chosen with phase velocities for bulk shear and longitudinal waves of 3250 and 5920 $^{m}/_{s}$ respectively. It is assumed that in this medium ultrasonic waves at the frequencies considered here (see below) are not subject to attenuation.

5.4.1 Transducer

A distinct difference compared with the experimental set-up is the fact that the model relates to a single-mode transducer instead of the combined shear-longitudinal transducer described in Section 3.2.2. In order to be able to assess experimental effects for both wave types, the calculations will be performed for both a *shear* and a *longitudinal* transducer.

The circular model transducer has a diameter of 6.3 mm ($^{1}/_{4}$"). Further relevant details are:[I]

- Piezoelectric disc

  The disc is made of the sintered ceramic *Lead Zirconate Titanate* (PZT). As already described in Section 3.2.2, the piezoelectric properties are introduced by polarizing the material using a strong electric field. Longitudinal or shear wave transducers are obtained by using a Z-cut or X-cut disc respectively, i.e. discs cut with the poling axis normal to or in the plane of the disc. The PZT ceramic is available in a range of types, each having its own specific properties. For the model transducer a type is chosen which is denoted as PZT-2 in reference [2].[II] The properties of this material, in as far as they are relevant to the model, are given in Table 5.1. All tensor quantities are written in the Voigt notation (see Table 2.1) and defined on a set of axes with x_3 as the poling axis.

  The model parameters related to the piezoelectric disc are summarized in Table 5.2. In order to facilitate comparisons with the experimental set-up, the disc thickness is chosen in such a way that the nominal shear and longitudinal transducer frequencies be-

I These details are partly based on information supplied by transducer manufacturer *Panametrics*.

II The choice of the PZT type is also suggested by the result of a low frequency (1 KHz) capacitance measurement on a 5 MHz shear wave transducer (Panametrics V1542), which can be related to the transducer capacitance at constant stress, equal to $A(\varepsilon_1^S + e_{15}^2/C_{55}^E)/d_p$.

come 5 and 10 MHz respectively. The thickness is derived from the phase velocity in the thickness direction c_p. It is assumed that the nominal transducer frequency is equal to this velocity divided by twice the disc thickness.

Table 5.1 Relevant properties of the piezoelectric ceramic PZT-2 [2].

Mass density	ρ	$[Kg/m^3]$	7600
Piezoelectric stress components	e_{15}	$[C/m^2]$	9.8
	e_{33}	$[C/m^2]$	9.0
Permittivity components	ε_1^S	$[pF/m]$	4462
	ε_3^S	$[pF/m]$	2302
Stiffness components	C_{55}^E	[GPa]	22.2
	C_{33}^E	[GPa]	113

Table 5.2 Parameters related to the piezoelectric disc.

Model parameter			Shear	Longitudinal
Piezoelectric stress constant[1]	e	$[C/m^2]$	$-e_{15} = -9.8$	$e_{33} = 9.0$
Permittivity constant	ε^S	$[pF/m]$	$\varepsilon_1^S = 4462$	$e_3^S = 2302$
Phase velocity	c_p	$[m/s]$	$\sqrt{(C_{55}^E + \frac{e_{15}^2}{\varepsilon_1^S})/\rho} = 2399$	$\sqrt{(C_{33}^E + \frac{e_{33}^2}{\varepsilon_3^S})/\rho} = 4416$
Specific wave impedance	Z_p	$[MPa \cdot s/m]$	$\rho\frac{\omega}{k_p} = 18.2$	$\rho\frac{\omega}{k_p} = 33.6$
Disc thickness	d_p	$[\mu m]$	$1/2\frac{\omega/k_p}{5 \cdot 10^6} \cdot 10^6 = 240$	$1/2\frac{\omega/k_p}{10 \cdot 10^6} \cdot 10^6 = 221$

- Backing medium

  In the transducer model, the only parameter related to the backing medium is the specific wave impedance Z_b, a value which largely determines the damping characteristic of the transducer. The value used in the model calculation for this impedance is chosen by considering the *ratio* of the first maximum and first minimum in the echo amplitude. Since the transducer is driven by a short pulse, these extreme amplitudes can be directly related to the waves which are excited at the interfaces of the piezoelectric disc

[1] The actual sign of e depends on the poling direction in the PZT, but does not affect the results of the model calculations.

with the protective layer and the backing medium respectively and travel towards the propagation medium. Using Equations 5B.25 and 5B.26 it can be argued that the ratio of their amplitudes is a function of the ratio of the wave impedances in the backing medium and the piezoelectric disc.

By comparing calculated with experimentally obtained waveforms and adjusting the backing impedance until the amplitude ratio approximately corresponded, the values were obtained which are given in Table 5.3. It should be noted that it is common practice to use a backing impedance roughly equalling 0.7 times the impedance in the piezoelectric disc, in order to acquire a broad bandwidth transducer. It can be shown that for this value the bandwidth is least affected by a low impedance at the front of the transducer, for example caused by a coupling layer [47].

Table 5.3 Parameter related to the backing medium.

Model parameter		Shear	Longitudinal
Specific wave impedance	Z_b [MPa·s/m]	10	23

- Protective layer

For this layer aluminium oxide (Al_2O_3) is chosen, a material with a high wear resistance. The relevant properties are given in Table 5.4. The stiffness components are defined relative to a coordinate system in which the x_3-axis is normal to the plane of the protective layer and the x_1-axis is parallel to the shear wave polarization direction.

Table 5.4 Relevant properties of the wear-resistant ceramic Al_2O_3 [1].

Mass density	ρ	[Kg/m³]	3986
Stiffness components	C_{55}	[GPa]	145
	C_{33}	[GPa]	494

The model parameters for the protective layer are listed in Table 5.5.

Table 5.5 Parameters related to the protective layer.

Model parameter		Shear	Longitudinal
Phase velocity	c_l [m/s]	$\sqrt{C_{55}/\rho} = 6030$	$\sqrt{C_{33}/\rho} = 11130$
Specific wave impedance	Z_l [MPa·s/m]	$\sqrt{\rho C_{55}} = 24.0$	$\sqrt{\rho C_{33}} = 44.4$
Layer thickness	d_l [μm]	127	

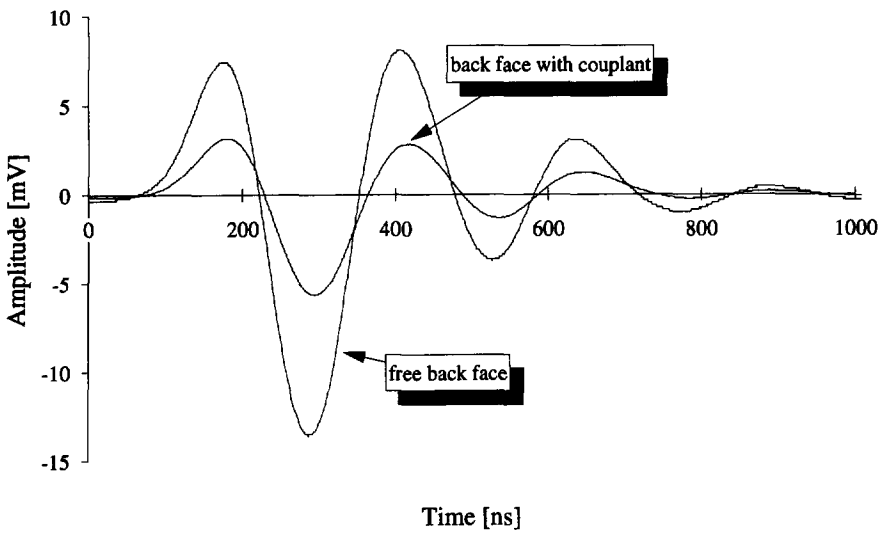

Fig. 5.11 A typical example of echo waveform distortion caused by applying shear wave couplant to the back face. The 3rd echo is shown for a 5 MHz shear wave in a 6 mm thick aluminium (Al 2024-T351) specimen.

5.4.2 Coupling fluid

The viscous nature of the couplant, which allows shear waves to propagate in it, also causes this medium to be attenuating and to have a frequency-dependent phase velocity and attenuation coefficient (Appendix 5C). As described in Section 3.2.4, the wave propagation properties of the couplant have been determined experimentally. However, the results give only a rough impression, as they do not give any insight into the frequency dependence. Nevertheless, this information is believed to be essential for the model.

Reflection measurements

The frequency dependence of the wave propagation properties of the couplant were investigated through reflection experiments. In brief, the experiments entail the determination of the reflection coefficient for longitudinal and shear waves travelling in a specimen towards an interface with the couplant. The specific wave impedance in the couplant can be calculated from these values, leading to the desired phase velocity and attenuation coefficient for the couplant. Wave *pulses*, which inherently contain components over a wide frequency range, are used for the measurement. Therefore, using the Fourier transform, the above calculations can be performed as a function of frequency.

The experiments are carried out using a plate-shaped aluminium specimen[I] for which

[I] Aluminium is used owing to its relatively low specific wave impedance, which increases accuracy.

the wave propagation properties are known. First, using a longitudinal or a shear wave transducer, an echo is produced for a free specimen back face. The waveform is stored using a digital oscilloscope, which enables computerized signal processing. The waveform is recorded relative to some arbitrary but stable trigger point in the pulse exciting the transducer.

Next, while ensuring that the transducer/coupling configuration and the triggering of the oscilloscope remain unchanged, the measurement is repeated for a back face on which a thick layer of shear wave couplant has been applied.[I] Since the reflection coefficient has now changed relative to that of a free surface, the waveform will be affected. Figure 5.11 shows a typical example of the two resulting waveforms.

Finally, using the discrete Fourier transform, the two waveforms are transformed to the frequency domain. The reflection coefficient from the aluminium specimen against the couplant, R_{mc}, can be calculated for each frequency component using the complex amplitudes for the free and coupled situations, W_{free} and W_{cpld} respectively, according to:

$$R_{mc} = -\sqrt[n]{\frac{W_{cpld}}{W_{free}}} \tag{5.60}$$

where n = echo number

The minus sign originates from the reflection coefficient for a free surface (−1). The specific wave impedance in the couplant, Z_c, follows from solving the expression for the reflection coefficient as a function of the wave impedance on either side of an interface (Eq. 3B.3):

$$Z_c = Z_m \frac{1+R_{mc}}{1-R_{mc}} \tag{5.61}$$

where Z_m = specific wave impedance in aluminium specimen

The phase velocity c_c and the attenuation coefficient α_c are found by using Equation 5C.10:

$$c_c = \frac{\omega}{k_c} = \frac{|Z_c|^2}{\rho_c \, re(Z_c)} \tag{5.62}$$

$$\alpha_c = \frac{\omega \rho_c \, im(Z_c)}{|Z_c|^2} \tag{5.63}$$

where $re(Z_c)$, $im(Z_c)$ = real and imaginary part of Z_c

[I] The couplant layer thickness must be sufficient to ensure that no reflections from within the layer will overlap with the back-face echo itself. For this purpose 1 mm suffices.

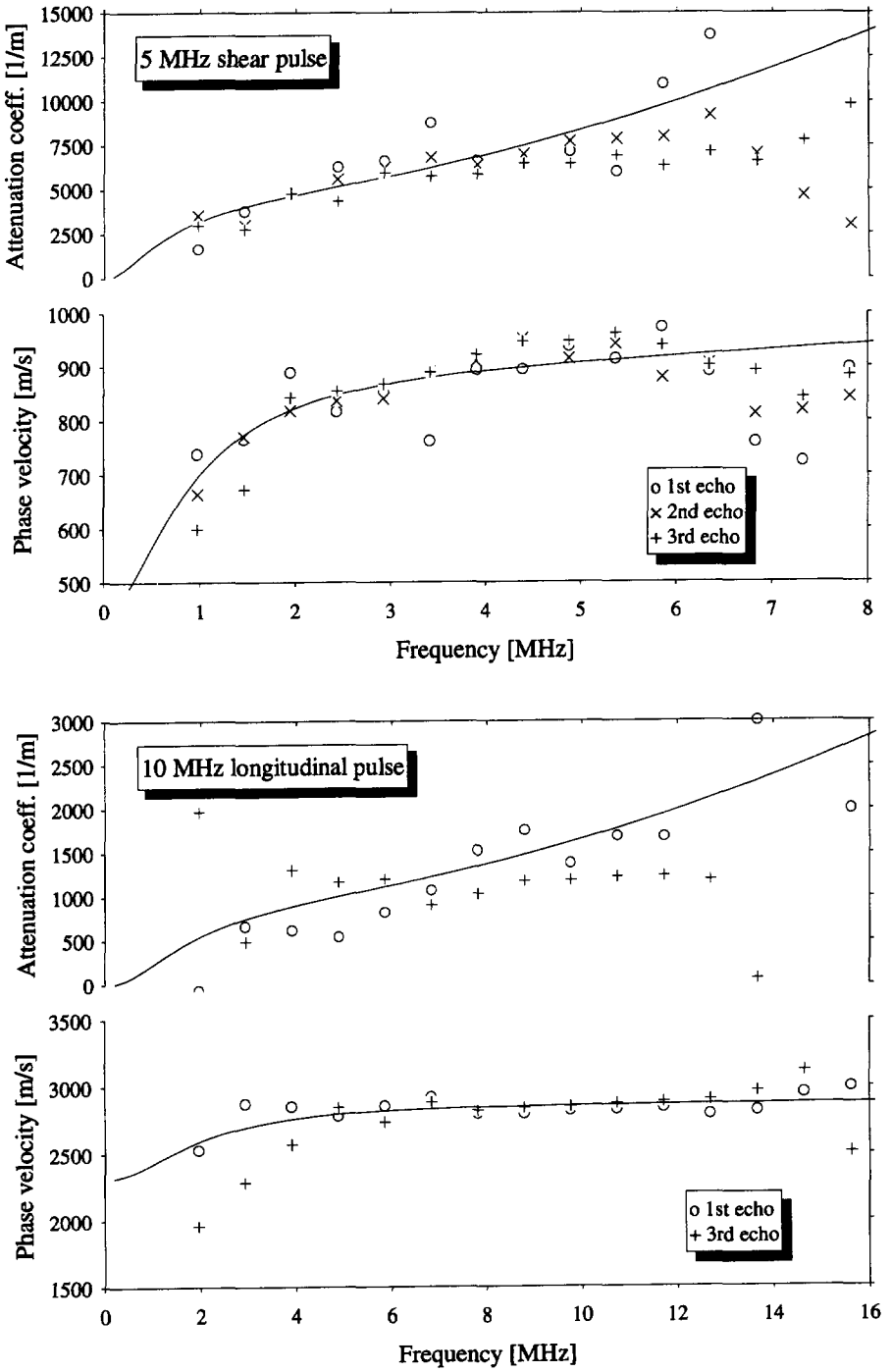

Figs. 5.12 & 5.13 Results of reflection measurements using shear and longitudinal wave pulses in a 6 mm thick Al 2024-T351 specimen. The solid lines indicate fits using a viscoelastic model.

Figures 5.12 and 5.13 give the results of reflection measurements using shear and longitudinal wave pulses with nominal frequencies of 5 and 10 MHz respectively.[1] These values correspond to those used in the experimental set-up and therefore give information concerning the most relevant frequency ranges. A mass density ρ_c of 1470 $^{Kg}/_{m^3}$ is used for the calculations, the value measured for the shear wave couplant used in the experimental set-up.

The graphs indicate that the phase velocity shows only a slight increase with frequency, whereas the attenuation increases more rapidly. It is interesting to make a comparison between these results and the order of magnitude of the directly measured velocity and attenuation, as presented in Figure 3.7. The overall agreement seems reasonable. Only the phase velocities for the two wave types, as resulting from the reflection experiments, seem to be somewhat lower. A definite explanation for this difference cannot be given.

It should be noted that frequency components at the lower and higher ends of the ranges have only a small amplitude. Consequently the experimental error will be significantly larger there. Another weak point in the reflection experiment stems from the fact that the calculation of the reflection coefficient involves the determination of the phase difference between frequency components of the waves, one reflected against a free back face and the other against a coupled back face. Even a small drift in the triggering of the digital oscilloscope or a slight change in the transducer-specimen coupling causes large errors in this phase calculation, especially for the higher frequency components.

The results obtained from the reflection measurements now need to be incorporated into the model calculations. The most straightforward way in which to do this is to directly fit a particular function to the phase velocity and attenuation coefficient data, e.g. using polynominals. It is found that by so doing, however, erroneous results in the calculations can easily occur. For example, it is then found possible for wave energy to be shifted to earlier times after passing through a layer of couplant. Obviously this does not agree with physical reality.

An alternative approach is therefore used, in which the constitutive behaviour of the couplant is described using a certain model. Fitting the parameters of this model to the experimental results will ensure that the behaviour of the couplant introduced into the calculations is *physically realizable*.

Newtonian fluid

As far as shear waves in a viscous fluid are concerned, the simplest model arises when shear stress is equal to the product of a *viscosity coefficient* η and the rate of shear deformation. In

[1] The longitudinal pulses originate from the combined shear/longitudinal transducer used for the experimental set-up. Owing to echo overlap the 2nd longitudinal back-face echo could not be used.

this *Newtonian fluid* [45] the stiffness component relevant for shear wave propagation, $\tilde{C}_{44}$ ($= \tilde{C}_{55} = \tilde{C}_{66}$), is equal to:[I]

$$\tilde{C}_{44} = i\omega\eta \tag{5.64}$$

From the Christoffel equation for attenuated plane waves (Eq. 5C.6) the following dispersion relation for shear waves is derived:[II]

$$i\omega\eta(k - i\alpha)^2 = \rho\omega^2 \tag{5.65}$$

Solving this for k and α leads to:[III]

$$k = \alpha = \sqrt{\frac{\omega\rho}{2\eta}} \tag{5.66}$$

and consequently the phase velocity c is:

$$c = \frac{\omega}{k} = \sqrt{\frac{2\omega\eta}{\rho}} \tag{5.67}$$

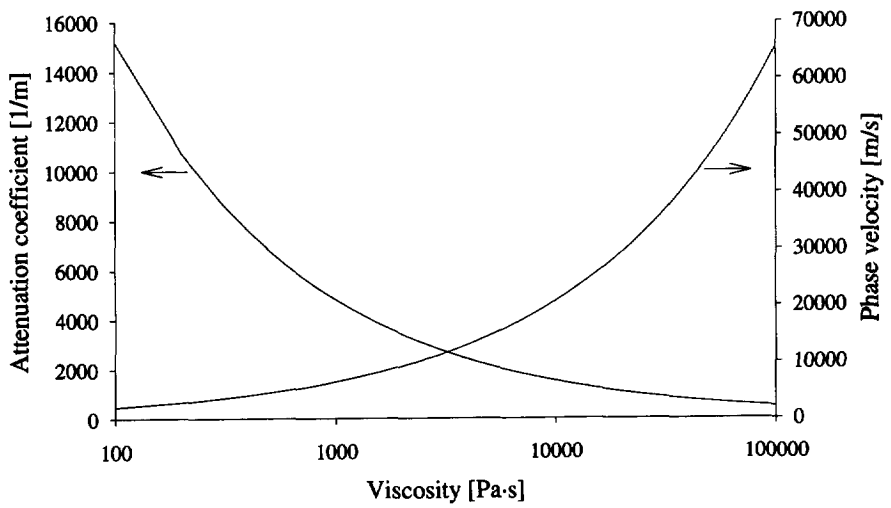

Fig. 5.14 Attenuation coefficient and phase velocity as a function of viscosity for 5 MHz shear waves in a Newtonian fluid with a mass density of 1470 Kg/m^3.

I The complex stiffness tensor $\underline{\tilde{C}}$ is defined in Appendix 5C.

II For this derivation a shear wave is considered propagating in the x_2-direction and polarized in the x_3-direction. However, Equation 5.65 is valid for an arbitrary shear wave as the fluid may be assumed to be isotropic.

III There are also imaginary roots for k and α, but after substituting these in the attenuated plane wave solution (Eq. 5C.4), they are found to represent the same displacement field.

Both damping and phase velocity are found to be proportional to the square root of frequency.

Figure 5.14 illustrates the influence of the viscosity coefficient for a fluid with a mass density of 1470 Kg/m^3. Recalling the experimental results shown in Figures 5.12 and 5.13 and assuming a typical couplant viscosity of 10 000 Pa·s, it is obvious that these values do not agree. It must therefore be concluded that a Newtonian fluid model is too simple a description for the properties of the couplant, at least as far as shear wave propagation is concerned.

Viscoelastic model for the constitutive behaviour

In order to describe the constitutive behaviour of attenuating media a number of *viscoelastic* models have been proposed in literature. A viscoelastic model consists of a combination of elastic springs and viscous dash pots. The force and displacement that would be involved in actual elements are replaced by stress and strain, as then a particular frequency-dependent complex stiffness can be obtained which determines the constitutive behaviour of a medium. The stiffness of a spring is determined by an elastic modulus C, while the stiffness of a dash pot with viscosity η is equal to $i\omega\eta$. Typical examples are the *Maxwell* and the *Voigt-Kelvin* models in which one elastic and one viscous element are connected in series and in parallel respectively [36, 49].

For the shear wave couplant a constitutive model is adopted as shown in Figure 5.15. It is formed by two elastic and two viscous elements and actually consists of two Voigt-Kelvin models placed in series. The model has no theoretical basis whatsoever, but is merely chosen because it can adequately describe the results of the reflection measurements presented above.

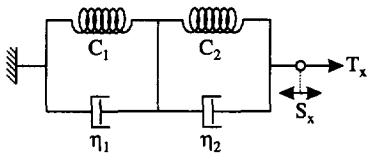

Fig. 5.15 Viscoelastic model for the constitutive behaviour of the couplant, i.e. the relation between stress $\underline{T}$ and strain $\underline{S}$. It is used to describe both shear (x = 4) and longitudinal (x = 1) wave propagation.

Obviously the model must have different values for the modulus or viscosity of the various elements where shear or longitudinal wave propagation is concerned. It should be noted that

Table 5.6 Parameters of the viscoelastic model for describing the constitutive behaviour of the couplant relevant to shear and longitudinal wave propagation.

Model parameter		Shear	Longitudinal
C_1	[MPa]	375	22100
η_1	[Pa·s]	140	2220
C_2	[MPa]	1250	12200
η_2	[Pa·s]	9.1	13.2

to comply with the fluid nature of the couplant, an extra viscous element needs to be placed in series in the case of shear wave propagation. This element would represent the viscosity at frequencies approaching zero. It is found, however, that such an element does not affect the constitutive behaviour in the frequency range relevant to the shear wave transducer. It is therefore omitted.

The values for the spring and dash pot elements in the viscoelastic model for the constitutive behaviour of the couplant (Fig. 5.15) are determined by fitting them to the results of the reflection measurements. In view of the limited experimental accuracy, data points are used only in the lower and middle frequency ranges, i.e. from approximately 1 to 7 MHz and 2 to 14 MHz for shear and longitudinal waves respectively. The resulting fits are indicated as solid lines in Figures 5.12 and 5.13, while Table 5.6 summarizes the corresponding moduli and viscosities.

5.5 Results

5.5.1 Typical back-face echoes

Before analysing the effect which certain parameters have on the outcome of pulse-echo measurements, calculation results will be presented for a configuration typical of the experimental set-up described in Chapter 3. In concrete terms this includes a damping resistance of 50 Ω for the pulser receiver, a coupling layer thickness of 100 μm and a 15 mm thick structural steel specimen. The pulse data used for the calculations are plotted in Figure 3.20 and have a time interval of 4 ns between consecutive values.

Figures 5.16 and 5.17 show the resulting first and second back-face echoes for the shear and

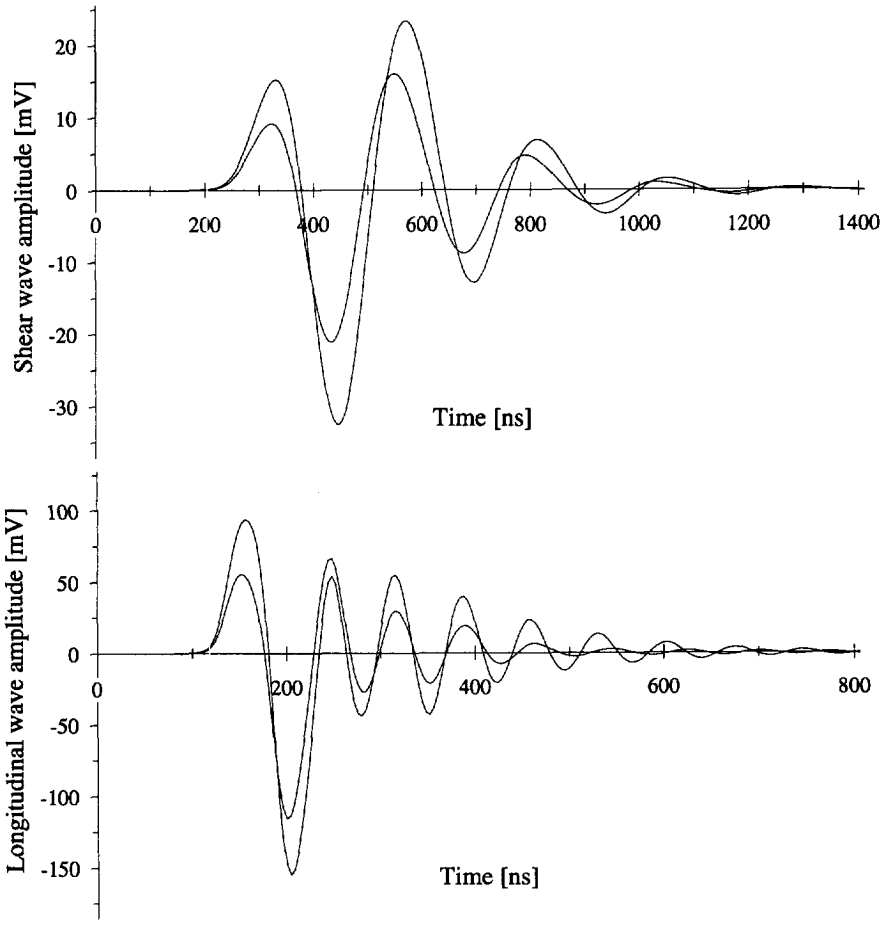

Figs. 5.16 & 5.17 Calculated first and second shear and longitudinal back-face echoes in 15 mm structural steel for a coupling layer of 100 μm and a damping resistance of 50 Ω.

longitudinal cases. The position which the waveforms have on the time axis is relative to the exciting pulse while ignoring the nominal time of flight, i.e. two or four times the specimen thickness divided by the phase velocity. The major part of the remaining offset is due to the time needed for the waves to traverse the protective layer of the transducer and the coupling layer during transmitting and receiving.

Although the model calculation cannot be expected to yield waveforms which closely match those of the experimental set-up, it is still interesting to make a comparison. Figures 5.18 and 5.19 show the echoes obtained with the combined shear-longitudinal transducer for the typical experimental conditions mentioned above.

The most striking difference is the magnitude of the wave amplitude, which is considerably smaller for the measured echoes. A possible reason for this is that, compared with a single-

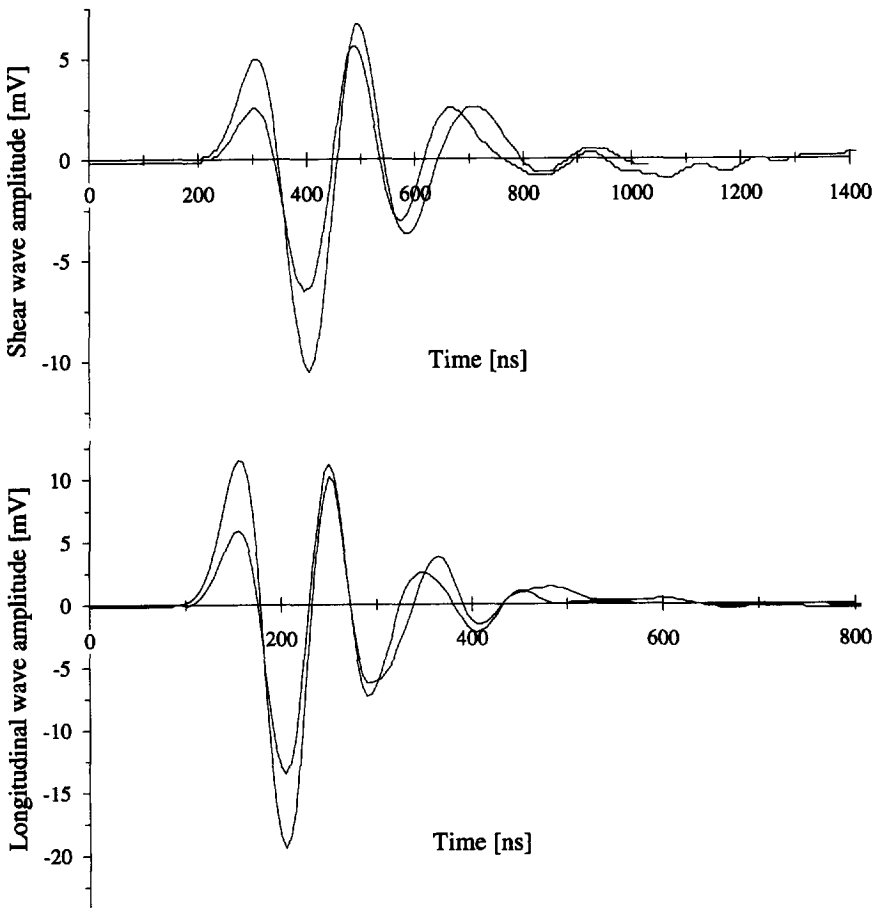

Figs. 5.18 & 5.19 First and second shear and longitudinal back-face echoes in 15 mm structural steel for a coupling layer of 100 µm and a damping resistance of 50 Ω, measured with a combined shear-longitudinal transducer.

mode shear or longitudinal transducer, the waves transmitted by a combined transducer have a smaller amplitude and that this type is also a less sensitive receiver. Furthermore, with regard to the longitudinal transducer in particular, a probable reason is the fact that electromechanical coupling includes normal stresses not only in the disc thickness direction. From the form of the $\underline{e}$-tensor (Eq. 3.3) it can be seen that normal stresses in the plane of the disc are also coupled. It may be expected, therefore, that the occurrence of radial oscillations reduces the efficiency of a longitudinal piezoelectric transducer [47]. It is assumed that this will not qualitatively affect the calculation results.

The shapes of the shear wave echoes compare reasonably well. However, for the longitudinal case the *tails* of the echoes are distinctly different. The calculated echoes show a long tail in the form of a damped oscillation with a period of about 70 ns. Based on an average phase velocity in the couplant of 2800 $^{m}/_{s}$ and a layer thickness of 100 μm, this period is found to correspond to the time needed for longitudinal waves to traverse the couplant layer twice. It must be concluded, therefore, that the calculated tail is due to *resonance* in this layer, enhanced by the large differences between the specific wave impedance in the couplant on the one hand and that in the adjacent media on the other hand. Such resonance has also been observed experimentally, but not nearly to the same extent. It is suspected that in practice it is easily obscured by transducer misalignment. In the analysis of a tilted transducer it will be seen that resonance in the coupling layer is dramatically decreased by even a small tilt angle.

It should be noted that the resonance phenomenon also occurs with shear waves. However, it is to be expected that this is not distinctly visible for a coupling layer of 100 μm thickness. The reason for this is that the damping in the couplant is much larger for this wave type and the period of the resonance is approximately equal to that of the transducer itself (200 ns).

5.5.2 Diffraction

Waves travelling through the specimen from transmitter to receiver are subject to the diffraction phenomenon. Shear wave diffraction in steel is considered as an example, using a 6.3 mm diameter transducer as transmitter and receiver. The modulus of the diffraction transfer function is plotted in Figure 5.20, calculated as a function of frequency for different distances of flight. In Figure 5.21 the same is done for the *phase advance*, i.e. the phase of the diffraction transfer function excluding the nominal phase change to which a wave is subject when travelling over the diffraction distance. The first graph shows that diffraction causes low frequency components to become relatively more attenuated, especially for larger distances. It can be seen from the second graph that phase advances always occur and that they increase with the diffraction distance.

It should be noted that for diffraction distances z which are large compared with the transducer radius R the modulus and phase advance can be expressed as a unique function of the

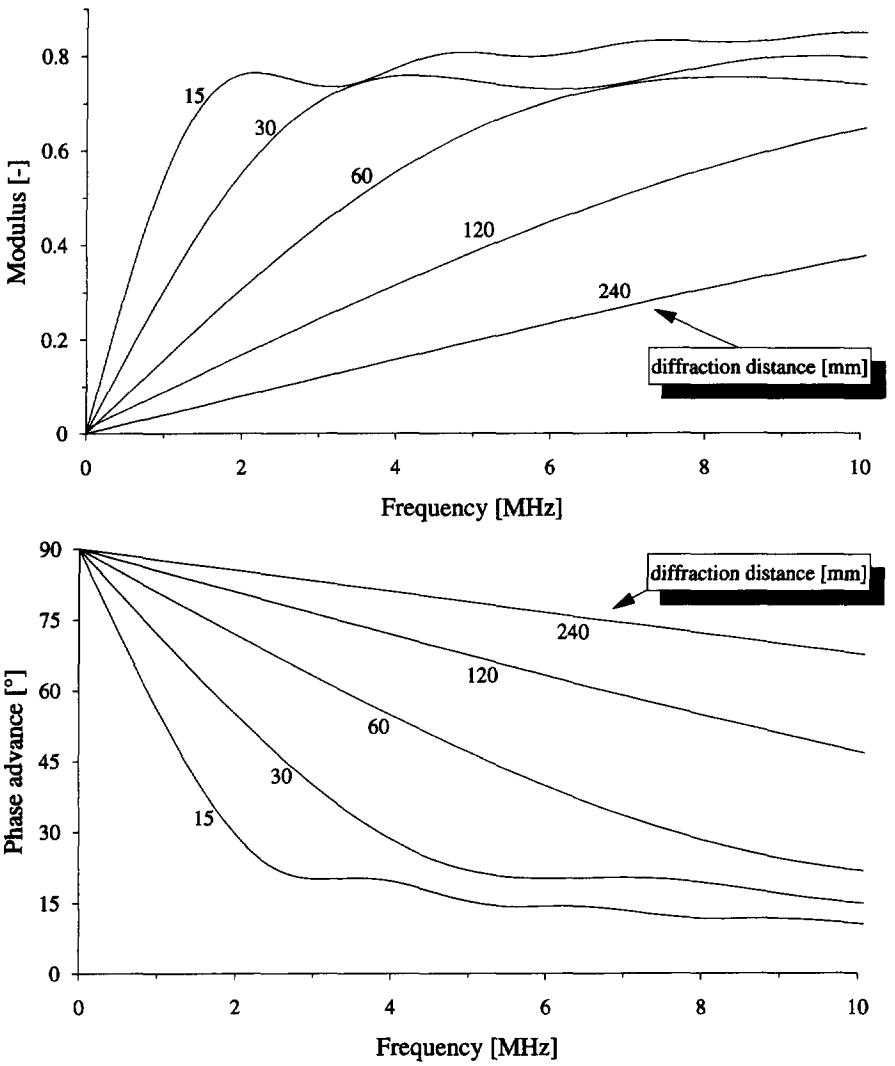

Figs. 5.20 & 5.21 Calculated modulus and phase advance of the diffraction transfer function for shear waves travelling in structural steel using a 6.3 mm diameter transmitter and receiver.

dimensionless parameter $z \cdot \lambda / R^2$, where λ is the wavelength in the specimen. The curves shown in Figures 5.20 and 5.21 would then almost coincide. This is not done, however, as one of the purposes of the model calculation is to assess subtle time-of-flight effects.

In a pulse-echo configuration the time of flight is determined as the interval between successive back-face echoes. As these echoes are diffracted over unequal distances, they are subject to different phase advances. For example, if a simple sinusoidal waveform is used, the time of flight measured will always be smaller than the nominal value, i.e. the transmit-

ter-receiver distance divided by the phase velocity [43]. Wave pulses contain a range of frequency components. The frequency-dependent attenuation and phase shift cause the transmitted waveform to be distorted. More precisely, due to the unequal diffraction distances, successive back-face echoes will be distorted differently. Therefore, the time of flight measured using the first zero crossings in the first and second back-face echo will inherently deviate from the nominal value. Examples can be seen in Figures 5.16 and 5.17, where the first zero crossings in the echoes do not coincide. This will be further discussed below.

5.5.3 Coupling layer thickness

As already described in Section 3.3.1, the coupling layer thickness has a dramatic influence on the outcome of time-of-flight measurements using the pulse-echo method. It is an obvious consequence, therefore, to focus the model calculations on this aspect. In this context the time interval between the first zero crossings in the calculated waveforms is interpreted as the *deviation* of an *experimentally determined time of flight* from the nominal value.

Figures 5.22 and 5.23 show the outcome of calculations for shear and longitudinal waves respectively travelling in structural steel specimens of different thicknesses. The results can be directly compared with the experimentally observed time-of-flight dependences shown in Figure 3.10. The overall agreement seems reasonable, although the time-of-flight deviations tend to be somewhat more pronounced in the calculated results.

For coupling thicknesses below what was referred to as a *limit thickness* in Section 3.3.1, i.e. about 80 and 90 μm for shear and longitudinal waves respectively, time of flight is affected strongly. The explanation for these marked changes is believed to be related to reflections within the coupling layer. This has already been extensively discussed in Section 3.3.1. It was suggested that the distortion introduced during reflection of the second back-face echo from the specimen against the combination of transducer and coupling layer is the main cause for the thickness-dependence of time of flight below the limit thickness.[1] This suggestion can be partly confirmed by considering the effect of replacing this reflection by a reflection against a free surface. Figure 5.24 shows the results calculated for shear waves in a 15 mm steel specimen. They show that for reflection against a free surface the time-of-flight deviation is significantly smaller. The difference is especially large for the smaller layer thicknesses, where the attenuation in the coupling layer is low.

Above the limit value for the coupling layer thickness, there are no notable changes in the longitudinal case. For shear waves on the other hand, time of flight shows a slight de-

[1] In this context the term *reflection* also implies the re-transmission of a wave by the receiving transducer.

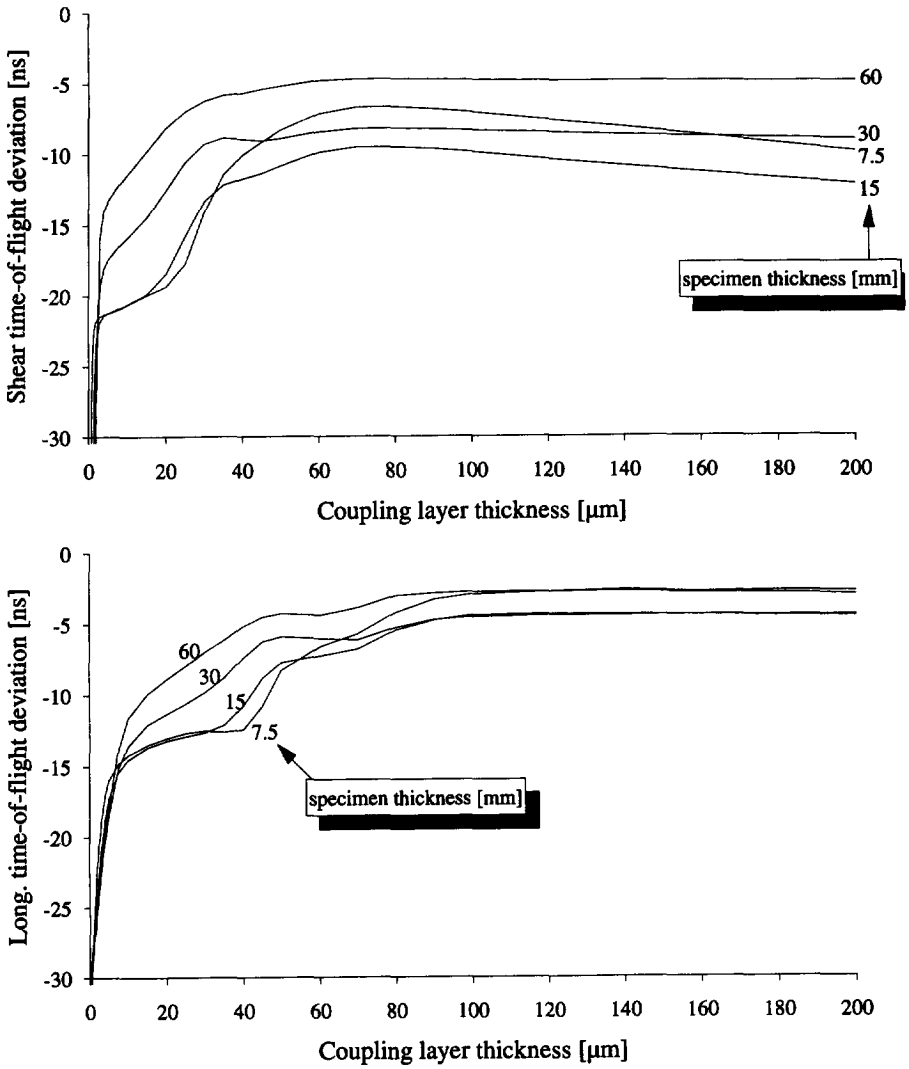

Figs. 5.22 & 5.23 Calculated deviation from the nominal shear and longitudinal times of flight in structural steel specimens with different thicknesses, as a function of the coupling layer thickness.

crease with layer thickness. This effect becomes less as the specimen becomes thicker. In the experimental results for shear waves (Fig. 3.10) a very slight decrease can also be observed, but it is questionable whether this is significant bearing in mind the limitations of the experimental accuracy.

Time-of-flight changes above the limit thickness cannot possibly be caused by reflections within the coupling layer. It is believed that the dispersive nature of the viscous couplant in combination with differences between the frequency spectra of the first and second back-face

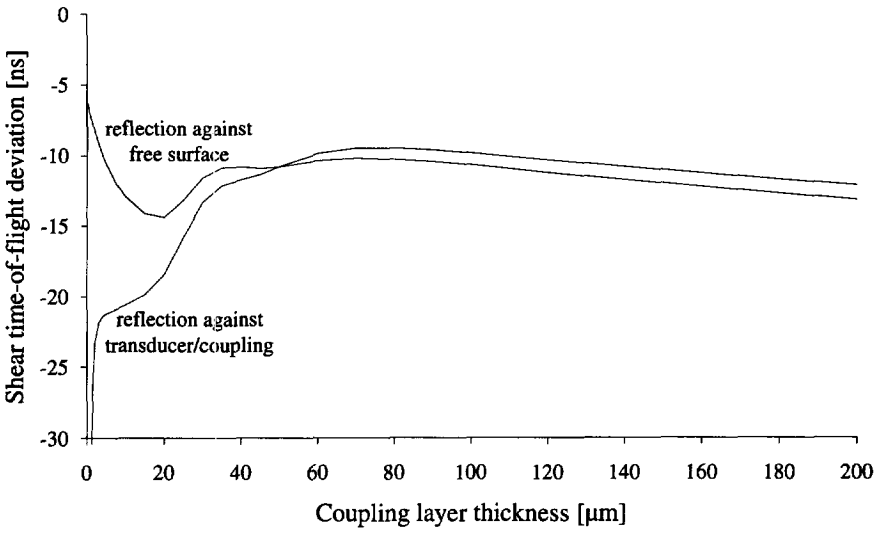

Fig. 5.24 The shear time-of-flight deviation as a function of the coupling layer thickness in a 15 mm steel specimen, calculated for the normal situation, where during its flight the second back-face echo reflects either against the transducer/coupling combination or against a free surface.

echoes are responsible. As a consequence, the shape of the two echoes will depend differently on the layer thickness and, since time of flight is determined between the first zero crossings in the echoes, an effect on the time of flight is to be expected. This is further discussed below.

The fact that the longitudinal time of flight is affected much less than the shear time of flight can be explained from the propagation properties of the couplant, which are clearly less dispersive in the longitudinal case (Figs. 5.12 and 5.13).

Finally, it should be noted that at very small thicknesses the time-of-flight deviation is determined mainly by the impedance of the protective layer relative to that of the propagation medium. In the case considered here, there is little difference between these values, causing the first part of the second back-face echo to have a very small amplitude. This results in deviations as large as –70 and –35 ns for shear and longitudinal waves respectively at zero coupling layer thickness.

The combined effect of couplant attenuation and diffraction in the case of thick coupling layers

Extra calculations are performed, in particular for shear waves, in order to gain more insight into time-of-flight effects in the case of thick coupling layers. Above the limit thickness the first part of a back-face echo (including the first zero crossing) can be considered as being part of a wave which is not reflected within the coupling layer at all. Therefore, changes in

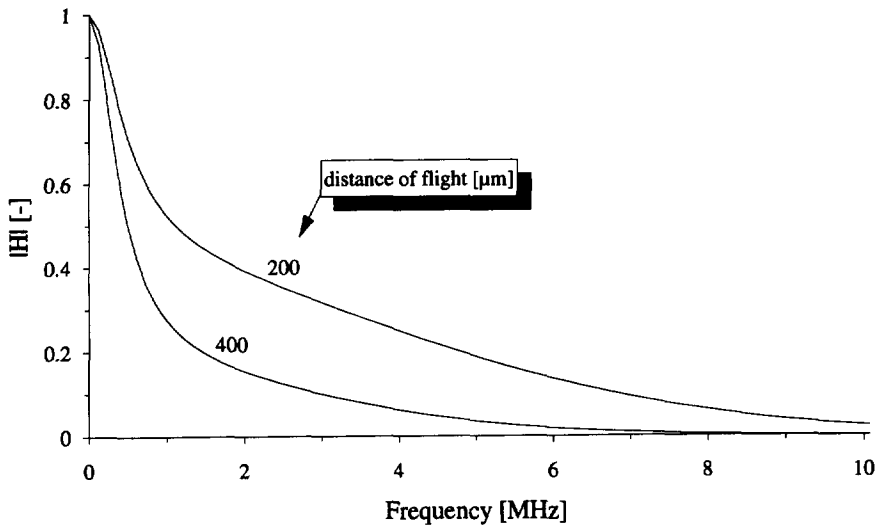

Fig. 5.25 Calculated modulus of the transfer function for shear wave propagation in the couplant.

the measured time of flight above the limit thickness can best be assessed by observing the distortion to which such a wave is subject.

First the modulus of the transfer function for wave propagation through the couplant is calculated. In Figure 5.25 the result is plotted for wave propagation distances of 200 and 400 µm, corresponding to the distances which the above wave travels in the couplant at layer thicknesses of 100 and 200 µm respectively. The graph shows a modulus which rapidly decreases with frequency.

Using this, together with the modulus of the diffraction transfer function (Fig. 5.20), the transfer function between the wave amplitudes transmitted into and received from the couplant are calculated as if no reflections occur in the coupling layer. For the first back-face echo this amounts to diffraction over twice the specimen thickness and wave propagation over twice the coupling thickness, taking into account the transmission coefficients from the couplant to the specimen and vice versa. For the second back-face echo the diffraction distance is four times the specimen thickness, and reflection from the specimen against the couplant is also considered. In Figure 5.26 the moduli of the resulting transfer functions are shown for four specimen thicknesses and two coupling layer thicknesses.

The model broad-band shear wave transducer has a nominal frequency of 5 MHz. However, in combination with these transfer functions most of the energy in the back-face echoes will be concentrated between 3 and 5 MHz for a 100 µm coupling layer and between 2 and 4 MHz for a 200 µm coupling layer. Clearly this shift to lower frequencies is due to attenuation in the couplant (Fig. 5.25).

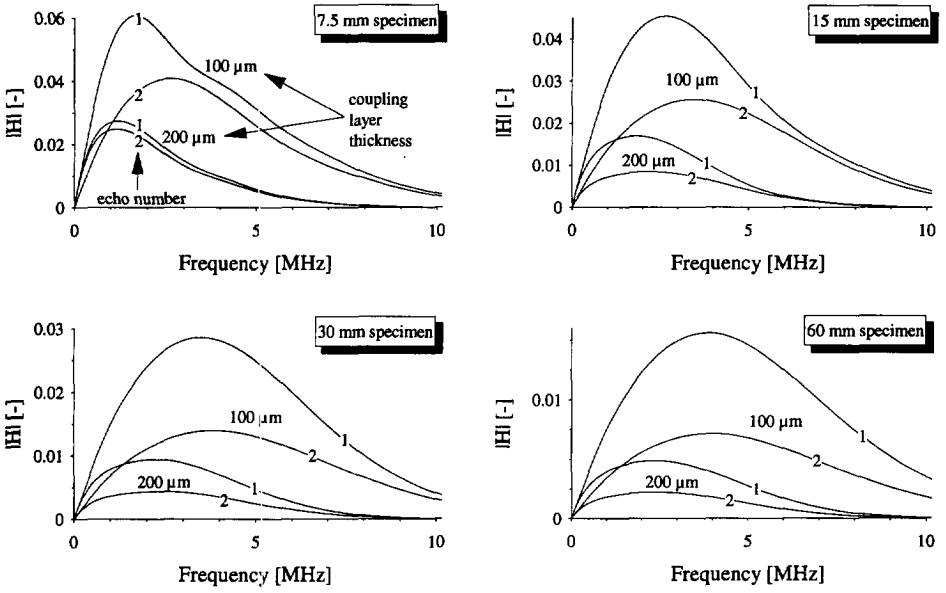

Fig. 5.26 Calculated moduli of the transfer functions between the shear wave amplitudes transmitted into and received from the couplant for the 1st and 2nd back-face echoes. The results from Figures 5.20 and 5.25 have been used, together with the appropriate reflection and transmission coefficients. The assumption is made that no reflections occur within the coupling layer.

For thick specimens (30 and 60 mm) and in the relevant frequency range, the moduli of the transfer functions for the first and second back-face echoes are roughly congruent. Furthermore, as a consequence of increasing the coupling layer thickness from 100 to 200 µm, the moduli are found to decrease proportionally. Although only the moduli of the transfer functions are considered and not the phase, the results suggest that the two back-face echoes are congruent and subject to a similar distortion when changing the coupling layer thickness. The situation is completely different for thin specimens. It is obvious from Figure 5.26 that the two echoes do not have the same shape and that they are also affected differently by the coupling layer thickness.

These findings agree with the results shown in Figure 5.22 for cases above the limit thickness, namely that the time of flight measured is affected by the coupling layer thickness only in the case of thin specimens (7.5 and 15 mm). The cause of this is diffraction in the specimen. Increasing the coupling layer thickness particularly attenuates the high-frequency components in the back-face echoes. By itself, this will not influence time-of-flight measurements, as the echoes are attenuated equally. However, in a thin specimen the back-face echoes are shaped differently, due to diffraction. This can be seen by comparing the diffraction transfer functions for 15 and 30 mm distances (Fig. 5.20) applying to the first and second echoes respectively in a 7.5 mm specimen. In a thick specimen, on the other hand, diffraction

will not change the shape of the echoes, but only their amplitude. The diffraction transfer functions for 120 and 240 mm distances indicate this for a 60 mm specimen.

5.5.4 Electrical settings

Section 3.4.2 contains a description of the electronic circuitry for the pulser-receiver used in the experimental set-up in combination with the piezoelectric transducer (see Fig. 3.19). The electrical settings of the pulser-receiver include the energy capacitance, damping

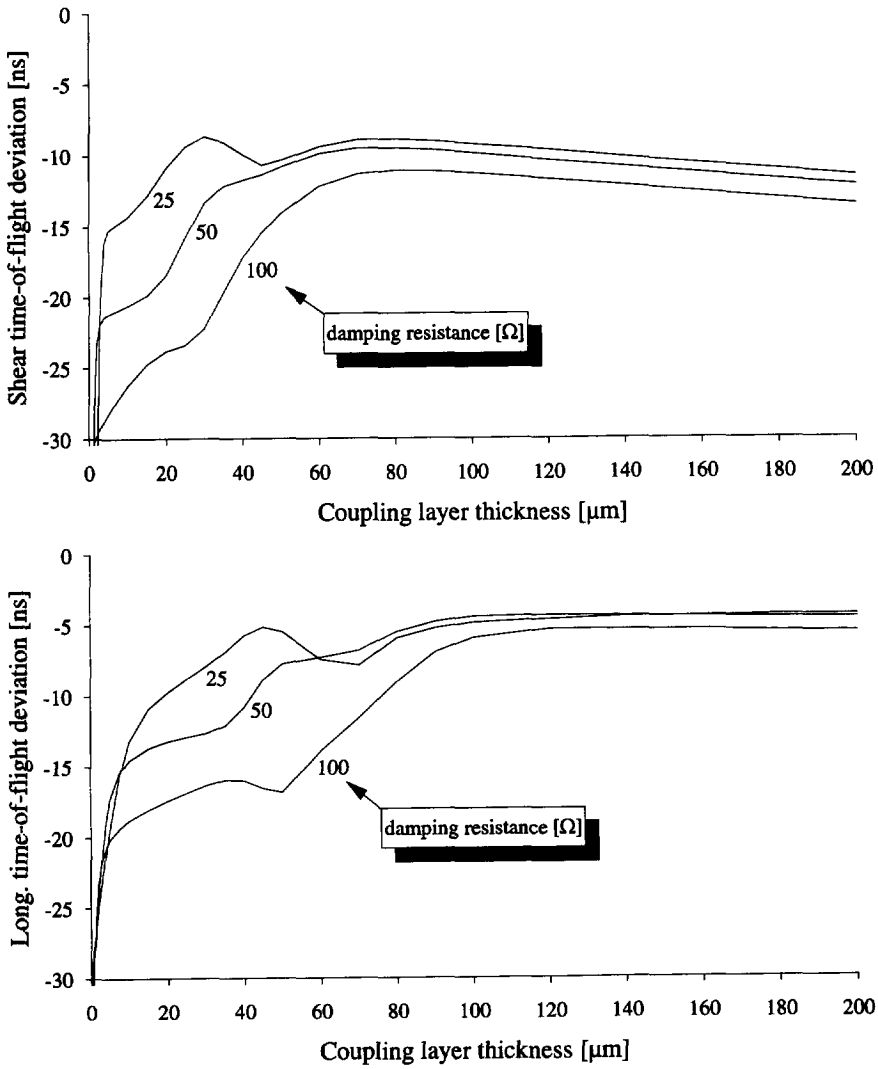

Figs. 5.27 & 5.28 Shear and longitudinal time-of-flight deviation in a 15 mm steel specimen, calculated as a function of the coupling layer thickness for different values of the damping resistance.

resistance, amplifier bandwidth and lower cut-off frequency. Changing one of these can either lead to a differently shaped pulse exciting the transducer or may distort the signal received by the transducer. Additionally, when the value of the damping resistor is changed, the operation of the transducer itself is affected, due to the different impedance terminating the transducer electrodes. In all cases the output signal ultimately available, which represents the series of back-face echoes, is distorted. This distortion is common to all back-face echoes. However, as the transfer function from transmitting to receiving transducer differs for each echo, each will be affected differently. It is to be expected therefore that the time of flight measured between the first and second echo is influenced by the electrical settings.

In the present calculations the attention is focused on the influence of the damping resistance. This quantity was introduced into the model through the source impedance Z_s of the pulser in combination with the corresponding waveform for the source voltage V_s. The time of flight is calculated as a function of the coupling layer thickness for shear and longitudinal waves in a 15 mm steel specimen using different values for the damping resistance. The results are plotted in Figures 5.27 and 5.28.

The most striking aspect of the results is the fact that time of flight is influenced much more significantly by the damping resistance if the coupling layer thickness is below the limit value. In the foregoing discussion concerning the influence of the coupling layer thickness below the limit value, it was concluded that the extra reflection to which the second back-face echo is subject is an important cause of the marked effect on time of flight. Due to this reflection, the waveforms of the two echoes will differ to a greater extent. As a consequence wave distortion, such as is induced by changing the damping resistance, can have more effect on the time of flight.

Above the limit thickness the damping resistance is found to have a somewhat larger influence on the shear time of flight than on the longitudinal time of flight. An explanation for this cannot be given.

It should be noted that the limit coupling thickness itself will also be affected by the damping resistance. Increasing the damping resistance widens the pulse exciting the transducer, and consequently delays the first zero crossing in the back-face echoes. For example, the limit thickness for longitudinal waves is increased from 90 to about 110 μm when changing the damping resistance from 50 to 100 Ω.

5.5.5 Transducer misalignment

The analysis of a tilted transducer is performed by dividing the transducer into 16 subtransducers. The effect of the tilt angle on time of flight and echo amplitude are considered.

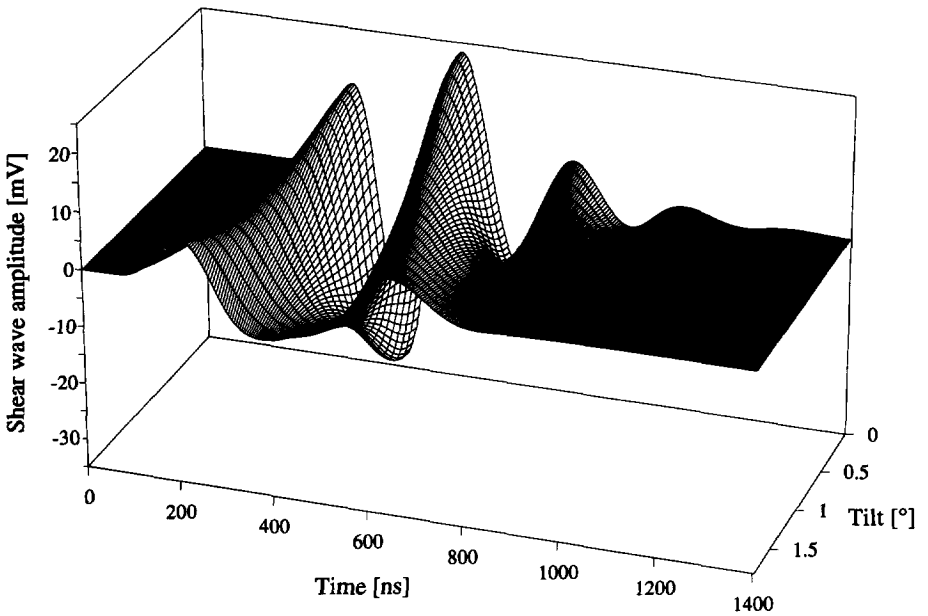

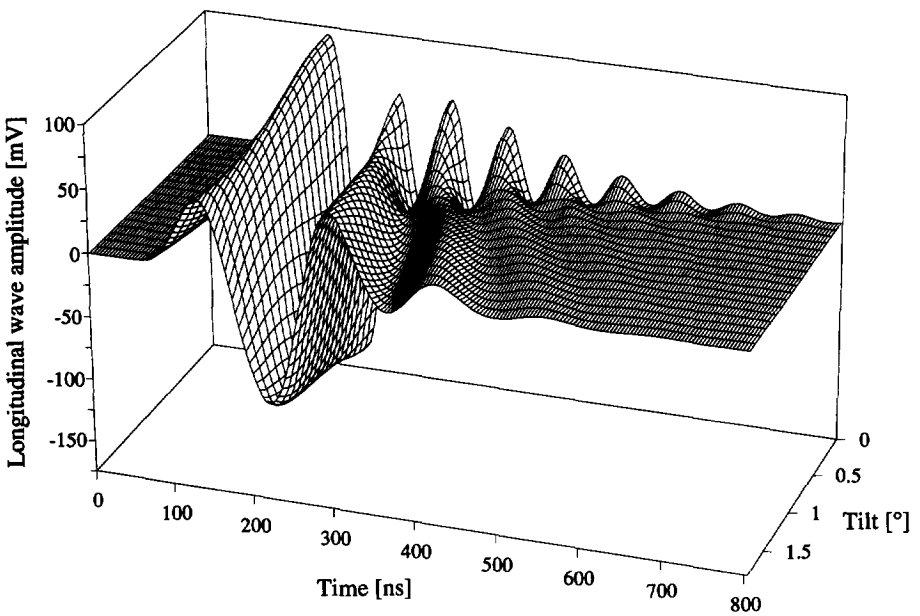

Figs. 5.29 & 5.30 First shear and longitudinal back-face echoes in a 15 mm steel specimen for a 100 mm coupling layer, calculated for increasing transducer tilt angles.

However, it is interesting to first note the effect of tilt on the waveform of back-face echoes. Figures 5.29 and 5.30 show the first shear and longitudinal back-face echoes in a 15 mm steel specimen for increasing transducer tilt angles. It can be observed that in both cases the echo amplitude decreases with the tilt angle. At the same time it is found that high frequencies are attenuated more than proportionally. This seems reasonable, in view of the increasing differences in distance of flight occurring at larger tilt angles.

The graph in Figure 5.30 also illustrates the suppression of the resonance tail in longitudinal

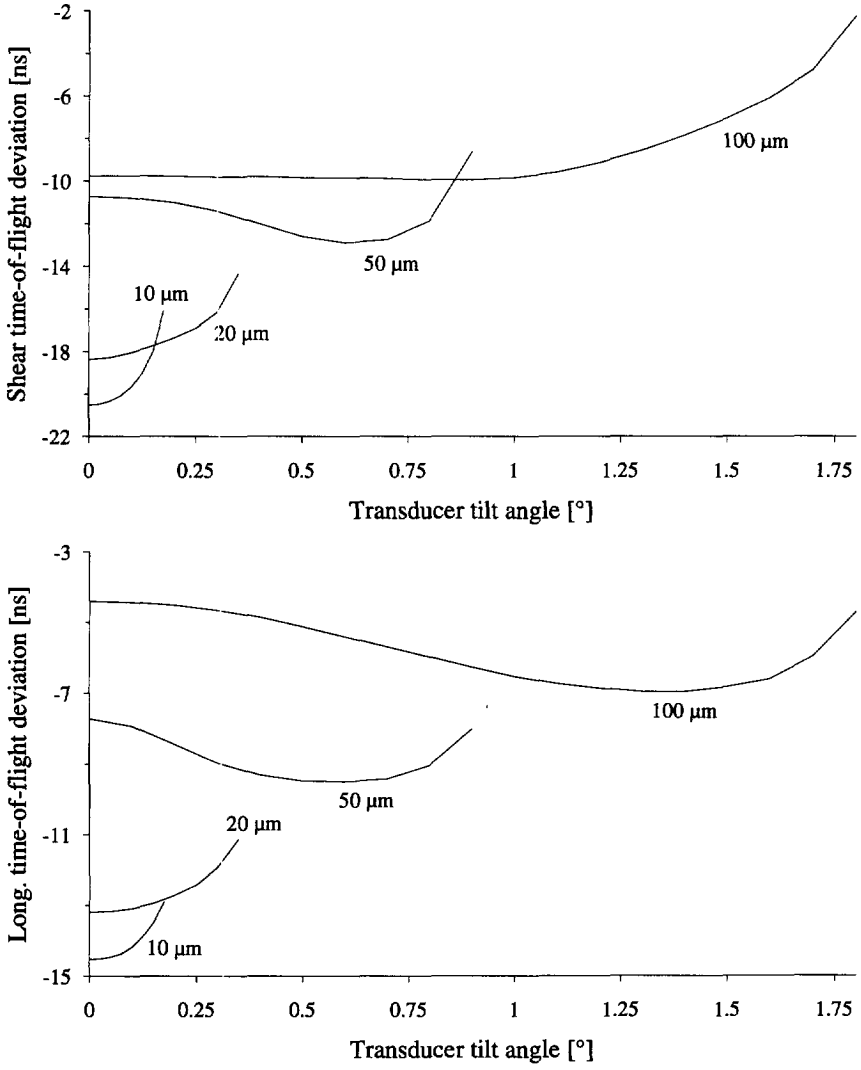

Figs. 5.31 & 5.32 Shear and longitudinal time-of-flight deviation in a 15 mm structural steel specimen, calculated as a function of the transducer tilt angle for different coupling layer thicknesses.

echoes, shown in Fig. 5.17 for perfect alignment, by transducer tilt.

Effect on time of flight

The shear and longitudinal time of flight in a 15 mm thick structural steel specimen is calculated as a function of the transducer tilt angle. In Figures 5.31 and 5.32 the results are shown for four different coupling layer thicknesses. The lines are plotted from zero to the maximum tilt angle possible for the respective layer thicknesses. As was discussed in the description of the model, it is questionable whether the results are valid up to this point. However, as the

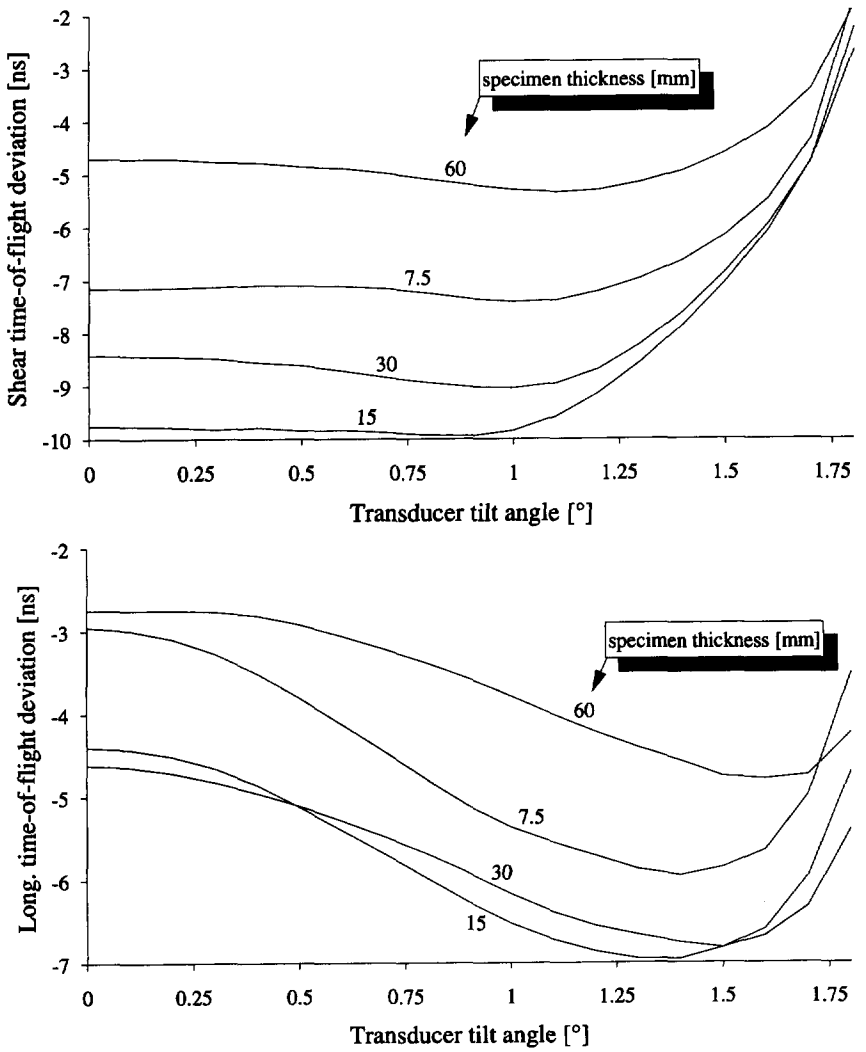

Figs. 5.33 & 5.34 Shear and longitudinal time-of-flight deviation in a steel specimen as a function of the transducer tilt angle, calculated for a 100 mm thick coupling layer and different specimen thicknesses.

results at small tilt angles are the most relevant, no attempt will be made to assess the maximum allowable tilt angle.

It is obvious that the time of flight for thin coupling layers is affected more by a given transducer tilt than the time of flight for thicker layers. A straightforward explanation cannot be given. It is a fact that the relative differences in the coupling layer thickness over the transducer area are larger for thinner layers. Moreover, as shown in the Figures 5.22 and 5.23, the effect on the time of flight is much larger for small thicknesses.

The results in Figures 5.31 and 5.32 also show that for shear waves and a 100 μm thick coupling layer, changes in the time of flight remain less than 0.2 ns for tilt angles up to 1°. In the longitudinal case the time-of-flight change is larger, namely 0.6 ns at 0.5° tilt. A possible explanation for this increased effect is related to the diffraction phenomenon. The high-frequency wave components in particular exhibit a strong directional sensitivity when being transmitted. Furthermore, in the longitudinal case these wave components are attenuated much less by the couplant than in the shear case. It seems likely, therefore, that transducer tilt, which involves an offset of the transmitted wave beam relative to the receiver, will more significantly influence the received longitudinal waveform.

The results presented above are for a 15 mm thick steel specimen. In Figures 5.33 and 5.34 the results are plotted for different specimen thicknesses and a 100 μm coupling layer thickness. It can be seen that the influence of transducer tilt on time of flight is not significantly affected by the specimen thickness.

Effect on echo amplitude

Transducer tilt also affects the amplitude of back-face echoes. This aspect is relevant when determining the polarization direction of birefringent shear wave components by measuring the amplitude as a function of the transducer orientation. In order to assess this, the amplitudes of the echoes are considered as already calculated for the case of a tilted transducer. In particular, the value of the first peak (a maximum) in each first back-face echo is determined.

In Figures 5.35 and 5.36, the amplitude change in the shear and longitudinal echoes respectively is plotted as a function of the transducer tilt angle for different coupling layer thicknesses. For shear waves it is found that the echo amplitude using thin coupling layers increases with the tilt angle, while a decrease can be observed for thick layers. This decrease is 1.9 dB at 0.5° tilt. In the longitudinal case the effects are less pronounced. For thick layers the amplitude decreases by only 0.8 dB at 0.5° tilt, while for thin layers there is either no amplitude increase or only a slight increase.

In the first example it seems obvious that a transducer tilt would cause a decrease in echo amplitude, due to the offset of the reflected wave beam relative to the receiving transducer.

There is no argument available to explain the amplitude increases found for thin coupling layers. They could perhaps be related to the interaction between the coupling layer and the transducer, which in such cases will be stronger.

As was the case with the effect of transducer tilt on time of flight, the effect on amplitude is not significantly different for other specimen thicknesses.

As was discussed in Section 3.3.2, the echo amplitudes shown in Figure 3.14 are af-

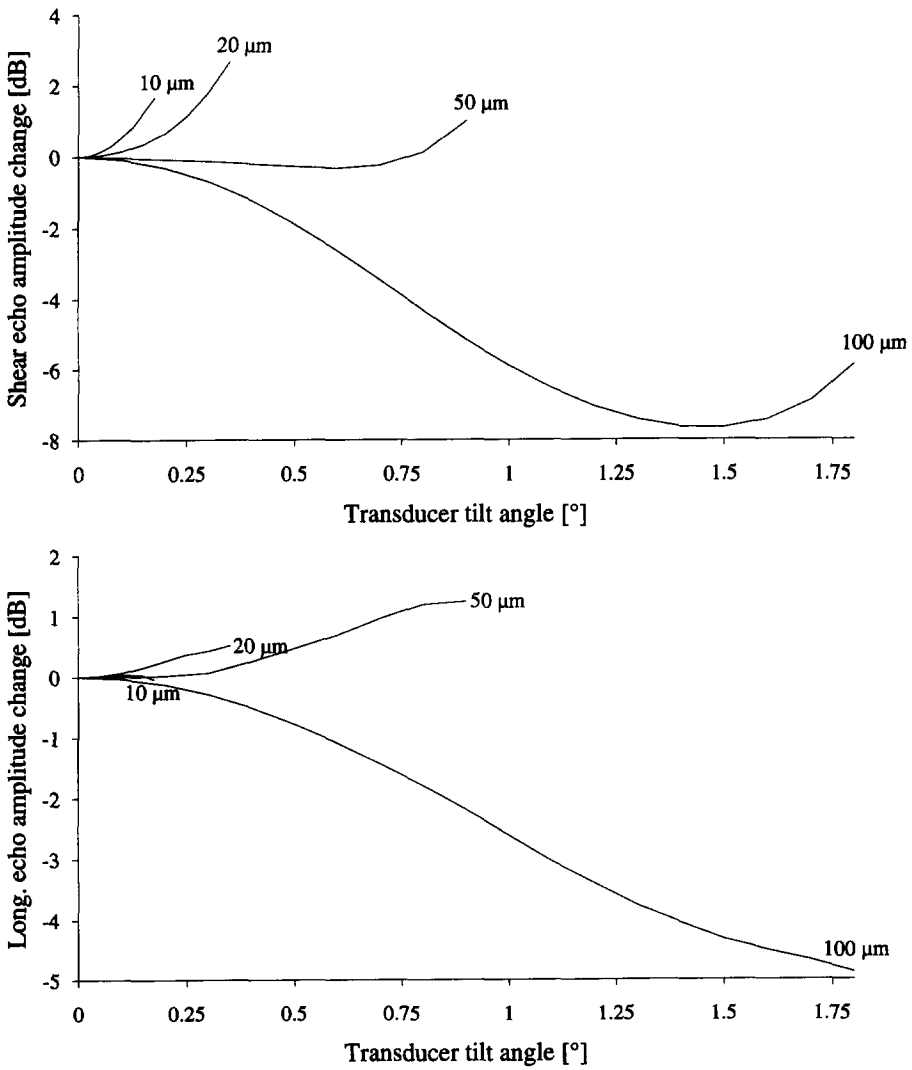

Figs. 5.35 & 5.36 Amplitude change in the first maximum of the first shear and longitudinal back-face echoes in a 15 mm steel specimen, calculated as a function of the transducer tilt angle for different coupling layer thicknesses.

fected by transducer misalignment. The amplitude variation between the polarization directions for maximum and minimum transducer tilt is about 0.8 dB for both shear and longitudinal echoes. Based on the estimated transducer misalignment, i.e. 0.5 ± 0.2°, the results of the model calculations would suggest amplitude changes of 2.8 and 1.1 dB for shear and longitudinal waves respectively. Thus, for shear waves, the calculated changes are found to be significantly larger. This cannot be explained, although it is noted that only a rough estimate is made of the transducer misalignment. Moreover, the model configuration can hardly be assumed to be an exact copy of the experimental set-up.

5.5.6 Cross-correlation method

In Section 3.2.3, several techniques for determining the time of flight were reviewed. Among these techniques the cross-correlation method was mentioned [17]. Here this method is applied to the results of the model calculations, i.e. the first and second shear and longitudinal back-face echoes in a 15 mm thick steel specimen evaluated as a function of the coupling layer thickness. These results are already in a form in which each echo is available in its own time window. By calculating the cross-correlation or correlation of these waveforms [5, 44] and determining the maximum of this function of time, the deviation from the nominal time-of-flight value is found.

Figure 5.37 shows the outcome of these calculations. It may be compared with the time-of-flight deviation as it was calculated using the first zero crossings (Figs. 5.22 and 5.23). It is obvious that the time of flight remains dependent on the coupling layer thickness

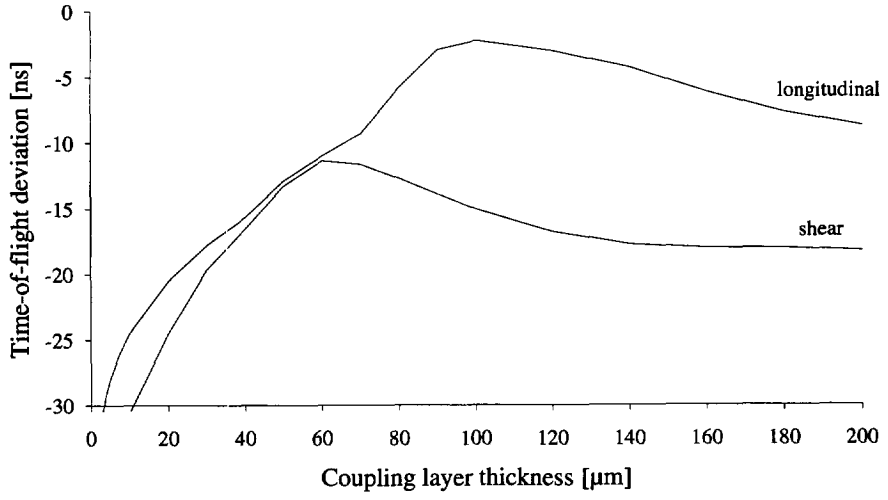

Fig. 5.37 Shear and longitudinal time-of-flight deviation in a 15 mm steel specimen as a function of the coupling layer thickness, determined by applying the cross-correlation method to the back-face echoes calculated by the model.

over the whole range considered.

When using the cross-correlation method, there is no limit layer thickness, i.e. a thickness value above which the extra reflections within the couplant no longer play a role. Increasing the coupling layer thickness only shifts the effect of reflections to later times within each back-face echo. It is clear that the influence of reflections is not spread evenly over the echo waveform. However, the correlation function is calculated over the whole of the waveforms of the first two back-face echoes. This suggests that the correlation function is dependent on the coupling layer thickness, even at large values. This appears to explain the time-of-flight deviation calculated according to the cross-correlation method.

It should be noted that for large coupling layer thicknesses time of flight is affected less in the case of shear waves than in the case of longitudinal waves. This may be due to the high attenuation for shear waves in the couplant, causing the amplitude of reflections to become relatively small.

5.6 Conclusion

In this chapter a model is described for the pulse-echo method. The model is approximately based on the experimental set-up for acoustoelastic stress measurements as described in Chapter 3. Model calculations for single-mode shear and longitudinal transducers yield echo waveforms that compare reasonably well with those measured using the combined shear-longitudinal transducer of the set-up. The echo amplitude, however, is found to be smaller.

Based on these calculations, several factors were considered which affect the results of a pulse-echo measurement. Besides the piezoelectric transducer itself, the factors include diffraction in the specimen, the viscous coupling layer, electrical conditions, and transducer misalignment. Relevant results were presented, as calculated using the model.

The most important aspect of the pulse-echo method is the *time of flight* measured. In the present method time of flight is determined between the first zero crossings in the first two back-face echoes. The model calculations showed that this measured time of flight inherently deviates from the nominal value, owing to diffraction in the specimen. Another important source of deviations was found to be the extra reflection of the second back-face echo against the combination of transducer and coupling layer. The results indicated that this plays a particularly important role when thin coupling layers are used, as in conventional practice. Attenuation is then low, and multiple reflections occur within the coupling layer. Above a certain limit layer thickness, these reflections are delayed beyond the first zero crossings in the echoes and no longer affect the measured time of flight. However, the calculations revealed that the combined effect of dispersion in the couplant and diffraction in the specimen can still slightly affect the time of flight. This was particularly found for shear waves, which are subject to more dispersion in the couplant than longitudinal waves, and for thin specimens, in which diffraction causes more differences between the echo waveforms.

It is clear that time-of-flight deviations will inevitably occur. From the point of view of reproducibility, however, the dependence on the coupling layer thickness is of much more importance, since in practice this quantity cannot be well controlled. This thickness determines both the delay of reflections within the layer and the level of dispersion for waves passing through it. The importance of the limit layer thickness lies in the fact that below this value the two phenomena affect successive back-face echoes in different ways, leading to large time-of-flight deviations. In contrast to this, above the limit value only dispersion is relevant, acting equally on all echoes. A significantly smaller influence on time of flight is the result.

As far as the *electrical settings* are concerned, the calculation results indicated a much larger effect on time of flight for coupling layers below the limit thickness. The distortion

caused by changing electrical settings has more effect below this value, owing to larger waveform differences in successive back-face echoes. In general it may be concluded that reducing such differences will improve the reproducibility of the pulse-echo measurements. Thus, in this case also, the use of thick coupling layers for time-of-flight measurements is to be preferred.

The results with respect to a *tilted transducer* demonstrated a decrease in the echo amplitude with an emphasis on high-frequency components. The calculated decrease in the echo peak amplitude was somewhat higher than that found experimentally. The effect on the measured time of flight was smaller for a thick coupling layer (100 μm) than for thinner layers. The consequences which this has in an actual set-up depend on the mechanical construction used to position the transducer.

There are several aspects of the model described in this chapter for which simplifications have been introduced in order to permit or facilitate calculations. The pulser is reduced to a simple voltage source with given impedance; for the transducer a one-dimensional model is used; the ultrasonic properties of the couplant were quantified by means of a viscoelastic model. It is justifiable to question the *applicability of the model* to an actual pulse-echo set-up, such as the one described in Chapter 3. In the present chapter, where possible, the calculated results were compared with those obtained experimentally, e.g. the echo waveforms, the measured time of flight as a function of the coupling layer thickness and the echo amplitude for a tilted transducer. Based on these comparisons, it is believed that the model provides an appropriate description of an experimental pulse-echo set-up.

Appendix 5A The Fourier transform

A quantity which plays a role in a particular physical process can be expressed in two different ways, namely:

- in the time domain, by describing the value of the quantity as a function of time t, e.g. f(t).
- in the frequency domain, by describing the amplitude and phase of the quantity as a function of (angular) frequency ω in the form of a complex function $F(\omega)$.

Each of these functions contains all information concerning the behaviour of the physical quantity in the process. The functions are related to each other through the *Fourier transform equations* [5]:[I]

$$F(\omega) = \int_{-\infty}^{+\infty} f(t)e^{-i\omega t}dt \qquad (5A.1^a)$$

$$f(t) = \frac{1}{2\pi}\int_{-\infty}^{+\infty} F(\omega)e^{i\omega t}d\omega \qquad (5A.1^b)$$

It should be noted that negative frequencies are also included.

Not every function has a Fourier transform. However, functions which represent *physically possible* signals, i.e. which are an accurate description of the behaviour of a physical quantity, can always be transformed.

The discrete Fourier transform

Consider a physical signal, the value of which is sampled at an *even* number of equidistant time values, i.e.:

$$f_k = f(t_k) \text{..... for } k = 0,1,2,...,N-1 \qquad (5A.2)$$

where f_k = signal value

$t_k = k \cdot \Delta t$

Δt = time interval

N = number of sampled points

The frequency for which exactly two samples are taken per cycle is called the *Nyquist criti-*

[I] A number of alternative formulations for the transform equations are also in use.

cal frequency ω_c and is equal to $\pi/\Delta t$. Higher frequency components cannot be shown to be present in the signal. Therefore, the Fourier transform of the discrete samples will yield only values in the frequency domain ranging from $-\omega_c$ to $+\omega_c$.

By approximating the continuous Fourier transform equations given above, the *discrete Fourier transform* equations can be found [44]:

$$F_n = \sum_{k=0}^{N-1} f_k e^{-2\pi ikn/N} \qquad (5A.3^a)$$

$$f_k = \frac{1}{N}\sum_{n=0}^{N-1} F_n e^{2\pi ikn/N} \qquad (5A.3^b)$$

where $F_n \approx \frac{1}{\Delta t} F(\omega_n)$

$$\omega_n = \frac{2\pi n}{N\Delta t}$$

The N discrete samples in the time domain, f_k, are transformed to N discrete samples in the frequency domain, F_n, and vice versa. It can be seen from the equations that in both domains the samples are periodic with a period N. It is important to realize that transforming a series of time-domain samples inherently assumes that the signal extends periodically outside the sampled range, with a period equal to the sample length $N \cdot \Delta t$.

It would seem that the frequencies ω_n extend to twice the Nyquist frequency. However, owing to the periodicity, the samples with indexes ranging from $N/2$ to $N-1$ are equal to those with indexes between $-N/2$ to -1 and thus correspond to the negative frequency range.

If the samples in the time domain are real numbers, which is most often the case with a physical signal, the transformed samples for negative frequencies are the complex conjugate of the samples for the opposite positive frequencies. Consequently, the transform is completely described by specifying only F_0 to $F_{N/2}$. In fact the samples F_0 and, due to the periodicity, $F_{N/2}$ must be real numbers.

A convenient technique to calculate the discrete Fourier transform is the so-called *Fast Fourier Transform* [44]. A straightforward evaluation requires a calculation time proportional to N^2, whereas for the FFT algorithm, it is proportional only to $N \log_2 N$. FFT works out much faster, especially for large N-values. One disadvantage, however, is that it requires N to be an integer power of 2.

Appendix 5B Wave excitation and detection in a piezoelectric plate

Introduction

Consider an electrically insulating material exhibiting piezoelectric behaviour defined by the *constitutive equations*:

$$D_i = \varepsilon_{ij}^S E_j + e_{ijk} S_{jk} \tag{5B.1}$$

$$T_{ij} = C_{ijkl}^E S_{kl} - e_{kij} E_k \tag{5B.2}$$

where $\underline{D}$ = electric displacement vector
$\underline{E}$ = electric field vector
$\underline{T}$ = stress tensor
$\underline{S}$ = strain tensor
$\underline{\underline{e}}$ = 3rd-order piezoelectric stress tensor
$\underline{\underline{C}}^E$ = stiffness tensor for constant electric field
$\underline{\underline{\varepsilon}}^S$ = 2nd-order permittivity tensor for constant strain

For the description of acoustic wave propagation in this material it is convenient to use a *quasi-static approximation* [1, 10]. By this means the electromagnetic part of the electric field is neglected and $\underline{E}$ can be exclusively expressed as the negative gradient of the electric potential ϕ:

$$E_i = -\frac{\partial \phi}{\partial x_i} \tag{5B.3}$$

Furthermore, as an insulator is being considered here, no free charge is available, and the divergence of the electric displacement field is zero:

$$\frac{\partial D_i}{\partial x_i} = 0 \tag{5B.4}$$

Plane wave propagation in piezoelectric material

Using the *equation of motion* in the absence of body forces:

$$\frac{\partial T_{ij}}{\partial x_j} = \rho \frac{\partial^2 u_i}{\partial t^2} \tag{5B.5}$$

where $\underline{u}$ = particle displacement
ρ = mass density

and the definition of the *infinitesimal strain tensor*:

$$S_{ij} = {}^1/_2\left(\frac{\partial u_j}{\partial x_j} + \frac{\partial u_j}{\partial x_i}\right) \tag{5B.6}$$

the expressions 5B.1 to 5B.4 lead to the following *wave equations*:

$$C^E_{ijkl}\frac{\partial^2 u_k}{\partial x_j \partial x_l} + e_{kij}\frac{\partial^2 \phi}{\partial x_k \partial x_j} = \rho\frac{\partial^2 u_i}{\partial t^2} \tag{5B.7}$$

$$\varepsilon^S_{ij}\frac{\partial^2 \phi}{\partial x_i \partial x_j} - e_{ijk}\frac{\partial^2 u_k}{\partial x_i \partial x_j} = 0 \tag{5B.8}$$

At this point *harmonic plane wave* solutions are assumed for the displacement $\underline{u}$ and the electric potential ϕ. They have an angular frequency ω, wave number k and a propagation direction along the unit vector $\underline{n}$. Their fields are thus proportional to:

$$e^{i(\omega t - k n_j x_j)}$$

After substitution, the wave equations lead to:

$$C^E_{ijkl} n_j n_l u_k + e_{kij} n_j n_k \phi = \rho\frac{\omega^2}{k^2} u_i \tag{5B.9}$$

$$\varepsilon^S_{ij} n_i n_j \phi - e_{ijk} n_i n_j u_k = 0 \tag{5B.10}$$

By eliminating the potential ϕ, while using the symmetry $e_{ijk} = e_{ikj}$, the following eigenvalue equation is found:

$$\Gamma_{ik} u_k = \rho\frac{\omega^2}{k^2} u_i \tag{5B.11}$$

$$\text{where } \Gamma_{ik} = \left(C^E_{ijkl} + \frac{e_{mij} n_m e_{nkl} n_n}{\varepsilon^S_{pq} n_p n_q}\right) n_j n_l$$

In fact this is the *Christoffel equation* for plane waves in a piezoelectric material. The Christoffel tensor $\underline{\underline{\Gamma}}$ is *piezoelectrically stiffened*, depending on the propagation direction $\underline{n}$. As in the non-piezoelectric case, the eigenvectors and corresponding eigenvalues of $\underline{\underline{\Gamma}}$ respectively define the particle displacement directions $\underline{u}$ and phase velocities ω/k of plane wave solutions. The terms between brackets in the definition of $\underline{\underline{\Gamma}}$ are also referred to as *stiffened elastic constants*, although they are not real elastic constants, as they are dependent on $\underline{n}$ and only applicable to plane waves.

Piezoelectric plate

Consider the configuration shown in Figure 5B.1. Two non-piezoelectric media are attached to a piezoelectric plate having flat and parallel surfaces with area A. Electrically conductive layers are present at the interfaces. These act as electrodes and are sufficiently thin to permit their influence on elastic wave propagation to be ignored. The thickness d of the plate, which is in the x_3-direction, is taken small relative to its other dimensions. It is assumed for this geometry that deviating effects at the plate edge are negligible and that only the dependence on x_3 needs to be considered for the relevant field quantities:

- Electric potential ϕ
  Since the electric field is written as the gradient of the potential (Eq. 5B.3), the components E_1 and E_2 vanish.
- Electric displacement $\underline{D}$
  Component D_3 is constant throughout the plate, owing to zero divergence (Eq. 5B.4).
- Stress $\underline{T}$
  Only stress components T_{i3} are relevant when considering elastic waves (Eq. 5B.5).
- Particle displacement $\underline{u}$
  Only displacement gradient components $\partial u_i/\partial x_3$ are non-zero.

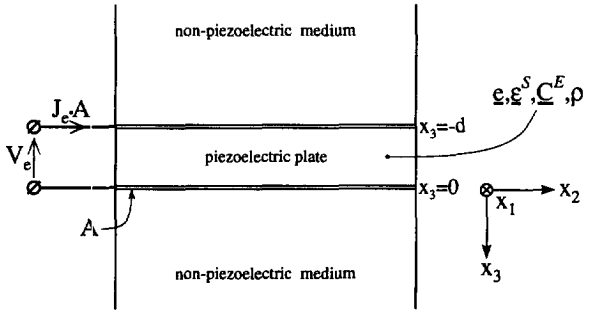

Fig. 5B.1 Piezoelectric plate with electrodes, sandwiched between two non-piezoelectric media.

For the piezoelectric plate configuration, the voltage across the electrodes, V_e, can be related to the electric field in the plate. As the gradient of the potential (Eq. 5B.3) is now identical to component E_3, this voltage follows from:

$$V_e = \int_0^{-d} -E_3(x_3)dx_3 = \int_{-d}^{0} E_3(x_3)dx_3 \qquad (5B.12)$$

The current density at the inner electrode surfaces can be related to the electric displacement in the plate. The electrical boundary conditions require that the component normal to the

electrode/plate interfaces, i.e. D_3, is continuous.[I] Therefore the electrode current density J_e must be:

$$J_e = \frac{\partial D_3}{\partial t} \tag{5B.13}$$

The first constitutive equation (Eq. 5B.1) is now reduced to what is relevant to the present configuration:

$$D_3 = \varepsilon_{33}^S E_3 + e_{3k3}\frac{\partial u_k}{\partial x_3} \tag{5B.14}$$

When reducing the second constitutive equation (Eq. 5B.2), it is convenient to simultaneously eliminate the position-dependent electric field component E_3 by substituting the expression above. This leads to:

$$T_{i3} = \left(C_{i3k3}^E + \frac{e_{3i3}e_{3k3}}{\varepsilon_{33}^S}\right)\frac{\partial u_k}{\partial x_3} - \frac{e_{3i3}}{\varepsilon_{33}^S}D_3 \tag{5B.15}$$

According to this description of the stress field in the plate, one part is proportional to displacement gradients $\partial u_i/\partial x_3$ through the stiffened elastic constants (Eq. 5B.11) for plane wave propagation in the x_3-direction. It thus represents the stress field caused by such waves. The other part of the stress field is proportional to electric displacement component D_3 and is therefore constant throughout the plate.

Simplified analysis

Generally, in an elastic medium, three plane waves can propagate in a given direction. These waves are polarized normal to each other along the eigenvector solutions of the Christoffel equation (e.g. Eq. 5B.11). The assumption is now made that the electromechanical coupling only includes one of the three wave solutions travelling in the thickness direction of the plate. This situation will arise if the vector formed by components e_{3i3} coincides with the polarization direction of that particular wave. The remaining two waves are then polarized normal to this vector and consequently their traction forces cannot be induced electrically (Eq. 5B.15).[II] Moreover, as the second term in Equation 5B.14 vanishes for these waves, they do not affect the field quantities $\underline{D}$ and $\underline{E}$.

A second assumption is also made at this point, namely that the elastic properties of the two

[I] Another requirement arising from the electrical boundary conditions is continuity of the tangential component of the electric field. As $\underline{E}$ is directed normal to the plate/electrode interfaces, fulfilment of this requirement will be guaranteed if the electrode material is assumed to be a perfect conductor.

[II] The polarization of a plane wave indicates not only the direction of particle displacement but also that of the traction vector acting on a plane normal to the propagation direction (see Appendix 3A).

adjacent non-piezoelectric media allow plane waves to travel in the x_3-direction with the same polarization direction as the coupled wave in the plate.

There is no fundamental argument for making these two assumption, but they do simplify the present analysis significantly. They also allow for a more concise notation using scalar quantities only. Let the unit vector $\underline{p}$ be directed parallel to the polarization of the coupled wave and thus, owing to the assumptions made, also parallel to the vector formed by components e_{3i3}. By defining:[1]

$$\begin{aligned} x &= x_3 & p_i e &= e_{3i3} \\ E &= E_3 & p_i u &= u_i \\ D &= D_3 & p_i T &= T_{i3} \\ \varepsilon^S &= \varepsilon^S_{33} \end{aligned} \tag{5B.16}$$

Equations 5B.14 and 5B.15 can be written as:

$$D = \varepsilon^S E + e\frac{\partial u}{\partial x} \tag{5B.17}$$

$$T = C\frac{\partial u}{\partial x} - \frac{e}{\varepsilon^S}D \tag{5B.18}$$

where C = eigenvalue of the piezoelectrically stiffened Christoffel tensor associated with the plane wave solution under consideration (Eq. 5B.11)

This is a linear and time-invariant set of equations, allowing all field variables, i.e. E, D, T and u, to be thought of as *time-harmonic functions* proportional to the same term $e^{i\omega t}$. Therefore, from now on these variables can be conveniently represented as complex quantities, with an amplitude and phase equal to their modulus and argument respectively, while ignoring the term $e^{i\omega t}$. Equations 5B.12 and 5B.13 permit the same notation for the electrical quantities V_e and J_e.

Plane wave excitation

In order to describe the excitation of plane waves, the mechanical conditions at the boundaries between the piezoelectric plate and the surrounding non-piezoelectric materials must be considered. For two rigidly bonded materials the traction force acting on the interface plane and the particle velocity must be continuous. For the one-dimensional plate configuration (Fig. 5B.1) these conditions read:

$$T = T' \tag{5B.19}$$

[1] The base of the natural logarithm and the piezoelectric stress constant e defined here can be distinguished by the way they appear in formulas.

$$\frac{\partial u}{\partial t} = \frac{\partial u'}{\partial t} \tag{5B.20}$$

where plane and primed quantities refer to piezoelectric and non-piezoelectric material respectively. If a stress field[I] is electrically induced in the plate (Eq. 5B.18), plane waves must be excited at its interfaces in order to maintain these boundary conditions. In view of the assumptions made above, only a single wave is excited on either side of each interface.

Consider an interface located at $x = \xi$, where harmonic plane waves are excited which travel into the piezoelectric and non-piezoelectric material. Their stress amplitudes, defined at the interface, are denoted as W and W' respectively. In the absence of waves from other sources, the stress fields in the two materials take the form of:

$$T(x) = W\, e^{\pm ik(x-\xi)} - \frac{e}{\varepsilon^S} D \tag{5B.21}$$

$$T'(x) = W'\, e^{\mp ik'(x-\xi)} \tag{5B.22}$$

The signs in the wave functions depend on the orientation of the two materials relative to the x-axis. The first boundary condition (Eq. 5B.19) yields:

$$W - \frac{e}{\varepsilon^S} D = W' \tag{5B.23}$$

Using the specific wave impedances in the two media, Z and Z', to relate the particle velocities of the waves to the traction forces W and W' acting on the interface plane (see Appendix 3A), the second boundary condition (Eq. 5B.20) leads to:[II]

$$\pm\frac{W}{Z} = \mp\frac{W'}{Z'} \tag{5B.24}$$

By solving these equations, the amplitudes are obtained of the two stress waves excited at the two plate interfaces. As the electric displacement D is considered a time-harmonic function, the electrode current density J_e is equal to $i\omega D$ (Eq. 5B.13) and thus:

$$W = -i\frac{Z}{Z+Z'}\frac{e}{\omega\varepsilon^S} J_e \tag{5B.25}$$

$$W' = +i\frac{Z'}{Z+Z'}\frac{e}{\omega\varepsilon^S} J_e \tag{5B.26}$$

I In this context stress is equivalent to a traction force acting on a plane normal to the x-axis.

II The wave impedance in the plate is calculated using the phase velocity ω/k following from the appropriate eigenvalue C of the piezoelectrically stiffened Christoffel tensor (see Eqs. 5B.11 and 5B.18), i.e. $Z = \rho\omega/k = \sqrt{\rho C}$.

Plane wave detection

Plane waves propagating in the thickness direction of the piezoelectric plate influence the electrical conditions at the terminals. This effect can be evaluated by integrating the expression for the electric displacement D (Eq. 5B.17) over the plate thickness and subsequently differentiating it with respect to time. This leads to:

$$J_e = \frac{i\omega}{d}\left[\varepsilon^S V_e + e\{u(0) - u(-d)\}\right] \tag{5B.27}$$

In this expression the mechanical influence is represented by the displacement difference between the two plate surfaces. Let the displacement field in the plate be caused by two harmonic plane waves with wave number k, travelling in positive and negative x-directions. Defining their stress amplitudes as W^+ and W^- at $x = -d$ and $x = 0$ respectively, the stress field associated with these waves can be written as:

$$T(x) = W^- e^{ikx} + W^+ e^{-ik(x+d)} \tag{5B.28}$$

which, according to Equation 3A.4, corresponds to a displacement field:

$$u(x) = \frac{i}{\omega Z}\left(W^+ e^{-ik(x+d)} - W^- e^{ikx}\right) \tag{5B.29}$$

where Z = specific wave impedance in the piezoelectric plate

Substitution of u(x) in Equation 5B.27 yields:

$$J_e = \frac{i\omega\varepsilon^S}{d} V_e + \frac{e}{dZ}(W^+ + W^-)(1 - e^{-ikd}) \tag{5B.30}$$

Appendix 5C Plane wave propagation in an attenuating medium

Christoffel equation

Consider a material with a constitutive behaviour which is linear and time-invariant, in the sense that if either stress or strain varies harmonically the other quantity will also do so, both quantities with the same frequency but not necessarily the same phase. Such constitutive behaviour offers a means of describing the dissipation of wave energy by the medium. For this purpose a *complex stiffness tensor* $\underline{\underline{\tilde{C}}}$ is implicitly defined as:

$$T_{ij} = \tilde{C}_{ijkl} S_{kl} \tag{5C.1}$$

where T_{ij}, S_{ij} = stress and strain tensors respectively, proportional to the time-harmonic function $e^{i\omega t}$

It should be noted that the constitutive behaviour of this material is described completely only if this stiffness tensor is known for all frequencies. In general therefore $\underline{\underline{\tilde{C}}}$ must be considered a (complex) function of frequency.

Based on the *equation of motion* in the absence of body forces:

$$\frac{\partial T_{ij}}{\partial x_j} = \rho \frac{\partial^2 u_i}{\partial t^2} \tag{5C.2}$$

where $\underline{u}$ = complex displacement
ρ = mass density of medium

the following *wave equation* can be formulated:

$$\tilde{C}_{ijkl} \frac{\partial^2 u_k}{\partial x_j \partial x_l} = \rho \frac{\partial^2 u_i}{\partial t^2} \tag{5C.3}$$

At this point a solution is sought in the form of an *attenuated plane wave* propagating along the unit vector $\underline{n}$ with a displacement proportional to:

$$u_i \div e^{-\alpha n_j x_j} e^{i(\omega t - k n_j x_j)} = e^{i\{\omega t - (k - i\alpha) n_j x_j\}} \tag{5C.4}$$

where α = attenuation coefficient
k = wave number

By defining a *complex Christoffel tensor* $\underline{\underline{\tilde{\Gamma}}}$, according to:

$$\tilde{\Gamma}_{ik} = \tilde{C}_{ijkl} n_j n_l \tag{5C.5}$$

the following *Christoffel equation* can be formulated:

$$\tilde{\Gamma}_{ik} u_k = \rho \frac{\omega^2}{(k - i\alpha)^2} u_i \tag{5C.6}$$

This eigenvalue equation describes the propagation of attenuated plane waves along $\underline{n}$ in a medium with a complex stiffness $\underline{\tilde{C}}$. In general three wave solutions follow in terms of three eigenvalues with corresponding eigenvectors. The eigenvalues are equal to $\rho\omega^2/(k^{(i)} - i\alpha^{(i)})^2$, where i = 1...3, and determine the phase velocities and attenuation coefficients of the wave solutions. The eigenvectors $\underline{u}^{(i)}$ indicate the corresponding polarization directions.

Specific wave impedance

The stress associated with the attenuated plane wave solution 5C.4 is found by substitution in Equation 5C.1:

$$T_{ij} = \tilde{C}_{ijkl} \frac{\partial u_k}{\partial x_l} = -i(k - i\alpha) \tilde{C}_{ijkl} n_l u_k \tag{5C.7}$$

leading to a traction force acting on planes normal to the propagation direction of:

$$T_{ij} n_j = -i(k - i\alpha) \tilde{C}_{ijkl} n_j n_l u_k = -i(k - i\alpha) \tilde{\Gamma}_{ik} u_k = -i \frac{\rho\omega^2}{k - i\alpha} u_i \tag{5C.8}$$

This expression is derived using the Christoffel Equation 5C.6. Since the particle velocity can be written as:

$$\frac{\partial u_i}{\partial t} = i\omega u_i \tag{5C.9}$$

the specific wave impedance Z for an attenuated plane wave, defined as minus the ratio of the above traction force $T_{ij} n_j$ and particle velocity $\partial u_i / \partial t$, is equal to:

$$Z = \frac{\rho\omega}{k - i\alpha} \tag{5C.10}$$

Thus, for cases where the attenuation coefficient α is non-zero, the specific wave impedance becomes a complex quantity.

Chapter 6

Conclusion

The subject of this thesis is ultrasonic stress measurements. A wide range of topics have been touched upon: the theory of acoustoelasticity; the obstacles to be overcome when performing the ultrasonic experiments; the experimental results; model calculations relating to the ultrasonic technique. The conclusions drawn here place these aspects in a broader context.

Acoustoelastic stress evaluation

In view of the experimental results described in Chapter 4, it is concluded that the *theoretical description* given in Chapter 2 is adequate. For materials with a texture-induced anisotropy ranging from negligibly small (aluminium) to extremely large (pipeline steel), the results can be well described by means of the tensor formulation presented. It is also believed that the concept of describing acoustoelastic material behaviour by means of a tensor quantity is extremely concise and that it is closely linked to the way in which elastic properties, for example, are described.

The results of the model calculations presented in Chapter 5 show that diffraction inherently causes deviating time-of-flight results, depending on specimen thickness and type of transducer (size and frequency characteristic). Consequently the *reference values* used for evaluating absolute stress levels will also be affected. They must therefore be used with care when the values are obtained under conditions different from those occurring during the actual stress measurement. The calculation model might make it possible to correct for this effect.

Experimental technique

The experimental results (Chapter 4) have shown that the *technique* itself, as outlined in Chapter 3, satisfies the requirements for acoustoelastic stress evaluation in steel using absolute shear and longitudinal time-of-flight data. Furthermore, the reproducibility of this type of measurement technique, using a coupling layer with increased thickness, was confirmed by the results of the model calculations.

Application

The following points may be noted concerning the application of the acoustoelastic stress evaluation technique described in this thesis:

- *Applied stress evaluation*, using shear waves only, can provide an additional tool for

performing various mechanical experiments under laboratory conditions. This includes cases where it is necessary to reposition the ultrasonic transducer between measurements. A clear example is the evaluation of the J-integral fracture parameter as described in Section 4.3.5.

- *Absolute stress evaluation*, using the combined shear-longitudinal transducer, is highly promising for steel plate. For other alloys, such as aluminium, a different type of transducer may be required in order to avoid overlap of the echoes from the two wave types.
- In the case of structural parts, stress evaluation is particularly favourable if the elastic and acoustoelastic properties are *homogeneous* over large plate areas. A typical example would be the aluminium plate used in aircraft construction.

References

1. Auld, B.A., Acoustic Fields and Waves in Solids, Vols. 1 & 2, John Wiley & Sons, New York, 1973.
2. Berlincourt, D., Piezoelectric Crystals and Ceramics, in "Ultrasonic Transducer Materials", (O.E. Mattiat ed.), Plenum Press, New York, 1971.
3. Blessing, G.V., Hsu, N.N. and Proctor, T.M., Ultrasonic shear wave measurements of known residual stress in aluminum, in "Nondestructive Methods for Material Property Determination", (C.O. Ruud & R.E. Green Jr. eds.), Plenum Press, New York, 1984, pp. 353-363.
4. Blinka, J. and Sachse, W., Application of Ultrasonic-pulse-spectroscopy Measurements to Experimental Stress Analysis, Exp. Mech., Vol. 16, 1976, pp. 448-453.
5. Bracewell, R.N., The Fourier Transform and its Applications, 2nd edition, McGraw-Hill, Singapore, 1978.
6. Chandrasekaran, N. and Salama, K., Relationship between stress and temperature dependence of ultrasonic shear velocity, in "Nondestructive Methods for Material Property Determination", (C.O. Ruud & R.E. Green Jr. eds.), Plenum Press, New York, 1984, pp. 393-403.
7. Clark, A.V., Mignogna, R.B. and Sanford, R.J., Acousto-elastic Measurement of Stress and Stress Intensity Factors around Crack Tips, Ultrasonics, Vol. 21, 1983, pp. 57-64.
8. Clark, A.V., Fukuoka, H., Mitraković, D.V. and Moulder, J.C., Acoustoelastic Measurements pertaining to the Nondestructive Characterization of Residual Stress in a Heat-Treated Steel Railroad Wheel, Materials Evaluation, Vol. 47, 1989, pp. 835-841.
9. Crecraft, D.I., The measurement of applied and residual stresses in metals using ultrasonic waves, J. Sound. Vib., Vol. 5, 1967, pp. 173-192.
10. Dieulesaint, E. and Royer, D., Elastic Waves in Solids - Applications to Signal Processing, John Wiley & Sons, Chichester, 1980.
11. Ewalds, H.L. and Wanhill, R.J.H., Fracture Mechanics, D.U.M. Delft - Edward Arnold London, 1991.
12. Elmore, W.C. and Heald, M.A., Physics of Waves, McGraw-Hill, New York, 1969.
13. Eringen, A.C. and Şuhubi, E.S., Elastodynamics. Vol. 1: Finite Motions, Academic Press, New York, 1974.
14. Hsu, N.N., Acoustical Birefringence and the Use of Ultrasonic Waves for Experimental Stress Analysis, Exp. Mech., Vol. 14, 1974, pp. 169-176.

15. Hsu, N.N. and Sachse, W., Generation and detection of plane-polarized ultrasound with a rotatable transducer, Rev. Sci. Instrum., Vol. 46, No. 7, 1975, pp. 923-926.

16. Hsu, N.N., Proctor, T.M. and Blessing, G.V., An Analytical Approach to Reference Samples for Ultrasonic Residual Stress Measurement, J. Testing and Eval., Vol. 10, No. 5, 1982, pp. 230-234.

17. Hull, D.R., Kautz, H.E. and Vary, A., Measurement of Ultrasonic Velocity Using Phase-Slope and Cross-Correlation Methods, Materials Evaluation, Vol. 43, 1985, pp. 1455-1460.

18. Hunter, J.B.C., Acoustoelastic Analysis of Center-Cracked Panels, Ph.D. Dissertation, Department of Applied Mechanics, Stanford University, June 1979.

19. Hunter, J., King, R., Kino, G., Barnett, D.M., Herrmann, G. and Ilíc, D., The use of acoustoelastic measurements to characterize the stress states in cracked solids, DARPA/AFML Review of Progress in Quantitative Nondestructive Evaluation, La Jolla, Calif., July 8-13 1979, Rockwell International Science Center, Thousand Oaks, Calif. 91360, 1980, pp. 422-428.

20. Imanishi, E., Sasabe, M. and Iwashimizu, Y., Experimental Study on Acoustical Birefringence in Stressed and Slightly Anisotropic Materials, J. Acoust. Soc. Am., Vol. 71, 1982, pp. 565-572.

21. Iwashimizu, Y. and Kubomura, K., Stress Induced Rotation of Polarization Directions of Elastic Waves in Slightly Anisotropic Materials, Int. J. Solids Struct., Vol. 9, 1973, pp. 99-114.

22. Jaffe, B., Cook, W.R. and Jaffe, H., Piezoelectric Ceramics, Academic Press, London, 1971.

23. Janssen, M. and Zuidema, J., An Acoustoelastic Determination of the Stress Tensor in Textured Metal Sheets using the Birefringency of Ultrasonic Shear Waves, J. Nondestr. Eval., Vol. 5, No. 1, 1985, pp. 45-52.

24. Janssen, M., Toepassing van het akoestoelastisch effekt ter bepaling van J als contour-integraal, Master's thesis, Delft University of Technology, 1985.

25. Janssen, M. and Zuidema, J., An ultrasonic method for the determination of the J contour-integral, In "Proceedings of the 6th European Conference on Fracture", (H.C. van Elst and A. Bakker eds.), Emas, Warley, UK, 1986, pp. 415-426.

26. Janssen, M., Evaluation of an Applied Plane-Stress Tensor Distribution Using Ultrasonic Shear Waves, Exp. Mech., 1988, pp. 226-231.

27. Janssen, M., Ultrasonic Stress Evaluation in Pipeline Steel, For N.V. Nederlandse Gasunie Groningen (report n° BB 00886462), December 1989.

28. Janssen, M., Ultrasonic Stress Evaluation in Steel using both Shear and Longitudinal Bulk Waves, NIL-Fracture project, report n° PG 90-06, The Netherlands Institute of Welding, The Hague, February 1990.

29. Janssen, M., The Ultrasonic evaluation of Absolute Stress Levels in Steel using Shear and Longitudinal Waves Simultaneously, In "Residual Stresses - III, Science and Technology", (H.Fujiwara, T.Abe and K.Tanaka eds.), Elsevier Applied Science, London, 1992, pp. 322-327.

30. Janssen, M., Reproducible Time-of-Flight Measurements with a Piezoelectric Transducer for Acoustoelastic Stress Evaluation, In "Proceedings of the Fourth International Conference on Residual Stresses", Society for Experimental Mechanics Inc., Bethel, 1994, pp. 140-147.

31. Kim, B.S., A P/S Mode Transducer with a Piezoelectric Ceramic of PZT Type: Theory and Fabrication, Materials Evaluation, Vol. 40, 1982, pp. 186-190 and p. 197.

32. Kino, G.S., Acoustoelasticity, in "Elastic Waves and Non-Destructive Testing of Materials", (Y.H. Pao ed.), Vol. 29, Am. Soc. Mech. Eng., New York, 1978, pp. 129-139.

33. Krautkrämer, J. and Krautkrämer, H., Werkstoffprüfung mit Ultraschall, Springer-Verlag, Berlin, 1975.

34. Mak, D.K. and Steinfl, R.B., Ultrasonic velocity measurements of Au-W composites, Nondestr. Test. Eval., Vol. 5, No. 1, 1989, pp. 39-48.

35. Malvern, L.E., Introduction to the Mechanics of a Continuous Medium, Prentice-Hall Inc., Englewood Cliffs, 1969.

36. Mason, W.P., Physical Acoustics and the Properties of Solids, O. van Nostrand Company Inc., Princeton, 1958.

37. Mott, G. and Tsao, M.C., Acousto-Elastic Effects in Two Structural Steels, in "Nondestructive Methods for Material Property Determination", (C.O. Ruud & R.E. Green Jr. eds.), Plenum Press, New York, 1984, pp. 377-392.

38. Muijderman, E.A., Inleiding Tribotechniek, Ontwerpleer III (w5) serie B, Afdeling der Werktuigbouwkunde, TU-Delft, 1978.

39. Ogden, R.W., Non-Linear Elastic Deformations, Ellis Horwood Ltd., Chichester, 1984.

40. Okada, K., Stress-Acoustic Relations for Stress Measurement by Ultrasonic Technique, J. Acoust. Soc. Jap. (E), Vol. 1, No. 3, 1980, pp. 193-200.

41. Okada, K., Acoustoelastic Determination of Stress in Slightly Orthotropic Materials, Exp. Mech., Vol. 21, 1981, pp. 461-466.

42. Pao, Y.H., Sachse, W. and Fukuoka, H., Acoustoelasticity and Ultrasonic Measurements of Residual Stresses, in "Physical Acoustics", (W.P. Mason & R.N. Thurston eds.), Vol. XVII, Academic Press Inc., Orlando, 1984, pp. 61-143.

43. Papadakis, E.P., Ultrasonic Phase Velocity by the Pulse-Echo-Overlap Method Incorporating Diffraction Phase Corrections, J. Acoust. Soc. Am., Vol. 42, 1967, pp. 1045-1051.

44. Press, W.H., Flannery, B.P., Teukolsky, S.A. and Vetterling, W.T., Numerical Recipes in Pascal (The Art of Scientific Computing), Cambridge University Press, New York, 1989.

45. Reiner, M., Rheology, in "Encyclopedia of Physics", (S. Flügge ed.), Springer-Verlag, Berlin, 1958, pp. 434-550.

46. Rice, J.R., Mathematical analysis in the mechanics of fracture, in "Fracture, an advanced Treatise", (H. Liebowitz ed.), Academic Press, New York, Vol. 2, 1968, pp. 192-311.

47. Silk, M.G., Ultrasonic Transducers for Nondestructive Testing, Adam Hilger Ltd, Bristol, 1984.

48. Smith, R.T., Stern, R. and Stephens, R.W.B., Third Order Elastic Moduli of Polycrystalline Metals from Ultrasonic Velocity Measurements, J. Acoust. Soc. Am., Vol. 40, 1966, pp. 1002-1008.

49. Stanford, E.G. and Fearon, J.H., Progress in Non-Destructive Testing, Vol. 2, Heywood & Company Ltd., London, 1960.

50. Tada, H., Paris, P.C. and Irwin, G.R., The stress analysis of cracks Handbook, Del Research Corporation, Hellertown, 1973.

51. Timoshenko, S.P. and Goodier, J.N., Theory of Elasticity, 3rd ed., McGraw-Hill, New York, 1970.

52. Tokuoka, T. and Iwashimizu, Y., Acoustical birefringence of ultrasonic waves in deformed isotropic elastic materials, Int. J. Solids Struct., Vol. 4, 1968, pp. 383-389.

53. Toupin, R.A. and Bernstein, B., Sound Waves in Deformed Perfectly Elastic Materials. Acoustoelastic Effect, J. Acoust. Soc. Am., Vol. 33, 1961, pp. 216-225.

54. Yamasaki, T., Hirao, M. and Fukuoka, H., Dependence of Acoustoelastic Constants on External Magnetic fields, In "Proceedings of 5th International Symposium on Nondestructive characterization of Materials", Karuizawa, May 1991.

55. Zuidema, J. and Soest, Th.M. van, An Acoustic Determination of the Direction of the Vibration of Ordinary Acoustic Shear Wave Transducers, J. Nondestr. Eval., Vol. 3, No. 2, 1982, pp. 77-84.

Summary

The *propagation of acoustic waves* through a material subject to elastic deformation is determined by the wave equation for an infinitesimal dynamic displacement superimposed on a finite static displacement. Based on this equation, a relation is established between acoustic data obtained using shear and longitudinal bulk waves and the components of a two-dimensional stress field.

Using this relation, applied stress levels may be evaluated by measuring the time of flight and polarization direction of birefringent shear wave components before and after the application of a load. Absolute stress levels may be evaluated by the additional measurement of the longitudinal time of flight, using reference values obtained in material which is free of stress.

The acoustoelastic behaviour of the material is expressed in the form of a two-dimensional tensor, which can be quantified by performing uniaxial tensile tests in at least two well-chosen directions.

An *ultrasonic technique* is developed based on the pulse-echo method and using a piezoelectric transducer capable of transmitting and receiving shear and longitudinal waves simultaneously. In actual practice the transducer-specimen coupling, consisting of a viscous fluid in order to accommodate shear waves, proves to be a weak link. It is found here that the use of a sufficiently thick layer improves the reproducibility of time-of-flight measurements to better than 1 part in 20 000, even after repositioning the transducer.

In the experimental technique a specially designed holder permits accurate positioning of the transducer on the specimen surface. Using a stepper motor, the transducer polarization direction can be set with a resolution of $^1/_8°$. During measurements a computer acquires time of flight, echo amplitude and specimen temperature and simultaneously controls back-face echo selection and stepper motor position.

Experiments are performed on aluminium alloy 2024-T351, two structural steel qualities and a pipeline steel. The results indicate that the acoustoelastic effect is considerably smaller in steel than in aluminium. Moreover, it is found that there is a relation between the elastic and acoustoelastic anisotropy. On the one hand the acoustoelastic behaviour of the hot-rolled structural steel qualities is found to be isotropic; in the cold-deformed pipeline steel, on the other hand, stresses in the axial direction induce an effect which is 1.8 times higher compared with stresses in the circumferential direction.

A number of stress evaluations were performed on aluminium. First a disc was compressed diametrically in various directions. The ultrasonically determined stress components in the centre of the disc correlate well with the elastic solution available. Following this, the plane stress field around the crack tip of a compact-tension specimen was determined, employing

both the relative and the absolute evaluation method. Using these stress values, the J fracture parameter was numerically integrated along several contours surrounding the crack tip. The results are reproducible and in good agreement with estimates from both linear elastic fracture mechanics and the finite-element method.

Measurements on the two structural steel qualities, with comparable composition but originating from different manufacturers, suggest almost identical acoustoelastic behaviour. This reproducibility suggests that absolute stress evaluation in this material is within reach. In the pipeline steel the large elastic anisotropy will in practice prevent shear stresses from being evaluated with an acceptable accuracy. On the other hand, it is possible to determine normal stresses in the axial and circumferential directions.

A *computer model* is developed in order to assess the factors affecting pulse-echo measurements. The piezoelectric transducer, the transducer-specimen coupling provided by a viscous fluid, and wave diffraction in the specimen are important elements in this model. In view of possible transducer misalignment, the case of a slightly tilted transducer is also considered. The ultrasonic properties of the viscous couplant, which are essential for the model calculations, are determined in separate experiments.

The calculation results show that, depending on specimen thickness, transducer size and frequency, diffraction in the specimen inherently causes the time of flight to deviate from the nominal value. This aspect needs to be considered when reference values are used which have been obtained under different diffraction conditions.

For thin coupling layers the time of flight is found to be affected even by slight variations in the layer thickness, as was already suggested by experimental results. Moreover, the electrical conditions relating to the transducer and transducer misalignment are found to have more effect on the measured time of flight. These results show the inadequacy of conventional practice, in which the transducer is positioned on the specimen surface using a constant pressure, thus leading to a continuously decreasing coupling layer thickness.

On the basis of the test results, the overall *conclusion* is that the method for acoustoelastic stress evaluation described in this thesis can be well applied using the experimental technique developed and that the method yields good results for a variety of metals. The model calculations support the alternative approach of using an intentionally thick layer of viscous fluid for the acoustic coupling of the piezoelectric transducer and the specimen.

Samenvatting

De *voortplanting van akoestische golven* door een materiaal dat onderworpen is aan een elastische vervorming wordt bepaald door de golfvergelijking voor een oneindig kleine dynamische verplaatsing gesuperponeerd op een eindige verplaatsing. Op basis van deze vergelijking is een verband afgeleid tussen akoestische gegevens verkregen met transversale en longitudinale bulkgolven en de componenten van een tweedimensionaal spanningsveld.

Met behulp van dit verband kunnen opgelegde spanningsniveaus bepaald worden door looptijden en polarisatierichtingen te meten van dubbelgebroken transversale golfcomponenten vóór en na het aanbrengen van een belasting. Absolute spanningsniveaus kunnen worden bepaald door ook de longitudinale looptijd te meten en gebruik te maken van referentiewaarden verkregen in spanningsvrij materiaal.

Het akoesto-elastisch materiaalgedrag wordt uitgedrukt in de vorm van een tweedimensionale tensor die kan worden gekwantificeerd door éénassige trekproeven uit te voeren in tenminste twee geschikt gekozen richtingen.

Er is een *ultrasone techniek* ontwikkeld die gebaseerd is op de puls-echo methode. Er wordt gebruik gemaakt van een piëzo-elektrische transducer die gelijktijdig transversale en longitudinale golven kan uitzenden en ontvangen. Om de voortplanting van transversale golven tussen transducer en proefstuk mogelijk te maken wordt een visceuze vloeistof gebruikt. In de praktijk blijkt deze koppeling een zwakke schakel te zijn. Onderzoek wijst uit dat een voldoende dikke laag de reproduceerbaarheid van looptijdmetingen verhoogt tot beter dan 1 op 20 000, zelfs na herplaatsing van de transducer.

Bij deze experimentele techniek maakt een speciaal ontworpen houder nauwkeurige plaatsing van de transducer op het proefstukoppervlak mogelijk. Verder kan, met behulp van een stappenmotor, de polarisatierichting van de transducer worden ingesteld met een resolutie van $^1/_8°$. Tijdens metingen registreert een computer de looptijd, echoamplitude en proefstuktemperatuur, terwijl tegelijkertijd de selectie van de juiste proefstukecho en de positie van de stappenmotor geregeld worden.

Er zijn *proeven* uitgevoerd aan de aluminium legering 2024-T351, twee constructiestaalsoorten en een pijpleidingstaal. De resultaten geven aan, dat het akoesto-elastisch effect in staal aanzienlijk geringer is dan in aluminium. Verder is gevonden dat er een verband bestaat tussen de elastische en akoesto-elastische anisotropie. Enerzijds blijkt het akoesto-elastisch gedrag van de warm gewalste constructiestaalsoorten isotroop te zijn, terwijl anderzijds, in het koud vervormde pijpleidingstaal, spanningen in axiale richting een 1,8 maal zo hoog effect veroorzaken als spanningen in de omtreksrichting.

Aan aluminium is een aantal spanningsmetingen uitgevoerd. Allereerst is een schijf in verschillende richtingen diametraal op druk belast. De ultrasoon bepaalde spanningscomponen-

ten in het midden van de schijf bleken goed te correleren met de beschikbare elastische oplossing. Vervolgens is rond de scheurtip in een "compact tension" proefstuk het vlakspanningsveld bepaald met zowel de relatieve als de absolute bepalingsmethode. Met behulp van deze spanningswaarden is de J breukparameter numeriek geïntegreerd langs een aantal contouren rond de scheurtip. De resultaten zijn reproduceerbaar en komen goed overeen met schattingen op basis van de lineair elastische breukmechanica en de eindige-elementenmethode.

De metingen aan de twee constructiestalen, die een vergelijkbare samenstelling hebben maar afkomstig zijn van verschillende fabrikanten, duiden op een bijna identiek akoesto-elastisch gedrag. Deze reproduceerbaarheid suggereert, dat absolute spanningsbepaling in dit materiaal tot de mogelijkheden behoort. In het pijpleidingstaal zal het, door de grote elastische anisotropie, praktisch gesproken onmogelijk zijn om schuifspanningen met een aanvaardbare nauwkeurigheid te bepalen. Normaalspanningen in axiale en omtreksrichting zijn daarentegen wel goed meetbaar.

Er is een *computermodel* ontwikkeld om de factoren die puls-echo metingen beïnvloeden te beoordelen. Belangrijke onderdelen van dit model zijn de piëzo-elektrische transducer, de transducer-proefstuk koppeling gevormd door een visceuze vloeistof en golfdiffractie in het proefstuk. Om het geval van een niet goed uitgelijnde transducer te kunnen beoordelen, wordt ook een enigszins scheve transducer beschouwd in het model. De ultrasone eigenschappen van de visceuze koppelvloeistof, die essentieel zijn voor de modelberekeningen, zijn via aparte proeven bepaald.

De berekeningsresultaten laten zien, dat afhankelijk van proefstukdikte en transducertype (afmetingen en frequentie), de looptijd afwijkt van de nominale waarde als gevolg van diffractie in het proefstuk. Dit aspect moet meegenomen worden, als referentiewaarden worden gebruikt die onder afwijkende omstandigheden bepaald zijn.

Zoals al door proefresultaten was aangegeven, blijkt bij dunne koppellagen de looptijd zelfs door hele kleine laagdikteveranderingen beïnvloed te worden. Ook blijken de omstandigheden aan de elektrische kant van de transducer en een onjuiste transduceruitlijning nu meer invloed op de gemeten looptijd te hebben. Deze resultaten geven de ongeschiktheid aan van de gangbare praktijk waarbij de transducer met een constante kracht op het proefstukoppervlak gedrukt wordt waardoor de koppellaagdikte voortdurend afneemt.

Gebaseerd op de proefresultaten, luidt de globale *conclusie* dat de methode voor akoesto-elastische spanningsmeting zoals beschreven in dit proefschrift goed toegepast kan worden met de ontwikkelde experimentele techniek en dat de methode goede resultaten geeft voor een verscheidenheid aan metalen. De modelberekeningen ondersteunen de alternatieve aanpak om een met opzet dik gekozen laag visceuze vloeistof te gebruiken voor de akoestische koppeling van de piëzo-elektrische transducer en het proefstuk.